Centre for Doctoral Training in Energy Storage and its Applications

Department of Chemical and Biological Engineering

The University of Sheffield

Experimental and Computational Analyses of Thermal Runaway in Lithium Iron Phosphate Cells and Battery Packs

Thesis submitted for the degree of Doctor of Philosophy

Peter Bugryniec

pbugryniec1@sheffield.ac.uk

June, 2021

Declaration

I hereby declare that this thesis is entirely of my own work and original in content, and that all sources have been accurately reported and acknowledged, and that this document has not, in its entirety or in part, been submitted at any other institution to obtain an academic qualification.

Abstract

Thermal runaway (TR) is a significant safety concern of Li-ion Batteries (LIBs) that can lead to hazardous events, such as fire and explosion of the battery, that presents a great risk to persons/assets in the vicinity of the battery system. However, through experimental investigation and computational modelling this phenomenon can be better understood, and hence, allow for improved LIB design that leads to safer systems.

The aim of this work was to further the understanding of TR in LFP LIBs, in conjunction with developing improved theory and greater understanding of LIB TR models. The work is split into two main studies. First, experimental studies, in which the TR behaviour of LFP cells by accelerated rate calorimetry (ARC) and oven testing is investigated to carry out a novel assessment of LFP cells at various state of charge (SOC) and under rapid heating scenarios. Second, computational studies, in which a novel advanced abuse model (AAM) is developed to model the TR of LIBs, which is then parameterised for the study of LFP cells and extended to investigate the thermal runaway propagation (TRP) resilience of LFP LIB packs. Within the development of the AAM a novel representation of the cell pressurisation is considered, viz. assuming that the electrolyte/gas mixture within the cell is at bubble point.

From the experimental work, results show, at SOC of 100% and 110%, the negative and positive electrode reactions are the main contributors to TR, while at lower SOC it is the negative electrode reaction that dominates. Cells at 100% SOC exposed to high temperatures during oven tests show, along with the ARC analysis, that the presence of the cathode and electrolyte reactions leads to an increase in the severity of a TR event for oven temperatures above 200°C. By comparing the heat generated in ARC and oven testing, it is shown that ARC does not fully capture the self-heating and TR safety hazard of a cell, unlike oven testing. This work gives new insight into the nature of the decomposition reactions and also provides an essential data set useful for model validation which is of importance to those studying LFP cells computationally.

In developing the AAM, the novel bubble pressure assumption is validated against experimental data, and it is shown that the AAM significantly improves the predictions of time to TR and of temperatures after TR. Further, it is shown that there is significant uncertainty in the parameters defining the decomposition reactions for LFP cells. Importantly, cell pressurisation is most dependent on the gases released by the solid electrolyte interphase reaction, and venting is dependent on cell burst pressure and reaction activation energies. The AAM is essential for accurate abuse modelling, due to its improved temperature predictions, and considerably enhances the LIB TR field of study.

In studying the TRP potential of LFP packs it is shown that TRP does not occur when an initiation cell undergoes total internal short circuit. This occurs, as, even though the abused cell undergoes complete TR, the amount of energy released by the abused cell does not raise the temperature of adjacent cells to the point that the energetic NE reaction develops significant decomposition rates. It is also shown that given different reaction parameters that lead to similar TR events of a single cell do not lead to significant variation in pack results. Finally, lower cell surface emissivities are shown to reduce the overall cell-to-cell heat transfer, and hence can enable safer lighter packs by simple cell surface alterations.

Acknowledgements

Firstly, I would like to thank my supervisors Dr Solomon Brown and Dr Jonathan Davidson for their unwavering support, guidance and knowledge. Without which this PhD would not be possible.

Next, I would like to thank David Palmer, a member of the technical staff in the Department of Chemical and Biological Engineering, for his assistance in experimental matters. I would also like to thank Dr Dennis Cumming for his assistance in analysing my experimental practices and results to ensure they are appropriate and accurate.

I would like to thank the Energy Storage and Its Applications (ESA) CDT for providing me with the opportunity to undertake this PhD. Further, I would like to thank Sharon Brown of the ESA CDT for her crucial role in ensuring the efficient organisation of the CDT. Additionally, I would like to acknowledge the Engineering and Physical Sciences Research Council for funding the Centre for Doctoral Training in Energy Storage and its Applications (EP/L016818/1).

Also, I would like to thank all the students I have work alongside of and those I have engaged with through collaborative work. Specifically, members of our shared office space that provided motivation, help and, most importantly, a fun and enjoyable working environment and social group. Without them the past four years would have felt much longer.

Finally, I would like to thank my family for their support, encouragement and for what they have taught me throughout life, and my friends for providing needed distractions and keeping me happy. Last, but definitely not least, my girlfriend Noa McAlistair for keeping me motivated and cheerful, and crucially ensuring sufficient supply of tea to see me through the long write up process.

List of Publications

A list of journal and conference papers that I have authored, or collaborated on, that have been published throughout the undertaking of this PhD is presented below. Brief statements of what parts of this thesis have contributed to publications are discussed. Ref. [1] was a collaboration in which my knowledge of the ARC was necessary for the lead author to undertake their required experiments. Refs. [2,3] publish the key ARC and oven results of Chapter 4, with relevant literature and methodology. Refs. [4,5] are collaborations that use the temperature predictions from a classical TR model after parameter sweeps of reaction kinetics and thermo-physical, respectively, as key data set in the papers investigations. Ref. [6] publishes preliminary results of LFP pack investigations carried out in the process of meeting the aim of Chapter 6. Ref. [7] publishes the development and key findings of the AAM from Chapter 5, along with relevant literature and methodology.

[1] T. S. Bryden, B. Dimitrov, G. Hilton, C. P. D. León, P. Bugryniec, S. Brown, D. Cumming, and A. Cruden, "Methodology to determine the heat capacity of lithium-ion cells," *Journal of Power Sources*, vol. 395, pp. 369–378, 2018.

[2] P. J. Bugryniec, J. N. Davidson, and S. F. Brown, "Assessment of thermal runaway in commercial lithium iron phosphate cells due to overheating in an oven test," *Energy Procedia*, vol. 151, pp. 74–78, 2018.

[3] P. J. Bugryniec, J. N. Davidson, D. J. Cumming, and S. F. Brown, "Pursuing safer batteries: Thermal abuse of $LiFePO_4$ cells," *Journal of Power Sources*, vol. 414, pp. 557–568, 2019.

[4] R. Milton, P. Bugryniec, and S. Brown, "Parameter estimation for thermal runaway of li-ion cells: a gaussian process approach," in *29th European Symposium on Computer Aided Process Engineering*, ser. Computer Aided Chemical Engineering, A. A. Kiss, E. Zondervan, R. Lakerveld, and L. Zkan, Eds. Elsevier, 2019, vol. 46, pp. 775–780.

[5] A. S. Yeardley, P. J. Bugryniec, R. A. Milton, and S. F. Brown, "A study of the thermal runaway of lithium-ion batteries: A gaussian process based global sensitivity analysis," *Journal of Power Sources*, vol. 456, p. 228001, 2020.

[6] P. J. Bugryniec, J. N. Davidson, and S. F. Brown, "Computational modelling of thermal runaway propagation potential in lithium iron phosphate battery packs," *Energy Reports*, vol. 6, pp. 189–197, 2020.

[7] P. J. Bugryniec, J. N. Davidson, and S. F. Brown, "Advanced abuse modelling of li-ion cells – A novel description of cell pressurisation and simmering reactions," *Journal of Power Sources*, vol. 474, p. 228396, 2020.

Contents

List of Figures

List of Tables

Nomenclature & Abbreviations

Roman symbols

A	area, m^2
A_i	frequency factor of reaction i, 1/s
C_i	reaction species for reaction i, dimensionless
C_p	specific heat capacity, J/kg K
E_a	activation energy, J/mol
H	heat of reaction, J/g
h_{batt}	height of cell, m
h_{conv}	convection coefficient, $W/m^2 K^4$
h_{enth}	enthalpy, kJ/kg
i	reaction order, dimensionless
j	reaction order, dimensionless
M	Mach number, dimensionless
m	mass, kg
M_i	molar mass for material i, kg/mol
P	pressure, kPa
Q	power, W
q	conductive heat flux, W/m
Q_i	heat generation term from source i, W/m^3
R	ideal gas constant, 8.3145 J/mol K
r	radius, m
R_i	gas constant for material i, kJ/kg K
T	temperature, K
t	time, s
t_{sei}	SEI layer thickness, dimensionless
U	internal energy, J
u	velocity, m/s
V	volume, m^3
v	specific volume, m^3/kg
W	work done, W
W_i	volume specific content of reactant i, kg/m^3
x	vapour fraction, dimensionless
x_b	mole fraction (bubble pressure model), dimensionless

Greek symbols

η_h	estimation void volume fraction within a cell

γ	ratio of specific heats, dimensionless
κ	conductivity coefficient, $\mathrm{W/m\,K}$
ρ	density, $\mathrm{kg/m^3}$
σ	Stefan-Boltzmann constant, $5.670 \times 10^{-8}\,\mathrm{W/m^2\,K^4}$
ε	emissivity value, dimensionless

Subscript

0	initial value
alt	alternate definition of a variable
amb	ambient
ave	average
b	re-defined property for the bubble pressure model
bubble	property related to bubble pressure model
carbon	anode (carbon) material
cell	overall property of a cell
decomp	decomposition reactions
e	electrolyte reaction
env	environment
est	estimate
g	gas
h	head space
i	place holder for a generic material, reaction or element
jelly	jelly roll
l	liquid
lv	difference between vapour and liquid values
mix	electrolyte-gas mixture
ne	NE reaction
pe	PE reaction
pos	cathode material
rxn	overall reaction values for a cell
s	solid
sat	saturation
sei	SEI reaction
smr	simmering reaction
surf	surface
t	varying with time
v	vapour
vap	vaporisation
vent	property related to cell venting

Superscript

$*$	a re-defined variable
0	initial value
max	maximum
mix	electrolyte-gas mixture

Acronyms

AAM	advanced abuse model
ARC	accelerated rate calorimetry
BES	battery energy storage
BMS	battery management system
BPV	bubble pressure venting
CC	constant current
CID	current interrupt device
CSBC	copper slug battery calorimetry

CV	constant voltage
DMC	dimethyl carbonate
DOF	degree of freedom
DSC	differential scanning calorimetry
EC	electrochemical (in reference to modelling) or ethylene carbonate (in reference to electrolytes)
EV	electric vehicle
FEV	fully electric vehicle
GHG	greenhouse gas
HEV	hybrid electric vehicle
HT	heat transfer (in reference to sub-models)
HWS	heat wait seek
LCO	lithium cobalt oxide
LFP	lithium iron phosphate
Li^+	positively charged lithium ion
LIB	lithium-ion battery
LMO	lithium manganese oxide
LTO	lithium titanate
MAH	mass composition A, with high burst pressure limit
MAL	mass composition A, with low burst pressure limit
MBH	mass composition B, with high burst pressure limit
MBL	mass composition B, with low burst pressure limit
NCA	lithium nickel cobalt aluminium oxide
NE	negative electrode (in reference to reactions) or polyethylene (in reference to materials)
$NiMH$	nickel metal hydride
NMC	lithium nickel manganese cobalt oxide
ODE	ordinary differential equation
PCM	phase change material
$PHEV$	plug-in hybrid electric vehicle
PP	polypropylene
PPV	partial pressure venting
PTC	positive temperature coefficient
PVC	polyvinyl chloride
$PVDF$	polyvinylidene difluoride
ROM	reduced order model
RSD	relative standard deviation
SEI	solid electrolyte interphase
SOC	state of charge
SOS	state of safety
TC	thermocouple
TR	thermal runaway
TRP	thermal runaway propagation
$VSP2$	vent sizing package 2

Chapter 1

General Introduction

1.1 Li-ion Batteries in the Wider Scope of Energy Storage

Greenhouse gas (GHG) emissions due to human activities are the widely accepted cause of global warming [1, 2]. To mitigate the dangerous effects of climate change requires, in part, CO_2 GHG emissions to reach a net zero value by the year 2050 [3]. Hence, there is the requirement to implement alternative energy sources, such as renewables and nuclear, to de-carbonise primary energy production, as well as utilising new technologies for: improved energy efficiency; fossil free fuels for transportation; energy storage; and carbon sequestration [4].

The automotive industry has been de-carbonising for the past decade through the development of hybrid (HEV) and plug-in hybrid electric vehicles (PHEV) based on the mature nickel metal hydride (NiMH) battery [5, 6]. Today, LIBs vastly outperform NiMH in terms of high energy capacity (see Fig. 1.1), high cycle efficiency and low self-discharge, whilst being available at a competitive price [6–9]. These characteristics have made Li-ion technology most favourable for EVs as it enables increased vehicle driving range. Hence, through ongoing development in LIB technology, it is predicted that consumer fully electric vehicles (FEV) will become 100% powered by Li-ion technology in the future [10].

Renewable energy sources, such as wind and solar, are being increasingly utilised [12–15]. However, due to renewables' intermittent nature and low inertia, new energy storage technologies are required to provide auxiliary services so that renewables can be fully utilised [16]. Many storage technologies have been proposed as useful to support the grid [17], see Fig. 1.2. However, due to the falling cost of manufacture and flexibility in providing multiple auxiliary services, LIBs are becoming a key energy storage technology for grid scale services [6, 18–21].

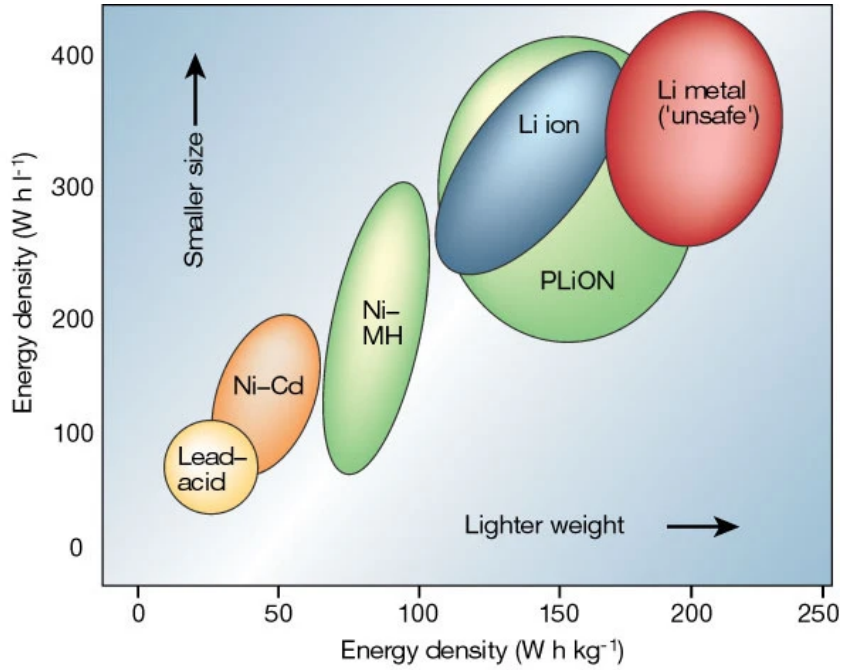

Figure 1.1: Comparison of battery technologies in terms of volumetric and gravimetric energy densities. Reproduced from [11].

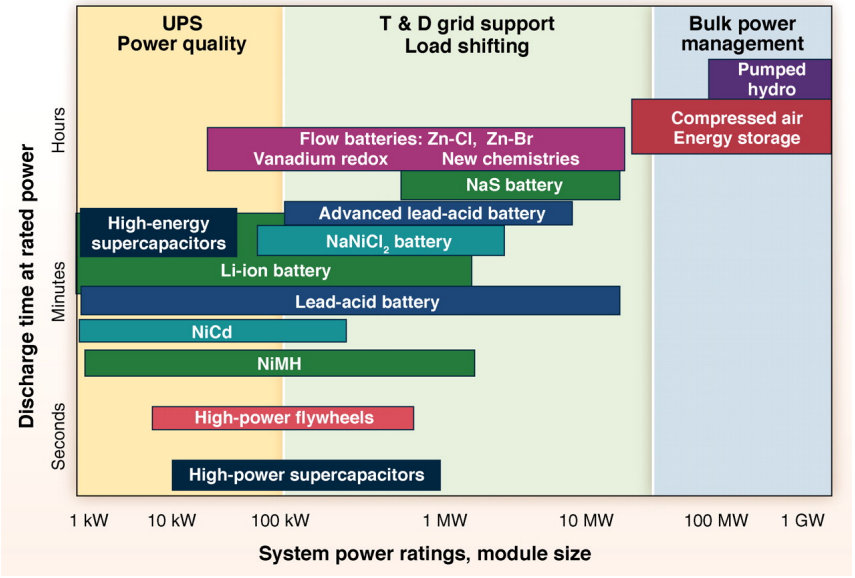

Figure 1.2: Comparison of different energy storage technologies in terms of discharge time and power. Reproduced from [22].

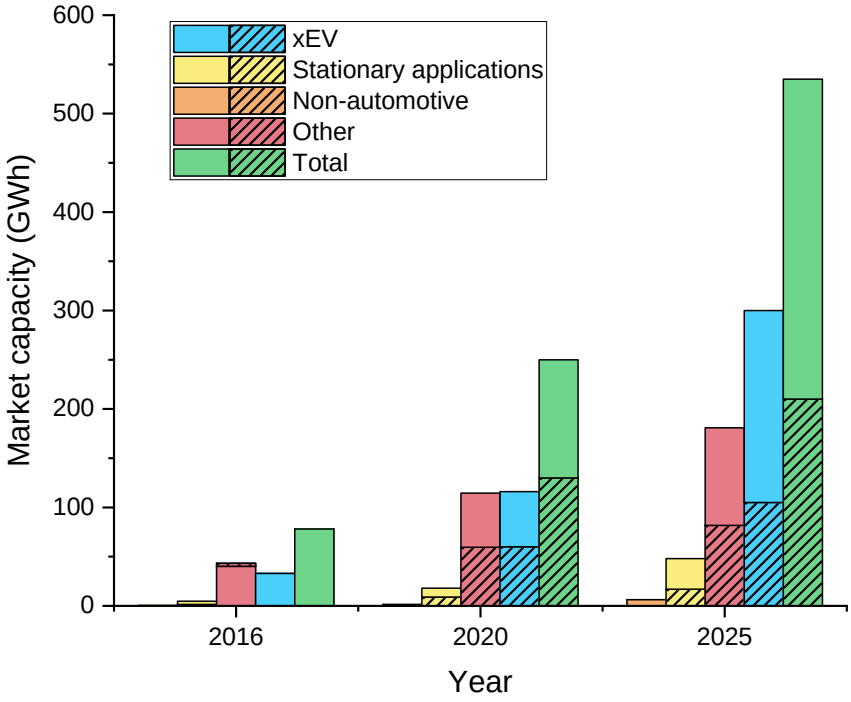

Figure 1.3: Li-ion total global market capacity trends. Solid filled bar is the higher prediction, line filled bar is the lower prediction. xEV is for hybrid and fully electric vehicles i.e. cars, buses etc.; Other includes consumer products, power tools etc.; Non-automotive accounts for applications such as marine. Data from [24]

Overall, the increasing growth of these applications is leading to a significant increase in the installed market capacity of LIBs (see Fig. 1.3). Highlighting the importance of LIBs in the present and the future. Further, as the energy demands of these applications grow, so does the requirement for LIBs to have greater energy capacity [23]. However, Li-ion cells do suffer from safety concerns, which, for increased energy capacity requirements of LIBs leads to greater safety risks. This is discussed in Section 1.3, first however, a description of the Li-ion cell in more detail is given so that the safety concerns of Li-ion cells can be fully understood.

1.2 Lithium-ion Batteries - An Overview

A battery, Li-ion or otherwise, is a collection of one or more cells electrically connected together in such manner to meet the electrical demands of a user [25]. With respect to LIBs, the broad term “lithium-ion” or “Li-ion” covers a type of electrochemical cell that utilises lithium ions to store charge. The chemical energy stored in a cell’s active materials is converted into electric energy by the means of an electrochemical oxidation-reduction (redox) reaction [25].

The construction and operation of the individual cells within a battery are described in Section 1.2.1, while the various Li-ion chemistries and their characteristics are outlined on Section 1.2.2.

1.2.1 Li-ion Cell Construction & Operation

A cell is constructed of several components: the electrodes, separator, current collectors and electrolyte, collectivity termed the jelly roll, which is housed in a container that can take several forms, i.e. cylindrical, prismatic or pouch [25]. Figure 1.4 shows the construction of a cell at decreasing scales, from the macroscopic scale of the cell down to the microscopic scale of the particles within a cell's active materials. This figure shows how these components are structured relative to each other.

In common LIBs the anode, cathode and electrolyte are made from carbon (graphite), metal oxides and lithium salts in an organic solvent, respectively [26]. The available cathode materials are further discussed in Section 1.2.2. Further details of the unit cell construction [27–31], electrode construction [32, 33], separator [26, 34, 35] and electrolyte can be found in the cited literature.

Figure 1.4 also shows, on the scale of the active particles, the movement of Li^+ and electrons during operation of a cell. A detailed description of cell operation can be found in Refs. [25, 30]. The redox reactions during operation is summarised (for the example of an LFP cell) by Eq. (1.1) and Eq. (1.2) for the anode and cathode respectively [36].

$$\mathrm{LiC_6} \longleftrightarrow \mathrm{C_6} + \mathrm{Li^+} + \mathrm{e^-} \tag{1.1}$$

$$\mathrm{FePO_4} + \mathrm{Li^+} + \mathrm{e^-} \longleftrightarrow \mathrm{LiFePO_4} \tag{1.2}$$

At the end of discharging, the negative electrode will be depleted of Li^+ while the positive will be saturated with Li^+, the reverse is true for a fully charged cell.

On charging and discharging a battery heat is generated by several reactions. These include reversible entropic reactions and irreversible sources such as Ohmic, contact, enthalpy and mixing [37]. Under normal operational conditions this heat is not an issue. But under extreme environments, inadequate battery cooling or electrical abuse, this heat can build up leading to a dangerous temperature rise [38].

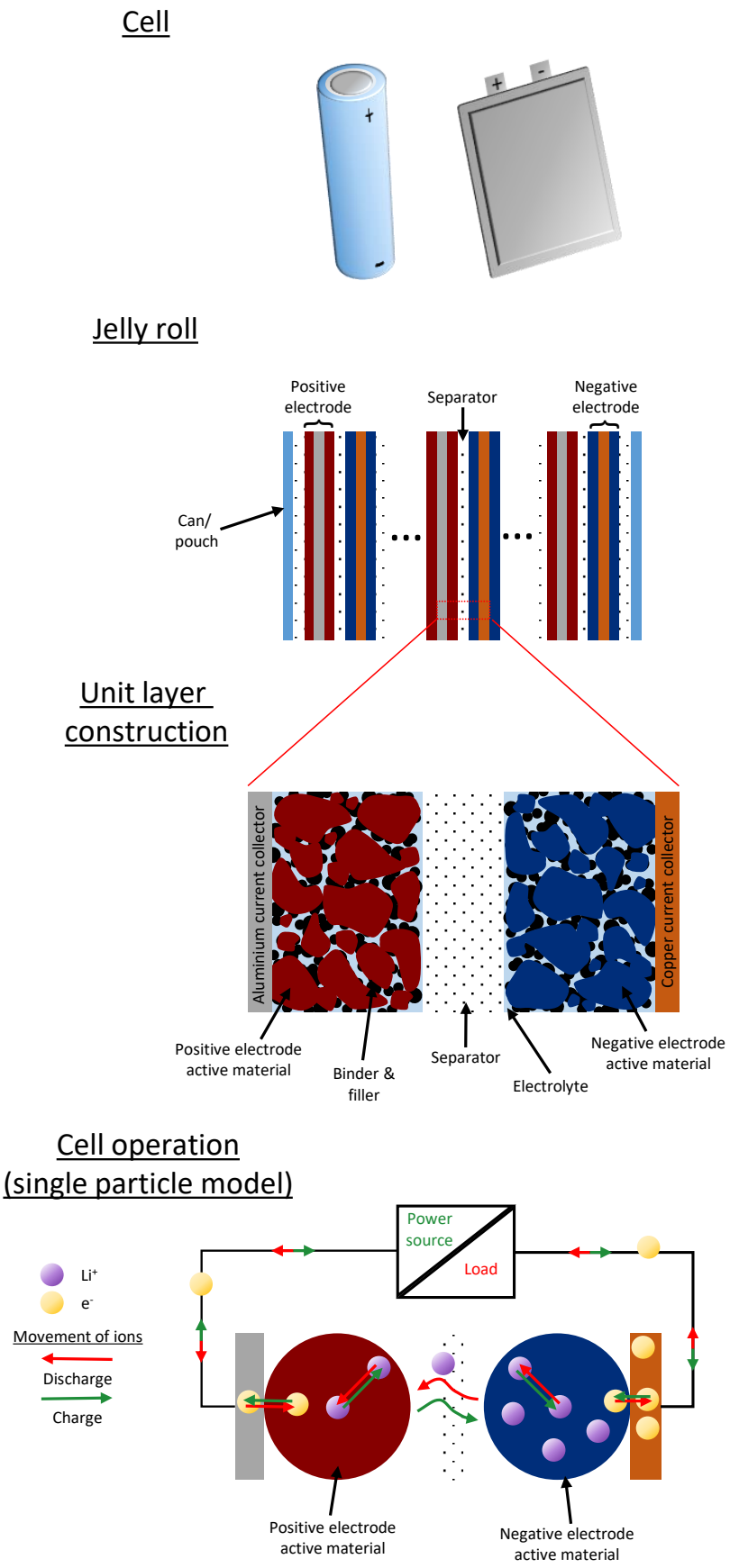

Figure 1.4: Schematic of Li-ion cell construction and operation.

1.2.2 Li-ion Chemistries and Their Cell Characteristics

The distinction between different types of Li-ion cells is by the chemistry of the cell. The chemistry commonly refers to the positive electrode's active material, while the negative electrode active material is commonly carbon based. There are many chemistries available, with the most prominent being:

- Lithium Cobalt Oxide
- Lithium Manganese Oxide
- Lithium Nickel Manganese Cobalt Oxide
- Lithium Iron Phosphate
- Lithium Nickel Cobalt Aluminium Oxide and
- Lithium Titanate (anode)

Table 1.1, presents a comparison of key features of these various Li-ion chemistries, along with common abbreviation that they are referred by. This table shows, that even within the category of Li-ion cells, there is much variation in the performance of a cell in terms of operational voltage, capacity, rate capabilities, cycle life and safety. From Table 1.1 it can be seen that LMO, LFP and LTO are best for power applications, while NCA and NMC are better for applications that require high specific energy. LFP and LTO cells also have long cycle lives, however these are currently the most expensive chemistries. A cell's chemistry also has an effect on cell safety, this is further discussed in Section 1.4. First, the safety concerns of Li-ion cells are introduced in the next section (Section 1.3).

Table 1.1: Characteristics of common Li-ion cell chemistries. Data sourced from Ref. [39].

Cell Chemistry	**Lithium Cobalt Oxide**	**Lithium Manganese Oxide**	**Lithium Nickel Manganese Cobalt Oxide**
Cathode/ anode	$LiCoO_2$/graphite	$LiMn_2O_4$/graphite	$LiNiMnCoO_2$/ graphite
Short name	LCO, Li-cobalt	LMO, Li-manganese	NMC (NCM, CMN, CNM, MNC, MCN)
Year of introduction	1991	1996	2008
Nominal voltage	3.6 V	3.7 V	3.6 V/3.7 V
Operating voltage range	3.0–4.2 V	3.0–4.2 V	3.0–4.2 V/4.3 V
Capacity	150–200 W h/kg	100–150 W h/kg	150–220 W h/kg
Rate capability, charge/discharge	0.7-1C / 1C	0.7-1C (3C max) / 1C (10C possible, 30C pulse)	0.7-1C / 1-2C
Cycle life	500–1,000	300–700	1,000–2,000
Cost	-	-	~420 $/kWh
Comments	Very high specific energy, limited specific power. Cobalt is expensive.	High power, lower capacity, safer than LCO, can be mixed with NMC for improved performance.	High capacity and power. Hybrid cell, suitable for many uses.
Role in current Li-ion market	An early Li-ion cell, no longer relevant.	Less relevant today, limited growth potential.	Leading system; dominant cathode chemistry with increasing market share.

Table 1.1 (cont.): Characteristics of common Li-ion cell chemistries. Data sourced from Ref. [39].

Cell Chemistry	**Lithium Iron Phosphate**	**Lithium Nickel Cobalt Aluminium Oxide**	**Lithium Titanate**
Cathode/ anode	$LiFePO_4$/graphite	$LiNiCoAlO_2$/ graphite	LMO or NMC/ Li_2TiO_3(titanate)
Short name	LFP, Li-phosphate	NCA, Li-aluminium	LTO, Li-titanate
Year of introduction	1996	1999	2008
Nominal voltage	3.2 V/3.3 V	3.6 V	2.4 V
Operating voltage range	2.5–3.65 VV	3.0–4.2 V	1.8–2.85 V
Capacity	90–120 W h/kg	200–260 W h/kg; 300 W h/kg predictable	50–80 W h/kg
Rate capability, charge/discharge	1C / 1C (up to 25C)	0.7C / 1C	1C (5C max) / 10C possible (30C pulse)
Cycle life	>2,000	~500	3,000–7,000
Cost	~580 $/kWh	~350 $/kWh	~1005 $/kWh
Comments	Flat voltage profile but low capacity. One of the safest. Used in speciality markets. Relatively high self-discharge.	Share similarities with LCO. Used primarily as an "energy" cell.	Long life, fast charging, but low specific energy and costly.
Role in current Li-ion market	Used in applications requiring high currents and durability. Moderate market growth.	Mainly used by Panasonic and Tesla. Has growth potential.	Limited to speciality applications due to cost, ultra-fast charging.

1.3 Thermal Runaway Hazard of Li-ion Batteries

The phenomenon most prominent in LIB safety is that of thermal runaway (TR). TR is an event in which a Li-ion cell undergoes an uncontrollable temperature rise, due to the exothermic chemical decomposition of the cells internal components, which can ultimately lead to extremely high temperatures, fire and explosion [38]. This presents significant hazards to people. Further, with the increasing capacity of LIBs there is a greater risk to safety, as a critical failure of a LIB will in turn be more energetic.

The extent of the problem of TR over the past decade is evident from the number of TR incidents, for example, in mobile phones, laptops, Boeing 747 aircraft, HEV/FEVs, E-cigarettes, "hoverboards" and head-phones [40–43]. Figure 1.5 shows several of these TR incidents, spanning different orders of magnitude of battery energy storage capacity, indicating the hazards possible to the general public. In the incidents mentioned here, overcharging, internal short, debris penetration and overheating have all been cited as a cause of TR in one case or the other. Thus highlighting the numerous ways in which TR can be triggered and hence the complexity of the problem.

There is limited data on the total number of LIB incidents worldwide, however fires are estimated to occur in 1 cell in every 1 to 10 million manufactured cells [55]. The Federal Aviation Administration (FAA) keeps a record of incidents involving smoke, fire, extreme heat or explosion associated with LIBs in the USA aviation sector. From 1991 to the 1st August 2019 there have been 265 recorded incidents, with the number increasing each year. In 2017-18, 94 events occurred, half of which were to do with portable battery packs and e-cigarettes, while 18% were due to phones. Further, in the first five months of 2019 alone there were 26 incidents [56]. E-cigarettes lead to a significant number of TR incidents, and are thought to be an increasing problem due to their prominence in the consumer market, which is cost competitive, and is leading to 18650 cells being sold at a low price through re-labelling damaged, or defective cells, that are disposed of by major manufactures [57].

There have been several EV fires initiated by a number of causes: penetration of debris into the pack, short circuit while charging, overcharging, overheating, water immersion into the pack and crashes [58]. Additionally, the hazards presented by TR may not be limited to the initial TR event and fire, as one FEV incident shows. In one occurrence, TR was initiated due to the vehicle crashing, while, hours after the initial battery fire was extinguished visible smoke and audible venting were present without fire, and a further 5 days later the car re-ignited [59]. Similarly, crash testing of Chevrolet Volts in different orientations led to the car catching fire immediately in one case, hours in a second case, while it was not until 1 and 3 weeks later in other cases [60]. This outlines how difficult it can be to confidently state that TR has been fully quenched and that no TR hazard remains.

Figure 1.5: Thermal runaway incidents across various scales of battery energy capacity, (a) E-cigarette explosion in a persons pocket [44] (insert: types of e-cigarettes [45]), (b) *Samsung Galaxy Note 7* smartphone post TR due to internal short due to manufacturing errors [46, 47], (c) "hoverboard" post TR while being on charge [48], (d) *Boeing 787 Dreamliner* auxiliary battery pre/post TR with no definitive cause known [49, 50], (e) *Tesla model S* on fire due to debris penetrating battery [51, 52] and (f) electric-hybrid bus on fire during charging [53, 54].

It is thought that the probability of EV fires, due to the failure of one cell from manufacturing defects, is 1 in 10,000 vehicles [58]. However, the Advanced Propulsion Centre UK/ Automotive Council UK has the goal of eliminating TR in battery packs by 2040 [61].

Further, as LIBs become increasingly used within consumer products, more LIBs are entering local/ council waste management facilities through household waste. The unintentional mixing of LIBs in general waste can lead to severe fire incidents. LIB have been thought to be the cause of large fires at both landfill and electrical waste recycling facilities [62, 63]. In the UK in 2017-18, 25% percent of 510 recorded fires at waste management facilities were attributed to LIBs, this is up from 20% in the previous year [62]. Also, LIBs are causing issues in the recycling of lead acid batteries, in which LIBs have been know to cause fires and explosions in the transport, storage, breaking and smelting operations of lead acid battery recycling [64].

In light of these occurrences, while the number of incidents relative to the total number of manufactured cells is small, it is stated by Spinner *et al.* [55] that the primary concerns with respect to LIBs and safety are a "result from a lack of knowledge and general fear of the unknown". This is understandable considering the vast and diverse uses of LIBs, and the varied ways in which TR can be initiated as well as the unpredictable behaviour of TR. This highlights the need for ongoing research to better understand and predict TR behaviour in order to inform the manufactures, policy-makers and the public leading to increased safety.

1.3.1 Thermal Runaway Process

A major concern with the operation and safety of LIBs is the phenomena of TR. TR is the result of processes, electrochemical, chemical, electrical and thermal, that are individually complex and influential to each other [26]. The safety characteristics of TR of a LIB system depends on [23, 26, 65–67]:

1. the cell type (geometry, materials and inherent electrochemical behaviour, materials activity and interactions);
2. conditions before misuse (state of charge, ageing effect, discharge rate, temperature);
3. type of misuse (over temperature, overcharge, etc.);
4. external measures (built in safety devices, cooling methods, confinement/ packaging); and
5. pack size and configuration.

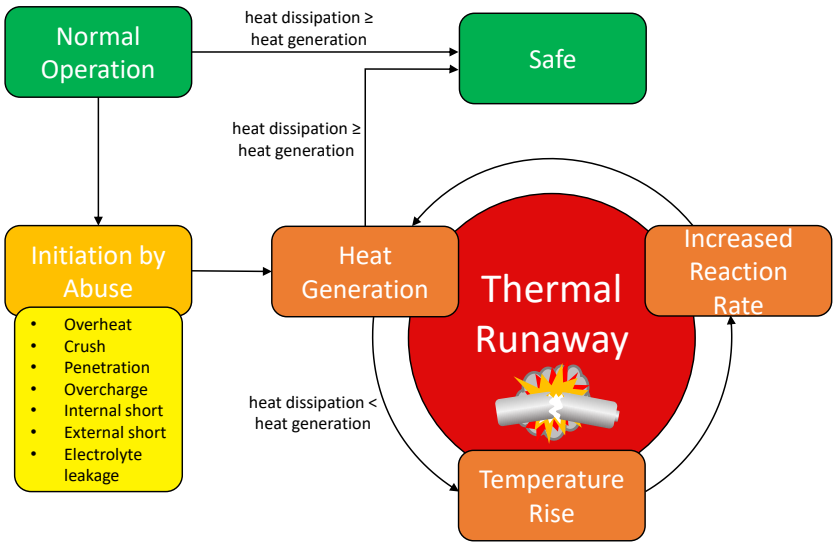

Figure 1.6: The thermal runaway process. A deviation from safe operation (green box) due to possible initiation sources (yellow box) leads to initial heat generation (orange box). The positive feedback loop of TR (cycle of orange boxes) is due to the exothermic decomposition processes of cell components.

The TR process is depicted in Fig. 1.6. It can be seen that the TR process is initiated by heat generation due to a primary abuse event, leading to an initial temperature rise. After which, generally speaking, TR is a process where exothermic reaction(s), from the decomposition of jelly roll components, have increased reaction rates due to an increase in temperature. With this, the self-heating generation rates increase, leading to further increases in temperature and hence reaction rates, and so on [26]. In such a situation, if the heat generated is greater than the heat dissipated, the temperature of the system rises significantly [68]. Further, as the temperature increases, so does the internal pressure of the cell due to gas evolution from the decomposition reactions [26]. The ultimate outcome of TR can be extremely high temperatures, combustion of flammable gases and explosion of the cell.

An important feature to note of TR is the relationship between heat generation and heat dissipation with temperature. The relationship between heat generation and dissipation can be depicted in a Semenov plot, see Fig. 1.7. This is commonly used to visualise TR reactions [26]. Line 4 of Fig. 1.7 depicts a heat generation profile which has an exponential relation with temperature when assuming Arrhenius law. Heat dissipation, represented by lines 1 to 3, has a linear relation with temperature when assuming Newton's law of cooling [68]. As can be seen by comparing the heat generation to the heat dissipation of line 1, the coolant temperature is sufficiently cold enough to control the temperature of the cell below T_1. However, most importantly, above T_1, for a given temperature rise, the heat generated can quickly out strip the heat dissipated leading to a catastrophic TR event.

Within a pack the hazard of TR is multiplied. If a cell catches fire it can spread to adjacent cells and its surroundings [69, 70]. Additionally, once ignited, a LIB fire can

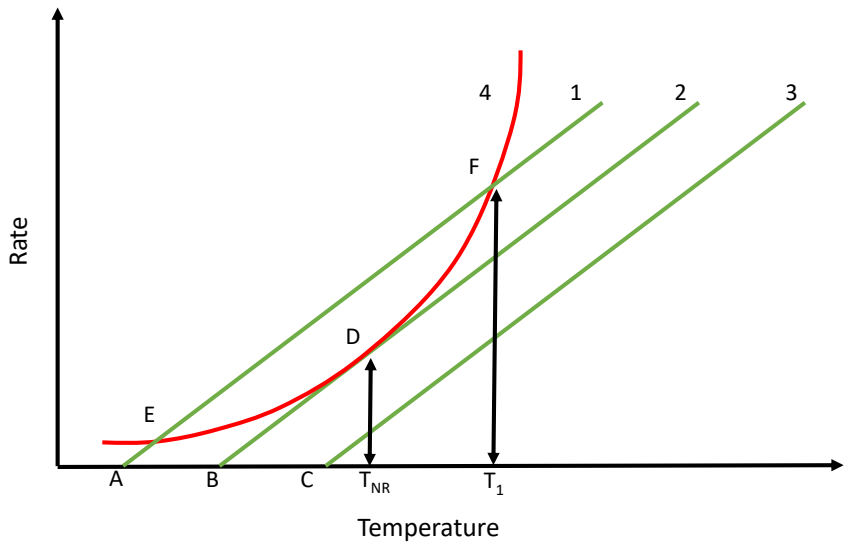

Figure 1.7: Representation of heat generation by decomposition reactions following Arrhenius law (red) and heat dissipation (green) for a generic vessel. A, B and C represent 3 different environmental temperatures. A is safe up to temperature T_1, B is at the critical temperature (point of no return) T_{NR} and C cannot control the thermal runaway. Edited from [68].

be very difficult to extinguish due to their self-fuelling nature [71]. Water can be used to quench the fire and cool the battery [72], aided by the use of surfactants [73, 74]. However, there is a further hazard of explosion as the lithium compound can react with the water to produce hydrogen gas [74].

1.3.1.1 Thermal Explosion Theory

As mentioned above the relationship between heat generation and dissipation is important in the TR process. This behaviour can be explained by the "Thermal Explosion" Theories developed by Semenov [75] and Frank-Kamenetskii [76]. Semenov's Theory assumes a container of self-heating fluid is at a spatially uniform temperature. In which the heated generated by the fluid, expressed by an Arrhenius equation, is balanced by Newtonian cooling. Frank-Kamenetskii theory assumes a self-heating solid exposed to a uniform ambient temperature. In which the increase in the solid's temperature is based on Fourier's heat conduction equation with heat generation expressed by an Arrhenius function.

These theories allow for determination of critical conditions, below which steady state exists and TR does not occur. The critical conditions are presented by the Semenov equation, see Eq. (1.3), and Frank-Kamenetskii equation,see Eq. (1.4), below [77].

$$Se = \frac{\Delta H A_0 E V}{USRT_c^2} \exp\left(\frac{-E}{RT_c}\right) = e^{-1} \tag{1.3}$$

Where H, A_0, E, V, U, S, R, T_c are the heat of reaction, frequency factor, activation energy, fluid volume, overall heat transfer coefficient, surface area, Gas constant and critical

temperature, respectively. For any shape, if the equation above with $T_c = T_{amb}$ leads to $Se < e^{-1}$ conditions remain stable.

$$\delta_c = \frac{\Delta H A_0 E r^2}{\lambda R T_c^2} \exp\left(\frac{-E}{RT_c}\right) \tag{1.4}$$

Where, with similar notation as above and, r is the characteristic radius of the solid. Depending on shape, i.e. infinite slab, infinite cylinder or sphere, δ_c equals 0.878, 2.00 and 3.32, respectively. Hence, for a specific shape, if the equation above with $T_c = T_{amb}$ leads to $\delta < \delta_c$ conditions remain stable.

The assumptions behind each theory lead to the Semenov equation being effective under the condition of the Biot number tending to 0 and defines the critical temperature of a fluid under isothermal conditions. While the Frank-Kamenetskii equation is effective under the condition of the Biot number tending to infinity and defines the critical temperature of a solid under isothermal conditions.

1.3.2 Decomposition Reactions

The process of TR in Li-ion cells is complex due to the fact that many exothermic reactions can occur within a Li-ion cell. These can include *reversible & irreversible* reactions, due to charge and discharge of the cell; and *chemical reactions*, due to decomposition of the cells components at elevated temperatures [78]. The heat generated during normal operation from the reversible & irreversible reactions (due to entropy and enthalpy changes, overpotentials, reaction heating and ohmic heating) can be readily dissipated to maintain safe operating temperatures, and hence presents little risk. However, the chemical decomposition reactions present a much greater hazard due the vast amounts of heat they can produce and the rapid rate at which they release it. The chemical decomposition reactions that can take place include the:

- solid electrolyte interphase (SEI) decomposition reaction (on the negative active material)
- negative electrode (NE) reaction
- positive electrode (PE) reaction
- electrolyte decomposition
- lithium metal reactions with electrolyte on overcharging
- lithium metal reactions with binder.

Each of these decomposition reactions have key properties such as: the temperature at which the reaction starts, the heat released by the reaction, and the rate of heat release.

Hence, understanding how each of the reactions behaves, and how they interact to produce an overall self-heating TR event, is essential to understanding Li-ion cell safety, as well as for identifying areas to improve abuse tolerance and mitigation strategies [79]. Additionally, understanding how different abusive events affect TR is important, as the process leading to TR, and hence the required mitigation strategies, can be different under different abuse events.

Experimental studies have gone some way to find the major contributing decomposition reactions leading to cell TR, and the order in which they occur. These are listed as [78, 80–83]:

1. *SEI decomposition reaction*: The SEI protects the negative electrode from reacting with the solvent electrolyte. This layer is metastable and at T > 85°C–120°C it decomposes exothermically leading to low-rate reactions that steadily increase with temperature [84].

2. *Negative solvent reaction*: At T > ~120°C the SEI layer no longer protects the negative electrode and the active material comes into direct contact with the electrolyte. Thus, an exothermic reaction between the intercalated ions and the electrolyte occur.

3. *Negative binder reaction*: The fluorinated binder can react exothermically with lithiated carbon.

4. *Positive solvent reaction*: For T > ~150°C the exothermic reaction is thought to be due to one of two chemical reactions. Either: a) the positive active material decomposing, releasing oxygen which reacts with the electrolyte, or b) direct reaction between the positive active material and the electrolyte. In either case, reduction of the positive active material is highly exothermic leading to high rate reactions with peak rates in excess of 100°C/min [84].

5. *Electrolyte decomposition*: At T > ~200°C the electrolyte can decompose.

Although the reactions are listed by their reaction onset temperature in the list above, the reactions themselves are not discrete. Each reaction may occur over a narrow or wide temperature range, see Fig. 1.8, leading to a summation of some or all of the heat generation rates and hence an increased temperature rate. Throughout these stages there are points where the separator material melts and flammable gases are produced, which is discussed in more detail below.

The decomposition of the SEI layer occurs in two stages [80], see Fig. 1.9. The first, which leads to an initial peak temperature rate, is a decomposition of the metastable SEI into stable SEI. The second, is a reaction of intercalated lithium with electrolyte leading to a new metastable SEI, which results in an increasing temperature rate with temperature (as long as lithium is able to diffuse from the anode particle to the electrolyte). The SEI

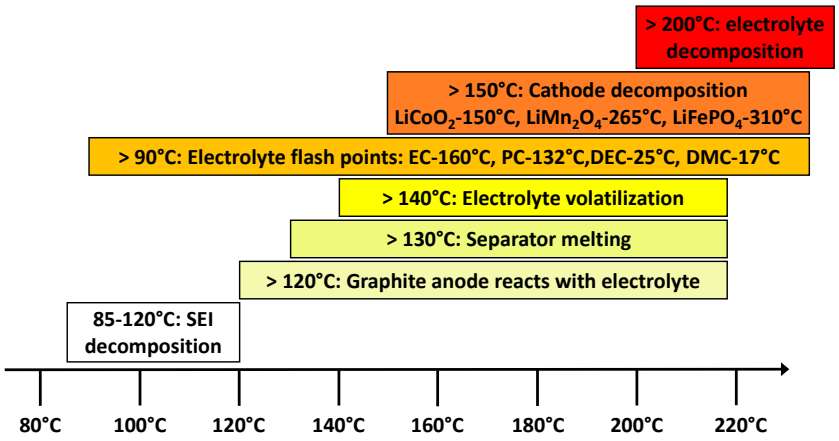

Figure 1.8: General thermal runaway sequence (edited from Ref. [83]).

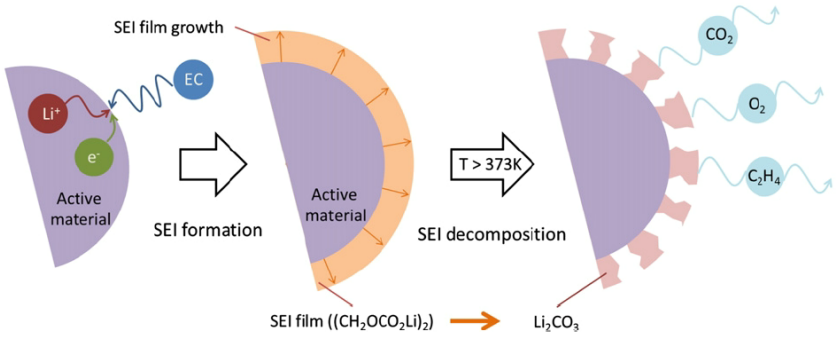

Figure 1.9: SEI formation and decomposition (reproduced from Ref. [36]).

formation involves charge transfer, where the electrolyte solvent (ethylene carbonate, EC) decomposes by reacting with a lithium ion to form the metastable SEI, $(CH_2OCO_2Li)_2$ [26, 36]. The decomposition reaction does not involve charge transfer, but decomposes to a stable product (e.g. Li_2CO_3) with the release of gases (e.g CO_2, O_2, C_2H_4) [36, 78].

Further still, as the temperature rises, the intercalated lithium in the negative electrode reacts with the organic solvents leading to the release of flammable hydrocarbons but no oxygen [26, 78]. As the gas is generated, pressure builds up in the cell, and while the temperature is above the flash point of the electrolyte, combustion does not occur as there is no free oxygen [26].

At 130°C–165°C the separator melts leading to a short-circuit between the electrodes and an additional source of heat generation [85–87]. Eventually the temperature is high enough for the decomposition of the cathode which also generates heat and gases, including oxygen and oxocarbons, leading to greater pressure and temperatures. The release of oxygen enables the burning of the highly flammable electrolyte, which is above the flash point, and flammable gases leading to the production of carbon dioxide and water [78, 88]. At higher temperatures still, 200°C–300°C, electrolyte solvents decompose directly [26]. When the pressure is above the safety vent limit gases are released through the vent. If

the pressure rise is too rapid/ great then the cell explodes. In either case, this leads to the ejection of flammable gases into air which burn due to the presence of oxygen [26, 89–91]. The ejection of highly flammable gases pose a further hazard [92]. Reactions between the binder also occur, but are relatively small in terms of heat generation in comparison with other reactions [78].

1.3.3 Cell and Battery Safety Devices

The safety of a battery, from a design aspect, can be considered to fall into two broad categories: inherent and inbuilt safety devices. The first category includes the choice of anode, cathode and electrolyte, and the use of additives for fire retardation and overcharge resilience [26, 93]. As discussed above, the electrodes and electrolyte lead to heat generation when they decompose. As such, choosing materials that generate less heat will lead to safer cells. The relative safety of different cathode materials is discussed in Section 1.4.

To help protect against abnormal conditions, cells, modules and packs have inbuilt safety features [23, 26, 93, 94]. Safety devices that are of most relevance to this work are safety vents and shutdown separators. Cell vents are designed to release the build up of internal pressure, from gas generation, at a specific pressure. However, once open they allow for atmospheric air to enter, bringing with it oxygen and moister, presenting a risk of combustion and further reaction of the electrolyte [95].

In Li-ion cells, the separator is a micro-porous polymer membrane, constructed of layers of polyethylene (PE) and/or polypropylene (PP) and prevents short circuit between the negative and positive electrodes. The separator within a cell can act as a safety device to help prevent TR by limiting current flow through a process known as separator "shutdown" at 130°C–140°C. This prevents Li^+ flow, and therefore reduces reversible and irreversible heat generation [96]. Shutdown is the only safety mechanism that can provide protection against internal shorts, so long as the heating rate is not too high [34] e.g micro-shorts due to dendrites. However, when the separator melts at 165°C–170°C large internal short circuits occur leading to vast ohmic heating [96, 97].

The safety devices used in practice may not be adequate to prevent cell TR and/ or pack TR propagation, as shown by the incidents discussed above. This is due to impurities, which cannot be eliminated in manufacturing process, or hotspots which may lead to short circuit over time, or other unexpected causes such as debris and damage [52, 98, 99]. Hence, there are a number of safety standards and tests LIBs have to be subject to, to understand their TR potential and hazards, as discussed in Section 1.3.4.

1.3.4 Standards and Abuse Tests

TR can originate from exothermic chemical reactions, mass or thermal transfer processes and also mechanical issues [37]. Hence, there are a number of different standards and testing protocols that cells, modules and packs must conform to for safety [100]. A comprehensive list can be found in Refs. [101, 102]. Further, possible abuse scenarios are simulated experimentally to understand the resulting TR event. The most common abuse tests include overheating, penetration, crush, overcharge and short-circuiting [58, 78]. Additionally, the abuse of cells under a worst case scenario, i.e. under adiabatic conditions, can be carried out through accelerated rate calorimetry (ARC). A detailed discussion of relevant abuse testing for the work carried out in this thesis is further provided in Section 2.1. An overview of common standards is provided below.

Safety standards are provided by regional organizations, e.g. the Underwriter Laboratory (USA), the UN (EU/ECE), the Korea Motor Vehicle Safety Standards (Korea), the Automotive Industry Standard (India) and the Chinese National Quality Control Standards, as well as international bodies, e.g. SAE, ISO and IEC.

These bodies provide the most widely used safety standards for assessing the safety of Li-ion cells, modules, batteries and systems. For the application of EVs, these standards are:

- SAE J2464 (international) [103] - covers the safety and abuse testing for electric and hybrid vehicles with rechargeable batteries. Featuring safety tests for cells, modules and packs for various vehicle applications with BESS above 60 V.
- SAE J2929 (international) [104] - covers the safety standards for Li-ion battery systems used in electric and hybrid vehicles. Featuring safety tests for cells, modules and packs but with a focus on the entire battery system.
- ISO 12405-4:2018 (international) [105] - covers the safety specifications for rechargeable energy storage systems, focusing on safety tests for packs used in electric road vehicles.
- IEC 62660-2/3 (international) [106, 107] - covers the reliability, abuse testing and safety requirements for Li-ion cells used in electric road vehicles.
- UN/ECER100 (EU and further countries) [108] - covers the safety requirements for EV BESS and their subsystems including cells.
- UL 2580 (USA) [109] - covers the methods to asses a battery assembly or its subcomponents, e.g. cells and modules, to withstand abuse conditions and to prevent the exposure of person to hazards as result of abuse.
- USABC (USA) [110] - covers the safety tests to be carried out on cells, modules and packs.

- SAND2017-6925 (USA) [111] - covers the recommendations for abuse testing rechargeable battery energy systems, from cell to pack level.
- AIS-048 (India) [112] - covers the mechanical abuse of cells and modules and the electrical abuse of cells to packs.
- QC/T 743 (China) [113] - covers the mechanical, electrical and thermal stability of Li-ion cells and packs for EVs.

Each of the above standards cover all, or many of, the same abuse tests. However, the criteria of abuse or pass/fail of a test can vary slightly between standards. These criteria also depend on the system level assessed (i.e. cell, module, pack, vehicle). Example pass/fail criteria for tests under reasonable misuse (e.g. external sort, thermal shock, vibration) are "no fire", "no explosion", "no rupture", and "no leakage", while for fire resistance the criteria is "no explosion" [108, 109].

The following sections, Sections 1.3.4.1 to 1.3.4.4, discuss the criteria of mechanical, electrical, environmental and chemical abuse tests, respectively.

1.3.4.1 Mechanical Abuse Standards

1.3.4.1.1 Mechanical Shock Test This test is used to evaluate the robustness of a device under test (DUT), i.e cell, module, pack, to harsh accelleration/ deceleration. Shock forces are given in terms of acceleration and duration to simulate different conditions. For example, conditions such as driving over a curb at high speed [105] or a vehicle crash [108]. The shocks are applied with a given pulse shape, such as a half-sine wave, characteristic of the simulated condition.

The harshest criteria is outlined by Ref.[103], requiring that cells $<0.5\,\text{kg}$ be subjected to an acceleration of 150G (at 10 ms shock duration). In comparison, Ref.[109] and Ref.[108] have peak acceleration criteria of 50G (at 15 ms shock duration) and 10 (at 80 ms shock duration), respectively.

1.3.4.1.2 Drop Test This test is used to simulate when a DUT is accidentally dropped while being installed/ removed form a system. The DUT, at a given SOC (typically the max operating SOC or 100%), is left to fall from a specified height onto a rigid flat surface or cylindrical steel object. The fall height varies from 1 m [109] to 10 m [111].

1.3.4.1.3 Penetration This test is used to simulate the incursion of a metal object into the DUT as it can cause electrical short circuit of the DUT. A sharp steel rod, commonly called a 'nail', is forced into the DUT at a constant speed. Variables in the

test include: nail diameter, and depth and speed of penetration, SOC and duration that the nail remains in the DUT after penetration. For a cell, a nail diameter of 3 mm is commonly used. With a nail speed of 8 cm/s^2 and penetration depth of 3 mm.

1.3.4.1.4 Immersion This test is used to simulate the submerging or partial flooding of a vehicle battery. A battery is fully submerged in salt water (with a similar composition to sea water) for a period of at least 1 h.

1.3.4.1.5 Crush/ crash This test is to simulate an external load that can damage a DUT, such as a vehicle crash. In the test, a DUT is crush be an initial degree (i.e. to 85% initial dimension), then after 5 min it is further crushed (to 50% initial dimension) [103, 108, 111, 113] or until there is and abrupt voltage drop [106].

The for applied during the crush test has to be limited to less than 1000 times the weight of the DUT, or 100 kN.

1.3.4.1.6 Vibration This test is used to evaluate the effect long term vibrations have on battery components. Vibration profile follow sine-waves or random amplitudes and frequencies. Sine-waves can be used to identify resonant frequencies of a DUT, with random profiles representing real world scenarios.

1.3.4.2 Electrical Abuse Standards

1.3.4.2.1 External short circuit test This test is used to evaluate the safety of a DUT under an external short and the ability of safety devices to prevent hazardous situations, mainly excess heat generation and the possible resulting TR, explosion and fire events.

A low resistance element, 5 mΩ [106, 108], 20 mΩ [105, 111] or 100 mΩ [105], is connected across the battery teminals. This is done in less than 1 s and maintained for a defined period of time. Soft shorts are defined as when the external resistance is similar to the cell internal resistance, while hard shorts are when the external resistance is much lower than the internal. Soft shorts can be used to ensure the response of the cell, rather than the current dependent protective devices, is evaluated [103].

1.3.4.2.2 Internal short circuit test Internal shorts are hard to simulate and several methods have been developed. As mentioned above, nail test can be used. Separator shut down tests, heat a cell up to a temperature just above the shutdown temperature to evaluate the effectiveness of the shutdown mechanism [103]. Forced internal short can be

implemented by inserting a L-shaped nickel particle between jelly roll layers. Such that under compression the particle pieces the separator and causes a short circuit [107]. An indentation test, similar to a crush test, can be used to deform the outer most electrode layers, by applying pressure to deform the cell, leading the tearing/ piecing of the separator and short circuit.

1.3.4.2.3 Overcharge/ overdischarge test This is carried out to evaluate the effects of charging a battery above or below its rated limits. Under overcharge, a constant current (e.g. 1/3C) is applied up to a set SOC. Depending on the standard this overcharge SOC can 110% to 200%. Overdischarging requires discharging the battery from fully charged until the tested device limits or interrupts discharging [108].

1.3.4.3 Environmental Abuse Standards

1.3.4.3.1 Thermal stability test This test is used to identify at what temperature TR begins. It requires a cell to be heated by 5°C steps with a 30 min wait period between each step up to 200°C above the maximum operating temperature of the cell or a catastrophic event occurs [108]. The maximum operating temperature is 300°C for Ref.[103]. After this, a second run is done with 2°C temperature increment to refine the TR onset temperature.

1.3.4.3.2 Thermal shock and cycling test The test is to evaluate the effect of expansion and contraction of a DUT from sudden changed in temperature. During the test a DUT is exposed to an upper and lower temperature limit (60°C/85°C and −40°C) for a specified amount of time.

1.3.4.3.3 Overheat test This test is used to evaluate the outcome of thermal management system failure. A DUT is cycled (e.g. 20 times charge/ discharge with no resting [103, 104]) with the cooling system disabled. The test is stopped when (a) the DUT interrupts charging/discharging, (b) the temperature is stable, or (c) the DUT is damaged [108].

1.3.4.3.4 Extreme cold temperature test This test evaluates the DUT when discharged at 1C at temperature of −40°C, −20°C, 0°C and 25°C [111]. The test is stopped if abnormal conditions, voltage or temperature, or physical damage occurs.

1.3.4.3.5 Fire test The fire test is used to asses the risk of explosion. Radiant-heat tests heat a sample to 890°C in less than 90 s and held for 10 min [103, 111]. Projectile

fire tests expose a DUT to a uniform fire [104, 109]. Grating table tests use a burning fuel pan [108]. The DUT is first preheated for 60 s at the distance of 3 m. Then the DUT is placed directly in the flame for 70 s. The test is passed if there is no evidence of explosion during the test.

1.3.4.4 Chemical Abuse Standards

1.3.4.4.1 Emissions tests These tests are used to asses the hazardous substances emitted during failure and to determine if they remain below safe concentrations. Requirements [105] state that concentrations of hazardous substances should not be allowed near the driver, passenger or load comportments.

1.3.4.4.2 Flammability test This test is to determine the flammability limit of the gases emitted from a battery [103, 104, 109, 111]. This can include using spark ignition sources in the testing enclosure or gas monitors.

1.4 Cell Chemistry and Safety: The Role of $LiFePO_4$ as a Cathode

As stated previously, cell chemistry plays a significant role in the TR of a cell. Li-ion cells with a $LiFePO_4$ (LFP) positive electrode are of interest for electrochemical energy storage applications due to their increased thermal stability and reduced hazard of TR [71, 114–117]. Chen and Richardson [71] explain why LFP is considered safer than other chemistries: at high temperatures the organic solvents making up the electrolyte can ignite in the presence of oxygen, which can then lead to fire and explosion of a cell. The chemistry of the positive electrode plays a crucial role in the availability of oxygen. This is because charged oxide cathodes, such as Li_xCoO_2, Li_xNiO_2, $Li_xMn_2O_4$, $Li_xNi_{0.8}Co_{0.2}O_2$, $Li_x(Ni_{0.8}Co_{0.15}Al_{0.05})O_2$, and $Li_y[Ni_xCo_{1-2x}Mn_x]O_2$ decompose and release oxygen at elevated temperatures. However, olivine-type $LiMPO_4$ (M= Fe, Mn, Co, and Ni) cathodes on the other hand are seen as safer alternatives as oxygen loss is inhibited by strong covalent P-O bonds.

For example, the calculated release of oxygen for a 18650 LFP cell is 0.5 g compared to 3.25 g for a comparative lithium cobalt oxide (LCO) cell [118]. In turn, the lack of oxygen limits the amount of electrolyte that can be ignited during TR, vastly reducing the amount of heat produced and in turn reducing the overall severity of TR.

The safety of Li-ion cathode material can be ranked from most safe to least safe in the order [71, 119]: $LiFePO_4$, $Li[Ni_{3/8}Co_{1/4}Mn_{3/8}]O_2$, $Li_{1+x}Mn_{2-x}O_4$, $LiCoO_2$, $LiNi_{0.7}Co_{0.2}Ti_{0.05}Mg_{0.05}O_2$, $LiNi_{0.8}Co_{0.2}O_2$, $LiNiO_2$ [119].

While other chemistries, such as the common $LiCoO_2$ (LCO), $Li_y[Ni_xCo_{1-2x}Mn_x]O_2$ (NMC) and $Li_xMn_2O_4$ (LMO), benefit from greater energy density and higher voltages compared to LFP [114, 120, 121], LFP has the advantages of being non-toxic, dependent on the resource abundance of iron, highly efficient and have high cycle life [122–124]. LFP are also claimed to have a lower cost, better rate capabilities and greater power densities [122, 123, 125]. Due to the documented safety of $LiFePO_4$ chemistry over other Li-Ion chemistries [71, 114, 115, 117, 126, 127], it is suggested that $LiFePO_4$ are suited to mobile and large-scale energy storage where safety and cost are extremely important [119, 128]. To date, the use of LFP chemistry in stationary applications is 170 MW out of a total 2.3 GW install global capacity of all Li-ion chemistries [129]. Their uptake is not as wide spread as other chemistries, as commercially they have some way to go to reduce cost, and to be competitive for mobile applications there needs to be an increase in specific energy capacity, while their power densities and rate capabilities are competitive [130]. However, if these criteria are met, it is not hard to see the value of such a stable Li-ion cell throughout electrochemical energy storage applications, and hence their increase in popularity. It is due to this fact that cells based on LFP chemistry have been chosen to study herein.

Even though the reported safety of LFP cells is good in laboratory tests, TR incidents still remain in the real world. It is apparent that safety concerns still remain for LFP battery solutions by the fire of an EV bus powered by an LFP battery pack that went into TR when charging [53, 54, 131].

While LFP cells are deemed to be safer than other chemistries from experimental findings, modelling their abuse behaviour can give greater insight to their stability under a wider variety of operational, environmental and abuse conditions. Although there has been extensive computational and modelling research into TR of LIBs, very little has been done in relation to cells with positive electrodes of LFP chemistry. To the author's knowledge only Refs. [38, 128, 132] model the TR of LFP Li-ion cells, their work is further discussed in Section 2.2. It is proposed here that cells utilising a lithium iron phosphate (LFP) cathode can address many TR safety concerns, while despite their attractiveness, LFP cells have not been studied to the same extent as other chemistries, experimentally and computationally. Hence, it is of great interest to further the understanding of this chemistry. This will be addressed through experimental investigations in Chapter 4, and through computational TR model developments and pack investigations in Chapter 5 and Chapter 6 respectively.

1.5 Role of Computational Modelling

Improving the performance and safety of LIBs requires a greater understanding of the physical, electrical and chemical processes occurring within the battery, from the scale of the active material particles up to the pack level. Modelling the behaviour of LIBs can be a more cost effective and time-saving method of furthering the understanding of LIBs than through experimental methods. Specifically with regard to increasing the safety of LIBs, the understanding of the TR behaviour of Li-ion cells is necessary, i.e. what causes its onset and how does the process progress.

Modelling TR can be implemented at various levels, from individual cells [e.g. 133–137] to packs [e.g 138–142]. In modelling TR of LIB, an accurate model of TR in a single Li-ion cell is most important, and the starting point for more advanced TR modelling. The fundamental principles of a cell TR model are a coupling of 1) heat transfer behaviour, and 2) exothermic chemical decomposition behaviour. The methods to develop TR models for LIBs will be discussed in detail in Section 2.2.

A thermal-abuse model can be used to ensure proper thermal management of a battery under normal operating conditions or in predicating TR behaviour [79]. It follows, that it can also be used to determine the best cell characteristics and battery design for mitigating disastrous thermal events, and in turn, aiding in the development of improved and safer battery designs.

Once a fundamental TR model has been developed and validated, it can then be extended to include other factors such as electro-chemistry, gas generation and combustion theory, and changes to material physical properties due to such things as temperature or deformation [133, 143–145]. These, in turn, allow aspects such as short-circuiting, impact damage, ageing, separator breakdown/ melting and heat transfer by fire to be incorporated for analysis of their effect on TR behaviour and cell safety [37]. Further, with an accurate single cell TR model available, studies of modules or packs can be undertaken.

There has been much work into the development of TR models for various Li-ion cell chemistries, with varying amounts of complexity and at various scales [e.g. 38, 78, 99, 132, 135, 146–148]. However, the study of TR in LFP cells, specifically in relation to modelling, is lacking. Additionally, the only modelling of LFP done to date (see Refs. [38, 132]) has not been validated, and when compared to preliminary experimental work done here, is shown to be significantly inaccurate. For these reasons, and the growing market share [39], LFP cells have been chosen as a case study within this thesis.

For the development and validation of an accurate model, including TR models, there is a need for real-word data. As will be shown in the Literature Review (Chapter 2), extensive data of this kind is not available for LFP cells. Hence, there is a need in this

work to gather the TR response of LFP cells under various thermal abuse scenarios to provide a more detailed understanding of LFP TR.

1.6 Summary

The *General Introduction* has outlined the increasing importance of LIBs to modern society, while highlighting the important and potentially hazardous phenomenon of TR that LIBs present. Computational modelling, aided by experimental testing, is fundamental to further understanding of the TR behaviour of LIBs. The intention of this thesis is to expand the knowledge of the TR behaviour of Li-ion cells and further the development of more advanced and robust LIB battery TR models, and discuss difficulties within them. The thesis will focus on LFP chemistry as a case study, due to its under-representation in the literature, and discuss any safety issues they may present. Although the development to the TR model will be sought for a specific case study, its principle works aim to be generally applicable to the field of study.

1.7 Outline of Thesis

In Chapter 2 a review of the literature with regard to the experimental and computational study of Li-ion cells and battery packs is presented. This covers the fundamental abuse test of over-heating, namely by ARC and oven testing. Additionally, other initiation criteria are discussed, i.e. types of short circuit, that are important to the understanding of TR in packs. The development, formulation and parametrisation of Li-ion cell TR models is covered, including the inclusion and coupling of other relevant behaviours, such as electrochemistry, short circuit and venting. The literature on TR in Li-ion modules/packs is presented, going from a cell model to pack models, and under experimental study. This literature review is used to outline specific aims and objectives to address areas in the literature that can be developed with respect to the thesis' intention of a more advanced TR model and better understand of TR in LFP cells.

Chapter 3 outlines the methodology for the experimental investigations undertaken. This includes the charging of cells, determining the heat capacity of a cell and assessing TR of cells by ARC and oven abuse testing. The chapter also covers the governing equations of the fundamental TR model, i.e. heat transfer and exothermic decomposition relations. Additionally, it presents the governing equations for an extended TR model including cell pressurisation and venting, as well as additional simmering reactions.

Chapter 4 investigates the TR behaviour of cylindrical 18650 LFP cells under ARC and oven testing. The TR behaviour is characterised in terms of stability and severity, and compared to similar cells of other chemistries from the literature. Further, a new method is

applied to estimate the heat generation from the temperature profile. From these finding, comments on the processes taking place during TR under different conditions are made, and hence, operational limits of the cell are suggested to mitigate TR. This chapter also provides essential data sets, to an extent not previously available, that are required for developing meaningful TR models of LFP cells.

Chapter 5 details the development of an advanced TR model for a LFP cell case study. This, in part, highlights the considerations that should be taken when utilising literature values of key parameters. It further highlights the difficulty in parametrising a composite structure when there is uncertainty about the knowledge of the internal structure. The advanced model includes simmering reactions and venting behaviour. This is discussed with regard to the improvement of TR predictions, as well as how the formulation of the governing equations for the pressure behaviour of the venting model and abuse parameters values affect the venting predictions. General comments are then made for the considerations that should be taken when venting behaviour is included into generic LIB TR models.

Chapter 6 applies the advanced TR model developed in the previous chapter to investigate the TR propagation potential of LFP packs, and how the inclusion of advanced behaviour affects the predictions of pack propagation. It also presents an investigation of the importance of radiative heat transfer in Li-ion packs.

Chapter 7 summaries the work of the thesis and outlines the key findings of Chapters 4 to 6, with reference made to the aims of the thesis. This chapter also outlines future work to be carried out to further develop the governing theory and parameterisation of abuse models, and to further investigate LFP packs.

Chapter 2

Literature Review

As highlighted in Chapter 1, TR is a major safety concern in regard to LIBs. Hence, with the vast use of LIBs through homes and industry, there is a need to reduce the probability and severity of LIB TR. This can be achieved through greater understanding of TR with the aid of computational and experimental studies, as the presented literature throughout this chapter will show. However, robust TR models are still lacking due to uncertainty in the parameterisation of models, calculation of cell pressure and the scarcity of information about the TR behaviour in LFP cells. The literature here will cover general points of experimental assessment of TR in Li-ion cells and modelling of Li-ion cells. Additionally, it will focus more specifically on the assessment of cylindrical 18650 cells and the LFP chemistry, as LFP 18650 cells are used through this work as a case study.

Section 2.1 discusses the fundamental experimental assessments of TR, including calorimetry and oven testing. Section 2.2 discusses the development of TR modelling. This includes considerations that need to be made about model dimensionality, the predicted TR process, the affect of heat transfer considerations, and discussion on cell pressurisation and venting. Section 2.3 discusses the assessment of TR in LIB packs through experimental and computational means. It covers the fundamentals of pack abuse, an overview of thermal management of packs, description of thermal runaway propagation (TRP) behaviour, important heat transfer pathways, and specific literature on LFP packs. Section 2.4 concludes the Literature Review, summarising the important methods for proper model construction and TR assessment, as well as highlighting areas in the literature that need developing.

2.1 Characterising Li-ion Cell Thermal Runaway

TR can originate from exothermic chemical reactions, mass or thermal transfer processes and also mechanical issues [37]. The triggering events in such cases can be due to one of

several abuse conditions. These include: internal/external short circuit, over-dis/charge, overheating, penetration, crushing or leakage [37, 58, 139]. Further, the onset of TR can be influenced by the cell/battery SOC, ageing and applied load [149]. As such, Li-ion cells have been widely subjected to various abuse tests, to simulate the above triggering events, from which TR behaviour can be characterised and cell safety quantified. Tests such as these are used to emulate specific abuse conditions that can occur during storage, transport or use of LIBs.

Li-ion cells can be considered as chemical systems with the potential to undergo exothermic decomposition at elevated temperatures. As such, overheating or thermal abuse tests are key to providing data on the fundamental characteristics, i.e. stability and severity [38], of TR. Stability is the resilience of a cell against TR. Stability is commonly measured by the temperature at which the cell goes into TR, where a higher temperature is more beneficial and safer. The severity is commonly measured by the amount of thermal energy released, or the maximum temperature reached, by the cell, where a lower energy release/ temperature is better. Thermal abuse testing can be carried out in several ways, including by calorimetry, most commonly differential scanning calorimetry (DSC) and accelerated rate calorimetry (ARC), and convection oven tests. Calorimetry and oven testing findings are further discussed in Section 2.1.1 and Section 2.1.2, respectively.

2.1.1 Calorimetry

Several types of calorimetry exist to investigate exothermic reactions. Such as, DSC and adiabatic calorimetry, including ARC and vent sizing package 2 (VSP2). Each calorimetry method has its own advantages of providing information about an exothermic reaction [150]. DSC is a useful tool to study small samples of cell components, such as the electrodes, the electrolyte and the reaction between the two, to quantify the heat of reaction, with some measure of reaction rates. However, it lacks pressure data, cannot extrapolate to normal/ abuse conditions and has a limited sample size, unrepresentative of a real system. ARC and VSP2 overcome these disadvantages and are able to follow runaway reactions adiabatically. ARC generally has a better temperature sensitivity over VSP2, 0.005°C/min [151] compared to 0.15°C/min [152], while VSP2 has a lower thermal inertia and is inherently better for gas analysis and vent sizing due to its sealed pressure vessel.

Li-ion cells of various chemistries, forms (i.e. cylindrical, prismatic and pouch) and scales (i.e. component/cell level) have been studied by adiabatic calorimetry methods. The most common methods are ARC [115, 153–155] and VSP2 [118, 122, 156], while custom apparatus are also used, such as constant power calorimetry [114, 157].

The ARC and VSP2 equipment are shown in Fig. 2.1. The fundamental principle of ARC and VSP2 equipment is to heat a sample to the point that exothermic reactions begin and to maintain a sample in an adiabatic condition when an exothermic reaction

is detected, while the heat generated by the reaction will accelerate the reaction [158, 159]. From this, the self-heating behaviour of the sample, usually a single Li-ion cell or cell components, under TR can be determined. Then, this self-heating behaviour is characterised by key values to describe the stability and severity of the cell in relation to TR.

ARC and VSP2 equipment maintain adiabatic conductions by slightly different methods due to the different equipment set-ups, see Fig. 2.1(a) and Fig. 2.1(b). However, both follow the principle of using external heaters to prevent heat loss from a sample. Further, both experimental set-ups have the capability of providing similar test information, i.e. temperature and pressure data. Detailed descriptions of ARC and VSP2 construction can be found in [158] and [159], respectively.

In both ARC and VSP2, the heat-wait-seek (HWS), also known as the heat-wait-search, method is employed to identify the initiation and progress of the exothermic reaction [151, 155, 161]. The HWS procedure, depicted in Fig. 2.2, operates as described by [158]: the calorimeter is heated to a desired start temperature and, during the wait period, the temperature is maintained while the sample reaches thermal equilibrium. After which, during the seek period, the sample rate is monitored, and the temperature is held constant or follows the sample temperature. If the temperature rate of the sample is below the predetermined limit that defines an exotherm, then heating is applied. This is repeated continually until an exotherm, i.e. a sample temperature rate above the present limit, is detected, or other end conditions, such as maximum operating temperature, are reached. If an exotherm is detected, then adiabatic conditions are maintained, without any further HWS steps, until the reaction has finished.

From this HWS method key values can be quantified, i.e. onset temperature, maximum temperature, maximum temperature rate and maximum pressure rate. The onset temperature is the temperature when the exothermic temperature rate of the cell, i.e. the rate due to self-heating, first exceeds the predetermined (critical) rate. Two onset temperatures can be quoted, the onset of self-heating and the onset of TR. The critical rate for determining the self-heating onset is typically in the range of 0.015–0.2°C/min [117, 153, 155, 162], where ARC accounts for the more sensitive (0.015°C/min) values. The onset of TR is defined as the point cell temperature rates exceed 1°C/min [155, 162]. For a selected critical rate, a higher onset temperature means the cell is more stable as self-heating/ TR start later. The maximum temperature, temperature rate and pressure rate describe the severity of the TR event, if any. Under adiabatic conditions, the maximum temperature the cell reaches can be used to directly calculate the energy released during TR. The temperature rate is directly proportional to the heat generation rate and, in turn, is an indicator of the cooling required to keep TR under control.

Custom constant power calorimetry rigs have been developed by Golubkov *et al.* [114] and Liu *et al.* [157], see Fig. 2.3. Each, although different in experimental set-up, follows

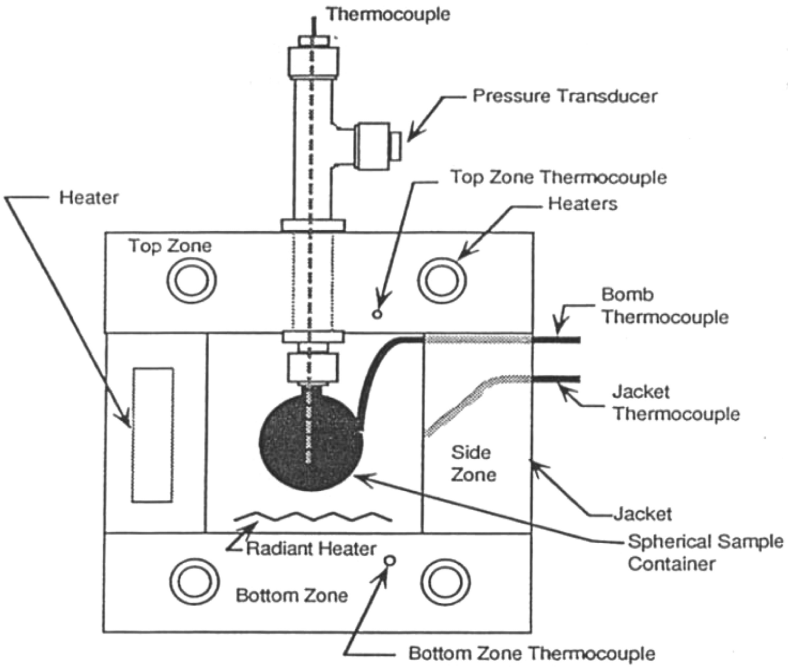

(a)

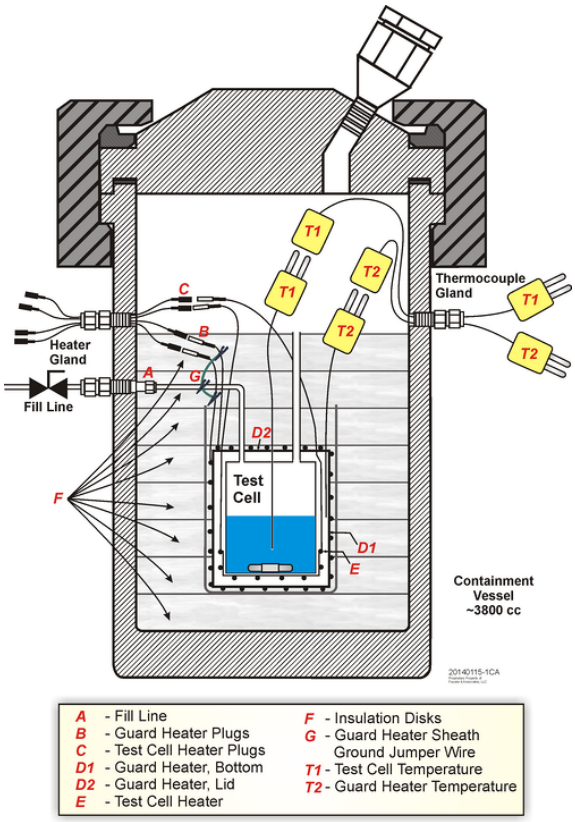

(b)

Figure 2.1: (a) ARC [151] and (b) VSP2 [160] schematics.

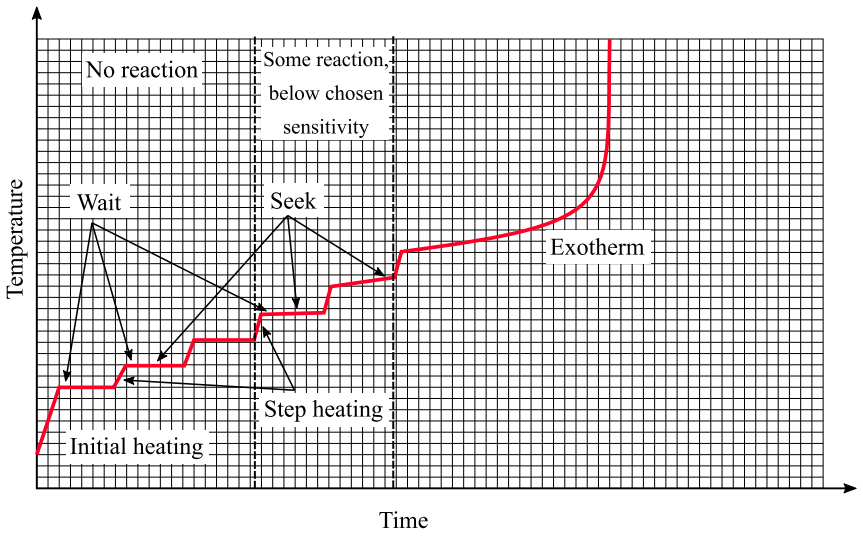

Figure 2.2: HWS operation modes.

a similar method, whereby a cell is heated at a constant power, while purely through insulation [157], or by additional heaters [114], adiabatic-like conditions are upheld during TR. The apparatus by Golubkov *et al.* [114], is constructed of a sealed reactor, with gas feed through, which allows pressure measurements and gas sampling. The apparatus by Liu *et al.* [157], known as Copper Slug Calorimetry, is small and simplistic. It consists of a copper slug wrapped in thick insulation, where an 18650 cell with an attached heater is inserted tightly into the slug. This allows for versatile experimental set up as the Copper Slug Calorimeter can be easily used in conjunction with other testing methods. Using the Copper Slug Calorimeter TR can be studied in ambient air, under cone calorimetry conditions to calculate flame power and allow gas sampling, and under inert environments.

DSC data enables one to understand the potential overlapping sequences of decomposition reactions within Li-ion cells, depending on their constituent components. As well as, determining the magnitude of heat release for each reaction. Figure 2.4 shows the characteristic DSC plots of Li-ion cell components compiled by Zheng *et al.* [163]. The key characteristics of these plots include: Q, the heat release power; ΔH, the enthalpy representing the total heat released; and T_x, the onset, peak and terminal temperatures, represented by the subscripts *onset*, *peak* and *end* respectively. The vertical position of each hill-shaped reaction plot, i.e. each coloured region, is determined by ΔH. The start and end of the plot is determined by the onset and terminal temperatures respectively, while the shape of the hill is determined by the value of Q at each temperature (see bottom left insert of Fig. 2.4). The lightning bolts represent the temperature at which a short circuit will occur due to separator breakdown, dependent on the separator material present in a cell. The arrows represent the magnitude of heat released by internal short circuit and evolved gas combustion events.

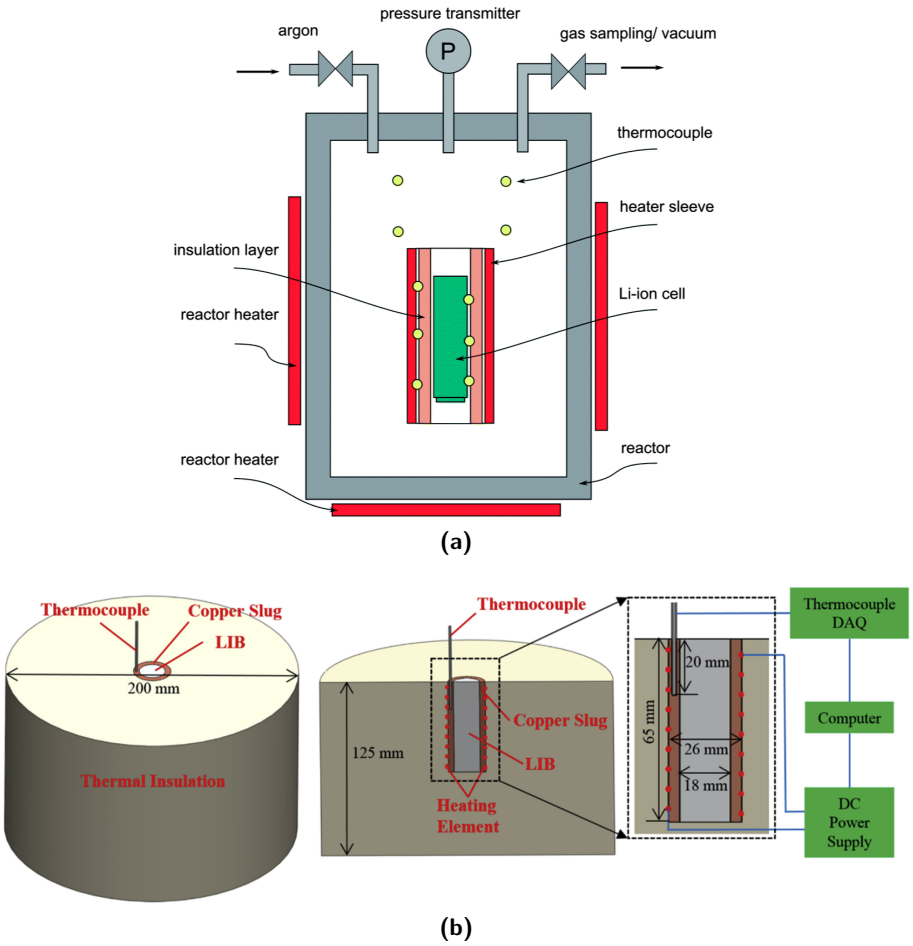

Figure 2.3: Constant power calorimetry: (a) Constant power reactor [114] and (b) Copper Slug Calorimeter [157] schematics.

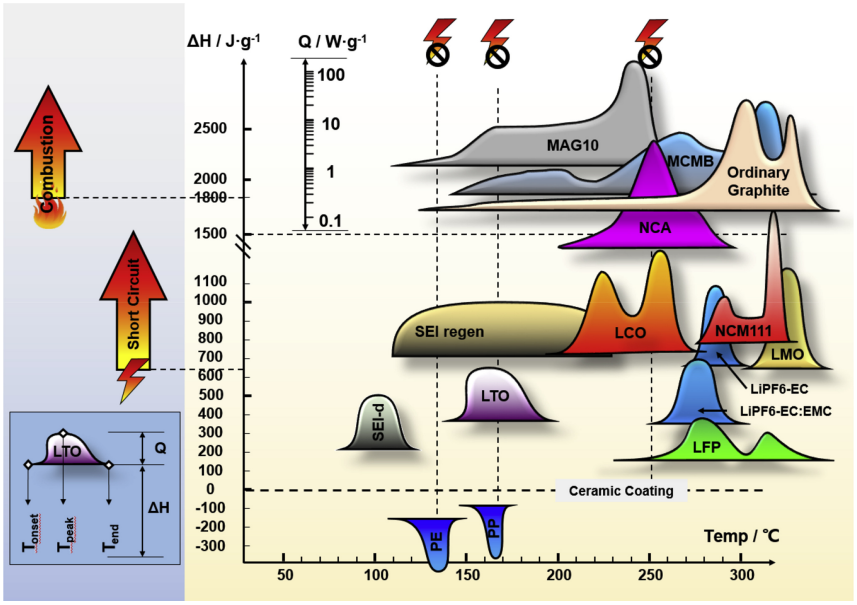

Figure 2.4: Characteristic DSC plots of Li-ion cell components compiled from the literature. Cells at 100% SOC with a DSC test scan rate of 10°C/min. (Reproduced from [163]).

Table 2.1: Heat released by negative (carbon) and positive (LFP) electrode reactions.

Reaction	Heat released, ΔH (J/g)	Reference
NE*	~1300 - 2800	[88, 166, 167]
PE	~150 - 340	[71, 88, 126, 164]

* Heat released in negative reaction includes SEI reaction.

2.1.1.1 Key Experimental Findings

The onset temperature, peak exotherm temperature and heat released of a charged LFP cathode under DSC analysis are 250°C, 280°C (with a second smaller peak at 315°C) and 147 J/g, respectively [164]. Comparatively, Takahashi *et al.* [126] reports the peak exotherm temperature at 360°C, with a reaction heat of 288 J/g. By comparison the onset temperature, peak exotherm temperature and heat released for LCO are 180°C, 231°C and 760 J/g, respectively. For NMC they are 270°C, 297°C and 290 J/g, respectively [119]. From this data, and its graphical presentation in Fig. 2.4, LFP is the safest on the basis of having a relatively high onset temperature and peak exotherm temperature with a relatively low heat of reaction [71]

Ben Mayza *et al.* [153] and Larsson and Mellander [165] compared the anode and cathode of LFP cells under DSC analysis. They found that the graphite anode is the major contributor to heat production, with peak heat flow in the anode ten times greater than that of the cathode, and also with greater heat flow for a larger temperature range. Table 2.1 lists the heat released by the NE (which includes the SEI reaction) and PE reactions. For LFP cells it can be clearly seen that the NE reaction is the major contributor to the TR potential of the cell.

Further, the sequence of reactions during TR can be inferred from the reaction onset temperatures and peak rate temperatures, which, from the literature, have been summarised in Table 2.2. The SEI reaction begins to release heat at 50–120°C with maximum heat release at 253–300°C [84, 166]. A carbon/graphite anode has a heat release onset temperature between 80–160°C and exhibits peak self-heating between 200–350°C [81, 153, 166–168]. LFP cathodes at 100% SOC have a heat release onset temperature between 180–250°C and exhibit peak heating between 210–360°C [115, 119, 126, 164, 169]. Takahashi *et al.* [126] also show that the fully discharged LFP cathode presents no self-heating up to 400°C. ARC tests on LFP cathodes in electrolyte show two exotherms [170]. The first is thought to be due to the decomposition of the salt (Lithium hexafluorophosphate, $LiPF_6$) additive in the electrolyte decomposing on the surface of the electrode, before the second reaction that is the decomposition of the LFP cathode itself. At high temperatures (>250°C), the electrolyte can ignite in the presence of oxygen releasing large amounts of heat [71]. Hence, for the solvent reaction to occur, decomposition of the LFP cathode is required (assuming that the cell is intact such that no oxygen can enter from the environment into the cell) [170]. The most significant reactions during TR are the strongly

Table 2.2: Key Temperatures relating to decomposition reactions.

Reaction	Self-heating onset temperature (°C)	Temperature at peak temperature rate (°C)	Reference
SEI	50–120	253–300	[84, 166]
NE	80–160	200–350	[81, 153, 166–168]
PE	180–250	210–360	[115, 119, 126, 164, 169]
Electrolyte	>250	-	[71]

exothermic combustion of carbonous material and Li oxidation, which are affected by the amount of available O_2 and intercalated Li in the anode (both greater at increased SOC), respectively [65]. This data, and that in Fig. 2.4, can be used to infer the process of TR in cells abused by ARC and oven tests.

Work by Jiang and Dahn [115] states that the addition of electrode binder to the LFP cathode prolongs the LFP reaction (not in electrolyte) over a larger temperature range. Specifically, the LFP reaction initiates at 300°C and ends at 320°C when binder is not considered, with the binder the reaction ends at 350°C. Jiang and Dahn [115] also shows the LFP reaction occurs at a much lower temperature in electrolyte. In electrolytes of $LiPF_6$ ethylene-carbonate/diethyl-carbonate (EC/DEC) and lithium bis(oxalato)borate (LiBOB) EC/DEC, the reaction starts at 190°C and 240°C, respectively, while ending at 240°C and 285°C, respectively.

The interactions between cell components are shown to be important when studying individual reactions. Through ARC experiments, Jiang and Dahn [115], showed that the onset of self-sustained exothermic reactions occurred at 150°C, 220°C and 310°C for LCO, NMC and LFP respectively when in solvents. However, when in solvents with LiFP6 salts, their onset temperatures became 220°C, 190°C and 180°C for the same chemistries. This shows that the addition of lithium salts suppress the onset of $LiCoO_2$ reaction while aiding the others.

Previous calorimetry experiments have quantified the severity of TR in 18650 LFP cells at 100% SOC. The onset of self-heating was determined to be ~90°C [171], while the TR onset temperature was determined to be 200°C [122, 156]. Further, it has been shown that the maximum temperature and temperature rate were between 240–259°C and 3–5.36°C/min, respectively [122, 156, 171]. Heats of reaction were calculated to be 184 J/g [171] and 31.06 J/g [117]. The large discrepancy may be due to the different experimental methods used, i.e ARC by [171] and VSP2 by [117]. In larger 26650 cylindrical LFP cells of 3 Ah capacity the maximum rates reached were on the order of 100°C/min [172].

By comparison, Lei *et al.* [171] showed that, at 100% SOC, LMO and NMC cells have reaction rates 3-4 orders of magnitude larger, maximum temperatures 2-3 times larger and heats of reaction an order of magnitude greater than LFP cells. Figure 2.5 shows

a typical temperature rate vs. temperature plot for cells subject to ARC. From which Lei *et al.* [171] show the significant reduction in overall severity of TR for LFP cells compared to LMO and NMC cells. Further ARC experiments by Lu *et al.* [117] compared the safety of LFP over LCO through testing of 18650 type cells. A fully charged LFP cell (3.6 V) had an onset temperature just below 200°C, peak temperature of 243°C, a maximum temperature rate of 5.39°C/min and reaction heat of 1.02 kJ. In contrast, a fully charged LCO cell (4.2 V) had an onset temperature of 130°C, peak temperature of 370°C, a maximum temperature rate of over 56 000°C/min and reaction heat of 7.85 kJ. Thus, showing the increased stability of LFP up to higher temperatures, less temperature rise at thermal runaway and increased safety as maximum heating rate is four orders of magnitude slower than for LCO.

Golubkov *et al.* [114] compared three 18650 cells (LCO/NMC 2.65 Ah, NMC 1.5 Ah and LFP 1.1 Ah) under adiabatic-like conditions with constant heating rates applied. Onset temperatures were respectively 149°C, 168°C and 195°C and peak temperatures of 853°C, 678°C and 404°C were observed. Comparison of the ARC [171] and constant power [114] methods shows that the detection of TR is later and the maximum temperature reached is higher in the constant power method. The higher temperature reached is thought to be due to the more rapid heating of the cell in the constant power method, hence decomposition and heating occur over a shorter time frame.

Liu *et al.* [116] investigated the heat release of 18650 Li-ion cells using copper slug battery calorimetry. They found LCO, NMC and LFP generated a maximum total heat when fully charged of 14.37 J/mAh (37.37 kJ/cell), 15.11 J/mAh (34.0 kJ/cell) and 9.13 J/mAh (13.7 kJ/cell) respectively. Under fire calorimetry, Chen *et al.* [173] showed LFP cells pose a lower explosion risk than LCO, with the latter releasing much more oxygen. The calculated released oxygen of fully charged LCO 18650 cell is 3.25 g which is much larger than LFP 18650 cell, releasing 0.5 g.

The process by which TR occurs, which is informative for developing accurate TR models so that reactions are simulated in the correct order and with the appropriate magnitude of heat relative to each other, has been described in little detail with regards to LFP cells. Ben Mayza *et al.* [153] propose the series of decomposition reactions that occur throughout TR in fully charged (4 V) 18650 LFP cells under ARC. Ben Mayza *et al.* [153] state that the first exotherm occurs at 90°C and lasts until 130°C and is due to the SEI decomposition. Then, at 150°C, a second exotherm is reported while at 245°C the cathode begins to decompose. Finally, a third exotherm at >260°C is attributed to oxygen reacting with the organic solvents. The cell reached a maximum heating rate of 6°C/min at approximately 285°C, corresponding to the electrolyte reaction taking place. Kvasha *et al.* [88] also suggest the decomposition sequence to be initiated by the SEI reaction, provoking the negative electrode reaction and leading to separator melting, followed by severe negative and positive electrode reactions with the electrolyte, where overall cell TR

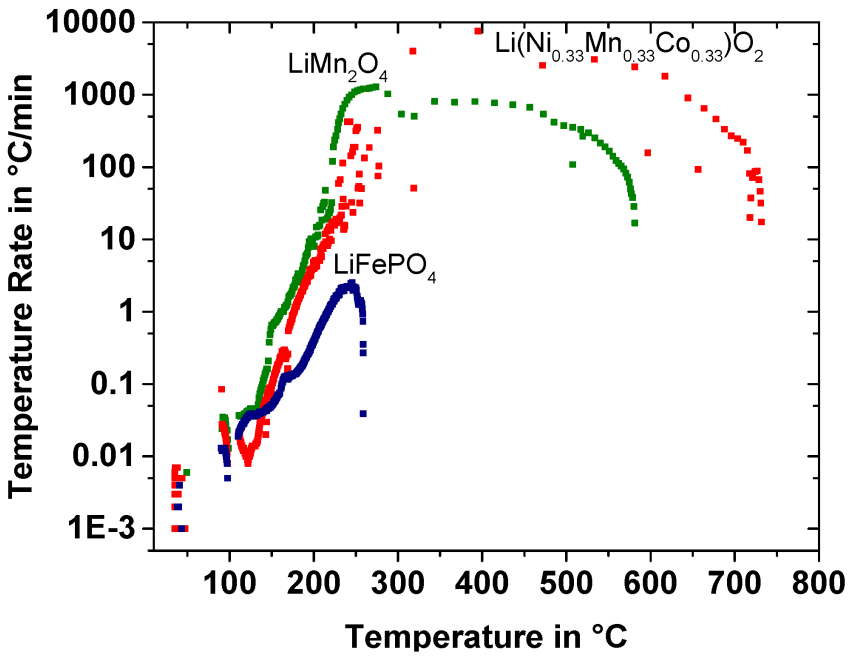

Figure 2.5: Typical results of an ARC test, shown are the plots of three commercial 18650 cells of different chemistries (reproduced from [171]).

is due to the negative electrode reaction. Even though separator melting occurs, TR is not caused by shorting of the cell due to the stability of the LFP cathode [174].

The effect of SOC on self-heating characteristics of cells has been thoroughly studied in relation to metal oxide based cathodes [118, 154, 155], but less so in LFP cells, with little discussion of the self-heating process at different SOC. Cells at a lower SOC are more stable and safer than their fully charged counterparts. Cells at a lower SOC go into TR at a higher temperature, reach a lower peak temperature, lose less mass, have lower pressure and temperature rates, and have a lower heat of reaction [116, 152, 154, 155]. Ishikawa *et al.* [154] and Mendoza-Hernandez *et al.* [155] have shown from ARC experiments, for LCO and LMO cells, that the temperature region in which non-self-heating occurs reduces with increased SOC, while the temperature region that self-heating and TR occur increases with SOC. They also showed that, depending on SOC and chemistry, a cell can go into multiple self-heating and non-self-heating (i.e. heating by the ARC) regions before self-heating is sustained or TR is triggered. They also showed that TR is not triggered below 22% SOC for LCO cells or 50% SOC for LMO.

With regards to LFP cells, Lu *et al.* [117] showed that, at 3.3 V compared to 3.6 V, the 18650 LFP cell (with no capacity stated) had: little change in onset temperature; a 10% reduction in absolute maximum temperature; 75% and 65% reduction in the maximum temperature rate and pressure rate respectively; and overall 54% reduction in heat of reaction. An overcharged LFP cell showed little change in the onset and maximum temperatures compared to a fully charged cell, while contrary to expectations there was a 45% reduction in maximum temperature rate for the overcharged cell compared to the

fully charged cell [122]. More specifically, 18650 1.1 Ah LFP cells at 100%, 75%, 50% and 0% SOC have been shown to have maximum temperature rates of 4.5°C/min, 0.7°C/min, 0.3°C/min and 0.4°C/min respectively, while presenting onset temperatures of 106°C at 0%, and 101°C at all other SOC [174]. Similar trends are seen in work by Kvasha *et al.* [88], however the onset temperature at 0% was recorded to be 218°C. TR, defined as rates above 1°C/min, is only seen in 18650 LFP cells at 100% SOC [88, 174], occurring at approximately 200–250°C and lasting until ~300°C. For larger 26650 cells, TR occurs at lower temperatures, approximately 175°C at 100% SOC, and at 190°C for 50% SOC [172]. This may be due to the lower surface-to-volume ratio of the larger 26650 cylindrical cells, leading to less effective heat loss, hence greater average internal temperature and therefore reaction rates, as shown in computational studies [99, 175].

The SOC TR dependence is discussed by [88]: for the carbon anode, as (cell) SOC increase there is a slight decrease ins onset temperature of the negative electrode-electrolyte reaction. But more significantly there is a large increase in its enthalpy from 230 J/g at 0% SOC to 1246 J/g at 100% SOC, while the main exothermic peak remains in the range of 296–307°C. However, for the LFP cathode, a (cell) SOC increase from 0% to 100% SOC leads to a 20°C reduction in onset temperature, while there is only a relatively modest increase in enthalpy from 114 J/g to 337 J/g over the same SOC values. Most of the increase in reaction heat occurs over the range of 0–50% SOC, where the total increases by 2.4 times, while over the 50–100% SOC it only grows by an additional 1.2 times. Overall, at 0% the main contributors to heat are the electrolyte and negative electrode reactions; at 50% and 100% it is the negative electrode that is the main contributor.

The reduction in onset temperature at lower SOC of Li-ion cells is due to the influence of lithiation on the thermal stability of the electroactive materials within a cell [155]. In the case of LFP cells, it has been shown that a lithiated (graphite) anode is more reactive than a delithiated (LFP) cathode [122, 153], i.e. in a fully charged LFP cell the anode may provide more heat during TR than the LFP cathode.

During ARC experiments it is common to see a drop in the temperature profile, which literature attributes to the heat of vaporisation as electrolyte and gases are vented [154, 155]. Ishikawa *et al.* [154] also showed that venting occurs at lower temperatures for higher SOC. While Chen *et al.* [173] showed that, under fire calorimetry, the time to venting shortened as SOC increased. Further, under constant power calorimetry, multiple venting occurrences have been seen [114]. One prior to rapid TR and one at the start of rapid TR, where gas was released over a 30 s period for LFP compared to <1 s for the other two chemistries, due to the slower decomposition of the LFP cell.

2.1.2 Oven Exposure

As stated previously, a convection oven experiment is a fundamental test which allows us to study the response of a cell when rapidly exposed to high temperatures. A battery may experience high temperatures due to extreme environmental conditions, improper thermal management or the failure of a neighbouring cell by other means. For these reasons, an oven experiment provides a more realistic scenario than ARC, with the severity of TR due to oven heating complimentary to ARC data.

Oven tests on cylindrical Li-metal-oxide cells, in which the cell is placed in an oven and heated to the desired temperature, show that ovens at higher temperatures cause TR more quickly and result in higher cell temperatures during TR [176]. This behaviour is also shown by Hatchard *et al.* [146] (where cylindrical 18650 cells are lowered into a preheated oven) in the investigation of LCO cells, and by Jiang *et al.* [177] in the investigation of the effect of electrolyte composition on TR stability and severity in LCO cells. Tobishima and Yamaki [176] also show that a relatively small increase in oven temperature can mean the difference between no TR and TR, e.g. an oven temperature of 150°C can lead to negligible temperature rise, whereas at 155°C there is rapid and extreme heating.

Under forced convection oven tests, Larsson and Mellander [165] subjected LFP pouch cells (7 Ah and 45 Ah) to a stepped temperature rise. This was so that the onset of TR could be detected. The lower capacity cell went into TR at a temperature of ~210°C, and reached a maximum temperature <250°C. Comparatively, the higher capacity cell had an onset and maximum temperature of ~183°C and ~350°C. The energy released during TR was approximately 10–30% of the stored energy. Further work by Larsson *et al.* [178] on a LCO 18650 cell under external heating showed a small reduction in cell temperature coinciding with the voltage drop due to the melting of the separator.

The method of thermal abuse, ARC (conducting a heat-wait-seek test) compared with thermal ramp heating (i.e. oven test), has been shown to affect the nature of the temperature rate during the exotherm of TR. Thermal ramp heating leads to higher reaction rates at lower temperatures for a given cell [171].

As with ARC, the onset of TR can be defined by the cell temperature rate. For thermal abuse methods (e.g. oven test, constant temperature rate and constant power) there is little literature covering the definition of thermal runaway onset. However, for a constant temperature rate heating test, Duh *et al.* [179] defines TR onset to be 100°C/min. With similar rapid heating occurring in oven tests, this definition can be applicable here. Hence, in experimental and simulated oven exposure tests the TR of a cell is considered to occur when the temperature rate is greater than 100°C/min.

An application of oven abuse experiments is shown by [146] and [148], in validating computational simulations of $LiCoO_2$ undergoing thermal runaway. However, a lack of

oven test data for LFP cells presents an obstacle in validating similar computational work on LFP cells [see, for example, ref. 38], and hence shows the necessity and practicality of this work.

2.2 Modelling Thermal Runway

Thermal runaway modelling is a complex problem to define due to the composite nature of a Li-ion cell, as described in Section 1.2.1, resulting in many parameters that need to be defined. Further, these parameters can be difficult to determine, especially for the late stages of TR where physical properties will change and unknown reaction products will be formed which can react with unknown kinetics [180]. However, there are two methods from which thermal abuse models can be developed, 1) by calorimetry, or 2) by a chemical reaction approach [79]. The calorimetry approach requires measuring thermo-physical properties of the cells components, along with calculated kinetic properties, from ARC or DSC experiments [79], to characterize reaction rate equations. This approach has the advantage that model parameters are relatively easy to quantify compared to the chemical reaction approach, which relies on the identification of all significant reactions and understanding how these decompose to form products.

Following the work by Dahn's group on developing a thermal abuse model for a carbon anode [81, 181], which was further extended to model the thermal abuse of a Li-ion cell by including a cathode reaction [146, 182], and finally the inclusion of the electrolyte decomposition reaction by Spotnitz and Franklin [78], the calorimetry approach of thermal abuse modelling has become the standard method within this field.

Within this, the reaction rate of a cell or its components is governed by Arrhenius type equation(s), in a form similar to that of Eq. (2.1):

$$\frac{dC_x}{dt} = -Ae^{\left(\frac{-E_a}{RT}\right)}C_x^i \tag{2.1}$$

which are characterised by the activation energy (E_a), frequency factor (A) and reaction order (i), for species C_x [80]. In turn, the heating rate can be directly calculated as a function of the reaction rate(s).

The reaction kinetics, of any component of a Li-ion cell, are defined by a "kinetic triplet" [183]. These are the reaction model, activation energy and frequency factor. MacNeil and Dahn [183] state that the reaction model can take several forms when describing the thermal decomposition of solids. The majority of the literature determines the parameters for the reaction kinetics by numerical analysis of thermal abuse experiments, namely ARC and DSC, on full cells and/or their components [79]. Determining reaction kinetics by regressing [81, 134, 181] the model to experimental DSC data can be done relatively

easily. Recent work has used inverse modelling to determine the reaction kinetics of Li-ion cells [180].

Given a reaction model, inverse modelling of E_a and A will result in a reasonable fit. The choice of model can affect the determined optimised activation energy and frequency factor, by a factor of 4 and several orders of magnitude respectively, with little change in residual of fit [183]. For example, Richard and Dahn [81] show that for the NE reaction, although the values for the reaction kinetics are different dependent on the assumed Li^+ transport process, the models predict an almost identical outcome.

However, the determined parameter values are dependent on the amount of experimental data gathered, and, outside of the bounds of the experimental data the confidence in the model is limited. This can limit the understanding of TR behaviour and reduce the circumstances in which the model predictions are valid. This can be overcome somewhat by determining calorimetry data for cells at different DSC sweep rates [134, 183], ARC started at different temperatures [80], different sample combinations [134] and other considerations including various SOC, cells that are aged, or cells under charge/discharge cycling [79]. With a wider set of experimental data the kinetic triplet can be determined from parameters that lead to the smallest sum of residuals and refinement of parameter selection. The use of ARC data (rather than DSC) has been shown to be more sensitive to the selection of reaction model and hence limits the choice of reaction model, while the low effective sweep rate provides a larger sweep range over which the exothermic reactions can be analysed, leading to further improved confidence in parameter selection. Further, MacNeil and Dahn [183] show that the kinetics triplets determined are reliable, however are non-unique.

The use of various different sample combinations enables the identification of important and unimportant reactions [134]. Reaction kinetics have also been defined as a function of conversion of the decomposition reaction [184]. From this it is shown that, for an NMC cathode in electrolyte, the change in activation energy and frequency factor increase as the reaction proceeds, presumably because the cathode becomes more stable as it releases oxygen. Further, temperature predictions are more sensitive to activation energy than other reaction parameters [184]. Richard and Dahn [80] show that for a lower reaction order the rate of reaction increases at a given temperature, while there is also an increase in maximum temperature rate and temperature of maximum rate. Regarding the NE reaction, Richard and Dahn [81] show that reaction parameters change with SOC [168].

Methods other than best-of-fit and trial-and-error have been utilised. Ping *et al.* [86] uses a deconvolution method applied to C80 calorimetry data of various component and full cell samples. TR of a sample representative of a full cell is shown, see Fig. 2.6 showing heat flow vs. temperature, to be made up of 7 peaks corresponding to 7 reactions. Peaks a, b, c, d, e, f and g are respectively attributed to the decomposition of the SEI layer, separator melting, short-circuiting, disproportionation and decomposition of the cathode (LCO),

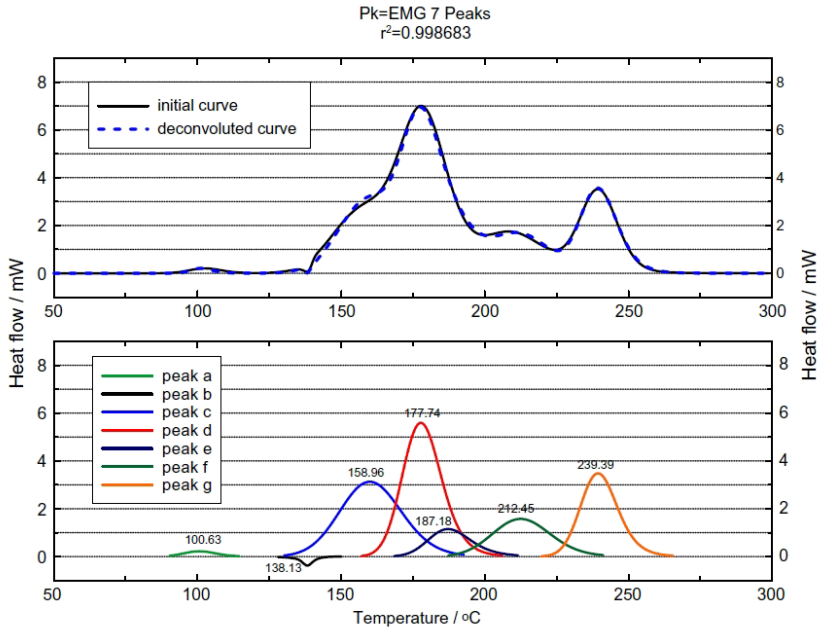

Figure 2.6: Deconvolution method to determine reaction parameters. Top) initial and deconvoluted C80 curves of heat flow at 0.2°C/min scan rate for a full cell, Bottom) individual curves making up deconvoluted curve. (Reproduced from [86]).

the reaction between intercalated lithium in the anode with the electrolyte, further LCO decomposition and the reaction of the electrolyte solvent with oxygen along with binder decomposition. However, while this method is successful at determining the contributions of heat generation in a whole cell, it first requires a database of possible reactions.

Unlike other work, Liu *et al.* [180] determines the parameters for the reaction kinetics by inverse modelling of the temperature vs. time profiles from Copper Slug Battery Calorimetry (CSBC) tests on cells at different SOC. Liu *et al.* [180] use only one modified Arrhenius expression to represent all the chemical processes occurring within a cell. For which, a third order polynomial for each of the kinetic parameters was determined as a function of SOC. Subsequent CSBC predictions were accurate, with no more than 5% error.

From the work by Liu *et al.* [180], it can be seen that utilising one global governing equation for the heat generated by the decomposition reactions allows for simpler determination of the kinetic parameters. Not only because there are less parameters to determine, but also due to avoiding the complex and difficult to interpret interactions of the four classical Li-ion cell TR reactions. However, by not simulating the reactions individually, a prediction of the TR sequence cannot be made and in turn determination of mitigation strategies would be limited. Additionally, there is a lack of simulation of other abuse conditions to enable the validation of estimated parameters.

2.2.1 Model Dimensionality

TR reactions can be assumed to be either 1) homogeneous, where the bulk material can be assumed to be of uniform temperature, or 2) heterogeneous, in which reactions propagate rapidly or combustion and explosion occur [40, 185]. The choice of assumption implies that homogeneous reactions can be modelled in 0D, while heterogeneous reactions have to be modelled in at least 1D to capture spacial differences in the progression of the reaction.

Kim *et al.* [99] shows that 3D modelling is important for studying geometrical effects on TR and for the study of non-uniform heat generation abuse scenarios, i.e. internal shorts/ point heat sources. However, 18650 cells under uniform heating can be accurately represented by a 1D radial model [99, 146].

1D radial models are adequate because, as Chen *et al.* [27] shows, the heat transfer is most important in the radial direction (because the thermal gradients are greater in the radial direction than the axial direction), while in the spiral direction heat transfer is minimal. This is because the effective thermal conductivity of the spiral is low, due to the many windings of an 18650 cell [27, 186]. Further, Shi *et al.* [186] also show that the thermal contact resistance between jelly roll layers has an effect on predicted temperatures. This additional thermal resistance can lead to greater radial temperature gradients, while the effective thermal conductivity of a cell increases with increased winding tension (of the jelly roll), as this reduces thermal contact resistance.

Although the Biot number of cylindrical cells is low enough to be valid for a 0D assumption, 0D models predict TR poorly and are greatly affected by the surface area-to-volume ratio of the cell [99]. Hatchard *et al.* [146] shows that a 0D model closely agrees with the results of a 2D planar model. However, the lumped method predicts safer operation up to slightly higher temperatures.

To reduce computational cost in a non-0D model, the small structure of the thin jelly roll electrode, current collector and separator layers can be modelled by a single continuous material with non-isotropic properties [99, 132]. Further, in 3D models of a cell, the spatially average temperature of the cell can be lumped to be implemented into coupled 0D reaction model. Coman *et al.* [143] shows this leads to less than 3% change in the results of a 18650 cell, comparing a fully 3D model (of heat transfer and decomposition reactions) to a model using the 3D heat transfer coupled with the 0D reaction model. However, this is only if the cell exhibits uniform heat loss coefficients on all sides, otherwise a volumetric heat source is not appropriate, i.e. the 0D model or the use of the volume averaged temperature in 3D. Further, if heat loss is uniform the results confirm that this relatively simple model for short-circuiting, which reduces computation time and complexity, still provides informative results about temperature.

2.2.2 TR Evolution

Modelling has shown the overlapping nature of reactions and the ability to predict the sequence of reactions, along with determining the significance of each reaction to overall heat generation. For example, the onset of reactions for $LiCoO_2$ cells are predicted to occur in the order of SEI, NE, PE, then the electrolyte [99, 146].

The self-heating and TR process under oven exposure is summarised for LCO cells [99, 146, 148, 187]: the self-heating process is found to proceed slowly at first. The NE reaction is relatively slow compared to the SEI reaction due to its dependence on the SEI layer thickness term. TR is initiated by the rapid positive solvent reaction, which in turn leads to a high rate negative solvent reaction occurring simultaneously and the occurrence of the electrolyte reaction.

For LCO cells, where TR occurred due to relatively high oven temperatures, most of the heat generated is due to the positive reaction [187]. Further the NE and electrolyte reactions are much more severe at higher oven temperatures than in the lower temperature case. Oven simulations at 175°C indicated that for $LiNi_zCo_{1-z}O_2$ cells the negative solvent and positive solvent reactions play the most crucial role in initiating TR, while for $LiMn_2O_4$ cells the solvent (electrolyte) reaction is more significant [78]. Peng *et al.* [187] note that increasing the stability or lowering the severity of the positive reaction would vastly increase the overall safety of the cell. Further, Lopez *et al.* [148] show that the inclusion of electrolyte decomposition reaction is necessary for an accurate simulation of a 18650 cylindrical ($LiCoO_2$) cell under a constant power oven test, while combustion source terms must be included to accurately simulate a cell that ignites upon thermal runaway. The negative-binder reaction, while having a high heat of reaction, has been shown to be insignificant due to the low volume fraction of binder in a cell [78].

Comparatively, at lower oven temperatures for LCO cells a similar reaction sequence occurs, i.e. SEI, NE and then PE, while the electrolyte reaction does not occur [187]. Compared to higher oven temperature exposure the SEI reaction progresses at a similar rate, while the NE and PE reactions are much slower. As such, the heating rates were relatively low, and so the heat from decomposition could be readily dissipated to the surroundings and TR did not occur [99]. Under these circumstances, most of the heat generated is due to the SEI and NE reactions [187].

The reaction evolution for LFP cells is less clearly defined. Kupper *et al.* [188] show the heating from the SEI reaction is not enough to lead to TR. Peng and Jiang [38] show that, for oven simulations at 275°C, reactions occur in the order of SEI, NE, electrolyte and, much later, PE. However, this model lacks validation, and the temperature profiles of TR do not resemble the general shape of TR of cells under oven abuse. In studying the effect of separator melt-down temperature on TR, Wang *et al.* [128] show that the PE reaction occurs before the electrolyte, which is predicted to occur before the NE reaction.

Wang *et al.* [128] state that TR is caused by both of the electrode decomposition reactions (when separator melting is above 220°C; for melting temperatures below this, it is Joule heating from short circuit that leads to TR), while Peng and Jiang [38] show that the peak cell temperature coincides with the PE reaction.

Higher C-rates are shown lead to TR to occur sooner and reach higher temperatures due to the higher electrochemical (EC) heat generation rates [189]. Ping *et al.* [189] work shows the effect the electrochemical heat has on the TR onset and hence the importance of accounting for it. Dong *et al.* [190] find that overcharging is a greater risk to TR, rather than high discharge rates, for NMC 1.5 Ah 18650 cells. However, in both Refs. [189, 190] there is no link to SOC and kinetic parameters.

The lack of accounting for internal short circuits has been cited as a cause of discrepancies in TR modelling [134]. The difference in TR behaviour due to different short-circuit scenarios has been modelled by Spotnitz and Franklin [78] and Zavalis *et al.* [191] utilising electrochemical governing equations. Coman *et al.* [143] accounted for short circuit through an additional Arrhenius equation for the heating due to electrical discharge of the short as a function of SOC. Kim *et al.* [99] use a 3D model to simulate an internal short of a cylindrical cell, by releasing 15% of the batteries stored energy into a volume equal to 0.5% of the total jellyroll at a point half-way along the radius of the cell. This showed several stages of sudden increases in self-heating rate, and also how the reaction front and temperature profile radiated out over time from the site of the internal short. Propagation through the cell, depicted in Fig. 2.7, can be explained as follows:

1. Initial reaction propagation extends along the axial and azimuthal (winding) directions, to form a hollow cylindrical reaction zone around the mandrel.
2. As the centre is hottest, reactions begin here and propagate axially to colder regions where reactants still remain.
3. As the cell is continually heated by decomposition reactions, the container is heated from bottom to top as the centre of the jelly roll (the hottest point) is connected to the can bottom.

Zhang *et al.* [192] find that the energy released by an internal short circuit has to be great enough to initiate critical reactions, i.e. PE reaction in LCO cells, to cause cell TR.

2.2.3 Heat Transfer Considerations

A high (combined radiation/convection) heat transfer coefficient allows the cell to heat up quicker, but also dissipate heat better, and hence withstand higher oven temperatures before TR occurs [187]. In general, for a higher heat transfer coefficient, when TR does

Figure 2.7: Simulated propagation front of the SEI decomposition reaction due to self-heating initiated by a local hot spot (each frame is 4 s apart). (Reproduced from [99]).

occur for a given oven temperature it is less severe but occurs sooner [148]. Further, an increase in convection coefficient allows higher exposure temperature without cell TR. Temperature predictions are affected little by changes in the cell conduction coefficient value, while temperatures are sensitive to changes in heat capacity [193].

Radiation from the cell surface has been shown to be important [27, 146], where under normal conditions during discharge, radiative heat transfer is 150% of that by natural convection [194]. A parameter sweep of emissivity values shows that for lower values of ε the cell is less effective at radiating/ absorbing heat, and in turn takes longer to warm, but importantly is more likely to go into TR sooner and more severely [146].

Under external heating, time to TR increases with reduced environmental temperature [82]. Surface-to-volume ratio is important in the TR process of Li-ion cells. A larger heat exchange area to cell volume leads to TR being initiated at lower oven temperatures and in a quicker time frame, if TR occurs at all [99, 175]. Although, a smaller heat exchange area to cell volume leads to a cell being heated more slowly from external heat sources, once self-heating is initiated, it means that the cell is less efficient at dissipating the internal heat. Hence, a greater accumulation of heat occurs, leading to a greater temperature rise and reactions proceeding faster.

For a fixed environmental temperature (or a fixed convection coefficient) there exists a critical convection coefficient (or environmental temperature) value, where at an infinite time the mean cell temperature remains below a critical value to avoid TR [82]. For example, for LCO cells the critical cell temperature was predicted to be 137°C [82]. For 18650 NMC/LTO cell, a critical ambient temperature of 162°C is predicted for a convective heat transfer coefficient of 20 $\mathrm{W/m^2\,K}$ [195]. To determine the critical ambient temperature,

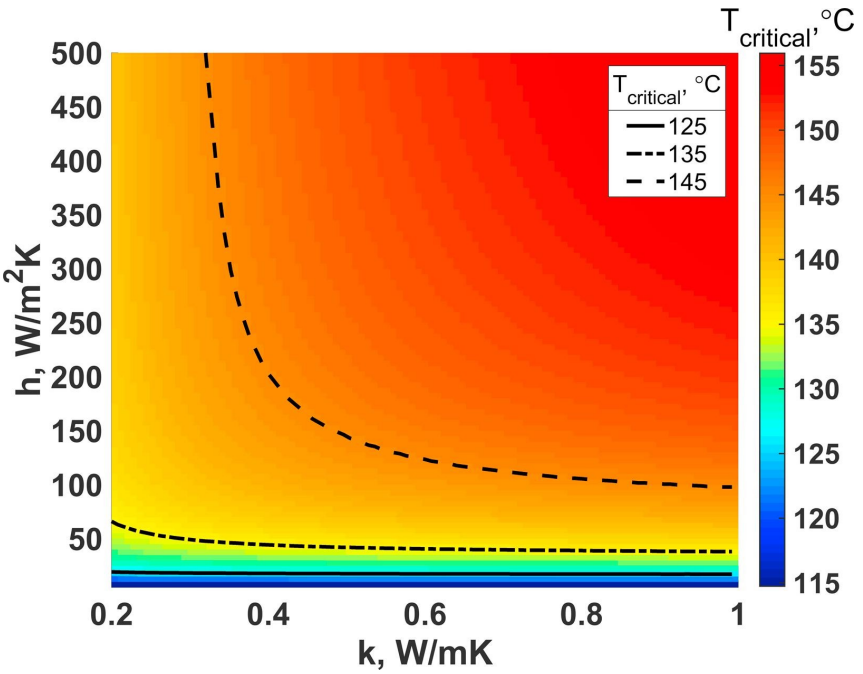

Figure 2.8: Colour plot of $T_{critical}$ for surface heat transfer coefficient, h, and radial conductivity coefficient, k, based on heat generation following the reaction model of Ref. [146]. Curves of three different critical temperatures are shown. (Reproduced from [196]).

Huang *et al.* [195] used non-dimensional Semenov and Thomas models which are shown to predict TR occurrence accurately when compared to typical oven model simulations.

Esho *et al.* [196] also calculates a theoretical critical temperature, i.e. the maximum allowable internal temperature, a cell can reach before TR is initiated by utilising the *Thermal Runway Number* (TRN) [197]. The TRN is a non-dimensional quantity, taking account of the whole heat transfer problem, where TR is said to occur when $TRN > 1$. Using this method, Esho *et al.* [196] show that small changes in allowable critical temperature (i.e. 125°C, 135°C and 145°C) can greatly affect the relationship between h and k that prevent TR, as shown in Fig. 2.8. For $T_{critical}$ =125°C, a value of $h = 20\,\mathrm{W/m^2\,K}$ or higher can prevent TR for all values of k in the range of 0.2–1 W/m K. However, at $T_{critical}$ =145°C, there is a lower limit of k below which the critical temperature cannot be prevented for any value of h between 0–500 $\mathrm{W/m^2\,K}$. Above this lower limit of k, there is an exponential decay of the required value of h as k increases.

Further non-dimensional analysis has been used by Cabrera-Castillo *et al.* [198] to define a quantity known as "*State of Safety*" (SOS). SOS values of 1 (safe) to 0 (completely unsafe), take account of temperature, voltage, current, SOC, state of health, impedance, mechanical deformation and variable derivatives. They show, as presented in Fig. 2.9, the SOS decreases more rapidly with voltage than temperature. Further, this method can be used in real time to indicate SOS during operation.

Stating the safety of the cell at a given instant from the stand-alone knowledge of a cell's surface temperature is not possible, as the difference between the cell surface and

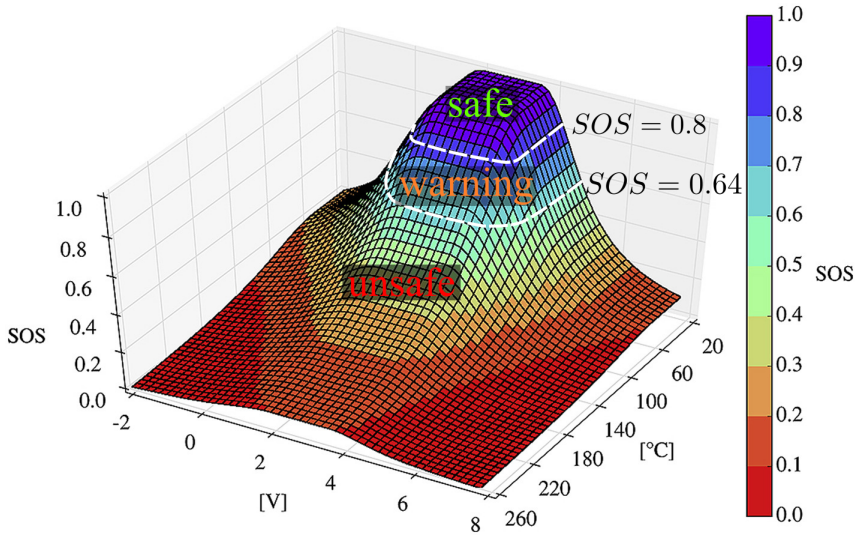

Figure 2.9: Surface plot of SOS for LFP 18650 cell considering voltage and temperature (Reproduced from [198] with added annotations).

the maximum cell temperature can be large and dependent on abuse scenario [27, 193]. The hottest temperatures of a cylindrical cell are at a point near the mandrel but not in the exact cell centre, due to the lack of heat generation from decomposition in the mandrel [27]. When a cell is heated slowly, the difference in surface and core temperature is minimal until the onset of decomposition reactions. However, under flash heating in an oven the core is cooler than the surface while heat conducts through the cell [193].

2.2.3.1 Computational Thermal Abuse Studies of $LiFePO_4$ Cells

Modelling of LFP cells is limited [for example 38, 128, 132, 188] and where it has been carried out, it is generally not validated, or is inaccurate when compared to experimental data.

Guo *et al.* [132] developed a 3D model of high capacity (55 Ah) prismatic LFP cell to analyse the response under oven abuse. In comparison to experimental data at an oven temperature of 155°C their model is inaccurate, over predicting the time to TR and greatly over predicting the severity. Hence, determination of cell safety with this model is limited. A lack of description of the decomposition model leads to an inability to determine the reasons for the inaccuracies. Guo *et al.* [132] state that inaccuracies are due to not including venting of gases and the resulting effect of Joule-Thomson cooling in the model. This is unlikely, as inclusion of this would further delay the onset of TR leading to a greater discrepancy between the experimental and simulation. However, the validity of these findings is somewhat questionable as both the experimental data and modelling data suggests TR will occur at oven temperature as low as 155°C, whereas under adiabatic conditions LFP cells are stable at temperatures of 195°C or more [114, 117].

Wang *et al.* [128] used a 2D coupled electrochemical-thermal model with abuse reactions modelled using typical Arrhenius relations to investigate the effects of separator melting temperature on TR. At melting temperatures above 200°C the major cause of TR is heating from decomposition reactions, as self-heating decomposition reactions are already occurring at high rates, below this temperature heat from short-circuiting is more significant. The simulations show that for separators at higher meltdown temperatures TR is delayed, i.e. thermal stability is increased. However, the maximum cell temperature due to TR, i.e. cell severity, is increased. While the findings by Wang *et al.* [128] provide informative qualitative data about the importance of cell melting temperature on the effect of TR, the lack of validation of their model means that the quantitative data on cell safety is questionable, while also it cannot be said how appropriate their reaction kinetics are.

Peng and Jiang [38] completed a comparative study of the safety of different LIB chemistries in a simulated oven test. They kept all parameters the same besides the kinetic parameters of the positive electrode reaction according to the chemistry in question. Their results quantitatively agree with that of experimental data on the stability and severity of different cathode chemistries. Having no experimental data to validate their simulation results for LFP, NMC and LCO/NMC, they claim their results are qualitatively similar to the findings of Golubkov *et al.* [114]. However, the results from [38] are not comparable to the experimental results of [114] as the experimental procedure of [114] heats the cell at constant rate and power, so is not representative of heating at constant temperature as in the oven test of [38]. Their results for LCO are qualitatively similar to that of the literature i.e. Hatchard *et al.* [146], however there are discrepancies in critical oven temperature and peak temperatures.

Kupper *et al.* [188] uses physico-chemical modelling to, in part, study the multi-stage SEI reaction in LFP cells. The SEI reaction is seen to have 2 peaks: the first peak is due to the formation of secondary species due to decomposition primary species, up to 120°C; the second peak (above this temperature) is due to the sequential formation of primary species (consuming electrolyte) and secondary species at equal rates, leading to a quasi-steady-state reaction. They show a single set of parameters can appropriately simulate multiple scenarios (ARC, DSC and internal short), and that initial self-heating due to the SEI reactions is not enough for TR, however they do not consider other decomposition reactions.

2.2.4 Modelling Li-ion Cell Venting

It is commonly stated that the time to TR is not predicted well due to the lack of modelling of venting, which leads to the cell cooling through the Joule-Thompson effect [146]. Further, the overestimate of simulated temperature rise is attributed to the same effect, as

venting will additionally transfer heat away from the cell [132, 148]. Hence, by not taking account of endothermic contributions during parameter fitting of reaction kinetics there is a loss of information about the reactions [143]. The difficulty arises in modelling the venting process, as it is a complex phenomenon involving the boiling and evaporation of electrolyte, expansion of pressurised gases and vapours on venting, and the mass transport of ejecta from the cell.

With regard to Li-ion cells specifically, little work has been carried out to model the venting of fluids through an orifice, which can be used to describe cell venting during the TR process. Only the works by Coman *et al.* [143, 199] are known to the author in which modelling of Li-ion cell venting is defined from first principles.

In the earliest work, Coman *et al.* [143] developed a lumped model of cell venting, considering heat generation from the four typical exothermic decomposition reactions, as well as heat loss by venting of electrolyte vapour, electrolyte boiling and solid mass ejecta. Through modelling of the thermal response of a cell under constant temperature rate oven exposure, it was shown that the time to TR is more accurately predicted with the inclusion of venting phenomena, as TR is delayed due to the time required for the cell to recover to its pre-venting temperature. The simulations predict that at the point in time when the internal pressure reaches the critical venting pressure, then the vapour present in the cell is instantaneously ejected. The loss of thermal energy from the cell by electrolyte boiling, mass ejecta and gas venting are estimated to be 1.7 kJ, 3.2 kJ and 4.1 kJ, respectively. The simulated temperature profile of venting is more rapid and extreme than the experimental data they compare it to. The magnitude of the temperature drop may be due the lumped model approximation overpredicting the volume averaged heat loss or due to the assumed model parameters, such as the mass of electrolyte, mass of ejecta and enthalpy of vaporisation. The overly rapid temperature drop, due to the instantaneous release of vapour, may be the cause of assuming a burst condition in which the vent opening is considered to be ideal and achieve full vent opening area instantaneously; in reality this may not always occur.

The assumptions made about the ejected vapour are significant. They do not consider the gas generation by the other (SEI, PE and NE) decomposition reactions. As discussed in Section 2.1.1.1, it is well-known for reactions to occur at temperatures below 100°C, and generate gases that can be considered significant contributors to the pressure build up and gas venting, which would significantly reduce the time at which they predict venting. The work by Coman *et al.* [143] is extended by Coman *et al.* [199]. Here, the electrolyte is more accurately modelled, defined by its major component the DMC solvent. The internal cell pressure is the sum of the saturation pressure of the electrolyte vapour and the pressure of the gas, while electrolyte boiling and ejecta are ignored. Gas generation is approximated by simulating the decomposition of the SEI layer, from which the reaction rate is used to govern the evolution of CO_2. The maximum mass of gas is estimated by fitting the

venting pressure limit to be exceeded at the same temperature as in the experimental data. The simulated pressure profile predicts the experimental data well. The exponential decomposition of the SEI leads to exponential gas generation and an accurate prediction of the exponential pressure increase. These results show that approximating the gases present (related to each reaction) by the most abundant gas (relative to each reaction) may be an acceptable simplification for accurate predictions.

The work by Coman *et al.* [143] shows that, while the physical description of venting is not ideal, its inclusion improves predictions of time to TR significantly. Through the developments by Coman *et al.* [199], an accurate prediction of pressure and temperature is made up to the point of venting. However, from their work it is clear that for a complete TR model, to predict temperature and pressure profiles beyond the point of venting, the inclusion of the four decomposition heat generation terms (SEI, NE, PE electrolyte), linking their reaction rates to gas generation, is required. Further, calculating the pressure of a multiphase, multi component fluid is more commonly done under the bubble point assumption [200], rather than by summation of liquid saturation pressure and gas pressure, as in [199]. Hence, determining if the bubble point assumption is valid for the electrolyte-gas composition in a cell under TR is of interest.

The work by Coman *et al.* [143] has been utilised by Wang *et al.* [201], while Ostanek *et al.* [202] extends the work by Coman *et al.* [143, 199]. Ostanek *et al.* [202] separates out the species equation for the change in mass of DMC, such that there are individual governing equations for the vapour and liquid phases. When the vent is closed vapour-liquid-equilibrium is assumed, but when the vent is open, the evaporation of liquid DMC to vapour is assumed to occur through a convection drying process. As in Ref. [143, 199], Ostanek *et al.* [202] calculates the cell pressure from the partial pressures of the DMC and generated gases. However, Ostanek *et al.* [202] includes a compressibility factor for the partial pressure of the DMC vapour. Further, Ostanek *et al.* [202] considers the gas generated by each reaction, where the amount of gas is approximated proportionately from the heat generated by each reaction. Ostanek *et al.* [202] also assumes CO_2, H_2, CO, C_2H_4, CH_4 are present and the mixture is consistent throughout the simulation to be that measured from post-failure experiments. Fluid properties were calculated from the *CoolProp* database [203].

Ostanek *et al.* [202], studying 18650 NMC cells, shows similar pressure behaviour predictions up to the point of cell venting (with vent pressure limit of 2158 kPa) as in [199]. However, Ostanek *et al.* [202] also predict a second pressure peak of 482 kPa, coinciding with the main TR event, due to the constrictions of the vent opening area. They also predict the total mass loss (including solids) and total moles ejected accurately. This they use as validation of the approximation of vent gas production proportional to heat production rates. They state that the electrolyte reaction is the main cause in gas production. It was shown that by increasing the evaporation rate constants (which could

be achieved through cell design or electrolyte formulation in practice) TR can be postponed and the severity reduced. Greater rates lead to quicker electrolyte loss after the vents open. Hence, more electrolyte is lost sooner, and at lower temperatures, so less is available for decomposition and heat generation. As such, not only does the electrolyte reaction produce less heat, but higher temperature reactions are suppressed as temperatures are not reached for their initiation.

Other work, by Cai *et al.* [204], has calculated the internal pressure of a pouch cell by using the ideal gas law and the number of moles of CO_2 produced from SEI decomposition. The number of moles of CO_2 is assumed to be equal to the number of moles of the SEI consumed, which itself is calculated from the change in SEI species. No comparison is made with experimental internal cell pressure, but the instance of pressure rise is predicted accurately when compared to the increase in strain of the cell surface (used as a proxy for pressure) due to gas generation. However, the increase in pressure is instantaneous when compared to the exponential increase in strain.

The effect of DMC (electrolyte solvent) deposition, from vent gas, onto cells has been investigated by Srinivasan *et al.* [205] as a fluid dynamics problem. However, the governing pressure to drive the gas flow along a channel are determined from experimental measurements. The explosion hazards of different cell vent gas compositions from experimental findings have been investigated by Baird *et al.* [206]. Using *Cantera* (a chemical kinetics program for gas transport and molecular properties) Baird *et al.* [206] calculate the lower flammability limit, laminar flame speed and overpressures of vent gas mixtures. Compared to experimental data their predictions agree well. They show LFP cells are safer due to lower flame speeds and maximum over pressure and due to greater lower flammability limits. This work is useful for vent sizing for battery packs.

2.2.4.1 Gas Generation

To aid the understanding of the sources of the gases, the chemical composition of the common components of Li-ion cells is first presented. For an LFP cell the anode is most commonly made of graphite (LiC_6), while the cathode is LFP ($LiFePO_4$). The organic solvents commonly used in electrolytes in Li-ion cells are dimethyl carbonate (DMC), ethylene carbonate (EC), ethyl methyl carbonate (EMC), diethyl carbonate (DEC) and propylene carbonate (PC) [91]. The molecular formula, along with the flash point and boiling point, for these solvents are presented in Table 2.3. Common electrolyte salts include: lithium hexafluorophosphate ($LiPF_6$), lithium perchlorate ($LiClO_4$), lithium hexafluoroarsenate monohydrate ($LiAsF_6$), and lithium tetrefluoroborate ($LiBF_4$) [91].

The SEI layer is formed of both stable inorganic compounds, such as lithium fluoride (LiF) and lithium carbonate (Li_2CO_3), and metastable organic compounds, such as lithium alkyl carbonate ($ROCO_2Li$), dilithium ethylene glycol dicarbonate ($(CH_2OCO_2Li)_2$) and

Table 2.3: Summary of common electrolyte solvents.

Solvent	Molecular Formula	Flash Point (°C)	Boiling Point (°C)
EC [207]	$C_3H_4O_3$	146	248
DMC [207]	$C_3H_6O_3$	18	91
EMC [207]	$C_4H_8O_3$	23	110
DEC [208]	$C_5H_{10}O_3$	445	126
PC [208]	$C_4H_6O_3$	445	242

lithium *n*-butoxide (ROLi) [209–212]. During the SEI decomposition reaction, the breakdown of the metastable compounds leads to the release of carbon dioxide, ethylene and oxygen [213, 214].

After the decomposition of the protective SEI layer, the organic solvents of the electrolyte can react with the metallic or intercalated lithium of the anode. In doing so, flammable hydrocarbons such as ethylene, propane and ethane are generated [78]. The decomposition of the LFP cathode is thought to occur directly, resulting in the release of oxygen [120, 215]. The electrolyte can react with the oxygen, leading to the production of H_2O [78]. Further decomposition of the electrolyte can occur at high temperatures (>200°C), releasing carbon dioxide, fluoride gases and various hydrocarbons by a multitude of reactions [91]. Reactions between the fluorinated binder and lithium can occur leading to carbon fluoride, hydrogen fluoride and hydrogen [78, 216]. Other than the binder reaction, fluoride gases such as HF can be produced from the decomposition of the electrolyte salt ($LiPF_6$) [217–219].

Additional to the reactions outlined above, flammable gases can be produced by further reactions mainly involving the electrolyte solvents, as outlined by Wang *et al.* [91]. Carbon monoxide can be produced by the reduction of CO_2 or the reduction of the electrolyte with intercalated lithium at the anode. Methane can be produced by the reduction of DMC with lithium in the presence of hydrogen. Similarly, ethylene can be produced by the reaction between the EC solvent and lithium, or between lithium and the SEI layer. Ethane can be produced by reactions between the DMC solvent and lithium, or the DEC solvent and lithium in the presence of hydrogen.

2.2.4.2 Vent Behaviour and Characteristics - LFP

LFP cells at 100% SOC produce relatively small amounts of gas, 50 mmol, compared to 265 mmol and 149 mmol for LCO/NMC and NMC 18650 cells respectively [114], as shown in Fig. 2.10. The gas venting process for the LFP cells consisted of releasing 20 mmol of gas when the burst plate opens, prior to TR, with the remaining gas being released over 30 s, due to the slow gas production, which is a long time compared to the sub 1 s period for the metal-oxide cells. The amount of gas produced is relativity constant between 25% and 100% SOC, as shown in Figure 2.11, however more gas is produced at 0% SOC

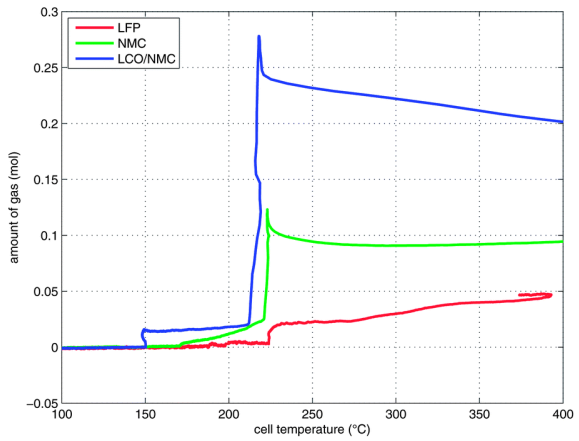

Figure 2.10: Cell gas generation with temperature. Reproduced from [114].

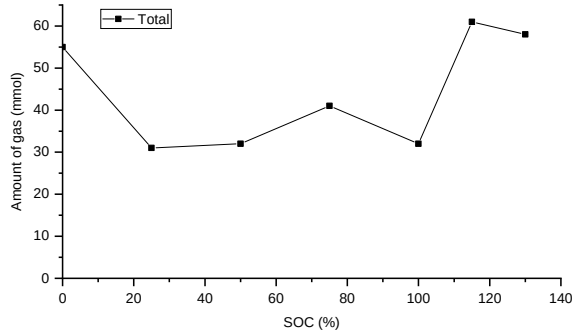

Figure 2.11: Amount of gas generated from 18650 LFP cells at different SOC [65].

and overcharged [65]. Overcharge 18650 LFP cells show stages of gas ignition upon vent rupture, followed by violent ejecta and stable combustion before final flame abatement, while the cell remained mostly intact with positive terminal still in place [220].

The gas composition, determined under an inert atmosphere, for LCO, NMC and LFP cells are similar, mostly consisting of CO_2 and H_2, with CO present in a higher concentration in metal-oxide cells than LFP cells [114]. The variation of gas composition between cells abused at different SOC has been studied by Golubkov *et al.* [65]. Their results, summarised in Figure 2.12, show that CO_2 and H_2 are the most abundant for all SOC. At 0% SOC, the gas is almost entirely CO_2, while at higher SOC H_2 and CO are increasingly abundant. The amount of ethylene and methane also increase between SOC of 0% and 100%.

The burst pressures of vent caps from 50 MTI cell components and 4 actual LG cells were calculated by Mier *et al.* [221]. They found the MTI burst pressure to be, on average, 2.158 MPa and to closely follow a normal distribution, while the LG vent cap burst at a pressure of 1.906 MPa. They also note that the burst disks of 30% of the MTI vent caps completely detached. Of the vent caps in which the burst disk remained attached, the burst pressure distribution remained close to the normal distribution. On the other hand, in the occurrences where the burst disk completely detached, the burst pressure was skewed

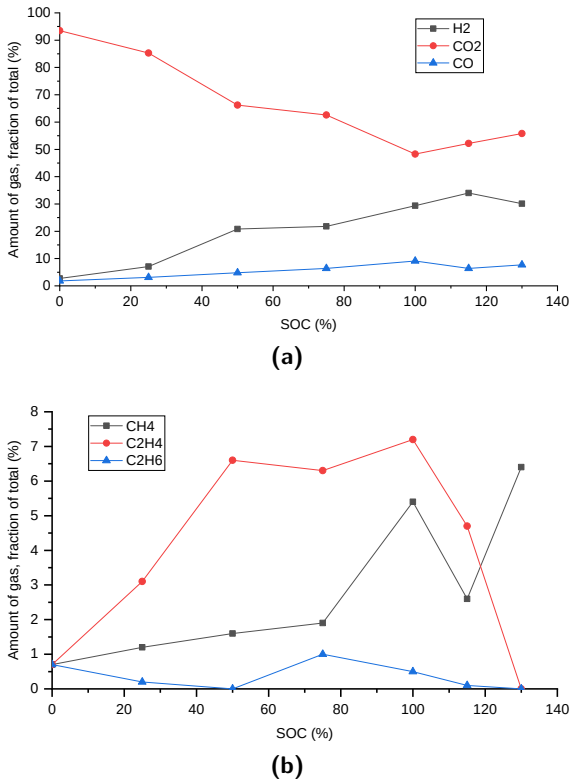

Figure 2.12: Variation of vent gas composition from 18650 LFP cells at different SOC: a) H_2, CO_2 and CO, b) CH_4, C_2H_4 and C_2H_6 [65].

towards a higher pressure. The measured opening area of the burst disk, approximately 9.87 mm^2 and 7.03 mm^2 for MTI and LG respectively, is shown to be significantly smaller than the maximum perforated plate opening, 24.98 mm^2 and 12.71 mm^2 for MTI and LG respectively. Also, the fact that the measured opening areas are similar indicates that the positive terminal and the opening around the burst disk, which is similar between cells, are the dominant features to choke the gas flow.

2.3 Thermal Runaway of Li-ion Battery Packs

TR studies of LIBs are largely of single cells, which is applicable to smaller devices where TR has little impact beyond the device, however, the TR of a cell in a battery pack has the potential to be more severe [90]. In a pack, the heat released from one cell under TR can propagate to the surrounding cells, raising their temperature to the point of self-heating, in turn causing a cascade failure from cell-to-cell, also known as TRP, that leads to total system failure [90, 222]. Hence, there is a need to be able to accurately predict TRP behaviour of packs. Experimental investigations are costly and time-consuming, so there is a need for modelling capabilities that can accurately predict cell TR and extend it to pack systems [223]. The development of a TRP model occurs in two stages (1) development of an accurate and validated model for single cell; (2) combining the single

cell model into pack with necessary heat transfer laws between cells [70]. This section presents key experimental and computational findings of TRP.

2.3.1 Fundamentals of Pack Abuse Studies

Pack studies are usually carried out at a small scale, on modules of less than 10 cells and usually without any pack casing [e.g. 90, 98, 222]. Some are larger, i.e. 40 cells, and consider the whole pack construction including wrapping, insulation and pack casing [89]. Initiating TR in a pack requires that, typically, just a single cell is abused. Abuse is implemented experimentally through one of several ways: a heater attached to a cell [222], nail penetration [89, 90, 98], radiant heating [224] or a cartridge heater in a cell casing replacing a full cell [55].

Computationally, the abuse of the initiation cell has been carried out, most commonly, by simulating heat generation due to a internal short circuit [e.g. 70, 225–227]. Less commonly, initiation heat generation has been governed by: cell cycling [140]; cell heat generation rates from experiments, e.g. calorimetry [138, 142] and fire tests [228]; or externally applied constant power heating [180]. Representing the heat generated by an internal short circuit occurring in a cell has been implemented in computational models in various ways, i.e. by:

- an instantaneous temperature rise [225, 229, 230];
- a release of a percentage of the stored electrochemical energy over a defined time period, either over a certain jelly roll volume [226], or over the whole cell [70, 140, 142];
- an Arrhenius equation to define the electrochemical reaction of a short [227]; and
- experimental heating rates from nail tests [141].

Abuse modelling in packs has been carried out defining heat generation in cells in its full form, i.e. using individual Arrhenius equations for each reaction [e.g. 70, 141, 226, 227, 231], and in a reduced form, where self-heating rate is defined either as;

- a function of temperature, estimated [230] or fit to calorimetry data [138, 229]; or
- as a function of time, estimated [140, 142] or fit to experimental abuse data [225, 228]; or
- a single, SOC dependent, Arrhenius equation [180].

The use of the full form of reaction equations within pack modelling, while requiring the most parameterisation, allows for the understanding of the reactions leading to cell

TR and, in turn, TRP. Further, if the abuse model for a single cell is valid over a variety of abuse conditions, then resultant pack simulation would in turn be more robust. The reduced forms of heat generation dependent on time or temperature, while providing a simplicity to the model, are limited beyond studying the experimental condition from which they were determined. Hence, they have a limited ability to predict pack behaviour abuse scenarios dissimilar to the initial experiment. The use of a single global Arrhenius equation, to account for all decomposition reactions, improves ease of model development and reduces computational complexity, while overall temperature predictions are accurate [180]. However, the lack of accounting for individual reactions leads to a lack of ability to predict reaction sequence.

2.3.2 Thermal Management of Packs

It is recommended that TR should be prevented in cells adjacent to a cell already under TR, rather than just postpone it [70]. Postponing TR can lead to greater average temperatures in adjacent cells leading to more severe TR events in said cells. Hence, the key to preventing TRP is adequate thermal management of the pack.

Thermal management can be passive (i.e. air, phase change material (PCM) etc.) or active (i.e. forced air or liquid). Methods include: cooling plates, mini channels, forced air flow, PCMs, refrigerant cooling, liquid cooling [141, 142, 227, 232]. Active systems can be complex, heavy, bulky and require a high power demand to drive the flow of fluid, while passive systems (i.e. PCMs) can suffer from low specific heat and thermal conductivity issues [233].

As the demand for batteries with a higher volumetric energy density leads to modules that are arranged with more tightly packed cells, the difficulty of thermal management increases [222]. Further, the thermal management systems are typically designed for general operation, where the heat from reversible and irreversible electrochemical reactions is relatively low, compared to what is generated during TR, and can be readily dissipated by thermal management system [222]. However, these systems generally cannot manage the heat generated by the high rate, high energy decomposition reactions, and fail to maintain favourable pack temperatures [140, 229].

Increasing cell-to-cell spacing, thus reducing heat transfer from an abused cell to adjacent cells, is an easy method to reduce TRP potential [138, 222]. However, this can greatly sacrifice pack volumetric energy density. Compared to air alone, carbon (graphite) composite-PCM (C-PCM) between cells has been shown to be beneficial at preventing TRP by greatly absorbing and dissipating heat, reducing surface temperatures of cells adjacent to the failed cell. This is due to the high thermal conductivity and heat capacity graphite in the PCM [89, 225, 226]. Further, the use of C-PCMs allows for TRP prevention at smaller cell-to-cell spacings when compared to air, due to the above reasons [225].

Thus, battery packs using C-PCM have relatively higher volumetric energy densities, while gravimetric energy density is lower due to the additional weight of the C-PCM. Further, if PCMs are used on their own they are shown not to be able to prevent TRP due to the low heat capacity of the material [234].

Similarly, a cold block design, using an aluminium block, is better than air or C-PCM at TRP prevention due to the even larger heat capacity and thermal conductivity of aluminium compared to a C-PCM [142, 226]. However, a copper C-PCM can result in a weight saving of up to 60% compared to an aluminium cold block design, but the copper wax block requires a wider cell-to-cell spacing (10 mm compared to 1 mm) to achieve the same performance as a solid aluminium block [142].

Another thermal management method using insulating "Mica" paper around the cells has been shown to reduce heat transfer to adjacent cells [227]. Active cooling methods, e.g. micro-channel cooling, are shown to be impractical for preventing TRP in battery packs as the pumping rates required are impractical [141]. The use of a radiant barrier, or intumescent material, between prismatic cells can successfully prevent propagation [222].

2.3.3 TRP Behaviour

The energy required to cause TRP may be relatively small, e.g. for NMC cells as little as 12% of the total heat released from one cell can lead to the TR of a neighbouring cell [98]. But TRP is shown to be prevented if the temperature of a cell adjacent to a failed cell is kept below the onset of severe reactions, e.g. in the work by Li *et al.* [235], the onset of the cathode reaction for LCO cells. However, even if the TR of one cell causes the front face of an adjacent cell to reach high temperatures (in excess of the onset of severe reactions) this hot spot is not enough to cause TR in the adjacent cell [236]. This occurs if the high temperatures only exist for a short period, and hence not enough heat is transferred to the adjacent cell that self-heating reactions develop. Hence, reporting the TRP potential is difficult as large temperature difference can be present within a cell, where the front edge of a cell adjacent to the abused cell can be hundreds of °C hotter than the backside [98, 236]. As such, depending on the location on a cell the temperature measurement is taken, there is a significant variation in recorded severity.

Similarly, during the rapid heating event of the abused 18650 cell there can be differences of 43°C to 71°C radially, between the centre and sides, of the surrounding cells [55]. Hence, predictions of TRP are affected by the accuracy to which a cylindrical cell's anisotropy is known [180]. This affects a cell's radial heat transfer, and in turn, indirectly affecting the cell-to-cell heat transfer. Further, as with TRP through the pack, propagation also exists within the cells [237]. Propagation through a cell is shown to be slower for cells going into TR later on in TRP due to their lower SOC as they have discharged energy into failed cells [238].

Pack propagation speed, i.e. time between subsequent row failures, increases for subsequent rows due to the pre-heating of the later cells by the heat generation of the former and increased combustion efficiency as more batteries burn simultaneously [180, 239]. Propagation speed has been shown to linearly reduce with the square of cell spacing (in a 3-by-3 pack) and is attributed to the radial decline of radiation with the square of distance [240]. For high energy NMC pouch cells, Li *et al.* [237] shows that for a five cell module propagation of TR through a cell is consistent at 10 s, but propagation between cells takes longer (on average 86 s). Further, TRP is slower for later cells, in contradiction of Liu *et al.* [180] findings. Propagation speed is shown to be linearly related with SOC, while the use of PCM has been seen to increase propagation speed due to low thermal conductivity and accumulation of heat in the PCM [240]. TRP of a module can be quicker in larger modules due to adjacent cells being insulated by each other, retaining heat leading to greater decomposition heating rates, while operational discharging of the cells further leads to quickening the onset of TR [241].

The location of the initiation cell within a pack has been show to effect TRP potential. Propagation has been shown to be more likely (for an eight 18650 cell laptop battery pack) when the failed cell is in contact with fewer cells and when those cells are in contact with the pack wall [230]. Similarly, Kizilel *et al.* [225] shows that cells in contact with the failed cell can reach different temperatures, depending on how many cells these neighbouring cells are themselves in contact with. Kizilel *et al.* [225] also showed that increased ambient temperatures and lower convection coefficient increase TRP potential.

With reference to statements about the location of initiation cell above: the increase in TRP potential is due to the increase in heat transfer from the initiation cell to individual neighbouring cells (when there are less neighbouring cells to absorb the heat), and less heat loss from the neighbouring cells due to relatively insulating plastic battery pack casing, leading to a greater temperature rise in these neighbouring cells [225, 230]. As such, the greater temperature increases the chance of TRP as reactions are initiated at higher temperatures. This shows the importance of how modelling can help direct experimental work by studying the initiation of TR at different locations within a module and identifying the cell most likely to induce TRP.

TRP is considered more likely when multiple cells that fail are aligned diagonally rather than laterally (determined by the use of two 250 W heaters in a module of four 18650 cells) because diagonally arranged cells are more closely packed [242]. Ouyang *et al.* [242] also state that batteries undergoing TR near the centre of a module would cause more severe TRP. However, this is only true for the constant heating method they used. This applies more heat (due to constant heating until TR detected) to more cells, rather than realistically where the heat released by decomposition would be shared between more cells if the failed cell was central, resulting in adjacent cells heating up less than when a failed cell is near the edge and adjacent to fewer cells.

2.3.4 Heat Transfer Pathways, Electrical and Fire Considerations

The heat transfer through cell tab connections is an important consideration in packs of cylindrical cells [90]. This is because the physical contact area between cylindrical cells is relatively small and hence heat transfer by cell-to-cell surface contact conduction is low, compared to pouch cells. Without tab connections heat transfer is dominated by fluxes at the cells surface [239]. Kizilel *et al.* [225] show that when tabs are considered, in modelling a pack of 18650 cells, a relatively large cell spacing of 2 mm (compared to a case where tabs are not considered) cannot prevent TRP as the heat transfer is dominated by that through the tabs and not the air. However, the use of a C-PCM matrix, due it its higher thermal capacity and conductivity compared to air, can absorb heat more readily from the cell under TR. For modules of cells under normal operation, cells will have similar surface temperatures and so convection would be dominant when surface conduction is excluded [194]. However, by Rad *et al.* [194] reasoning, under TR of a cell in a module there would exist large cell-to-cell temperature differences, so radiation would be significant. Reductions in contact resistances as cells deform during TR, when not accounted for in simulations, can lead to overpredictions of heat transfer [235].

The importance of different heat transfer mechanisms is numerically investigated by [243] for a 3-by-3 pack of NMC 18650 cells with an "M" type tab connection where cell spacing, tab width and tab solder radius were varied. In all cells (excluding the trigger cell), in all cases over the ~30 min simulation, the heat is transferred into cells by tab conduction and radiation, while heat is lost by convection. For increased cell spacing the magnitude of heat transfer reduces for all cells besides the trigger cell. The trigger cell has a reduced heat transfer contribution from conduction, while heat transfer by radiation is increased, overall the total heat loss increases. In the trigger cell radiative heat transfer is the most dominant, while it plays an important roll in cells in view of, but not connected to, the trigger cell. Conduction dominates in cells connected to trigger cell. Soldering area primarily, and intuitively, affects heat conduction. A greater soldering radius leads to improved and greater heat transfer by conduction. Hence, this has a greater effect on cells that already have a high proportion of heat conduction, i.e. cells connected to trigger cell. The same is true for increased tab width.

Fire presents a significant heat transfer path [231]. For example, considering NMC 18650 cells, nearly 3 time more energy can be generated by the burning of vent gases than what is released from the reactions inside the cell [157]. The fire originates due to the ignition of ejected electrolyte when in the presence of oxygen [98, 180]. This increases the TRP potential if: 1) vented gases/ flames are directed at neighbouring cells close by; or 2) if cells are enclosed in a casing, as is most common [55, 231, 244, 245]. For enclosed cells, the flame behaviour can lead to complex heat transfer around the pack as the flames engulf other cells causing local hot spots at unpredictable locations [224]. Further, Srinivasan *et al.* [205] predict that DMC, which is ejected as a cell vents, can condense out of the

ejecta and be deposited on cells within a pack, where on the TR of the vented cell the DMC in-turn burns due to the high temperatures, enhancing TRP. In a pack that allows venting to the open atmosphere, Feng *et al.* [98] show the flames had little effect of heating other cells. However, Chen *et al.* [239] show that when flames are not contained the down ward radiation from the flame enhances propagation.

The series or parallel connectivity between cells within a pack has a significant impact on the overall TRP potential [90, 222]. For cells in series, or where a failed cell is disconnected from the parallel string, TRP is unlikely [89]. This is due to the temperature rise in cells adjacent to the failed cell is usually short-lived and the heat is dissipated throughout many cells and from the pack. However, for cells in parallel the chance of TRP increases due to additional heating from ohmic sources. This occurs as a failed cell in a parallel string acting as an external short, allows all other cells in that string to discharge [222, 246]. This leads to several detrimental factors :

1. concentration of heat generation around the already failed cell,
2. prolonged heating of adjacent cells, and
3. a release of over 100% of a cell's rated energy capacity.

In turn, leading to greater average cell temperatures than compared to similar series connected cells, and an increase in the likelihood of TRP [90, 222]. Further, the nearest cells to the failed cell (with the shortest electrical connections) discharge the most severely and undergo greater TR events. The mitigation of cell shorting is commonly achieved through blocking or discharge diodes, which prevent current flow from healthy cells to shorted cells [90].

Additionally, the configuration of the tab connections is shown to affect TRP potential. A branched configuration shows less damage (lower temperatures, voltage drops and visible signs) to the cells surrounding the abused cell, compared to a similar module connected in a serpentine manner [222]. Greater damage is seen in the serpentine layout as it allows greater electrical discharge in the abused cell that has shorted due to separator melting. Also, venting leads to unpredictable consequences inside a battery pack due to ejecta causing shorts away from the failed cell [89]. Thus making it difficult to predict the overall outcome in detail.

2.3.5 LFP Pack TRP Behaviour

Little research has been undertaken into the TRP of LFP packs. Of that available, experimental investigations of 18650 LFP packs under forced convection cooling are shown to be resilient to TRP as they require an order of magnitude more energy (178 kJ to 430 kJ)

to be supplied to the pack to initiate TRP compared to the cell rated energy capacity (17.4 kJ) [247]. Modelling of an LFP pack constructed of pouch cells by Larsson *et al.* [228] shows that 1 mm cooling plates between all cells and 5 mm fire walls between modules of 10 cells are effective at preventing TRP. However, neither of these studies investigate the reasoning and limit of this resilience.

2.4 Summary

The literature regarding ARC has shown that it is a useful method to quantify the stability and severity of TR for (non LFP) Li-ion cells at various SOC and to determine a safe operating window for a cell in terms of SOC and temperature. It has also been shown that ARC data can be used to understand the stages of TR in a cell. The mechanisms relating SOC and severity present information for analysing the ARC data, while the thermal maps show that investigation is required to determine if self-heating is self-sustaining and hence a safety issue. It is of interest here to obtain data of this nature regarding LFP cells, such that a thorough and comparable analysis could be made of LFP cells to determine under what conditions self-heating reactions are self-sustaining and at what SOC TR occurs. Hence, enabling a detailed description of the TR process and outlining the conditions necessary to avoid TR.

The literature regarding oven heating has outlined methodology and the general characteristics of TR for (non LFP) Li-ion cells in response to ovens at various temperatures. It shows that it is a necessary technique to understand if there is drastic change in TR severity for a small increase in oven temperatures, whilst also outlining the increased severity compared to that of ARC. It also outlines the necessity of such data for other areas of TR research e.g. model validation, which is lacking for LFP.

Hence, to address gaps in the literature on the SOC dependence and oven heating response of LFP cells, this thesis, in part, will characterise the safety of LFP cells under thermal abuse conditions (ARC and convection oven tests) to quantify their safe operating window in terms of SOC and temperature, and identify the hazards they pose. Calorimetry will be carried out under near-adiabatic conditions and represents the worst case scenario of a cell undergoing heating, as there is zero heat loss from the cell. ARC also allows us to infer the process by which TR occurs, which is necessary for developing accurate models of TR by ensuring that the reactions are simulated in the correct order and with the appropriate magnitude of heat relative to each other [153]. A convection oven test allows us to study the response of a cell when rapidly exposed to high temperatures, representing what might occur due to environmental conditions or as a result of heating from a neighbouring cell which has failed by other means.

The literature regarding modelling TR in Li-ion cells has shown that the calorimetry approach, i.e. governing the decomposition of cells by Arrhenius formulation, is most common and able to produce adequate predictions. However, a lack of validation of previous LFP models requires further work to comprehensively understand parameterisation of LFP cells. Further, the inclusion of venting behaviour is shown to improve TR predictions. However, unlike the literature, it is more appropriate to consider that the system is at bubble point. Hence, this should be investigated to determine if appropriate for LIBs. The literature has shown the importance of considering cells assembled into packs to assess TRP potential. However, little work has examined TRP for LFP at pack level, nor quantified the importance of radiation to TRP.

Chapter 3

Methodology

The methodology chapter is split into three sections, that of experimental methods, Section 3.1; that of governing equations for a single cell TR model, Section 3.2; and that of modelling a battery pack, Section 3.3. The experimental section discusses ARC and oven abuse testing, as well as cell charging and determination of cell specific heat. The experimental methods, though important independent of any other work, are also important to the understanding, development and parametrisation of the TR model. Section 3.2 presents a classical Li-ion cell TR model, including governing equations for heat transfer in a solid body and heat generation from cell decomposition reactions. This is then extended to included additional behaviour of cell venting and simmering reactions. Finally, Section 3.3 presents how the battery pack is constructed, how governing equations are applied over the geometry and the abuse scenario implemented.

3.1 Experimental Methods for Assessing Cell Thermal Runaway Behaviour and Determining Cell Properties

The thermal runaway behaviour of Li-ion cells is assessed, in this work, by analysing the thermal and physical response of cells when thermally abused. The thermal abuse tests carried out are ARC and oven testing. ARC testing allows for thermal abuse under near adiabatic conditions and represents a worst case scenario of a cell under heating, to allow the inference of the TR process. The convection oven test compliments the ARC test, allowing one to study the response of a cell when it is rapidly heated to a high temperature, where rapid heating is more representative of realistic scenarios. The procedures of ARC testing and oven testing are described in Section 3.1.1 and Section 3.1.2 respectively.

For each ARC and oven abuse experiment, every cell that is tested is required to be at a specific SOC to investigate the effect of the SOC on the TR behaviour. The methodology for charging the Li-ion cells to the required SOC prior to an abuse test is presented

in Section 3.1.3. Further, for investigating heat generation during TR and TR model development, the value of the cells specific heat capacity is required. The methodology for determining the specific heat capacity of a cell is presented in Section 3.1.4.

3.1.1 Accelerated Rate Calorimetry Procedure

Fig. 3.1 presents a schematic of the ARC equipment, see Fig. 3.1(a), resulting data plot, see Fig. 3.1(b) and operating procedure, see Fig. 3.1(c). The ARC, see Fig. 3.1(a), contains a sample, i.e. a cell, inside the ARC jacket. A thermocouple is attached to the surface of the sample/ cell surface. The jacket is constructed of three zones, top, bottom and sides, which are individually heated and monitored by individual thermocouples. Adiabatic conditions are maintained by keeping the bomb (cell surface) temperature and jacket temperature exactly equal. During exothermic reactions, the adiabatic condition is upheld by maintaining a temperature difference of zero by using proportional, integral and differential control algorithms. Alongside temperatures, pressures can be monitored.

The ARC test is conducted following the standard method of operation known as the *Heat, Wait, Seek* (HWS) procedure. The HWS procedure is illustrated in Fig. 3.1(c) and undergoes the following steps:

1. The HWS procedure consists of heating the walls of the chamber by a small amount, ΔT, such that the chamber temperature increases, which in turn increases the temperature of the cell contained in the chamber.

2. A wait period (Δt_1) then follows to allow the cell to become in thermal equilibrium with the chamber walls.

3. Following this, in the seek period (Δt_2), the surface temperature of the cell is monitored and the chamber set to follow the cell temperature.

4. Temperature rate check:

   (a) If the rate of change of temperature with respect to time of the cell surface is greater than a predefined value ($rate_{onset}$), then the ARC enters exotherm mode, such that the system is in near adiabatic conditions.

   (b) If the temperature rate condition is not met the heat-wait-seek steps are repeated until this condition or the maximum temperature condition is satisfied.

From the resulting exothermic data, TR behaviour of a cell can be outlined with key characteristics such as: the exothermic onset temperature (T_0), heat of decomposition (ΔH), maximum temperature (T_{max}) and self-heating rate (dT/dt).

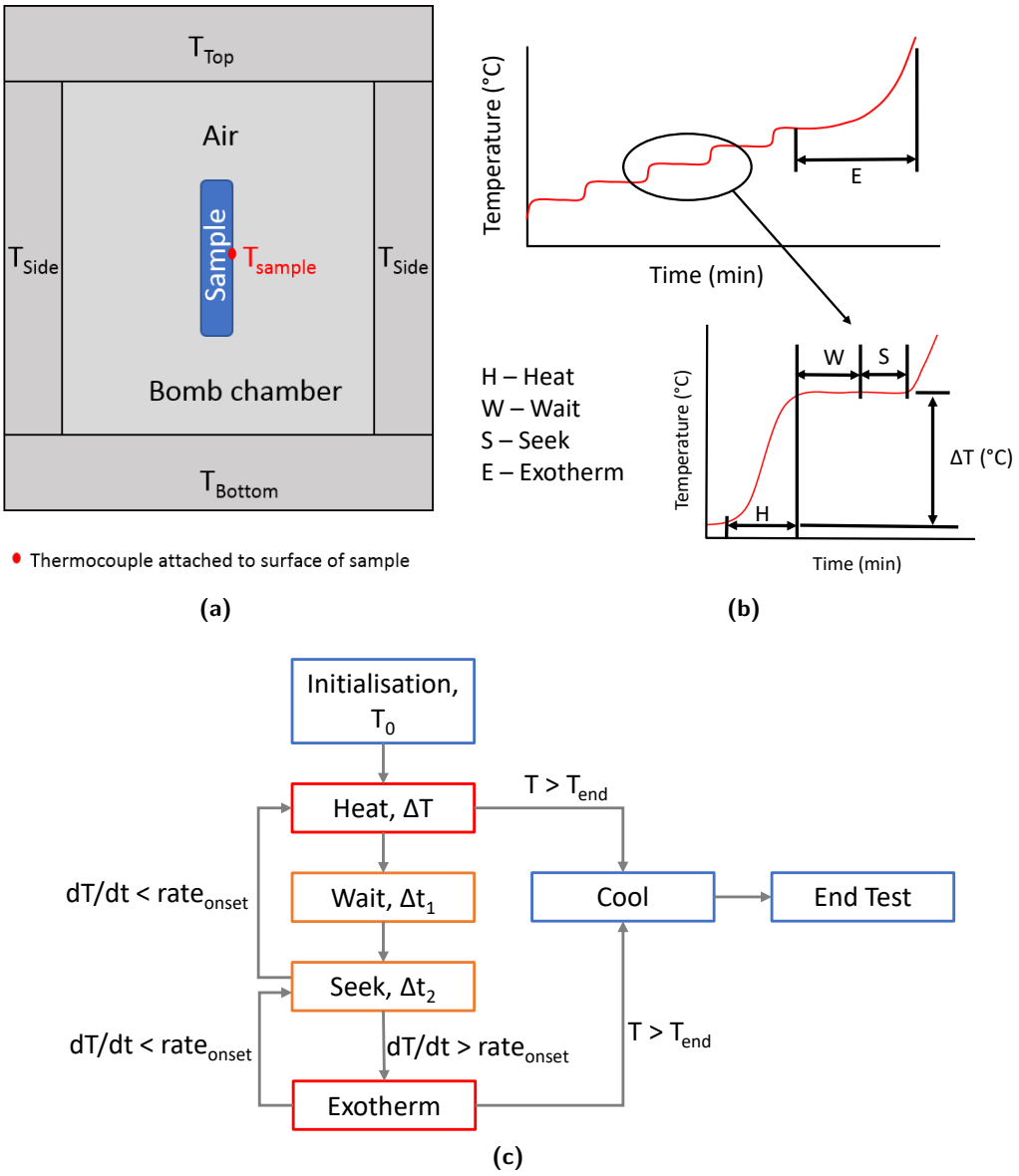

Figure 3.1: ARC HWS procedure. (a) illustration of an ARC (b) illustration of resulting data plot (c) flow diagram of HWS procedure.

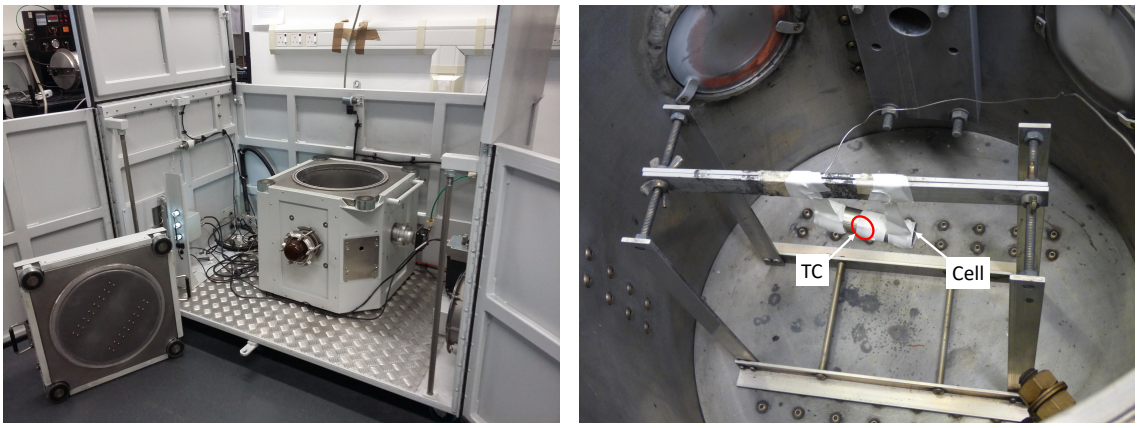

(a) (b)

Figure 3.2: Experimental set up of ARC test. (a) Thermal Hazard Technology ARC EV+ (b) close up of cell suspended in the ARC with thermocouple (TC) attached.

More specifically, the ARC tests were performed using a *Thermal Hazard Technology ARC EV+* calorimeter, as shown in Fig. 3.2(a). The HWS method was set up with the following conditions:

- a start temperature of 50°C,
- end temperature of 315°C (the maximum operating temperature of the ARC),
- temperature step of 5°C,
- temperature rate sensitivity of 0.02°C/min, and
- a wait time of 60 min.

A full list of the standard operating parameters for this procedure is presented in Table 3.1.

The selection of temperature rate sensitivity, temperature step and seek time have an effect on the resulting calculated self-heating onset temperature. A lower temperature rate sensitivity allows for a more accurate determination of the onset of self-heating due to lower reaction rates. A larger temperature step leads to faster experimental times as it results in fewer HWS steps. However, self-heating will be determined to a lesser precision. For example, if a large temperature step is taken, i.e. 20°C, over the temperature range of 80–100°C knowing that self heating begins at 92°C, then self-heating can only be picked up at earliest at 100°C. Whereas, if a temperature step of 5°C is used, then self heating can be detected much closer to the true value. Conversely, a smaller temperature step increases the experimental time for a diminishing increase in accuracy.

The onset of self-heating of the cell is taken to be when the cell surface temperature rate is >0.02°C/min. TR of the cell is taken to be when this rate is >1.0°C/min. The ARC test was carried out on LFP cells at 0%, 28%, 63%, 100% and 110% SOC (charged

according to the procedure in Section 3.1.3). The test was repeated at least three times at each SOC. Following the test, thermocouple placements on the cells' surface were visually checked to ensure that they were still firmly attached. This was done to ensure that the temperature reading would be accurate throughout the entirety of the test run. In the event that the thermocouple became loose, additional repeats were taken to ensure at least three accurate repeats were available for comparison.

The physical arrangement of the LFP cell in the ARC is depicted in Fig. 3.2(b). The cell was removed from its shrink wrapping and an N-type thermocouple was attached to the surface of the cell with glass cloth tape. The cell was then suspended from an aluminium frame to ensure it did not come into contact with the walls of the ARC vessel. The cell was attached to the frame using glass cloth tape, to ensure that there was negligible heat transfer between the cell and frame, allowing the phi-factor (a factor to compensate for the thermal mass of the holder) to be taken as unity.

To further ensure the robustness of the data gathered, calibration and drift checks were periodically carried out every 10 tests or every 4 weeks, which ever came sooner. The calibration test is required to determine the temperature offset between the ARC temperature and the sample temperature. It is carried out in a similar manner to the standard HWS test, except that the sample is inert and the temperature sensitivity is twice that of the standard HWS test (i.e. 0.01°C/min). The scheduled calibrations can account for external environmental temperatures or the build up of debris on the chamber walls from TR that may alter the temperature offset. Here the sample thermocouple is attached to a thin sheet of aluminium (approximately 2 mm×20 mm×50 mm) placed in the bottom of the ARC chamber and isolated from the chamber floor by a thermally resistant ceramic plinth.

The drift test is then performed to ensure there is no positive or negative feedback, again carried out with an inert sample, but with a temperature rate sensitivity equal to that which would be used in a standard HWS test. A positive drift would bring the onset of self-heating forward, making some or all of the exothermic data irrelevant, while a negative drift would mask the onset of self-heating, leading to the onset of self-heating to be reported to be at a higher temperature than in actuality. If any drift is detected the calibration is re-run until the drift test is successful. A full list of the standard operating parameters for the calibration and drift check procedures are presented in Table 3.1.

3.1.2 Oven Test Procedure

The oven test was carried out using a *VWR DRY-Line 53* natural convection oven (internal dimensions 401×401×330 mm), shown in Fig. 3.3(a), with a maximum set temperature of 220°C. The oven was preheated to the desired abuse temperature before a cell (at 100% SOC) was placed on a steel wire shelf in the centre of the oven. With minimal

Table 3.1: ARC operating parameters.

Parameter	HWS	Calibration	Drift Test
Start temperature, °C	50	50	50
End temperature, °C	315	315	315
Temperature step, °C	5	50	20
Temperature rate sensitivity, °C/min	0.02	0.01	0.02
Wait time, min	60	60	60
Calculation temperature step, °C	0.2	0.2	0.2
Cool temperature, °C	35	35	35
Door release temperature, °C	50	50	50
Maximum safety pressure, bar	200	200	200
Maximum temperature drop, °C	25	25	25
Maximum pressure drop, bar	20	20	20
Maximum exotherm rate, °C/min	1000	1000	1000
Maximum pressure rate, bar/min	1×10^5	1×10^5	1×10^5
Driver heater power, %	20	20	20
Data logging temperature step, °C	0.5	1.0	1.0
Data logging time step, min	0.5	0.5	0.5
Exotherm logging temperature step, °C	0.5	1.0	1.0
Calibration mode settling time, min	-	60	-

surface-to-surface contact between the cell and the shelf, heat conduction from the shelf was assumed to be negligible. The oven and cell surface temperatures were measured by K-type thermocouples and recorded using a *Pico USB TC-08* data logger and PC. The shrink wrapping on the cell was removed to improve the contact between the thermocouples and cell surface. The test began from the moment the cell was placed in the oven and ran for 90 minutes. Figures 3.3(b) and 3.3(c) show the placement of the thermocouples on the cell and in the oven. The two cell thermocouples were attached to the long edge of the cell (i.e. not the flat end terminals) with glass cloth tape, 1 cm from either end of the cell. The thermocouple measuring the oven temperature was placed at the same height as the cell but away from the cell surface and out of the path of vented gases to minimize any affect the heating from the cell or gas jet would have on the oven temperature reading. All cells were tested at 100% SOC (charged according to the procedure in Section 3.1.3) and had been stored in ambient conditions beforehand.

3.1.3 Charging Cells to Required SOC

To charge an LFP cell to the required SOC for either the ARC or oven test, the following procedure was adhered to: cells were charged to their required SOC using the constant current - constant voltage (CC - CV) method on a *MACCOR 4000M* battery cycler, under ambient conditions. Prior to charging, as cells were stored partially charged, all cells were discharged at 0.5C until 2.5 V, then at CV until the current dropped below 0.01C. To charge, a CC of 0.5C (0.75 A) was applied until the charge voltage was reached e.g. 3.65 V

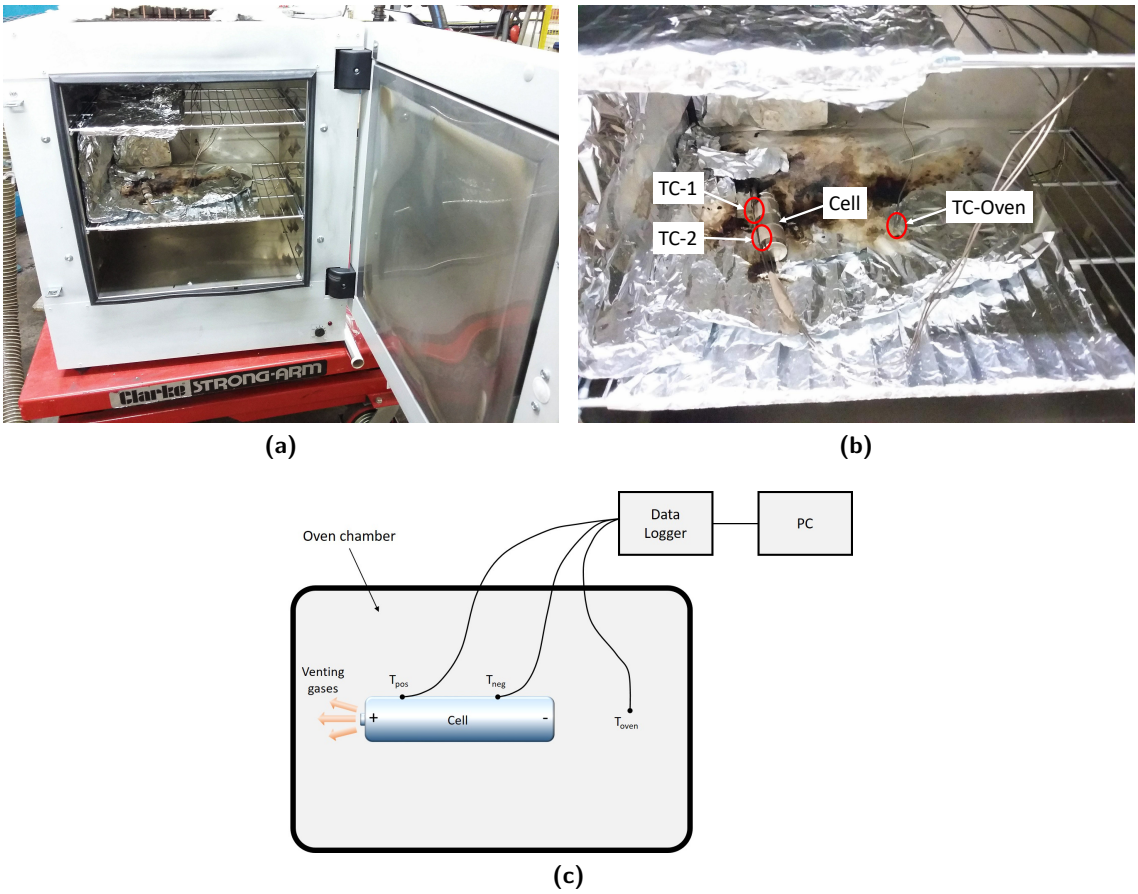

Figure 3.3: Experimental set up of oven test. (a) convection oven (b) close up of cell in oven with TC placements (c) schematic of oven set up.

for 100% SOC, thereafter a CV (of e.g. 3.65 V) was applied until the charge current dropped below 0.01C. For a SOC of 28% and 63%, the cells were charged at 0.5C, with a CC cut off criterion determined by the corresponding charge capacity for the desired SOC (420 mAh and 945 mAh respectively). For 0% SOC, the cell was discharged but not recharged. For overcharge at 110%, the cell is charged at 0.5C until 4.2 V, then at 0.2C to reduce ohmic heating, cut off is determined by measured capacity (1650 mAh).

3.1.4 Determining Cell Specific Heat Capacity

To determine the cell's average specific heat capacity an adiabatic calorimetry test was undertaken, following the methodology as described by Bryden *et al.* [248], utilising an ARC (specifically a *Thermal Hazard Technology ARC EV+*). The basic principle employs the First Law of Thermodynamics:

$$\Delta U = Q_{net} - W_{net} \tag{3.1}$$

where ΔU (W) is the time dependent change in internal energy of a body, Q_{net} (W) is the net heat supplied to the body and W_{net} (W) is the net work done by the body. Further, $Q_{net} = Q_{in} - Q_{out}$, where Q_{in} (W) and Q_{out} (W) are the heat transferred to and from the body.

In an adiabatic system, with no work being done, Eq. (3.1) can be rewritten as:

$$mC_p\Delta T = Q_{in}\Delta t \tag{3.2}$$

where ΔU is substituted by the change in enthalpy ($mC_p\Delta T$) on the assumptions of:

1. The cell being considered as a system of solid and liquid materials, as the amount of gas present within the cell under normal conditions is negligible. The mass of gas is on the scale of 1×10^{-3} g [199] verses a cell mass of approximately 40 g.
2. That over the temperature range of the experiment (approximately 15°C to 55°C) there is no change of phase of the cells materials. Specifically, the evaporation of the liquid electrolyte does not occur, as the lowest boiling point of the solvents that are used in the liquid electrolyte is 91°C, see Table 2.3.

Furthermore, it is assumed the mass, m (kg), and specific heat capacity, C_p (J/kg K), remain constant. In turn, the heat capacity of the body can be determined from Eq. (3.2) if $\Delta T/\Delta t$ (K/s) and Q_{in} are known.

Equation (3.2) can be used to find the specific heat capacity of a body, specifically the Li-ion cell, by using the following methodology to determine the temperature rate of the body, for a supplied heater power $P = Q_{in}$. The test is carried out on a single cell, as well

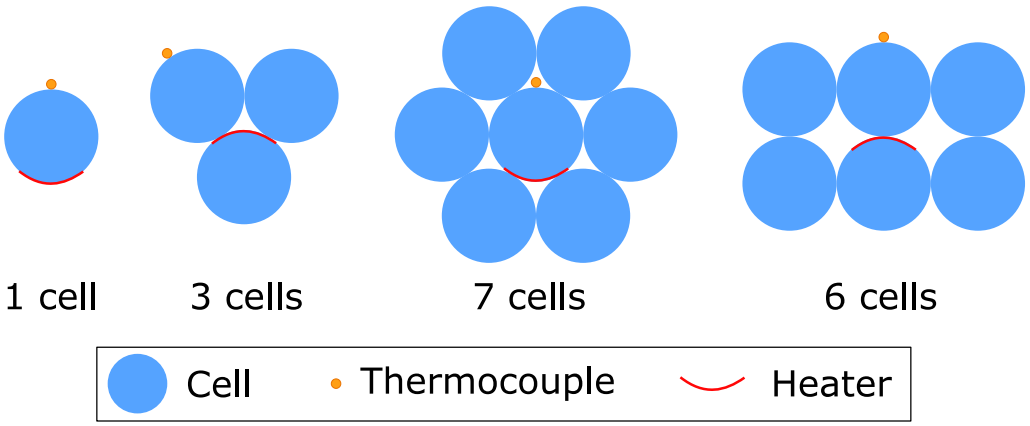

Figure 3.4: Different sample sizes and cell arrangements for heat capacity experiment.

as groupings of multiple cells. For the single cell, a *Kapton* heater (rated at 1 W when connected to a 12 V supply) is applied directly to the surface of the cell. A thermocouple is applied to the cell surface on the opposite side, see Fig. 3.4, while the temperature is recorded by the ARC instrument. Both the heater and thermocouple are secured in place with aluminium tape. Similar set-ups are carried out for groupings of multiple cells, see Fig. 3.4. Together, the cell(s), aluminium tape and heater are termed the "sample".

The mass of the cell(s) and heater are recorded before the sample is assembled, and once assembled, the sample is also weighed. In doing so, the mass of aluminium tape used can be determined by the difference between the unassembled mass and assembled mass, see Eq. (3.3).

$$\sum_{i=1}^{n} m_{cell,i} + m_{heater} + m_{tape} = m_{sample} \tag{3.3}$$

Due to practical reasons, having to attach the thermocouple once the sample is in place in the ARC, the sample mass does not account for the tape to hold down the thermocouple. However, the amount used for this purpose is limited to the smallest practical amount and negligible to the sample.

The assembled sample is suspended, by glass cloth tape from an aluminium frame, such that it is in the centre of the ARC chamber, see Fig. 3.5. This is to ensure that the sample does not come into contact with the chamber, where it would be inappropriately heated, and also, such that no heat is lost through suspending the cell, as the glass cloth tape provides a negligible heat conduction pathway. The thermocouple is attached to the sample with aluminium tape, while the heater's electrical wires are connected the ARC's auxiliary cables, which allow for an electrical interface between the interior of the ARC chamber and the external environment, see Fig. 3.5(a). The external connection of the auxiliary cables are attached to a 12 V power supply.

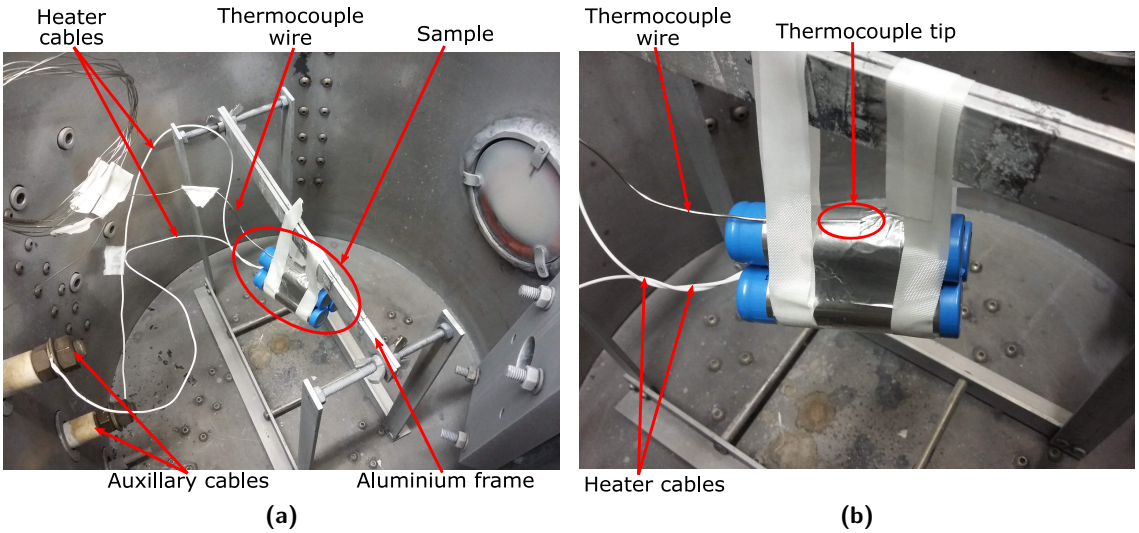

Figure 3.5: Experimental set up of heat capacity test. (a) sample in ARC chamber (b) close up of sample.

The ARC chamber is then sealed and the test begins by setting the ARC chamber to temperature approximately 5°C greater than ambient. The ARC is held at this condition until the sample temperature is within 0.5°C of the chamber temperature, where the system is deemed to be in equilibrium. At this point the ARC is put into "exotherm" mode, in which the ARC instrument controls the chamber temperature such that it matches the sample temperature. In turn, the sample can be considered to be in an adiabatic environment. As no heat is being generated, the sample should remain at a constant temperature. If this does not occur the system can be considered faulty and the set-up checked and previous sets repeated. Otherwise, the heater power can be switched on. At which point the sample will start to heat up and the ARC will also heat up to maintain adiabatic-like conditions. The heater remains on until the sample reaches 55°C, as this nears the safe operating limit of the LFP cell of 60°C, after which, it is turn off and the ARC set to "cool down" mode. This concludes the experiment.

The exothermic operating region of the experiment allows the calculation of the adiabatic temperature rate, dT/dt, of the sample. The supplied heater power, P, is calculated from the measured heater values of 0.0956 A and 11.97 V [248]. These values were measured once and assumed the same for each experimental run. Hence, the total specific heat capacity, $C_{p,tot}$, of the sample can be determined from Eq. (3.2) by substituting dT/dt and P accordingly. The average specific heat capacity of a single cell can therefore be determined from:

$$m_{sample}C_{p,tot} = m_{tape}C_{p,Al} + \sum_{i=1}^{n} m_{cell,i}C_{p,cell} \tag{3.4}$$

where $C_{p,Al} = 913\,\mathrm{J/kg\,K}$ [249], and in which the heat capacity of the heater is neglected. This process is repeated for a given sample to determine any variation in determined $C_{p,cell}$

values. The number of repeats is given in further detail in the result of the heat capacity test in Section 4.2.1.

3.2 Modelling and Simulation Methodology

The governing equations describing the TR model of a Li-ion cell are arranged into several "sub-models" for ease of reference. These sub-models consist of the heat-transfer sub-model (see Section 3.2.1), abuse sub-model (see Section 3.2.2) and venting sub-model (see Section 3.2.3). These sub-models and how they are coupled to one another to form the overall advanced abuse model (AAM) is shown in Fig. 3.6. The heat-transfer sub-model describes all applicable heat transfer pathways through conduction, convection and radiation, with heat source terms coupled from the abuse and venting sub-models. The abuse sub-model describes the exothermic chemical decomposition of the cell, considering the four general decomposition reactions commonly quoted in Li-ion TR modelling. Further, the abuse model is extended to include an additional heat generation term (see Section 3.2.2.1), named here as a "simmering reaction", specific for the cells under study. The venting sub-model describes the internal pressure increase of the cell throughout TR and the heat lost upon venting for rigid body cylindrical cells. This is developed beyond the literature to take account of CO_2/DMC mixture at bubble point, see Section 3.2.3.2.

3.2.1 Heat Transfer Sub-Model

The heat transfer in a single cell is governed by the energy balance between the rate of heat generated inside the cell and the rate of heat dissipated from the cell to the environment [37]. It is assumed that no convective heat transfer within the liquid electrolyte occurs inside the jelly roll. This is because the flow of the electrolyte is assumed to be restricted by the porous structures it occupies. Hence, the conservation of heat energy within the cell is described by Fourier's Law for a solid body:

$$\rho C_p \frac{\partial T}{\partial t} + \nabla q = Q \tag{3.5}$$

where ρ (kg/m^3) is density, C_p (J/kg K) is the specific heat capacity, T (K) is temperature. C_p is used instead of C_v as, under normal conditions, it is assumed that the cell (composed of 85% to 95% solid materials with the remainder liquid) can be represented by a solid body that has negligible change in volume when heated and is also subjected to constant atmospheric pressure. The conductive heat flux, q (W/m), is described as:

$$q = -\kappa \nabla T \tag{3.6}$$

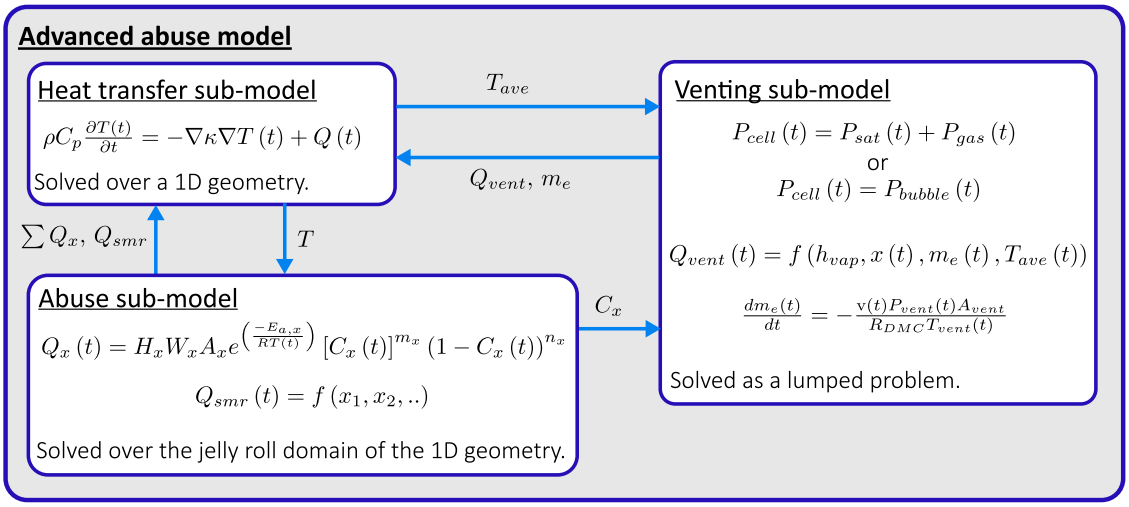

Figure 3.6: Coupling of sub-models within the AAM (reproduced from [250]).

where κ (W/m K) is the thermal conductivity coefficient. At the surfaces where heat transfer to and from the cell is applicable, assuming convective and/or radiative heat transfer can be present, the boundary condition is then:

$$\mathbf{n} \cdot q = h_{conv}(T_{env} - T_{surf}) + \varepsilon\sigma(T_{env}^4 - T_{surf}^4) \tag{3.7}$$

where $\mathbf{n} \cdot q$ (W/m^2) is the heat flux normal to the surface, h_{conv} (W/m^2 K) is the convection coefficient, ε is the emissivity value, σ is the Stefan-Boltzmann constant (W/m^2 K^4), while subscripts *surf* and *env* denote the surface and environmental temperatures respectively.

The heat generation term Q (W/m^3) in Eq. (3.5) can include various sources. At present, in this work, the source terms considered are from: the 4 classical decomposition reactions, encompassed in Q_{decomp} (W/m^3);the simmering reaction, Q_{smr} (W/m^3); and heat loss by venting, Q_{vent} (W/m^3). Hence, Q can be written as:

$$Q = Q_{decomp} + Q_{smr} + Q_{vent} \tag{3.8}$$

The definitions of the terms on the right-hand side of Eq. (3.8) are given in the following sections.

3.2.2 Abuse Sub-Model

Here the four most commonly considered and fundamental reactions involved in the TR of Li-ion cells are discussed. They are the solid electrolyte interface (SEI) decomposition, reaction of intercalated lithium with electrolyte at the negative electrode (NE), positive material decomposition (PE) and electrolyte decomposition (E) [78]. The governing equations, Eqs. (3.9) to (3.15), for these reactions are following those outlined by Refs. [99, 128, 146].

The rate of reaction, R_x (1/s), for the SEI, positive and electrolyte reactions are described by Eq. (3.9). This form is used as it describes the general equation for the thermal decomposition of solids, simplified from MacNeil and Dahn [183]. T Where subscript x corresponds to one of the reactions *sei*, *pe* or *e*. A_x (1/s) is the frequency factor, $E_{a,x}$ (J/mol) is the activation energy, R and T the ideal gas constant (8.3145 J/mol K) and temperature (K) respectively, C_x (1) the reaction species while i_x (1) and j_x (1) are constants.

$$R_x = A_x e^{\left(\frac{-E_{a,x}}{RT}\right)} C_x^{i_x} \left(1 - C_x\right)^{j_x} \tag{3.9}$$

The negative electrode reaction in Eq. (3.10) is similar, with the additional term taking account of the change in thickness of the SEI layer as it decomposes. Where t_{sei} (1) is the non dimensional thickness of the SEI layer and $t_{sei,0}$ (1) the initial thickness.

$$R_{ne} = A_{ne} e^{\left(\frac{-E_{a,ne}}{RT}\right)} C_{ne}^{i_{ne}} \left(1 - C_{ne}\right)^{j_{ne}} e^{\left(\frac{-t_{sei}}{t_{sei,0}}\right)} \tag{3.10}$$

The change in reaction species for each decomposition reaction and SEI layer thickness is given by Eqs. (3.11) to (3.15).

$$\frac{\partial C_{sei}}{\partial t} = -R_{sei} \tag{3.11}$$

$$\frac{\partial C_{ne}}{\partial t} = -R_{ne} \tag{3.12}$$

$$\frac{\partial t_{sei}}{\partial t} = R_{ne} \tag{3.13}$$

$$\frac{\partial C_{pe}}{\partial t} = R_{pe} \tag{3.14}$$

$$\frac{\partial C_e}{\partial t} = -R_e \tag{3.15}$$

The volume specific heat generation terms Q_x (W/m^3) from each decomposition reaction are given in Eqs. (3.16) to (3.19). In which, H_x (J/kg) is the specific heat of reaction and W_{carbon} (kg/m^3), W_{pos} (kg/m^3) and W_e (kg/m^3) are the volume specific content of

carbon, positive active material and electrolyte respectively.

$$Q_{sei} = H_{sei} W_{carbon} R_{sei} \tag{3.16}$$

$$Q_{ne} = H_{ne} W_{carbon} R_{ne} \tag{3.17}$$

$$Q_{pe} = H_{pe} W_{pos} R_{pe} \tag{3.18}$$

$$Q_{e} = H_{e} W_{e} R_{e} \tag{3.19}$$

Hence, the total heat generation from the decomposition of the cell is:

$$Q_{decomp} = Q_{sei} + Q_{ne} + Q_{pe} + Q_{e} \tag{3.20}$$

and is used in Eq. (3.8).

3.2.2.1 Simmering Reaction

The cells under study in this work are observed to produce heat in a relativity low but stable manner well after the main TR event. This is attributed to a slow unknown reaction or set of reactions. Due to the behaviour which is observed, it is termed the "simmering reaction". Although the TR reactions considered in Section 3.2.2 are formulated using an Arrhenius function, typical of chemical reactions, this form is not used for the simmering reaction. This is because of the unknown nature of the simmering reaction, i.e. the reactive pathways/species and rate limiting factors, that make quantifying the parameters of the Arrhenius function difficult. A typical Arrhenius function requires activation energy, frequency factor, reaction heat, specific mass and reaction species, hence, to reduce the number of unknown parameters, a simple formulation to describe the simmering reaction, Q_{smr} (W/m^3), of the LFP cell is presented, see Eq. (3.21):

$$Q_{smr} = \begin{cases} 0 & \text{before venting} \\ Q_{smr}^{max} \dfrac{T_{ave} - T_1}{T_2 - T_1} t_{smr} & \text{at and after the point of venting} \end{cases} \tag{3.21}$$

Arbitrarily, before venting the simmering reaction is considered to be zero. After venting, the simmering reaction is assumed to be a function of an estimated maximum reaction heating power, which is linearly related to two dimensionless terms. The first is a function

of the average cell temperature and the other a function of time. The average cell temperature is limited between bounds, see Eq. (3.22), and determined through parameter fitting the TR model when applied to oven simulations. The linear temperature relation and temperature bounds are implemented such that during the main TR event (i.e. the decomposition of the four major reactions) the simmering reaction is restricted This is done on the assumption that in reality the reaction would be limited by the availability of reaction species and/or oxygen. However, this formulation still allows the simmering reaction heat generation rate some dependence on the cell temperature after the main TR event. In turn, the formulation encompasses the complex interdependent relationship between the cell temperature, reaction rate and (theoretical) species generation/ oxygen availability of, what is considered to be, a metastable reaction after the main TR event.

$$T_1 \leq T_{ave} \leq T_2 \tag{3.22}$$

The term t_{smr} in Eq. (3.21), defined by Eq. (3.23), determines the length of time the simmering reaction proceeds for, linearly reducing from 1 to 0 over the time interval $t_{smr,length}$ (i.e. the assumed length of the simmering reaction). In Eq. (3.23), t is the simulation time, in s, and t_{vent} (s) is the time at which venting occurs. The following conditions are assumed: $t_{smr} = 1$ at $t = t_{vent}$, and $t_{smr} = 0$ at $t = t_{smr,length}$. The quantity t_{smr} is estimated, assuming possible periods over which the reaction is sustained, while also being fit (through oven simulations) such that the temperature gradient of the cell, long after the main TR event, is predicted well.

$$t_{smr} = max\left(\frac{t_{smr,length} - (t - t_{vent})}{t_{smr,length}}, 0\right) \tag{3.23}$$

Through fitting, the parameters of Eq. (3.21) and Eq. (3.23) were determined to be $Q_{smr}^{max} = 85\,\mathrm{kW/m^3}$, $T_1 = 120°\mathrm{C}$ and $T_2 = 218°\mathrm{C}$, while $t_{smr,length} = 600\,\mathrm{min}$ was estimated.

The above methodology provides a description of the simmering reaction that can be easily parametrised. This considers the complex slow rate reactions that are present for relatively long time frames from unknown reaction pathways and species.

3.2.3 Venting Sub-Model

The venting of a cell is governed by the internal cell pressure. A new methodology is developed here to determine the cell pressure from bubble point pressure of the CO_2/DMC mixture. This is termed the bubble point venting (BPV) method. This new method is developed based on the work by Coman *et al.* [199], in which the pressure is calculated from the liquid saturation and gas pressures. This is referred to as the partial pressure venting (PPV) method. The PPV method is reproduced for comparison with the BPV method. An overview and comparison of these methods is shown in Fig. 3.7. The remainder of this section discusses the governing equations of PPV method as developed by Coman *et al.*

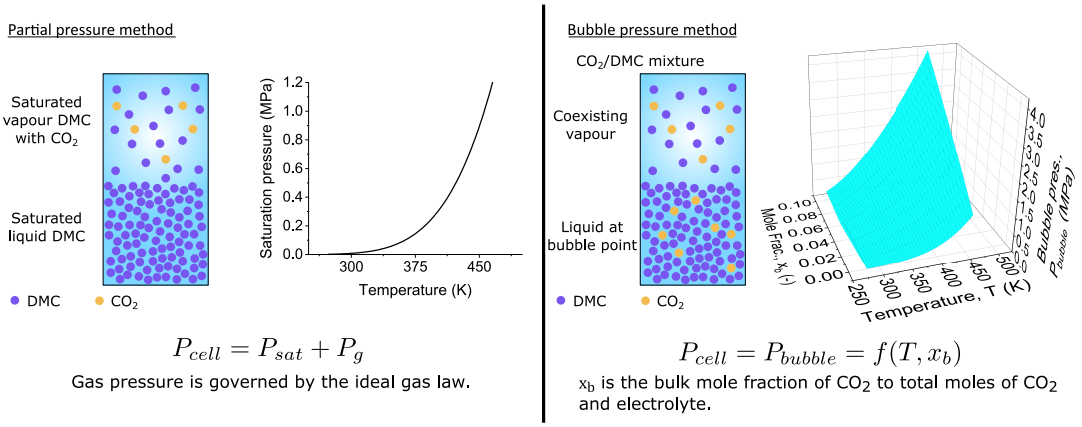

Figure 3.7: Comparison of theory behind venting sub-model methodologies.

[199]. Subsequently, Section 3.2.3.1 discusses the coupling of the vent model to the other sub-models, while Section 3.2.3.2 discusses the development of the BPV method.

The venting sub-model describes an unsteady flow energy and mass balance for an open system, with the following assumptions outlined by Coman *et al.* [199]:

- The enthalpy of the electrolyte mixture is averaged between the saturated liquid $h_{enth,l}$ [kJ/kg] and saturated vapour $h_{enth,vap}$ [kJ/kg] phases (note the enthalpy of vaporization $h_{enth,vap}$ is more commonly denoted by the subscript fg i.e. h_{fg} or in the notation used here $h_{enth,fg}$):

$$h_{enth} = h_{enth,l} + x h_{enth,vap} \tag{3.24}$$

  where x is the vapour fraction, which is the ratio of the mass of electrolyte vapour $m_{e,v}$ over the total mass of electrolyte m_e:

$$x = \frac{m_{e,v}}{m_e} \tag{3.25}$$

- The liquid and solid phases are assumed incompressible, while the vapour and gas phases are assumed to have ideal gas behaviour. During venting, as the system temperature and pressure remain away from critical values, the ideal gas assumption is assumed to hold for the vapour.

- As the amount of gas in the system is small, the energy contribution from the gas phase is neglected from the energy balance.

- Only the Dimethyl Carbonate (DMC) component of the electrolyte is considered as it is the major component, while the $LiPF_6$ salts are ignored.

- No solid mass is considered to be transported away within the ejecta during venting.

For an open system, Eq. (3.26) describes the general unsteady energy equation considering enthalpy change [150, 199]. This is derived from the general energy equation considering internal energy. This is achieved as it is assumed that the solid and liquid phases are incompressible. Hence, the contributions to internal energy change from solid or fluid volume change are zero [150], further as it is an open system there is also no change in pressure. So internal energy can be represented by enthalpy alone.

$$\sum \dot{Q}_{net} - \dot{m}_{out} h_{enth,out} = \frac{d(m h_{enth})}{dt} \tag{3.26}$$

where $\dot{Q}_{net}$ [W] contains any heat source and heat flux terms, mass loss from the system is given by $\dot{m}_{out}$ [kg/s], h_{enth} [kJ/kg] is the enthalpy of the electrolyte mixture, m and h are the mass and the specific enthalpy of the entire system respectively.

For the closed system, prior to the vent opening, the mass loss $\dot{m}_{out}$ is zero and hence the mass of electrolyte remains constant. However, for the open system, after the burst pressure is reached and the vent opens, the mass loss can be calculated by:

$$\dot{m}_{out} = -\frac{dm_e}{dt} \tag{3.27}$$

The enthalpies for each phase are given by:

$$h_{enth,s} = C_{p,s}(T - T_{ref}) \tag{3.28}$$

$$h_{enth,l} = C_{p,l}(T - T_{ref}) \tag{3.29}$$

$$h_{enth,v} = C_{p,v}(T - T_{ref}) \tag{3.30}$$

where the enthalpy is measured against a reference temperature of 0 K.

Taking the general unsteady energy equation, Eq. (3.26), and replacing the appropriate parameters with those described by Eq. (3.24), Eq. (3.25) and Eqs. (3.27) to (3.30). The energy balance for a 0D system, which can be solved to determine the temperature of the cell, becomes:

$$\begin{aligned}\left\{m_s C_{p,s} + m_e \left[(1-x) C_{p,l} + x C_{p,v}\right]\right\} \frac{dT}{dt} &= \sum \dot{Q}_{net} \\ &- m_e \frac{dx}{dt} h_{enth,vap} - h_{enth,vap} \frac{dm_e}{dt} (x-1)\end{aligned} \tag{3.31}$$

where m_s [kg] is the mass of the cell's solid components i.e. electrodes, separator and current collectors and cell case, $C_{p,s}$, $C_{p,v}$ and $C_{p,l}$ (all in kJ/kg) are the specific heats of

the solid components, electrolyte vapour phase and electrolyte liquid phase respectively, dT/dt [K/s] is the temperature rate of the cell and dx/dt [1/s] is the rate of change of the vapour fraction. The average specific heat for the combined solid components is calculated by:

$$C_{p,s} = \frac{\sum C_{p,i} m_i}{m_s} \tag{3.32}$$

where the index i corresponds to the individual cell components e.g. carbon anode (ano), LFP cathode (cath), copper foil (Cu), aluminium foil (Al), polymer separator (sep) and steel case (steel).

The vapour fraction, x, is calculated from the following equation:

$$\frac{dx}{dt} = -\frac{dm_e}{dt}\frac{v_e}{m_e v_{lv}} - x\frac{dv_{lv}}{dt}\frac{1}{v_{lv}} - \frac{dv_l}{dt}\frac{1}{v_{lv}} \tag{3.33}$$

where the specific volume of the electrolyte mixture v_e [m^3/kg] is given as:

$$v_e = v_l + x v_{lv} \tag{3.34}$$

and v_{lv} [m^3/kg] is the difference in the specific volumes of the saturated vapour v_v and the saturated liquid v_l, given by:

$$v_{lv} = v_v - v_l \tag{3.35}$$

The relations defining the specific volumes of saturated vapour and saturated liquid for DMC are defined later, in Chapter 5 when parameters are defined for specific modelling scenarios, along with other material properties of DMC.

The mass flow rate, dm_e/dt, is calculated assuming the vented electrolyte mixture behaves as a gas passing through a nozzle, for which the isentropic flow equation can be applied [143, 199]:

$$\frac{dm_e}{dt} = -\frac{u P_{vent} A_{vent}}{R_{DMC} T_{vent}} \tag{3.36}$$

where u [m/s] is the vapour velocity, P_{vent} [kPa] is the pressure at the outlet of the vent, A_{vent} [m^2] is the cross-sectional area of the burst disk opening, R_{DMC} [kJ/kg K] is the gas constant of the electrolyte, and T [K] is the temperature of the vent gas at the outlet.

For the assumed isentropic venting process, the variables P_{vent}, T_{vent} and v are defined as [199, 251]:

$$P_{vent} = \frac{P}{\left(1 + \frac{\gamma - 1}{2} M^2\right)^{\frac{\gamma}{\gamma - 1}}} \tag{3.37}$$

$$T_{vent} = \frac{T}{1 + \frac{\gamma - 1}{2} M^2} \tag{3.38}$$

$$\mathrm{v} = M\sqrt{\gamma R_{DMC} T_{vent}} \tag{3.39}$$

where P [kPa] is the internal cell pressure, γ is the ratio of specific heats for the electrolyte mixture, M is the Mach number and T [K] is the average cell temperature. This work, following [199], assumes the vapour is calorically perfect, leading to a constant specific heat ratio. Before venting occurs, and no flow is present, then P_{vent} and T_{vent} equal P and T respectively. The Mach number is determined by the following equation [199, 251]:

$$M = \begin{cases} 0 & \text{if } P < P_{burst} \quad \text{no flow} \\ \sqrt{\frac{2}{\gamma-1}\left[\left(\frac{P}{P_{amb}}\right)^{\frac{\gamma-1}{\gamma}} - 1\right]} & \text{if } P_{amb} > P\left[\frac{2}{\gamma+1}\right]^{\frac{\gamma}{\gamma-1}} \quad \text{subsonic flow} \\ 1 & \text{if } P_{amb} \leq P\left[\frac{2}{\gamma+1}\right]^{\frac{\gamma}{\gamma-1}} \quad \text{choked flow} \end{cases} \tag{3.40}$$

Prior to venting due to the lack of flow $M = 0$, while P_{burst} is the pressure limit of the burst disk (at all times).

The internal cell pressure is defined as the sum of the partial pressures of the electrolyte vapour P_{sat} and decomposition gases P_g. Hence, the internal cell pressure is:

$$P = P_{sat} + P_g \tag{3.41}$$

The saturation pressure of the mixture is defined specifically for the DMC electrolyte later in Chapter 5. In general, P_{sat} is only valid when the system is closed. This is because the system cannot be in vapor-liquid equilibrium when it is open. Hence, P_{sat} vanishes at the point of venting. The partial pressure of the gas is calculated using the ideal gas law:

$$P_g = \frac{m_g R_g T}{V_h} \tag{3.42}$$

where m_g [kg] is the mass of gas, R_g [J/kg K] is the gas constant and V_h [m^3] is the head space volume of the cell that the electrolyte vapour and decomposition gases occupy. The head space volume is defined as:

$$V_h = \eta_h V_{cell} \tag{3.43}$$

where V_{cell} [m^3] is the overall cell volume, and η_h is the estimated fraction that the cell's void volume occupies compared to the overall volume.

The initial value for the mass of gas in the cell is calculated from the ideal gas law, taking account of the partial pressure of the electrolyte vapour:

$$m_{g,0} = \frac{\left[P_0 - P_{sat}\left(T_0\right)\right] V_h}{R_g T_0} \tag{3.44}$$

where the equation is solved for the initial values of pressure (P_0) and temperature (T_0).

The change in mass of gas, Eq. (3.45), is determined by using the reaction rate dC_{rxn}/dt from the abuse sub-model:

$$\frac{dm_g}{dt} = -m_{g,rxn}\frac{dC_{rxn}}{dt} + \frac{dm_e}{dt} \tag{3.45}$$

The first term on the right-hand side of Eq. (3.45) governs the gas production rate, where $m_{g,rxn}$ is the maximum amount of gas produced by the decomposition reactions. The reaction rate (dC_{rxn}/dt), used to determine the gas production, is calculated from the overall decomposition of the cell, C_{rxn}. Here, in the development of the AAM, an averaged and normalised reaction rate of all reactions is used, see Eq. (3.46). This is unlike Coman *et al.* [199] that only considers the SEI reaction. Considering all reactions allows for the importance of individual reactions on gas generation and venting to be determined. Although it is known that secondary and interdependent reactions occur during TR [252], here for simplicity and compatibility with typical TR modelling [e.g 38], the gas generation governed by Eq. (3.46) is only dependent on the primary (SEI, NE, PE and electrolyte) reactions. Further, the formulation of Eq. (3.46) implies equal weighting of reactions to the overall decomposition of the cell. Inherently, following on from this, the maximum amount of gas produced is equally split over the four reactions. The second term on the right-hand side is the mass flow from the system, as defined by Eq. (3.36).

$$C_{rxn} = \frac{\frac{C_{sei}}{C_{sei,0}} + \frac{C_{ne}}{C_{ne,0}} + \frac{1-C_{pe}}{1-C_{pe,0}} + \frac{C_e}{C_{e,0}}}{4} \tag{3.46}$$

Within the calculation of the average cell decomposition value, Eq. (3.46), each reaction species (for the SEI, NE and electrolyte reactions) is normalized by its respective initial value. For the PE reaction this is additionally standardised through one minus the reaction species. This is because unlike the other reactions the PE reaction initiates at 0 not 1. In turn, each of the four terms on the right-hand side of Eq. (3.46) are initially at 1, and tend to 0 as the cell undergoes TR.

3.2.3.1 Complete Coupling of the Three Sub-Models

To couple the 0D venting sub-model to a non-zero dimensional heat transfer sub-model minor alterations have to be made. First, the mass loss of electrolyte, governed by the venting model, has to be incorporated into the definition of the total mass of electrolyte,

m_e. Hence, m_e is rewritten as:

$$m_e^* = m_e^0 - m_{e,vent}^0 + m_{e,vent} \tag{3.47}$$

where m_e^0 is the total initial mass of electrolyte in the cell, $m_{e,vent}^0$ is the amount of electrolyte estimated to be ejected upon venting, while $m_{e,vent}$ is the amount of electrolyte ejected as a function of time. This formulation is used as during venting the model would otherwise predict total loss of electrolyte. As such, the model is limited to ejecting $m_{e,vent}^0$ amount of electrolyte. The value of $m_{e,vent}^0$ is fitted such that the model predicts a magnitude of temperature drop upon venting comparable to that observed in the experimental data. Hence, upon venting, $m_{e,vent}$ tends from $m_{e,vent}^0$ to 0. The change in $m_{e,vent}$ is determined by:

$$\frac{dm_{e,vent}}{dt} = -\frac{uP_{vent}A_{vent}}{R_{DMC}T_{vent}} \tag{3.48}$$

replacing Eq. (3.36).

From the energy balance equation, Eq. (3.31), two relations can be defined such that the 0D venting sub-model can be coupled to the heat transfer-abuse model. These are the heat loss during venting Q_{vent} and the change in cell heat capacity $m_{cell}C_{p,cell}$. From the right hand-side of Eq. (3.31), Q_{vent} can be defined as:

$$Q_{vent} = -m_e^* \frac{dx}{dt} h_{enth,vap} - h_{enth,vap} \frac{dm_e^*}{dt} (x-1) \tag{3.49}$$

while from the left hand-side, $m_{cell}C_{p,cell}$ can be defined as:

$$m_{cell}C_{p,cell} = m_s C_{p,s} + m_e^* \left[(1-x) C_{p,l} + x C_{p,v}\right] \tag{3.50}$$

The average cell properties m_{cell} and $C_{p,cell}$ are known, as they have been determined experimentally in Section 4.2.1. In addition, the physical properties for the DMC electrolyte and an assumed electrolyte mass (taken from literature) are also known. Hence, relations to estimate the mass and specific heat capacity of the solid components can be defined. The mass of solid components can be determined from:

$$m_{cell} = m_s + m_e^* \tag{3.51}$$

whereby substituting in the relevant initial values of cell mass and electrolyte mass gives a value for the non-time varying mass of the solid. The solid mass is taken to be constant as it is assumed that:

1. No solid component material is lost during venting

2. The conversion of mass from solid to gas can be neglected in terms of mass balance. This is because the mass of gas generated by decomposition of relevant materials is negligible (on the order of 1×10^{-3} g).

Similarly, in order to simplify and due to a lack of data on the cell's temperature dependent specific heat capacity at temperatures seen under thermal abuse, the specific heat capacity of the solid components are assumed to be constant. The specific heat of the solid components can be estimated from Eq. (3.50) by re-arranging for $C_{p,s}$ and substituting in relevant initial values. Thus Eq. (3.32) can be replaced from the fundamental 0D venting model. With m_s and $C_{p,s}$ known, relevant time varying physical properties, i.e. density and specific heat, for the cell can be defined as:

$$\rho_{cell,t} = \frac{m_s + m_e^*}{V_{cell}} \tag{3.52}$$

and

$$C_{p,cell,t} = \frac{m_s C_{p,s} + A}{m_s + m_e^*} \tag{3.53}$$

where

$$A = \begin{cases} m_e^* \left[(1-x)\, C_{p,l} + x C_{p,v}\right] & \text{before venting} \\ (m_e^0 - m_{e,vent}^0) C_{p,l}^{DMC} & \text{after venting} \end{cases} \tag{3.54}$$

The time varying specific heat capacity of the cell (Eq. (3.53)) is only valid up to the point of venting. After venting the remaining electrolyte is assumed to be completely in the liquid phase. With this assumption the electrolyte takes a specific heat capacity value for pure liquid DMC at the initial temperature, not in a saturated phase. This assumption is undertaken for simplicity. This is because the constitution of the DMC after venting is hard to predict. This in itself is due to:

1. the data for the DMC electrolyte physical and thermodynamic properties are only defined up to temperatures of 600 K, this is below the maximum cell temperature observed experimentally (see Section 4.2.3), and

2. for temperatures at and above the experimental venting temperature, and at atmospheric pressure (i.e. assumed cell properties after venting) the saturation table states that the DMC would be in the gas phase.

From this it is clear that the assumption of the DMC electrolyte being in the liquid phase after venting is significant. However, this has not been explored further as the prediction of the transition from liquid to gas is difficult and beyond the scope of this work.

Finally, as the abuse model is dependent on mass of reactants, i.e. m_e, the specific mass of electrolyte is replaced by:

$$W_e = \frac{m_e}{V_{jelly}} \tag{3.55}$$

3.2.3.2 Venting-Sub Model Development: Bubble Pressure

The BPV method is developed to account for the correct phase equilibria of the CO_2/DMC system, rather than assume an ideal mixture of an ideal gas and a saturated liquid as in PPV method. The BPV method is governed by the mole fraction x_b, which is the bulk ratio of moles of CO_2 to total moles of the CO_2/DMC mixture (see Eq. (3.57)), while the vapour-liquid fraction is not calculated. This is to avoid iteratively determining the vapour-liquid fraction and mole fraction of each component in each phase, as this would be slow to calculate and beyond the scope of this work. As such, the vapour properties are neglected from the BPV method as the amount of vapour is assumed to be small and has negligible effect on the thermo-physical properties. Hence, fluid parameters (i.e. the heat of vaporisation $h_{vap,b}$, specific heat of the liquid phase $C_{p,l}^{mix}$ and internal cell pressure P_{bubble}) are redefined for the CO_2/DMC mixture in terms of temperature, T and x_b. The re-defined governing equations are presented below (Eqs. (3.56), (3.61) and (3.65)), after the method in which the bubble pressure properties are determined has been discussed.

To determine the thermodynamic properties of the CO_2/DMC mixture, the commercial software *REFPROP - NIST Standard Reference Database* [253] was employed. Data was taken from the saturation tables for a liquid at bubble point with coexisting vapour, over the temperature range 270 K to 460 K, repeated for various liquid phase mole fraction ratios from 0.0001/0.9999 to 0.1/0.9 (CO_2/DMC). Data was only taken over this temperature range as the bubble point assumption is only valid up to the point of venting, which occurs at approximately 450 K. The bulk mole fraction only goes up to 10% CO_2 as the gas generation estimated from Coman *et al.* [199] leads to a mole fraction significantly under this value. Within *REFPROP*, the mixing rule used was the *KW0 Generalized mixture model* with the following coefficients: $\beta_T = 0.967$, $\beta_V = 1$, $\gamma_T = 1.0856$, $\gamma_V = 0.9926$, $F_{ij} = 1.5222$. The reference states used were those set as default within *REFPROP*, being: $h = 1170\,\text{kJ/kg}$, $s = 11.7\,\text{kJ/kg K}$, $T = 298.15\,\text{K}$ and $P = 0.001\,\text{MPa}$.

From the methods described above the bubble pressure, the liquid and vapour phase enthalpies, and the liquid phase specific heat capacity are determined. The internal cell pressure is determined by the bubble pressure of the mixture, replacing the sum of the partial pressure in Eq. (3.41):

$$\begin{aligned} P_{bubble} = {} & 5.652 - 3.531{\times}10^{-2}T - 42.38x_b + 5.495{\times}10^{-5}T^2 \\ & + 0.1643Tx_b - 11.56x_b^2 \end{aligned} \tag{3.56}$$

where T is temperature and x_b is the mole fraction:

$$x_b = \frac{m_g/M_g}{\frac{m_g}{M_g} + \frac{m_e^*}{M_{DMC}}} \tag{3.57}$$

where m_e^* is described by Eq. (3.47), and m_g by Eq. (3.45). In order to determine the initial mole fraction x_b^0, the initial amount of gas in the bubble pressure model is set to the same value as used in the Coman *et al.* [199] model as to make a fair comparison between methods.

The heat of vaporisation of the CO_2/DMC mixture is not given by *REFPROP*. However, the isobaric heat of finite vaporisation can be estimated from the definite integral of the isobaric heat of infinitesimal vaporisation, q_P, as described by Akasaka *et al.* [254]:

$$\begin{aligned} q_{P|\omega_a \to \omega_b} &= \frac{1}{\omega_b - \omega_a} \int_{\omega_a}^{\omega_b} q_P(\omega) d\omega \\ &= \frac{h_{enth}(P, \omega_b) - h_{enth}(P, \omega_a)}{\omega_b - \omega_a} \end{aligned} \tag{3.58}$$

where $h_{enth}(P, \omega)$ is the molar enthalpy of the system and ω is the dryness fraction, see Eq. (3.59):

$$\omega = \frac{x_{system,i} - x_{l,i}}{x_{V,i} - x_{l,i}} \tag{3.59}$$

where $x_{j,i}$ are the mole fractions of the i^{th} component for the phases $j = system, l, v$ (system, liquid and vapour). Hence, the total heat of vaporisation of a fluid at the bubble point ($\omega_a = 0$) to the dew point ($\omega_b = 1$) can be estimated from Eq. (3.58), resulting in:

$$\begin{aligned} h_{vap,est} &= \frac{h_{enth}(P, 1) - h_{enth}h(P, 0)}{1 - 0} \\ &= h_{enth,v}(P) - h_{enth,l}(P) \end{aligned} \tag{3.60}$$

A similar relation can be described for the isothermal heat of finite vaporisation, where the enthalpies are a function of T, not P. Hence, the reported liquid phase and vapour phase enthalpies for a CO_2/DMC mixture (from *REFPROP*) as a function of temperature can be used to replace $h_{enth,v}$ and $h_{enth,l}$ in Eq. (3.60) at each system molar fraction. From this, a function of the heat of vaporisation can be fit for each temperature and molar fraction:

$$h_{enth,vap,b}(T, x_b) = \sum_{i=0}^{4} \sum_{j=0}^{4} a_{i,j} T^i x_b^j \tag{3.61}$$

Table 3.2: Quality of Fit of P_{bubble}, $C_{p,l}^{mix}$ and $h_{enth,vap,b}$ Functions.

	$\mathbf{P_{bubble}}$	$\mathbf{C_{p,l}^{mix}}$	$\mathbf{h_{vap,b}}$
R^2	0.9995	0.9993	0.9930
RMSE	0.0209	0.0038	8.4910

where the coefficients $a_{i,j}$ are given by Eq. (3.62).

$$a_{i,j} = \begin{pmatrix} 365.2 & 2.091\times10^{4} & -6.206\times10^{5} & 5.114\times10^{6} & -1.128\times10^{7} \\ 2.917 & -7.097 & 911.4 & -6355 & 0 \\ -1.359\times10^{-2} & -6.391\times10^{-2} & 3.152\times10^{-1} & 0 & 0 \\ 1.799\times10^{-5} & -1.194\times10^{-5} & 0 & 0 & 0 \\ -6.189\times10^{-9} & 0 & 0 & 0 & 0 \end{pmatrix} \tag{3.62}$$

The enthalpy of vaporization for the bubble pressure model is denoted by $h_{vap,b}$.

The updated heat of vaporisation, $h_{enth,vap,b}$, is used in the determination of the venting cooling power:

$$Q_{vent,b} = h_{enth,vap,b}\frac{dm_{mix}}{dt} \tag{3.63}$$

where m_{mix} is the total mass of electrolyte and gas mixture as given by Eq. (3.64), and $\frac{dm_{mix}}{dt}$ is only valid upon venting.

$$m_{mix} = m_e^* + m_g \tag{3.64}$$

The specific heat capacities for the liquid phase and vapour phase utilized in Eq. (3.50) and Eq. (3.53) are replaced by:

$$\begin{aligned} C_{p,l}^{mix} = {} & 2.111 - 3.312\times10^{-3}T - 0.614x_b + 7.959\times10^{-6}T^2 \\ & + 2.031\times10^{-3}Tx_b + 4.997\times10^{-1}x_b^2 \end{aligned} \tag{3.65}$$

The polynomials of P_{bubble}, $C_{p,l}^{mix}$ and $h_{enth,vap,b}$ have R^2 and RMSE values as listed in Table 3.2, and show a high quality of fit.

The specific heat capacities of the cell, solids and the heat loss due to venting are re-defined as:

$$\rho_{alt} = \frac{m_{cell}}{V_{cell}} = \frac{m_s + m_e^*}{\pi r_{batt}^2 h_{batt}} \tag{3.66}$$

where ρ_{alt} is the alternate definition of cell density,

$$C_{p,alt} = \frac{(m_s C_{p,s}) + (A_b)}{m_s + m_e^*} \tag{3.67}$$

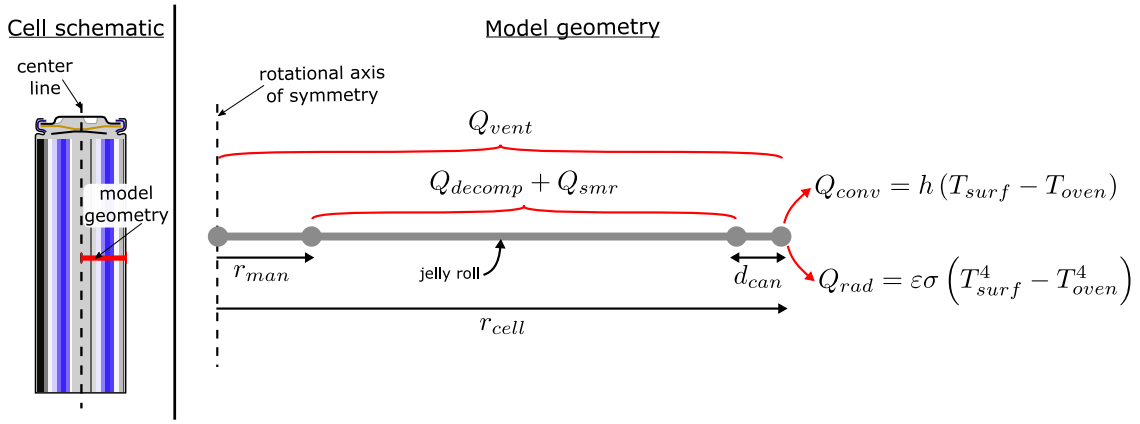

Figure 3.8: Single cell geometry for AAM development. Left - cell schematic showing orientation of 1D model geometry. Right - Detailed illustration of 1D geometry including the regions in which the specific heat gain and loss terms are applied.

$C_{p,alt}$ is the alternate definition of cell specific heat capacity, where A_b accounts for the heat capacity of the electrolyte. A_b is a function of the liquid phase heat capacity of the mixture before venting, while after venting it is a function of the DMC heat capacity as a pure liquid; this is as defined for the previous model (see Eq. (3.54)).

$$A_b = \begin{cases} m_e^* C_{p,l}^{mix} & \text{before venting} \\ (m_e^0 - m_{e,vent}^0) C_{p,l}^{DMC} & \text{after venting} \end{cases} \tag{3.68}$$

The heat capacity of the solids is constant with time throughout the simulation and is defined as:

$$C_{p,s} = \frac{m_{cell} C_{p,cell} - m_e^0 C_{p,l}^{mix}(T_{int}, x_b^0)}{m_s} \tag{3.69}$$

3.2.4 Model Geometry and Implementation

The AAM is developed over a 1D geometry, see Fig. 3.8, and represents an axi-symmetric, one dimensional slice through an 18650 cylindrical cell. The heat transfer equations are applied over the entire cell geometry, while the decomposition reactions and simmering reaction are applied over the jelly roll domain. The venting sub-model is solved through a coupled 0D component, see Fig. 3.6, from which the heat loss due to venting is determined and applied over the entire cell geometry.

The model is developed in the commercial finite element modelling software *COMSOL Multiphysics* [255]. The heat transfer sub-model is implemented using the relevant built-in equations within *COMSOL*. The reaction rates of the abuse sub-model are implemented through domain ordinary differential equations (ODEs), while the mass rate of the venting sub-model is implemented by a global ODE.

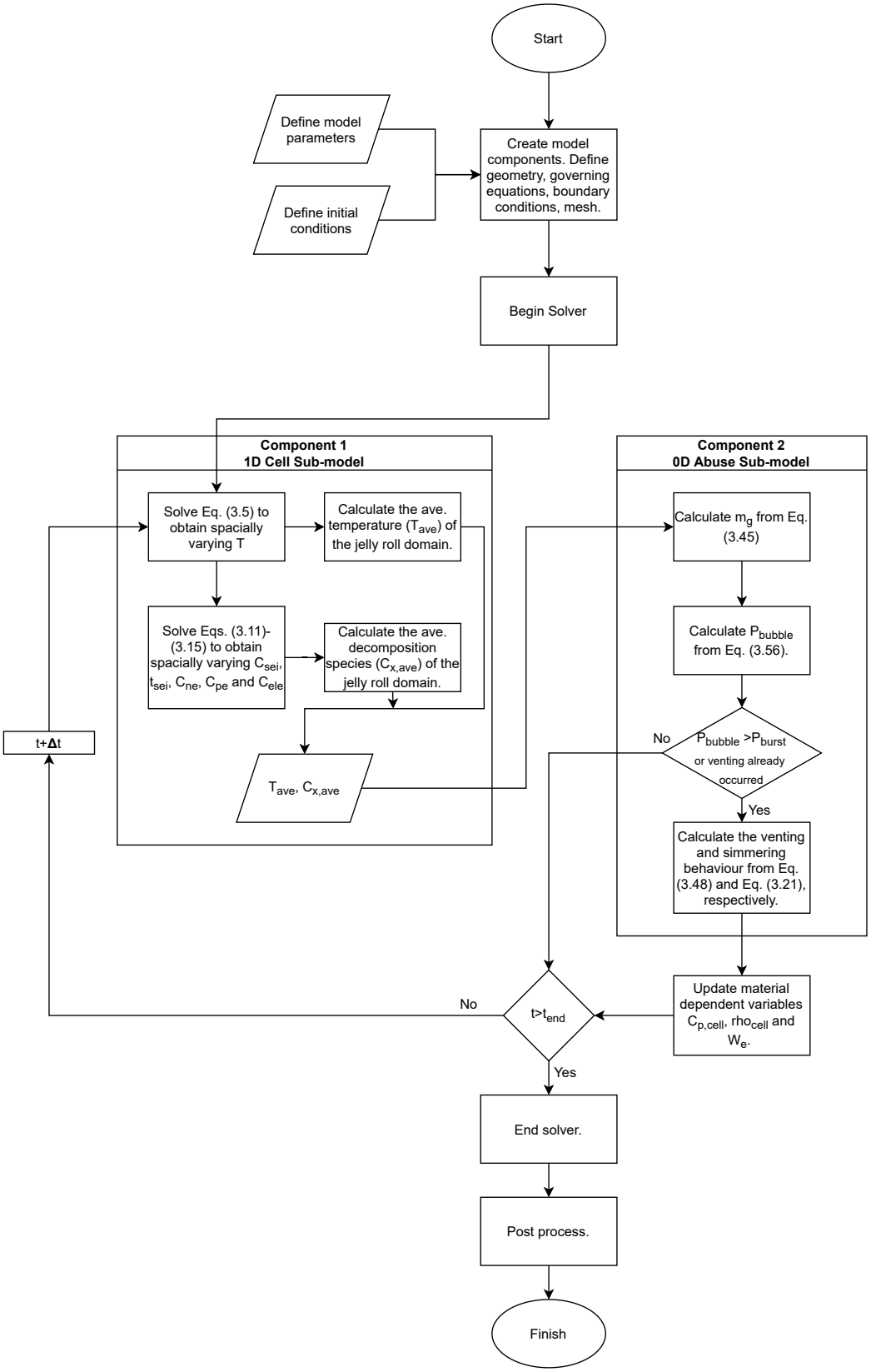

Figure 3.9: Flowchart showing the major steps of the model solution process for determining the values of dependent variables and the occurrence of venting.

The process of solving the model is summarized in Fig. 3.9. It shows the steps taken to solve the equations that govern the dependent variables. It is assumed the reader will understand the interdependency of the steps presented and the equations that are not referred to. It also shows the process of averaging the 1D temperature and decomposition variables to be used in the 0D model. Further, it presents the condition at which venting occurs, leading to the simmering reaction and calculation of electrolyte mass loss along with the resulting change in material dependent variables.

3.3 Pack Model Description

The pack model is developed in consideration of key findings from the *Literature Review* (Chapter 2). These key findings include:

- Modelling the decomposition reactions in all cells allowing for the propagation path and severity to be quantified [70, 180, 225, 226, 229, 230];
- Typically inducing TR in the initiation cell by simulating an internal short circuit, modelled by an initial high temperature [225, 229, 230], or by modelling a small fraction of the cell's electrochemical energy released over a prescribed time, i.e. 10 s, in a specified volume of the jelly roll [70, 226];
- Accounting for tabs as they have been shown to be an important heat transfer path [90], that can mean the difference between predicting a safe outcome if not accounted for and an unsafe, TRP, outcome if considered [225];
- The location of the initiation cell, as TRP is more likely to occur when a cell initiated into TR is in contact with the least number of neighbouring cells, and also when these neighbouring cells are in contact with fewer cells, while cells packed closer together lead to greater TRP severity [225, 230].

The battery pack is taken to be constructed of 9 LFP 18650 (1.5 Ah) cells, the same cells as those studied throughout Chapters 4 and 5. The model geometry for the battery pack is presented in Fig. 3.10. The 3-dimensional model is built in *COMSOL Multiphysics 5.2a* [255]. The cells are arranged in a square matrix (3 cells by 3 cells) with an inter-cell spacing d_{cc}, see Fig. 3.10(b), while air is assumed to fill intra-pack spacing, i.e. the voids between cells. The cells are connected by an 'S' shaped nickel busbar, representing an arrangement of 9 cells in parallel. The cells are wrapped in a thin layer of shrink wrapping (see Fig. 3.10(d)), while the pack is assumed to surrounded by air on all sides. The geometrical dimensions and material properties of the cells and the pack are given in Table 3.3.

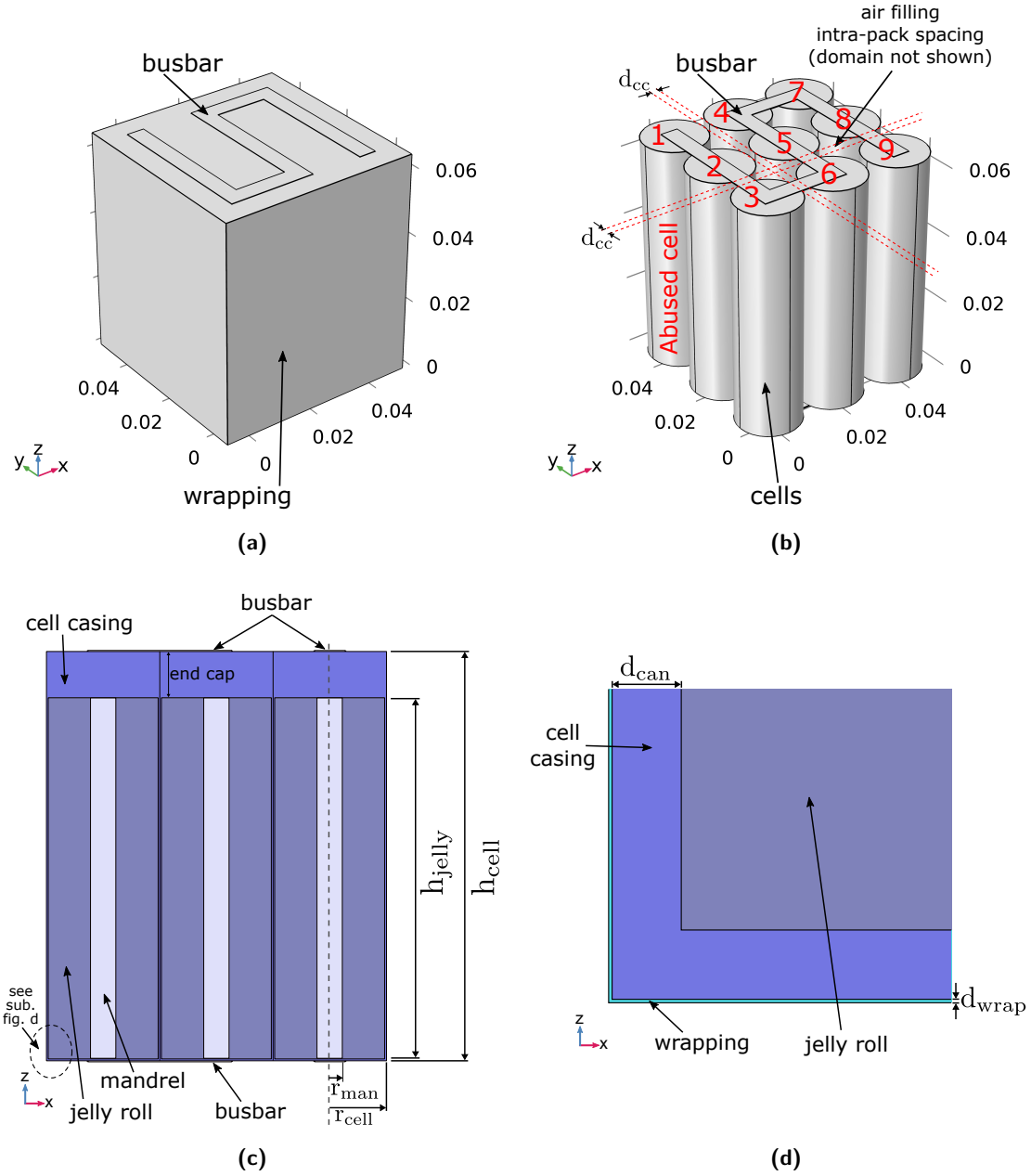

Figure 3.10: Pack geometry: a) pack with shrink wrapping (dimensions in m); b) pack without shrink wrapping (dimensions in m) showing inter-cell spacing $d_{cc} > 0$ mm, with cell reference numbers and abused cell indicated (by red text); c) cut through the x-z plane at y=0 (for a pack where $d_{cc} = 0$ mm) showing the internal cell geometry; and d) enlargement of a cut through the x-z plane at y=0 showing the relative thickness of shrink wrapping and cell case.

Table 3.3: Pack study parameters.

Parameter	Unit	Value
Geometry		
Cell height, h_{cell}	mm	65
Jelly roll height, h_{jelly} [*]	mm	57.3
Cell radius, r_{cell}	mm	9
Jelly roll outer radius, r_{jelly}	mm	8.7
Mandrel radius, r_{man}	mm	2
Cell casing thickness, d_{can} [†]	mm	0.3
Wrapping thickness, d_{wrap} [‡]	µm	15
Tab thickness, d_{tab}	mm	0.15
Tab width, W_{tab}	mm	5
Material Properties		
Wrapping - specific heat, $C_{p,wrap}$ [§]	J/kg K	1,000
Wrapping - density, ρ_{wrap} [‖]	kg/m^3	1,380
Wrapping - thermal conductivity, κ_{wrap} [‖]	W/m K	0.2
Wrapping - emissivity, ε_{wrap} [¶]	-	0.5
Nickel - specific heat, $C_{p,Ni}$ [‖]	J/kg K	440
Nickel - density, ρ_{Ni} [‖]	kg/m^3	8,890
Nickel - thermal conductivity, κ_{Ni} [‖]	W/m K	90.9
Cell - specific heat, $C_{p,cell}$	J/kg K	Eq. (3.53)
Cell - density, ρ_{cell}	kg/m^3	Eq. (3.52)
Cell - axial thermal conductivity, $\kappa_{axi,cell}$ [¶]	W/m K	30
Cell - radial thermal conductivity, $\kappa_{rad,cell}$ [¶]	W/m K	0.5
Cell - emissivity, ε_{wrap} [**]	-	0.8
Air - specific heat, $C_{p,air}$ [††]	J/kg K	Eq. (3.70)
Air - density, ρ_{air} [††]	kg/m^3	Eq. (3.71)
Air - thermal conductivity, κ_{air} [††]	W/m K	Eq. (3.72)
Abuse Condition		
Ambient temperature, T_{amb}	°C	60
Initial pack temperature, T_{int}	°C	60
Internal short circuit power, P_{short} [‡‡]	W	1,728
Internal short circuit initiation time, $t_{int,short}$	s	2
Internal short circuit period, t_{short}	s	10
Decomposition and Venting		
Parameter sets MAH, MAL, MBH and MBL for individual cases.[§§]		

[*] Mandrel is the same height as the jelly roll.
[†] Defines the vertical distance between the outer surface of the cell at the negative terminal and the bottom of the jelly roll.
[‡] Pack shrink wrapping.
[§] Value from Ref. [256].
[‖] Value estimated from the ranges given in Ref. [257].
[¶] Estimated.
[**] From Ref. [258].
[††] From Ref. [255].
[‡‡] $P_{short} = V_{cell} Q_{cell} / t_{short}$, where V_{cell} is the nominal cell voltage (V), here 3.2 V, and Q_{cell} is the cell capacity in Coulombs (C), here determined for a cell a with 1.5 Ah capacity.
[§§] See Table 5.6.

Each cell geometry in the pack considers the main internal cell features, i.e. the mandrel, jelly roll and cell casing, see Fig. 3.10(c). The height of the jelly roll (which the mandrel is also equal to) and the thickness of the can are given in Table 3.3. The difference in height between the jelly roll and the overall cell height represents the end cap. The intricate structures of the end cap, such as the vent opening and burst disk, are not represented.

The construction of the cell domains in this manner allows the volume specific heat generation from the decomposition reactions to be correctly applied only to the jelly roll region. For computational efficiency, simplifying the wound jelly roll structure to a single domain, the cell is modelled as a single homogeneous material with a fixed average heat capacity and density properties whilst considering anisotropic thermal conductivity, see Table 3.3 for values.

The shrink wrapping is assumed to be Polyvinyl Chloride (PVC). The values of the material properties of the PVC and the nickel tabs are listed in Table 3.3. The air material is defined by COMSOL's built in parameters for air [255]. The specific heat capacity, thermal conductivity and density of air are defined by Eqs. (3.70) to (3.72) respectively. For Eqs. (3.70) to (3.72), T represents temperature in kelvin, while Eqs. (3.70) and (3.71) are valid over the temperature range 200–1600 K. Furthermore, P is pressure (Pa), R is the ideal gas constant (8.314 J/mol K) and M_{air} is the molar mass of dry air (0.028 97 kg/mol).

$$\begin{aligned} C_{p,air} = {} & 1047.63657 - 0.372589265T + 9.45304214 \times 10^{-4}T^2 \\ & - 6.02409443 \times 10^{-7}T^3 + 1.2858961 \times 10^{-10}T^4 \end{aligned} \tag{3.70}$$

$$\begin{aligned} \kappa_{air} = {} & -0.00227583562 + 1.15480022 \times 10^{-4}T - 7.90252856 \times 10^{-8}T^2 \\ & + 4.11702505 \times 10^{-11}T^3 + 7.43864331 \times 10^{-15}T^4 \end{aligned} \tag{3.71}$$

$$\rho_{air} = \frac{PM_{air}}{RT} \tag{3.72}$$

All heat transfer behaviours are governed by *COMSOL*'s inbuilt functionality of the *"Heat Transfer"* package [255]. Within the pack, heat transfer by conduction through all domains and surface-to-surface radiation between cells is considered, while convection in the air domain is ignored. At the surface of the pack, the boundary conditions assume free convection and radiation between the surface and the environment. The direction of radiation for the surface-to-surface radiation between cells is controlled by opacity. The free convection coefficients for the vertical walls and, the bottom and top surfaces, of the pack are governed by the Nusselt number correlations for flat vertical and horizontal plates. The convection coefficients are calculated through *COMSOL*'s *external natural*

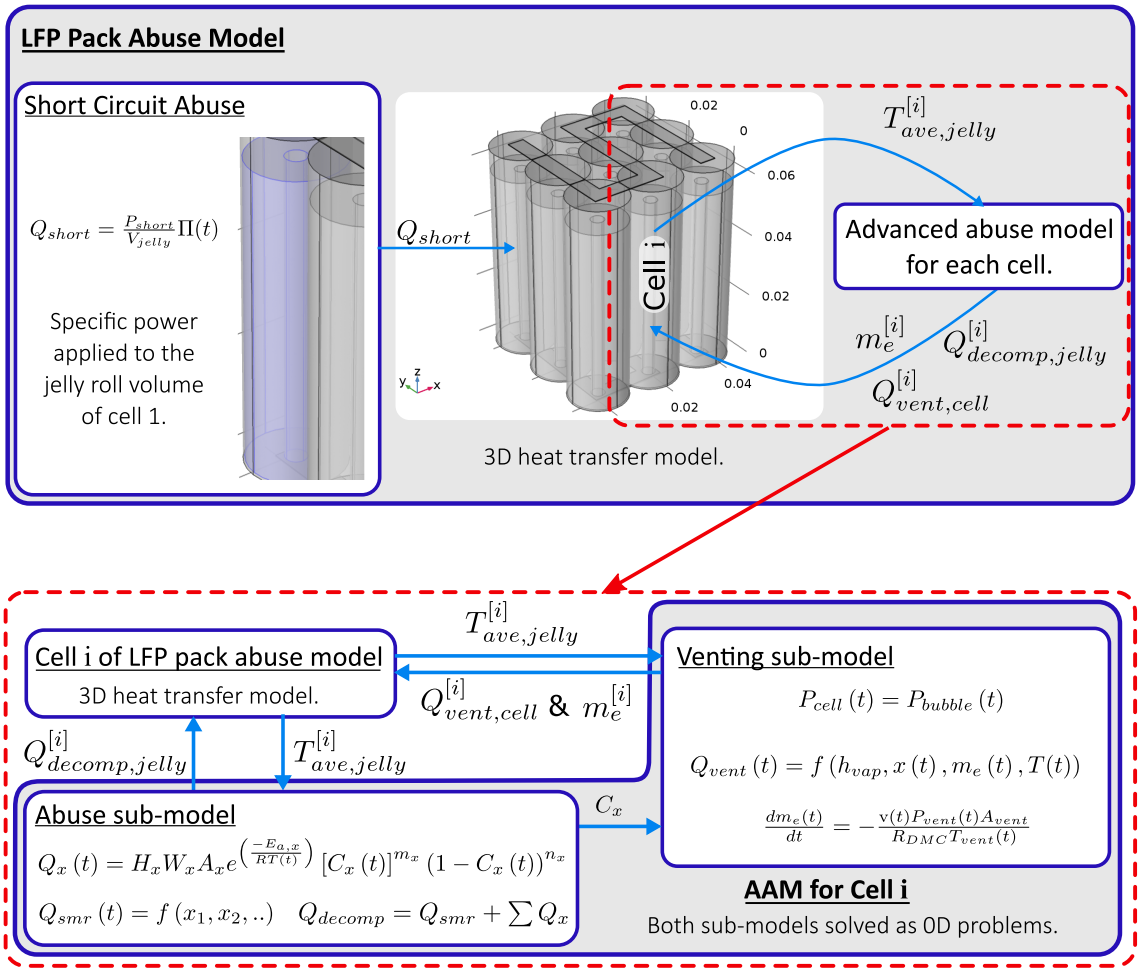

Figure 3.11: LFP pack abuse model flow chart.

convection option, for *vertical walls* (for the pack walls), *horizontal plate upside* (for the top surface) and *horizontal plate downside* (for the bottom surface). The convection coefficient is defined by the characteristic length, absolute pressure (101 kPa), and the external air temperature. For the vertical walls the characteristic length is the height of the walls, while for the horizontal surfaces it is the area of the surface divided by the parameter of the surface.

The AAM, governed by the equations in Section 3.2.2 and Section 3.2.3, is used to describe the decomposition reactions and venting of each cell. The decomposition reactions, for computational simplicity, are solved as a 0D problem for each cell. The temperature variable in the Arrhenius formulations and venting formula for each cell are set to be the average temperature of the jelly roll for each cell respectively. From the 0D decomposition reactions, the calculated volumetric heat generation of each cell is applied over the jelly roll domain of each respective cell. The volumetric heat loss due to venting of a cell is applied over the entire cell. The coupling between the 3D heat transfer model and the 0D AAM is shown in Fig. 3.11.

The abuse of the battery pack is considered to occur under a worst case scenario, i.e. the pack is initially at a high temperature, 60°C, which is representative of the maximum operating temperature of the cell as stated by the manufacture [259], and exposed to high environmental temperatures, also 60°C. TR is induced in the initiation cell by assuming a large internal short circuit. This is simulated by releasing 100% of a single cells electrochemical energy ($E_{cell} = 17.28\,\text{kJ}$) for a period ($\Delta t_{short}$) of 10 s over the jelly roll domain. The volume specific power of the short, Q_{short} (W/m^3), is governed by a rectangular function:

$$Q_{short} = \frac{P_{short}}{V_{jelly}} \Pi(t) \tag{3.73}$$

where $\Pi(t)$ is the rectangular function,

$$\Pi(t) = \begin{cases} 0 & \text{if } t < 2\,\text{s} \\ 1 & \text{if } 2\,\text{s} \leq t < 12\,\text{s} \\ 0 & \text{if } t \geq 12\,\text{s} \end{cases} \tag{3.74}$$

and P_{short} is the heating power of the short,

$$P_{short} = \frac{E_{cell}}{\Delta t_{short}} \tag{3.75}$$

A corner cell (in this case cell 1, see Fig. 3.10(b)) is taken to be the cell abused by an initiation scenario. Again this is to study a worst case scenario, as the literature suggests that the cell in contact with the pack case (environment boundary) and that is also neighbour to the least amount of cells will cause the worst TR event.

Figure 3.12 presents the meshed geometry (with the air and wrapping domains removed). The meshed geometry contains 110 622 domain elements, which, for the governing equations applied leads to 223 551 degrees of freedom.

Two simplifications are made to the model regarding physics implemented, 1) exclusion of electrochemical behaviours, which can be used for calculating Ohmic heating through failed cells when cells are connected in parallel, and 2) exclusion of heat transfer my vent gas convection or gas combustion and flame behaviour. Both of these simplifications ignore important heat sources [90, 180, 231]. Although electrochemical behaviour and related heating is important for an exact understanding of risk, a simplified model purely accounting for abuse behaviour, such as the one here, can still provide practical information on the possibility of TRP occurring. The results from the model can identify important heat transfer pathways and aid the design of mitigation strategies. The exclusion of heat transfer by vented gas can be applicable in situations when cells are free to vent to the atmosphere such that gases/flames are not contained within the pack [224, 231]. Furthermore, it is applicable in cases where a cell's ejecta/flame does not directly impinge on other cells, i.e. in cells arranged side-by-side (as in this case), unlike cells arranged end-

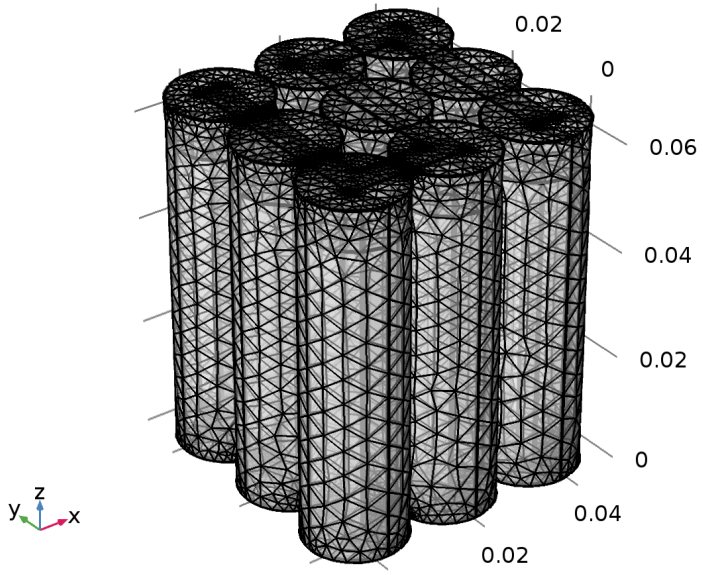

Figure 3.12: LFP pack - mesh.

to-end (along the axis of 18650 cell) where the vent of one cell directs towards the negative terminal of others [222, 245, 260]. As this pack is held together by shrink wrapping, any gases/flames generated are assumed to be able to easily escape through destruction of the wrapping local to the positive terminal, hence heat transfer by gases/ flames can be neglected here.

3.3.1 Preliminary Studies

For the aid of determining the robustness of the pack model, two preliminary studies are undertaken to investigate two important considerations that can affect predictions. The first determines the effect of model dimensionality on predictions, while the second determines the effect of model mesh density on predictions. These studies are presented below.

3.3.1.1 Model Dimensionality

The parameterisation of the single cell LFP model was done using a 1D geometry, however, the pack model (described in detail in Section 3.3) utilises a 3D geometry for heat transfer, while solving the AAM in 0D. Hence, it is of importance to investigate the effect of cell geometrical dimensionality on the results of comparable simulations. This is to determine if any changes occur in predictions and ensure no significant differences are present that could affect the quantification of safety and TRP.

To carry out this investigation, a comparison is made between oven temperature simulations using both the 1D and 3D single cell models. The parameterised 1D model, utilising parameter set MAL, was used as a reference value. The 3D model of the cell uses the exact same parameters as the 1D model, while for a fair comparison, the end caps (terminals) of the 3D cell are taken to be insulated. This removes additional heat transfer surfaces that are not accounted for in the 1D model, while all other boundary condition remain the same. The 3D model is meshed using *COMSOL*'s *Physics-controlled Extremely Coarse Mesh* [255] (the same meshing criteria used later for the pack model), resulting in 3,006 domain elements. See *M1* of Fig. 3.14 for a depiction of the mesh for this study, and the corresponding row of Table 3.4 for the related computational degrees of freedom.

3.3.1.2 Model Dimensionality Results and Discussion

Figure 3.13 compares the results of the 1D model for the LFP cell under study and the 3D heat transfer/ 0D abuse model. The 1D model is reproduced from Chapter 5 for the model with parameters MAL, while the 3D model used identical parameters to this. Figure 3.13(a) shows the predicted cell surface temperature for the entire time period for the two simulation studies and also the experimental data of cell surface temperature. Figure 3.13(b) shows an enlarged view of the cell surface temperature around the venting event. Figure 3.13(c) shows the average cell decomposition species, with dominant reactions highlighted that lead to the reduction in average reaction species throughout simulations. Figure 3.13(d) shows the average jelly roll volume temperature from simulations.

From Figure 3.13(a) three differences in predictions between the 1D and 3D models can be seen: 1) the 3D model heats up quicker; 2) the location of peak cell temperatures are different; and 3) the severity of TR (i.e. maximum cell surface temperature reached) is less for the 3D model.

As stated above, the 3D model heats quicker. However, as the end caps are insulated in this comparison, then axial heat transfer can be ruled out as an additional heat transfer surface and not a factor leading to more rapid heating in the 3D model. Even though the 3D model heats up quicker than the 1D model, the time to venting (as a reference point) only advances by 1 min under either oven temperature exposure, see Fig. 3.13(b). This is due to the higher temperatures in the 3D model (early on) leading to initial decomposition occurring sooner than for the 1D model, see Fig. 3.13(c), hence gas production and venting are earlier.

The advance in surface temperature remains until just prior to the maximum temperature (~26 min) for the lower oven temperature case. This coincides with the end of the NE reaction. Under the higher oven exposure temperature, the advance in surface temperature

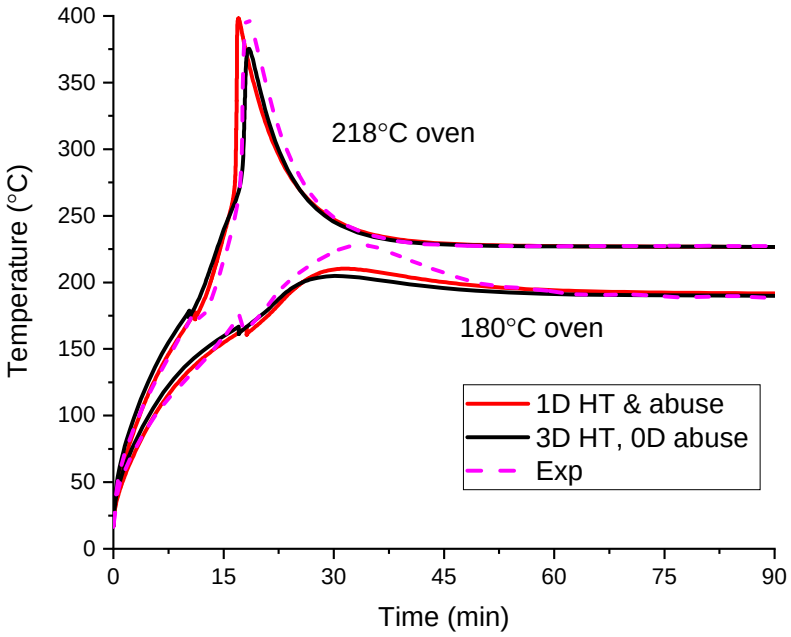

(a)

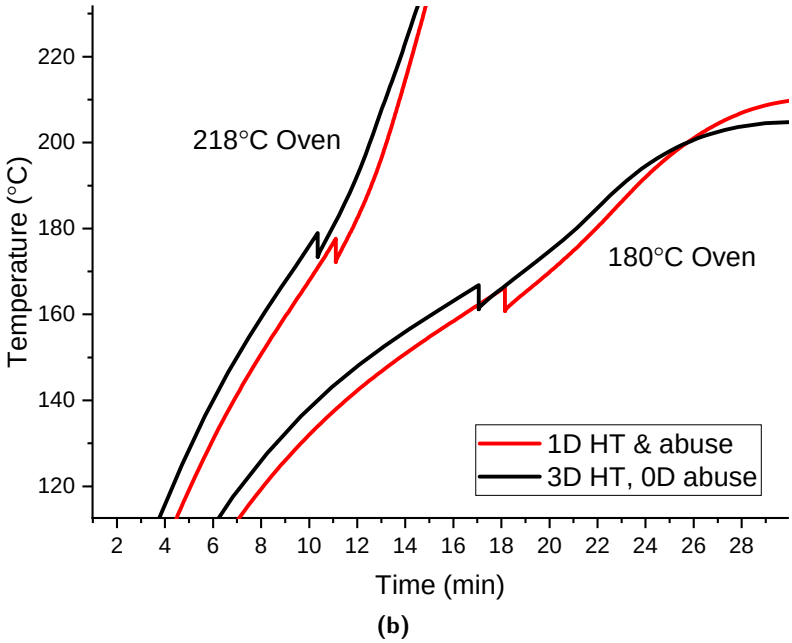

(b)

Figure 3.13: Comparison of oven temperature simulations of a single cell with different dimensionalities. (a) maximum surface temperature, (b) enlargement of venting event, (c) average cell decomposition and (d) average jelly roll temperature.

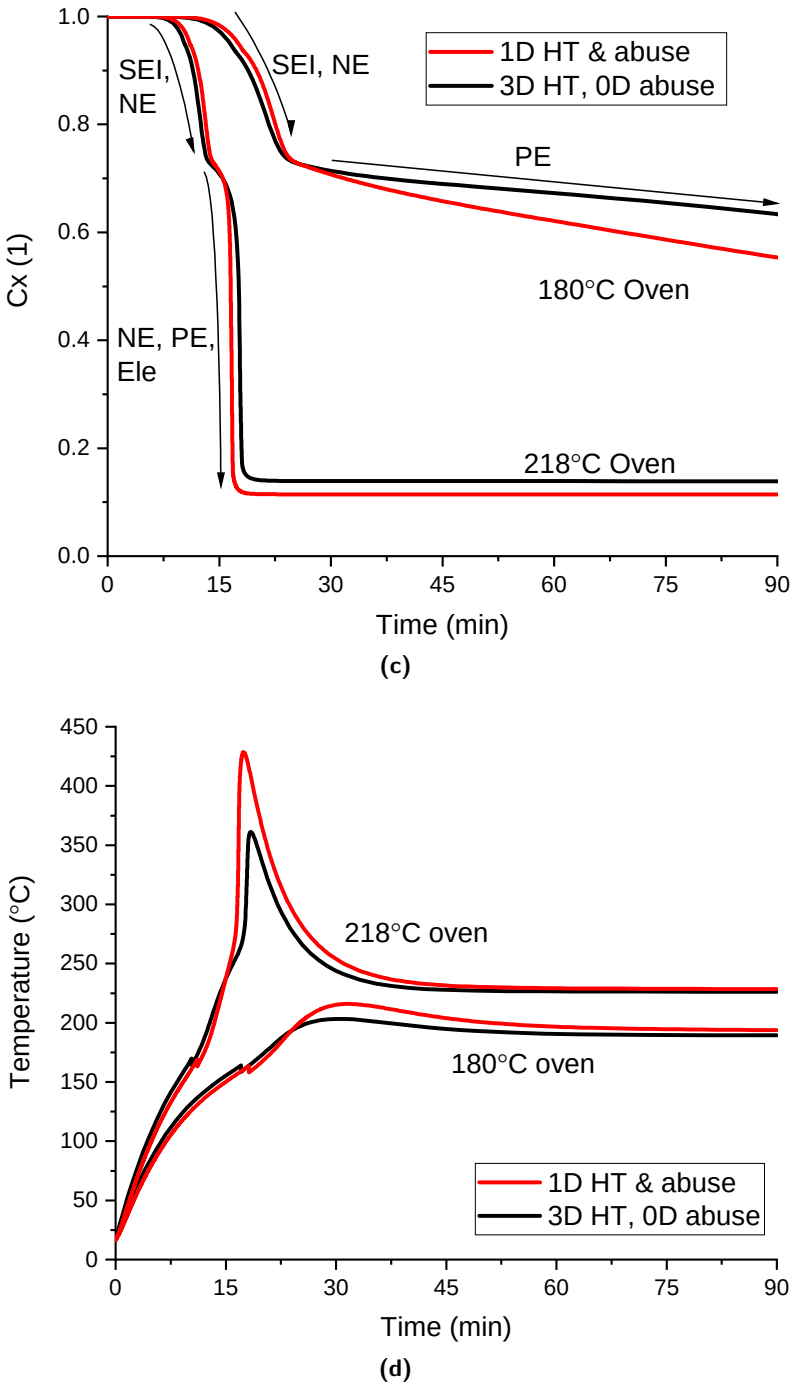

Figure 3.13 (cont.): Comparison of oven temperature simulations of a single cell with different dimensionalities. (a) maximum surface temperature, (b) enlargement of venting event, (c) average cell decomposition and (d) average jelly roll temperature.

remains until just prior to the occurrence of the fast decomposition reactions (~15 min), see Fig. 3.13(a). This has implications on the time to maximum cell temperature.

Although the 3D model heats up quicker, only the lower oven temperature case reaches a peak temperature sooner than the 1D model. In the higher oven temperature case, the 3D model has a delayed rapid temperature rise compared to the 1D model, and hence delayed peak temperature. This is attributed to the fact the 1D model assumes a jelly roll the length of the cell, while the more realistic 3D representation has a smaller jelly roll volume than the 1D model. Hence, the total heat produced in the 3D model is less due to volumetric heat generation being applied over a smaller volume than in the 1D model. As such, at each stage of TR, less heat is produced.

With this, at temperatures below 200°C there is a low rate of reactivity (as seen by the change in species Fig. 5.7) and hence a low rate of heat generation by energetic reactions, so the temperature is dominated by convection from the oven. However, above this temperature the rapid PE and electrolyte reactions have an increasing contribution to heat generation (leading to greater NE heat generation). But, as stated previously, in the 3D model the total heat generation is lower for a given temperature. Therefore, the TR positive feed back loop is weaker and the occurrence of the rapid reactions are delayed, leading to a delayed maximum temperature. This behaviour is less apparent in the lower oven exposure case as severe reactions do not occur, hence peak temperatures are not delayed. Further to this, it can be seen from Fig. 3.13(c), particularly for cells abused at 180°C, that the reaction rates are greater in the 1D case (inferred from the steeper gradient of the average reaction species) than the 3D model, when the fast PE reactions are present, due to the higher average jelly roll temperature in the 1D model, see Fig. 3.13(d).

Similarly, due to the smaller jelly roll volume, there is less total heat produced which leads to lower overall severity of TR in both cases of the 3D model compared to the 1D model. For the higher oven temperature case, the reduction in predicted severity is seen by a maximum temperature prediction 25°C lower than the experimental value, see Fig. 3.13(a). The difference is greater in the higher oven temperature case as more heat is produced by decomposition (~10.5 kJ compared to ~3.4 kJ for the higher and lower oven exposure cases respectively, see Table 5.7), than for the lower oven temperature case where maximum temperature is greatly dominated by the oven temperature.

Although Fig. 3.13 has shown that there are overall differences between using the 1D and 3D model, these are slight, and the 3D model produces an acceptable prediction of TR. Hence, with the knowledge of the small delay to the occurrence of the TR event and the slight reduction in predicted TR severity, simulations and analysis of a pack can be undertaken considering (with the use of the 3D model) propagation may be postponed due to the delayed TR event of a cell or, if propagation is boarderline, cautious assessments of safety should be made considering the under prediction of severity.

Table 3.4: Number of mesh elements for each mesh study.

Mesh	ID	Nº. of elements	DOF
Extremely coarse	M1	3,006	4,576
Extra coarse	M2	5,368	8,053
Coarser	M3	10,303	15,394
Coarse	M4	22,150	32,342

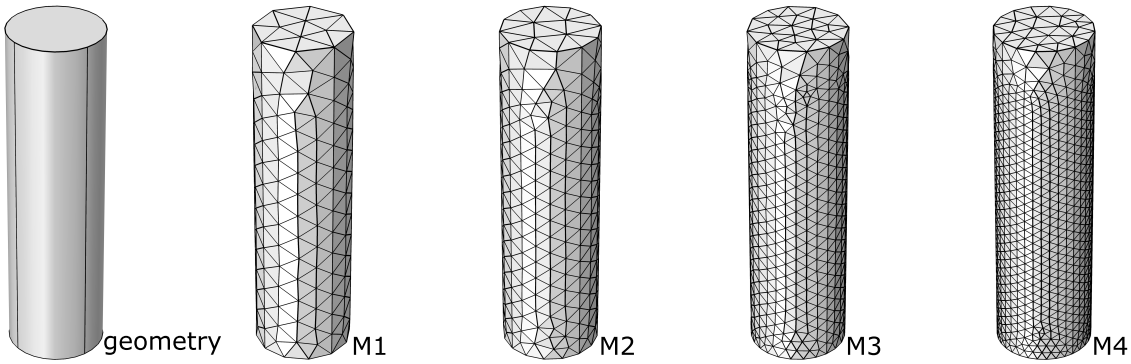

Figure 3.14: Meshes of geometry for each mesh study.

3.3.1.3 Mesh Analysis

A mesh analysis should carried out to determine the effect of mesh density on TRP predictions. However, due to computational limitations, the 3D pack model has to be simulated using an "extremely coarse" mesh, which also prevents undertaking a mesh analysis on the pack its self. Hence, the 3D single cell model is used as an approximation for the pack to determine if there are any changes in predictions between an "extremely coarse" mesh and relatively finer meshes that could significantly affect the quantifications of cell safety and hence pack TRP potential.

Initially, the same 3D model is used as in the dimensional analysis above, while abuse is only carried out by oven exposure at 218°C. Further simulations are performed at increasing mesh densities. The mesh is selected through and controlled by *COMSOL*'s *Physics-controlled Mesh* [255] options. The number of mesh elements for each simulation, with corresponding degrees of freedom, are presented in Table 3.4, while Fig. 3.14 show the meshes for each refinement.

3.3.1.4 Mesh Analysis Results and Discussion

Figure 3.15 presents the relative error of simulations using meshes M1–M3 when calculated against the results of the simulation using the finest mesh, M4. The relative error is overlaid on the cell surface temperature results of the simulation using mesh M4. Three instances in time are annotated on Figure 3.15. These are: I – the point of venting, II –

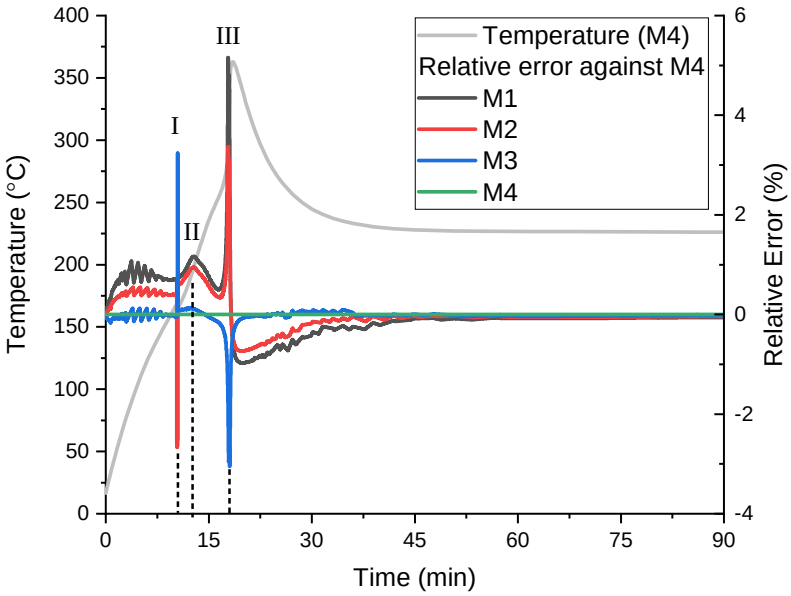

Figure 3.15: Mesh sensitivity study of a single cell under oven abuse. Annotations indicates times at which significant relative errors occur.

a short time after venting, and III – the TR event. Figure 3.15 shows that, during the period of 0 min to 45 min (i.e. when the cell is heating up due to heat transfer from the oven, undergoing TR and then cooling down to the oven temperature) the relative error is the greatest. Whereas, when the cell is in near equilibrium with the oven temperature (in the period >45 min to end) then the relative error is effectively zero. There are significant peaks (up to 5%) in the magnitude of relative error at points I and III for meshes M1–M3, while less significant relative errors occur around point II for meshes M1 and M2. For points I and III, this coincides with the occurrences of very steep temperature gradients due to venting and TR, respectively. Hence, it is clear that the relative error is greatest when the temperature rates are the greatest. As is to be expected, the finer meshes M2 and M3 lead to reduced relative errors, while M3 leads to almost zero relative error through the simulation besides at points I and III.

The points I–III are further presented in Fig. 3.16(a) to clearly show their locations on the temperature graph, while these points are further enlarged and presented in Figs. 3.16(b) to 3.16(d) so details can be precisely examined. Figure 3.16(b), shows the enlargement of point I, the venting event. From this it is clear that the large increase in relative error occurs due to the offset in time at which venting occurs between each simulation, as cells heat up quicker in simulation M1 and M2, while the general behaviour, such as magnitude of temperature drop due to venting, is similar in all cases. For point II, see Fig. 3.16(c), a deviation of the temperature of simulations M1 and M2 from M4 occurs, again, due to the earlier increase in temperature, in this case as self-heating begins. At point III, see Fig. 3.16(d), these offsets in time amplify the relative error. As, for a given point in time due to the steep temperature gradients there is a large difference in

Table 3.5: Key values throughout thermal runaway, with corresponding relative errors calculated against mesh M4.

Mesh	Time to vent		Max. temp.		Time to max. temp.	
	(min)	Err. (%)	(°C)	Err. (%)	(min)	Err. (%)
M1	10.36	−0.91	361.14	−0.49	18.43	−0.36
M2	10.40	−0.54	361.38	−0.42	18.43	−0.36
M3	10.48	0.05	361.34	−0.43	18.56	0.38
M4	10.45	0.00	362.90	0.00	18.49	0.00

temperature. As the large relative errors are caused by small offsets in time, a further investigation of the relative errors of key TR values is undertaken.

The relative errors of the key values of *time to venting*, *maximum cell temperature* and *time to maximum cell temperature* are presented in Table 3.5. From this table we see that M4, with no strong relation between error and mesh elements, has converged onto an accurate solution. Also, the coarsest mesh (M1), comparable to what is used in the pack study, has an error of less than 1% for all key values, much lower than apparent in Fig. 3.15. As such, while the plot of relative errors indicates a relatively high percentage error (~5%), this is entirely due to small errors in the onset time of key events (where the temperature changes very rapidly). Hence, the use of a similarly coarse mesh (i.e. M1) for the pack study can be done with confidence.

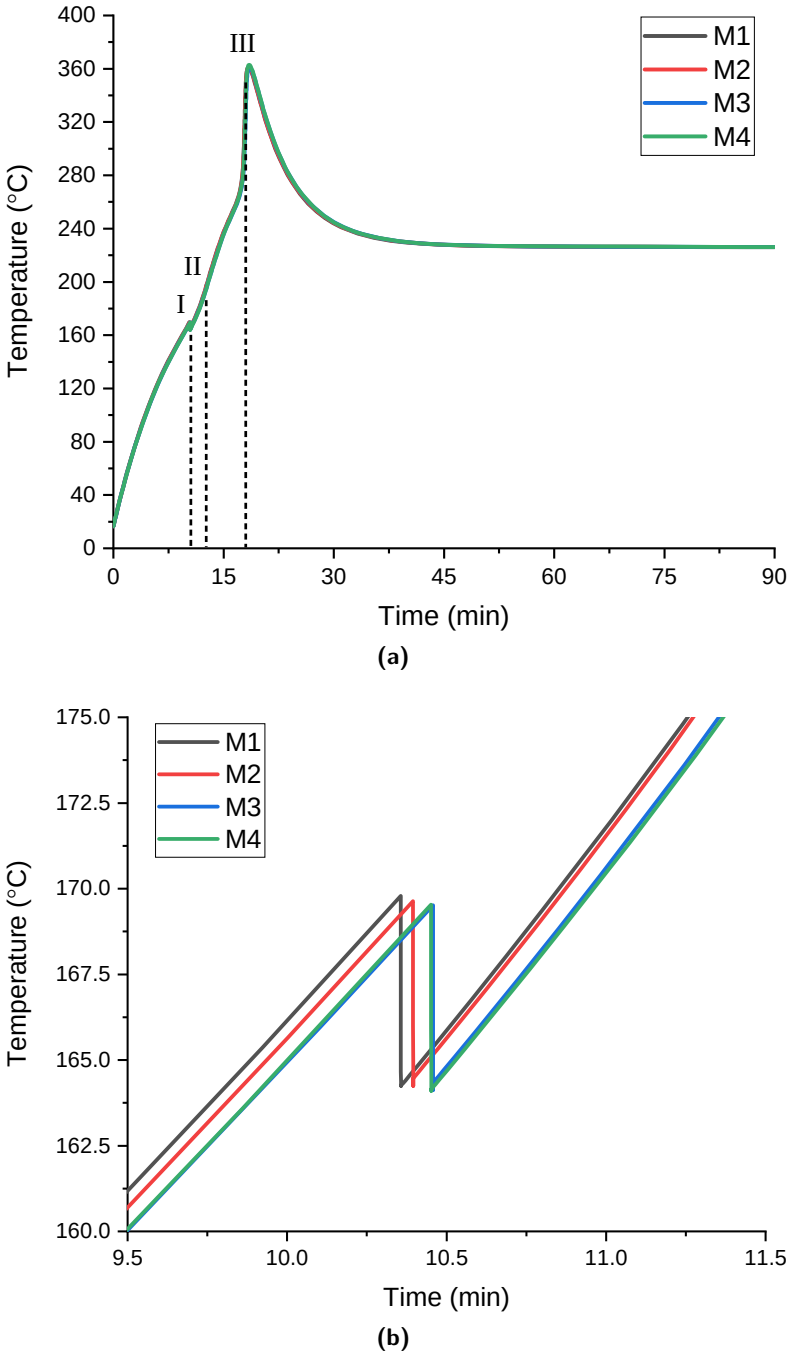

Figure 3.16: Inspection of the occurrence of significant relative errors. (a) temperature plot identifying areas of significant relative error, (b) enlargement of area I, (c) enlargement of area II and (d) enlargement of area III.

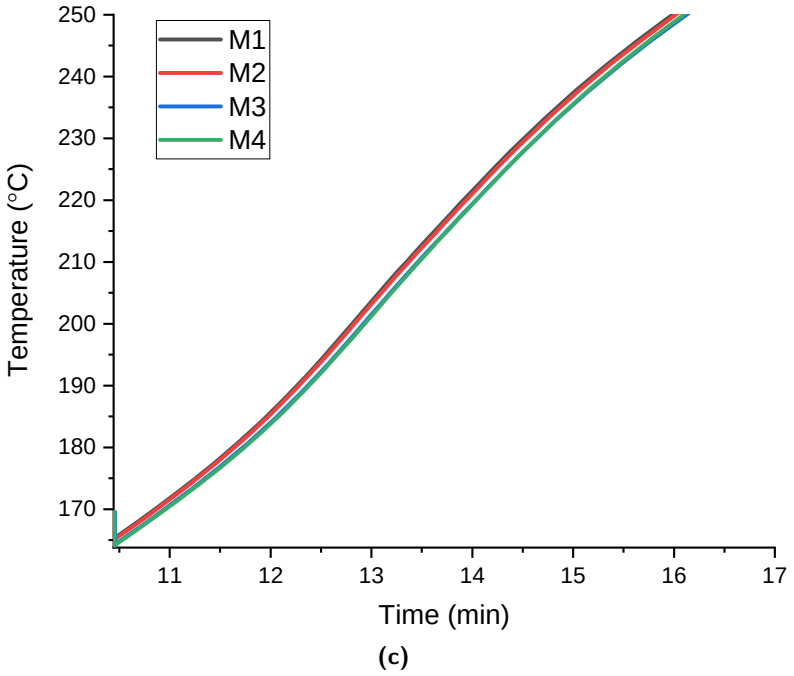

(c)

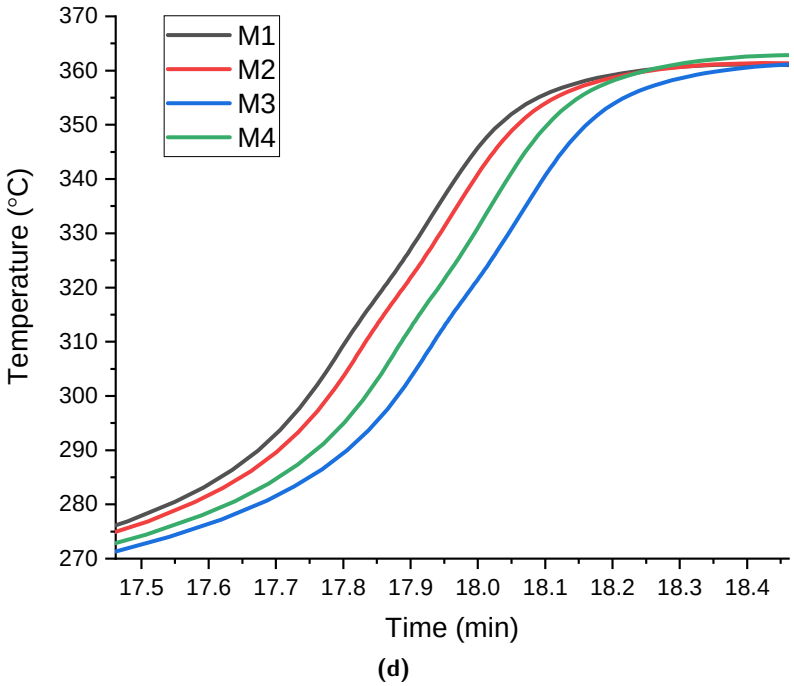

(d)

Figure 3.16 (cont.): Inspection of the occurrence of significant relative errors. (a) temperature plot identifying areas of significant relative error, (b) enlargement of area I, (c) enlargement of area II and (d) enlargement of area III.

3.4 Summary

The Methodology utilises tried and tested experimental techniques, i.e. ARC and oven testing which are fundamental to assessing Li-ion battery TR behaviour. It also presents the methods to determine cell specific heat. Although there are questions about the effect of sample size on the validity of calculated results. The governing equations for the modelling of cell TR have been described by the heat transfer, abuse (accounting for the decomposition reactions) and venting sub-models. Further, the AAM is presented with developments to the governing theory for determining cell pressure, i.e. by the BPV method rather than the PPV method, and the inclusion of a novel simmering reaction. Finally, a typical pack geometry is presented, including the coupling of the 3D thermal model to a 0D abuse model for computational efficiency.

Chapter 4

Experimental Investigation of the Safety of LFP Cells

Aims & Objectives

The aim of this chapter is to address gaps in the literature in regard to the TR behaviour of LFP cells under thermal abuse. In doing so, obtain the necessary data required for developing LFP TR models in Chapter 5. The objectives to address these gaps are:

(1) to carry out a comprehensive analysis of 18650 LFP cells under ARC at various SOC to allow for a detailed understanding of the self-heating characteristics as a function of SOC and temperature;

(2) to carry out convective heating oven abuse tests to analyse the thermal response under rapid heating, providing essential data for LFP TR model validation;

(3) to quantify the severity of TR, present a detailed description of the TR process and discuss how TR can be avoided in LFP cells using the results from objectives (1) and (2);

(4) to determine the energy released in each abuse test/scenario for a comparison of test suitability in determining cell safety and TR characterisation.

4.1 Introduction

In this chapter an investigation of LFP cells' safety is undertaken through two thermal abusive tests to enable characterisation of the resulting TR behaviour. In turn, the cells' safe operating window in terms of SOC and temperature can be quantified, along with

Table 4.1: Technical specification of *ENIX Energies* 1500 mAh 3.2 V 18650 cell [259].

Specification	Value
Chemistry	$LiFePO_4$
Dimensions	18.2 (D) × 64.8 (H) mm
Weight	42 g approx.
Standard capacity	1550 mAh at 0.5C 1500 mAh at 1.0C
Capacity range	1450–1550 mAh
Charge voltage	4.20 ± 0.05 V
Nominal voltage	3.2 V
Charge cut-off voltage	3.65 ± 0.05 V
Discharge cut-off voltage	2.5 V
Cut-off current	0.01C
Internal resistance	60 mΩ
Cycle life	2000 cycles
Max. continuous discharge current	4.5 A
Pulse discharge current	10 A, 5 s
Working temperature	Charge: 0–55°C Discharge: −20–60°C
Storage temperature	−20–45°C

identifying any hazards the cells pose. The first abusive scenario is an ARC test, while the second is abuse by overheating in an oven test. Calorimetry is carried out under near-adiabatic conditions and represents the worst case scenario of a cell when heated, as there is zero heat loss from the cell. ARC also allows us to infer the process by which TR occurs, which is necessary for developing accurate models of TR by ensuring that the reactions are simulated in the correct order and with the appropriate magnitude of heat relative to each other [153]. A convection oven test allows us to study the response of a cell when rapidly exposed to high temperatures, representing what might occur due to environmental conditions or as a result of heating from a neighbouring cell which has failed by other means. Additional to investigating the safety of the LFP cells, the cells are also characterized in terms of their physical, thermo-physical and electrical properties. This is to precisely determine the LFP cells' dimensions, mass, specific heat capacity and electrical energy capacity.

The investigation into the safety of LFP cells, in relation to the potential of cell TR and TR severity, was carried out on commercially produced cylindrical 18650 LFP cells. Cells of this form factor were chosen due to them being readily available, their place as an industry standard in many applications and to allow for comparison to the large amount of literature regarding other Li-ion chemistries also in the form of 18650 cells. The commercial cells tested herein were specifically *ENIX Energies* 1500 mAh 3.2 V 18650 cells, hereafter referred to as *the LFP cell* throughout this chapter. The precise cell chemistry is currently unknown and unavailable from the manufacturer, however known cell properties from the manufacturer's data sheet are summarised in Table 4.1.

In order to achieve the objectives outlined at the start of this chapter, the following was carried out:

- to achieve objective (1), the ARC test was carried out, according to the methodology in Section 3.1.1, with cells at 0%, 28%, 63%, 100% and 110% SOC, of which the results are presented in Section 4.2.2;
- to achieve objective (2), the oven abuse test was carried out, according to the methodology in Section 3.1.2, on cells at 100% SOC, with results presented in Section 4.2.3;
- to achieve objective (3), the results of the ARC and oven test are analysed and compared to each other and literature findings, with the discussion presented in Sections 4.2.2 and 4.2.3;
- to achieve objective (4), a new methodology to estimate the energy released by cells due to TR under oven exposure is formulated and implemented, and the heat released by cells in each abuse test are in turn calculated, presented and discussed in Section 4.2.4, along with recommendations with regard to abuse testing for ensuring robust quantification of Li-ion cell safety.

4.2 Results and Discussion

The *Results and Discussion* are organised as follows: first, a record of experiments is presented listing the experiment under taken by each cell, the cell mass and cell electrical capacity, then Sections 4.2.1 to 4.2.3 present the results and discussion of the heat capacity, ARC and oven abuse tests respectively. Following this, Section 4.2.4 compares the different abuse methods, while Section 4.4 concludes the experimental chapter.

Table 4.2 presents the record of experimental tests, indicating which cells underwent ARC, oven and heat capacity tests. The table also presents the SOC of each cell under ARC, while all oven test cells were at 100% SOC. Finally, included in the table are the measured masses of cells, either with or without shrink wrapping, and the measured electrical capacity determined at a 1C discharge rate after 20 cycles. From this, the average mass of the cells is calculated to be 40.48 g with shrink wrapping and 38.89 g without shrink wrapping. The average electrical capacity of the cells was determined to be 1.48 Ah.

Table 4.2: Record of experimental tests.

Cell Nº.	**Test**	**Mass, unwrapped (wrapped). [g]**	**Capacity at 100% SOC [Ah]**
01	n/a	-	1.54
02	Oven (200°C)	-	1.54
03	Oven (220°C)	-	1.49
04	Oven (180°C)	-	1.50
05	ARC (100% SOC, R4)	39.77	1.49
06	ARC (100% SOC,R5)	39.97	1.50
07	n/a	-	-
08	Oven (220°C)	39.96	1.48
09	Oven (220°C)	39.82	1.47
10	Oven (180°C)	40.05	1.49
11	n/a	40.05	1.48
12	Oven (200°C)	39.74	1.47
13	Oven (200°C)	39.89	1.48
14	Oven (220°C)	39.90	1.49
15	Oven (180°C)	39.85	1.47
16	Oven (180°C)	39.85	1.49
17	Oven (220°C)	39.95	1.49
18	ARC (100% SOC, R1)	39.71	1.47
19	Oven (180°C)	39.68	1.45
20	Oven (220°C)	39.88	1.47
21	Oven (220°C)	39.86	1.47
22	Oven (220°C)	39.73	1.46
23	ARC (100% SOC, R6)	39.99	1.48
24	ARC (100% SOC, R2)	39.74	1.48
25	ARC (100% SOC, R3)	39.85	1.49
26	ARC (0% SOC, R4)	40.08	1.49
27	ARC (0% SOC, R1)	39.98	1.49
28	ARC (33% SOC, R1)	39.93	1.47
29	ARC (33% SOC, R2)	39.89	1.47
30	ARC (66% SOC, R1)	39.91	1.47
31	ARC (66% SOC, R2)	39.79	1.47
32	n/a	39.80	1.47
33	ARC (66% SOC, R4)	39.81	1.47
34	ARC (66% SOC, R3)	39.77	1.48
35	ARC (33% SOC, R3)	40.00	1.47
36	ARC (0% SOC, R2)	40.03	1.49
37	ARC (0% SOC, R3)	39.88	1.47
38	ARC (100% SOC, R7)	39.95	1.48
39	n/a	39.96	1.49
40	C_p	(40.45)	1.48

continued on next page

Table 4.2 (cont.): Record of experimental tests.

Cell Nº.	Test	Mass, unwrapped (wrapped). [g]	Capacity at 100% SOC [Ah]
41	ARC (110% SOC, R1)	39.76	1.48
42	ARC (110% SOC, R2)	40.42	1.49
43	ARC (110% SOC, R3)	39.84	1.48
44	C_p	(40.57)	1.49
45	C_p	(40.53)	1.49
46	C_p	(40.47)	1.48
47	C_p	(40.34)	1.48
48	C_p	(40.42)	1.49
49	C_p	(40.55)	-
	Ave.	39.89 (40.48)	1.48

4.2.1 Specific Heat Capacity Calculation

As stated in Section 3.1.4, for the calculation of the specific mass of the cells, the average heating rate of the sample is required. An example of how this is determined is presented in Fig. 4.1. Figure 4.1 shows the sample temperature and the mean temperature of the ARC (from its three temperature readings) over time, along with the difference between the sample and ARC temperatures over time. From this figure, it can be seen that, at $t = 0\,\text{s}$ the ARC temperature is ramped up, and for a period of time after, the sample is heated to the target start temperature. Once the sample and ARC temperatures are within 0.5°C of each other (see the blue temperature difference line of Fig. 4.1 and the threshold temperature difference), the sample and ARC are said to be in equilibrium. At this point the sample heater is switched on, and the time denoted as t_{start}. At this point the ARC follows the temperature of sample, creating pseudo-adibiatic conditions, until the sample reaches the safety cut off temperature (55°C). This point in time signifies the end of the test, denoted by t_{end}.

The sample heating rate is calculated over the period t_{start} to t_{end} in which the sample heater is on and the cell is under adiabatic conditions. Figure 4.1(b) presents data solely of this period. From this, the slope can be calculated by fitting a linear trend line to the data, with the slope of the trend line taken to be the average heating rate. The specific heat capacity can be determined from this rate (for each test), and the mass and heater measurements, following the methodology of Section 3.1.4. For each test configuration, these values and the calculated specific mass of the cell are presented in Table 4.3.

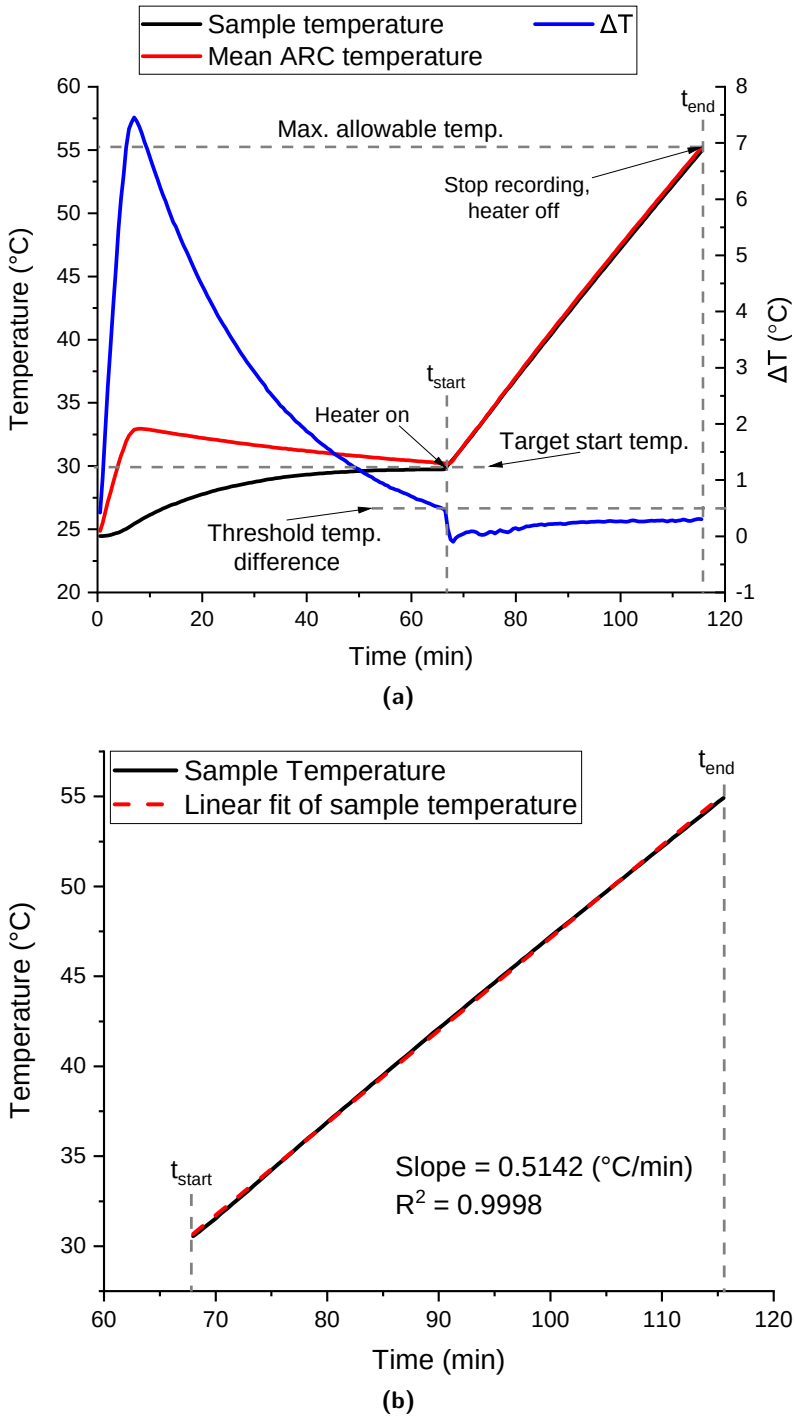

Figure 4.1: Example of heat capacity test results. (a) temperature vs. time plot for all time, and (b) temperature vs. time plot for constant power heating period used to determine the sample temperature rate.

Table 4.3: Calculation of specific heat of LFP cells.

	Run 1	**Run 2**	**Run 3**	**Run 4**	**Run 5**	**Run 6**	**Run 7**	**Run 8**
Number of cells	1	1	1	3	3	3	6	7
Masses								
Mass of sample, inc. Al tape and heater (kg)	0.047	0.047	0.047	0.129	0.129	0.129	0.247	0.292
Mass of heater (kg)	0.006	0.006	0.006	0.006	0.006	0.006	0.006	0.006
Mass of sample, cells and tape (kg)	0.041	0.041	0.041	0.123	0.123	0.123	0.244	0.286
Total mass of cells (kg)	0.041	0.040	0.040	0.122	0.121	0.122	0.243	0.283
Mass of Al tape (kg)	0.000	0.000	0.000	0.001	0.002	0.002	0.001	0.003
Heater data								
Voltage (V)	11.969	11.969	11.969	11.969	11.969	11.969	11.969	11.969
Current (A)	0.096	0.096	0.096	0.096	0.096	0.096	0.096	0.096
Power (W)	1.145	1.145	1.145	1.145	1.145	1.145	1.145	1.145
Sample temperature rate								
Rate (K/min)	1.493	1.504	1.570	0.510	0.514	0.516	0.283	0.272
Rate (K/s)	0.025	0.025	0.026	0.009	0.009	0.009	0.005	0.005
Specific heat calculation								
C_p Al tape (J/kg K)	913	913	913	913	913	913	913	913
C_p sample, inc Al tape, exc. heater (J/kg K)	1124	1119	1073	1095	1086	1081	996	883
C_p cell (J/kg K)	1126	1120	1074	1097	1088	1083	996	883

A summary of the calculated specific heats of the cells ($C_{p,cell}$) is presented in Fig. 4.2. This figure shows the mean $C_{p,cell}$ values and standard deviation for samples constructed of 1 and 3 cells, which have been repeated 3 times, and the single values of $C_{p,cell}$ calculated for samples containing 6 and 7 cells. From this figure it can be seen that, as the number of cells in the sample increases, the calculated $C_{p,cell}$ reduces. The difference between $C_{p,cell}$ values of samples with 1 and 3 cells is slight, with the $C_{p,cell}$ of 3 cell sample within the variation of the 1 cell sample. However, the $C_{p,cell}$ values for the 6 and 7 cells samples are significantly lower than the 1 and 3 cell samples.

The low $C_{p,cell}$ of 6 and 7 cell samples are attributed to the fact that the heat conduction surfaces are minimal between cells. As such, in the 7 cell sample, where the central cell has the heater applied to it and the thermocouple attached to the opposite side of the same cell (see Fig. 3.4), the thermocouple heats up at a faster rate than a solid block the same mass of the sample and C_p would. Similar behaviour is thought to occur in the 6 cell sample, in which the thermocouple is place on a cell opposite the heater attached to the neighbouring cell (see Fig. 3.4), however to a lesser extent due to the minimal contact of the heater with the cell that the thermocouple is attached to. In these cases the cell and hence the thermocouple temperature are recorded at a greater rate than the overall sample. Inherently, as a larger temperature rate implies a lower specific heat value, where all other things are equal, the $C_{p,cell}$ of 6 and 7 cells samples are significantly lower than 1 and 3 cell samples. With this, it is recommended that the one cell sample method is the most appropriate way to measure cell specific heat capacity. As such, from the mean values of the 1 cell sample tests, the LFP cells in question are quoted to have a $C_{p,cell} = 1107\text{kJ/kg K}$. Although the 1 cell sample is recommended as being the most appropriate method to determine $C_{p,cell}$, the utilization of a 1 W heater results in the heating of the cell up to the maximum allowable within approximately 20 min. Hence, it is further recommended that the heater power is scaled such that the test lasts approximately 60 min in order to reduce fluctuations in the temperature rate and to gather more data points.

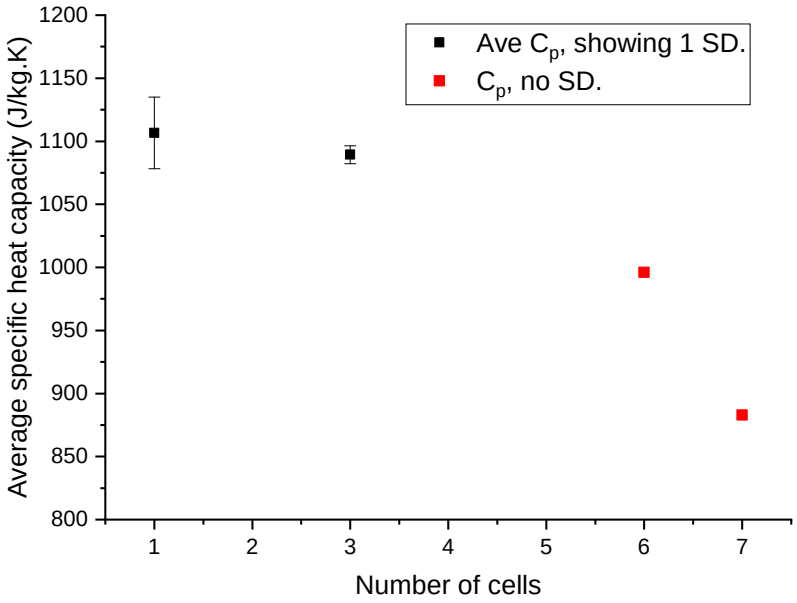

Figure 4.2: Comparison of calculated specific heat capacity of LFP cells depending on number of cells in sample. Standard deviation (SD) of specific heat capacity shown for sample sizes of 1 and 3 cells.

4.2.2 Accelerated Rate Calorimetry

The cell surface temperature vs. time plots of the ARC experiment results are presented in Fig. 4.3. The sub-figures Figs. 4.3(a), 4.3(c), 4.3(e), 4.3(g) and 4.3(i) present the full range of data, from initiating the test until the end of the test at the 315°C cut-off temperature. The sub-figures Figs. 4.3(a), 4.3(c), 4.3(e), 4.3(g) and 4.3(i) relate to cells charged to 100%, 0%, 28%, 63%, 110% SOC, respectively. Enlargements of the period of time over which venting occurs for each SOC, 100%, 0%, 28%, 63%, 110%, are presented in Figs. 4.3(b), 4.3(d), 4.3(f), 4.3(h) and 4.3(j), respectively. Throughout Fig. 4.3, the notation of R1, R2, R3, etc. in the figure key, is used to denote the individual test runs at each SOC. Hence, each individual test run can be uniquely identified by stating, for example, "run 28%-R2" referring to run 2 of the 28% SOC data.

This same data is also presented in temperature rate vs. temperature plots, as in Fig. 4.4, which normalises the data allowing for better comparison between experimental runs. Figure 4.4 presents the temperature rate vs. temperature data for the exothermic regions (where the ARC is operating in exotherm mode) of the T *vs.*t data of Figs. 4.3(a), 4.3(c), 4.3(e), 4.3(g) and 4.3(i).

It should also be noted that all cells, regardless of SOC, remained intact up to 315°C. This implies that, with operational cell vents, the rate of gas generation was not great enough to lead to a build up of internal cell pressure that could cause the cell case to fracture (on inspection by the naked eye) or explode.

By comparing runs for a given SOC in Fig. 4.3, it appears apparent that there is significant variation between results. However, due to the temperature dependence of the reactions, it is more informative to compare runs on a temperature rate vs. temperature basis, see Fig. 4.4. It can be seen from Fig. 4.4 that, given a cell's SOC, there is an overall agreement between the temperature rate of different experimental runs. Further, to validate the results, a comparison between the data gathered here to that of comparable LFP cells is made. This is shown in Fig. 4.5 for cells at 100% SOC. As can be seen from Fig. 4.5, there is good agreement between literature sources and the results found here, for the magnitude and profile of reaction rate up to approximately 250°C. After this temperature differences are seen between the literature values, however the results found here are between the literature findings. As such, considerable confidence in the ARC results presented herein is upheld, and further analysis presented.

From Fig. 4.3 it can be seen that, in almost all the runs, upon the detection of a cell's exothermic behaviour the ARC remains in exotherm mode. This can be seen for example in run 100%-R4 of Fig. 4.3(a). In which, after the stepwise behaviour of temperature (during the HWS period), in the time up to 15 h, no more step increases in temperature occur. Exceptions to this do occur, i.e. 100%-R6 (approximately at 36 h, see Fig. 4.3(b)), 0%-R1/R4 (R1, approximately at 30 h; R4, several instances after 30 h, see Fig. 4.3(d)), 28%-R2 (approximately at 19 h, see Fig. 4.3(e)) and 110%-R1/R2 (approximately at 12 h to 20 h, see Fig. 4.3(i)). These additional instances of HWS steps are indicated on Fig. 4.3 by "HWS step".

For the cells at 0% SOC, the additional HWS steps occur over a relatively large period of time, and in the case of 0%-R4, there are several additional periods of time when this occurs. The cause of the additional HWS periods is attributed to the high stability of the cells when discharged. Where the low reactivity of the cell leads to little heat generation and very low temperature rates below the defined 0.02°C/min onset value. For the occurrences of step increase in temperature in the cells at 28% SOC and 100% SOC, there is only a single additional HWS step, rather than a period of several steps as in the 0% SOC example. Looking at the region over which the HWS step occurs, i.e. 100°C–110°C, for the 28% SOC occurrence, we can see from Fig. 4.4(e) that over the temperature range the rate follows the same trend as the other runs. Hence, the HWS step is treated as an anomaly. In the 100% SOC occurrence, the single HWS step occurs after the instance of venting. For 100%-R6, the temperature reduction due to venting is small compared to other runs, e.g. 100%-R1. For similar small temperature reductions on venting, i.e. 100%-R5 and 110%-R3, a reduction in rate and plateau (indicated on Fig. 4.3) in the temperature is seen, see Figs. 4.3(b) and 4.3(i) respectively. This plateau is attributed to additional vent gas being slowly released and cooling the cell. Hence, given the comparable profiles of 100%-R1/R5 and 110%-R3, the additional HWS step of 100%-R1 is thought to be negligible. In the case of the 110% SOC occurrences, the additional HWS steps occur after an earlier onset of self-heating (compared to 100% SOC cells), due to the reduced

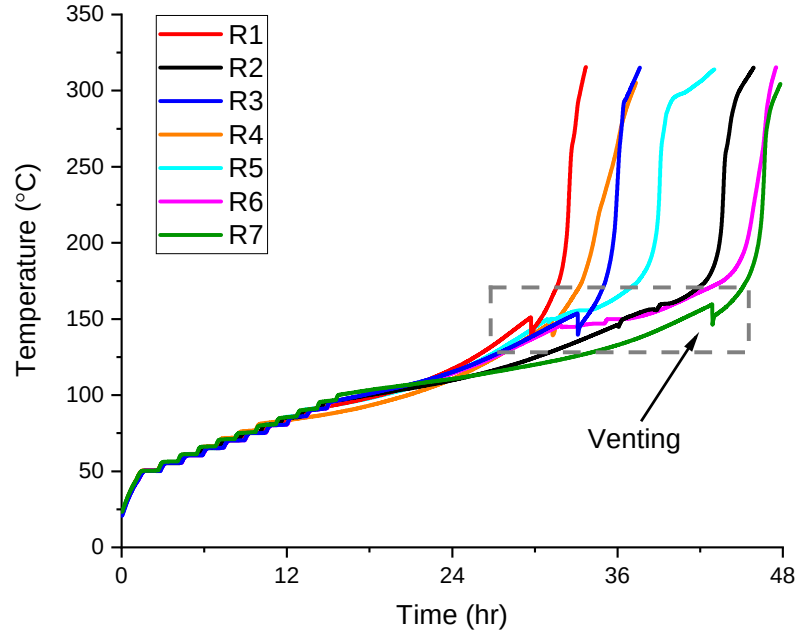

(a) 100% SOC - all time

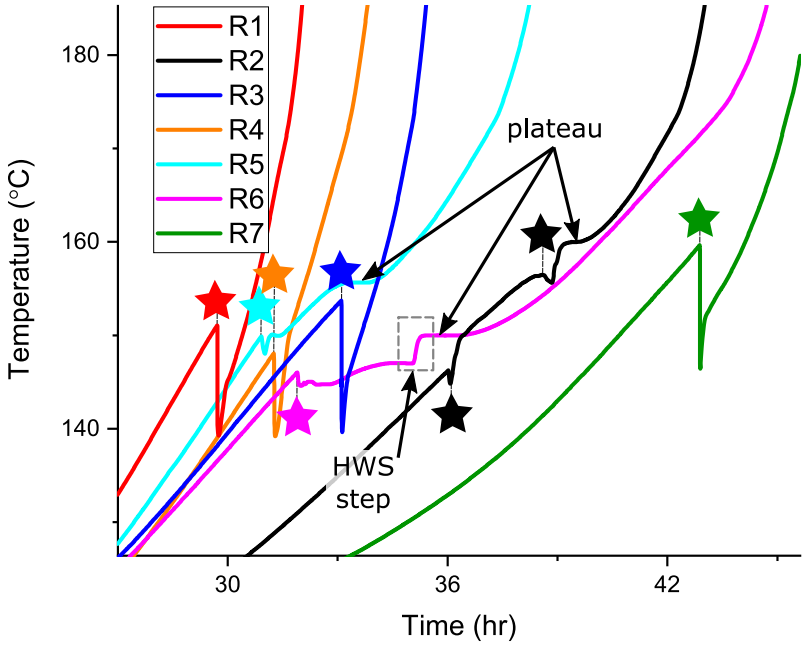

(b) 100% SOC - venting

Figure 4.3: ARC temperature vs. time plots for cells at different SOC. The dashed box on "all time" plots indicates the period over which venting occurs and is enlarged in the corresponding "venting" plots. Stars on venting plots indicated individual venting events for each run.

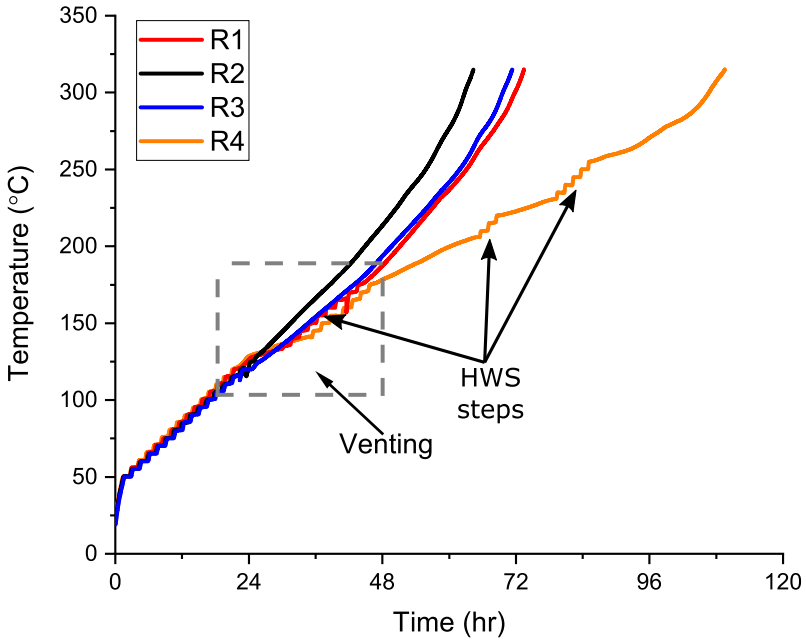

(c) 0% SOC - all time

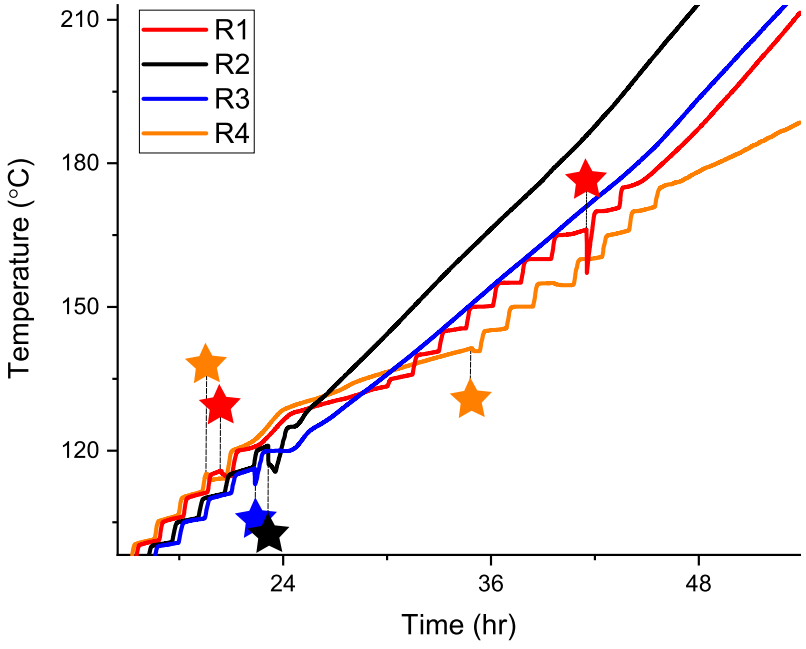

(d) 0% SOC - venting

Figure 4.3 (cont.): ARC temperature vs. time plots for cells at different SOC. The dashed box on "all time" plots indicates the period over which venting occurs and is enlarged in the corresponding "venting" plots. Stars on venting plots indicated individual venting events for each run.

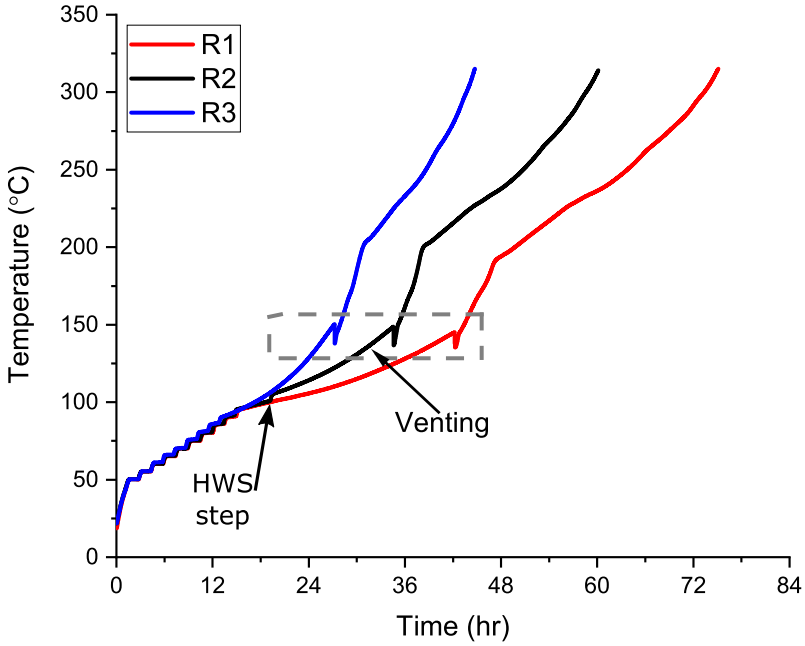

(e) 28% SOC - all time

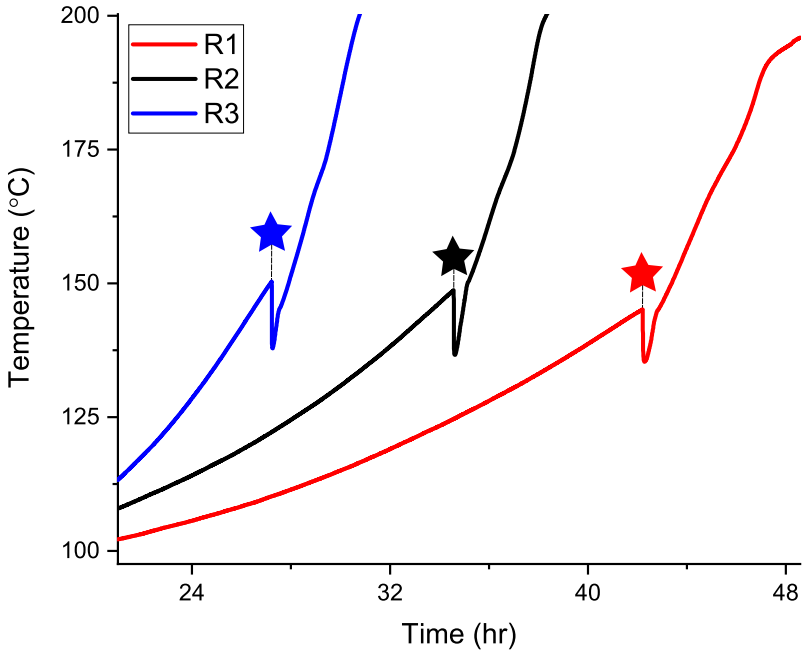

(f) 28% SOC - venting

Figure 4.3 (cont.): ARC temperature vs. time plots for cells at different SOC. The dashed box on "all time" plots indicates the period over which venting occurs and is enlarged in the corresponding "venting" plots. Stars on venting plots indicated individual venting events for each run.

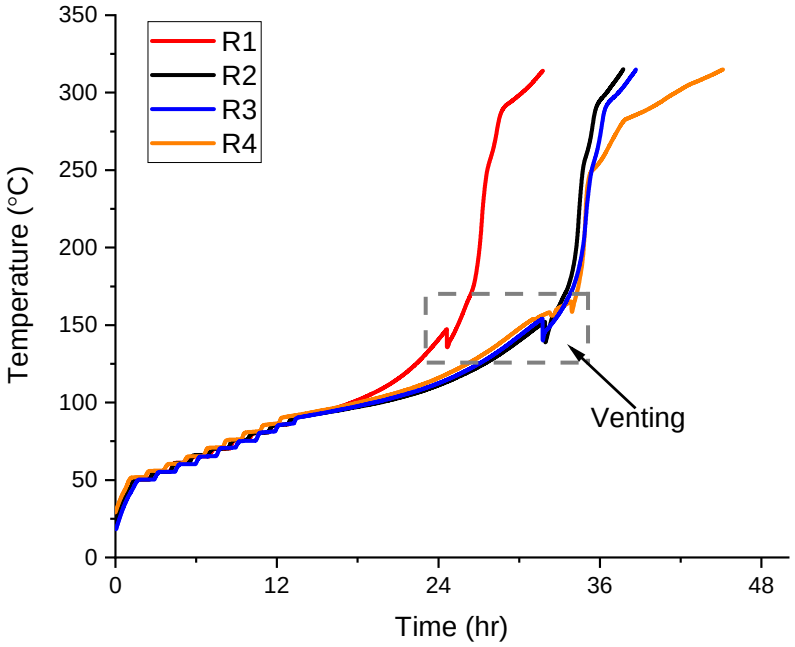

(g) 63% SOC - all time

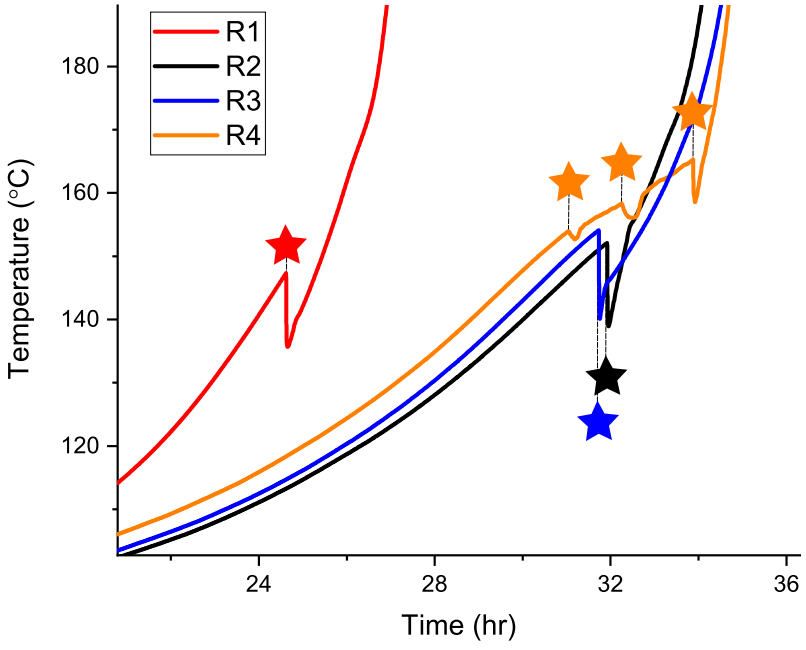

(h) 63% SOC - venting

Figure 4.3 (cont.): ARC temperature vs. time plots for cells at different SOC. The dashed box on "all time" plots indicates the period over which venting occurs and is enlarged in the corresponding "venting" plots. Stars on venting plots indicated individual venting events for each run.

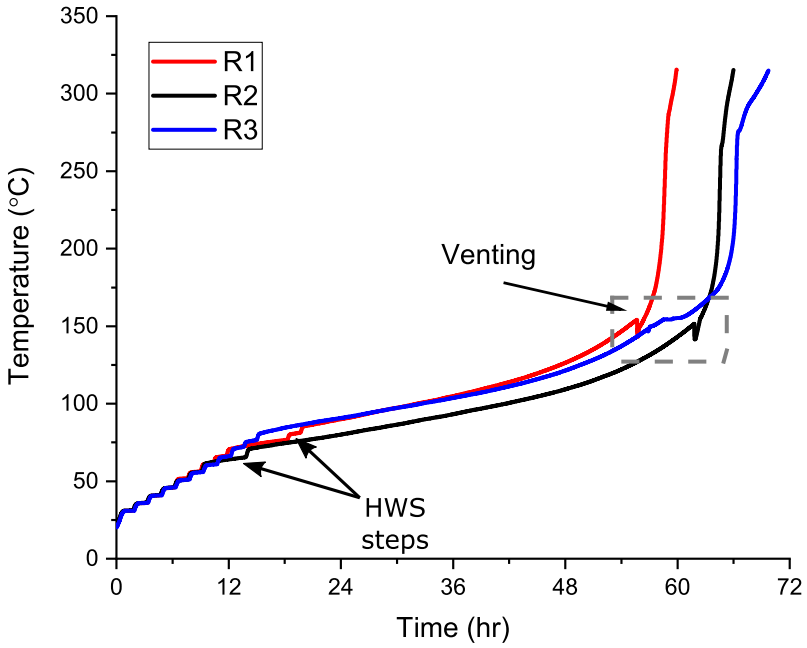

(i) 110% SOC - all time

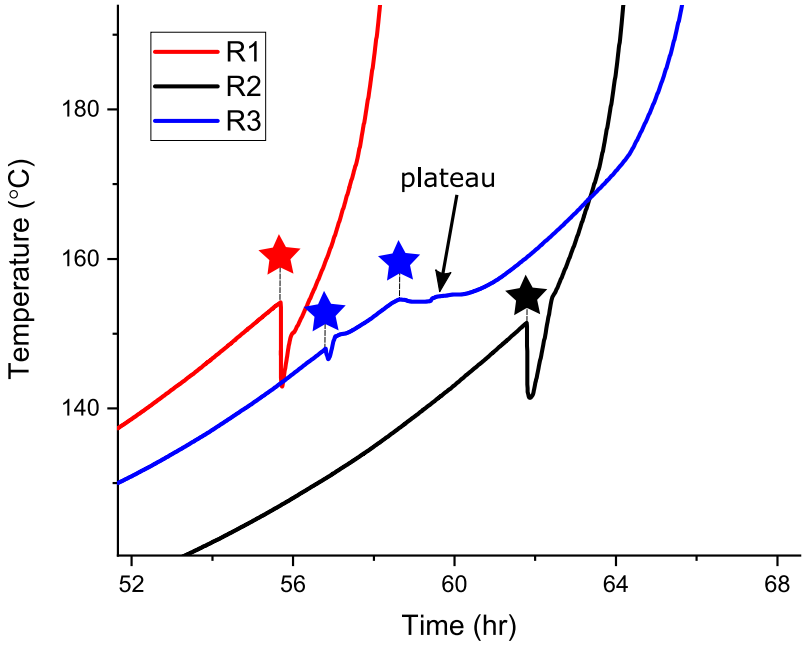

(j) 110% SOC - venting

Figure 4.3 (cont.): ARC temperature vs. time plots for cells at different SOC. The dashed box on "all time" plots indicates the period over which venting occurs and is enlarged in the corresponding "venting" plots. Stars on venting plots indicated individual venting events for each run.

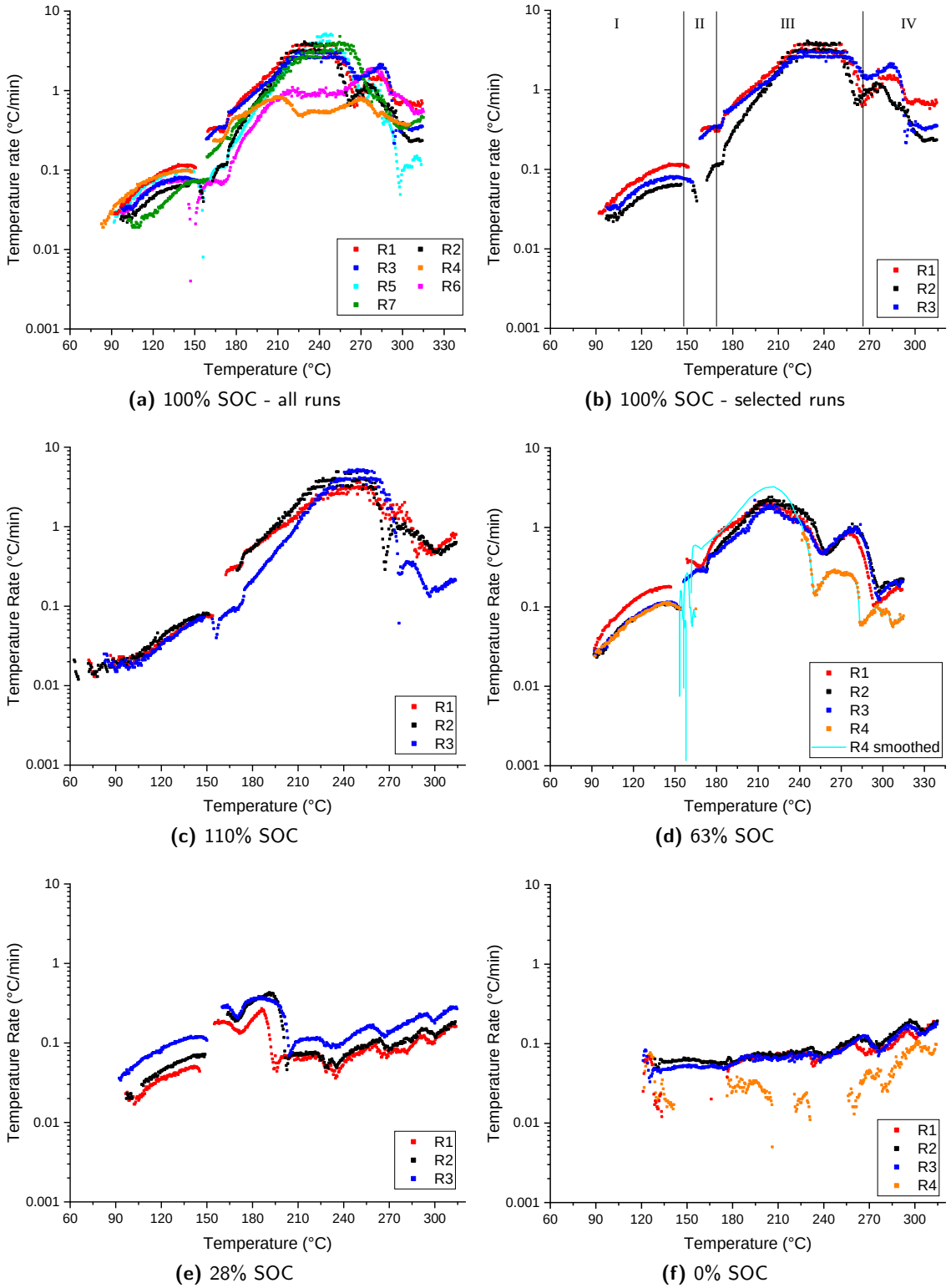

(a) 100% SOC - all runs

(b) 100% SOC - selected runs

(c) 110% SOC

(d) 63% SOC

(e) 28% SOC

(f) 0% SOC

Figure 4.4: Cell surface temperature rate against cell surface temperature from exothermic period of HWS test for various SOC (note logarithmic scale on y-axis). Regions I-IV in sub-figure (b) indicate stages of self-heating.

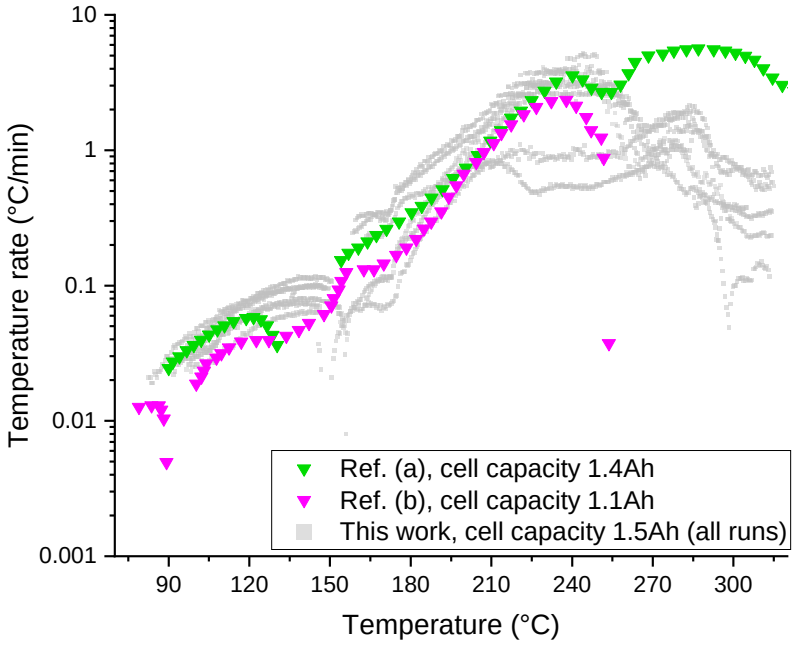

Figure 4.5: ARC results of LFP 18650 cells at 100% SOC compared with literature (Ref. (a): [153], Ref. (b): [171]).

stability of the cell from overcharging. Hence, the additional HWS step lead to heating the cell between the unstable Li metal reaction and the onset of the SEI reaction.

Figure 4.3 also shows that cell venting occurs in all cases, leading to various scales of temperature loss. In many cases, excluding 0% SOC cells, a single venting event leading to a 10°C to 15°C temperature loss occurs. For cells at 0% SOC, when single temperature loss is seen it is on the order of 3°C to 5°C. For runs in which an initial small loss of temperature occurs upon venting, typically further small venting events or plateau(s) in temperature occur. The total loss of temperature for each run and the average temperature drop for each SOC is shown in Fig. 4.6. As can be seen from Fig. 4.6, there is a significant amount of variation in the venting behaviour, more so than the rate behaviour. Figure 4.6 also shows that there are runs for the 100% and 110% SOC cases that have significantly smaller temperature drops, skewing the mean temperature drops at these SOC to be significantly lower than at 28% and 63% SOC.

As stated above, and referring to Fig. 4.4, for a given SOC the temperature rate behaviour is similar for all runs. However, notable variations are present between runs in the 100%, 63% and 0% SOC results, see Figs. 4.4(a), 4.4(d) and 4.4(f) respectively. ARC test on cells at 100% SOC have been repeated 7 times. From Fig. 4.4(a), it can be clearly seen that runs 4 and 6 do not show the same maximum rate (at approximately 240°C) as the other runs. Further, runs 5 and 7 show a slightly higher and delayed peak reaction rate when compared to runs 1-3. This shows there is variation in abuse behaviour within commercially manufactured cells. In later discussions only runs 1-3 are considered as they represent the most common profiles, this allows for a clear understanding and presentation

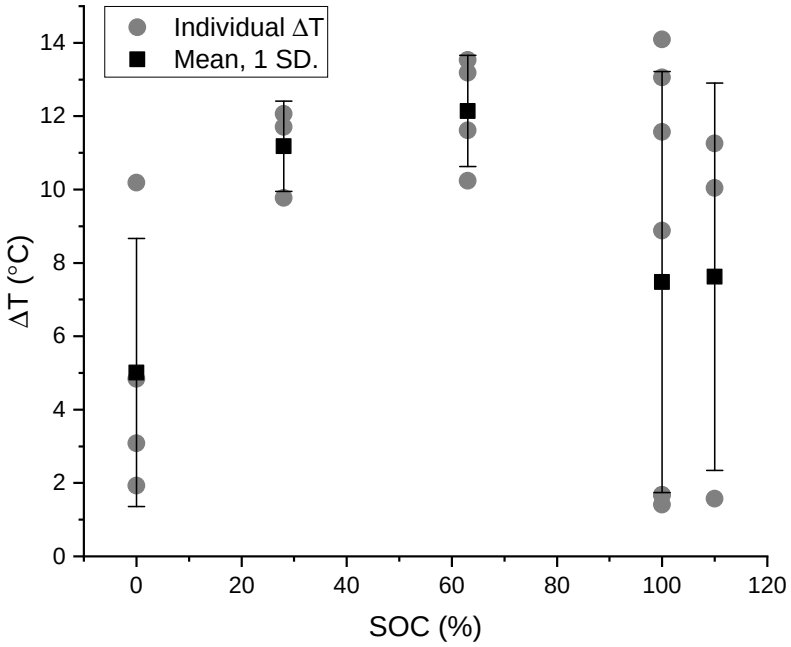

Figure 4.6: Temperature loss of cells upon venting due to thermal abuse in ARC experiments.

of results. Further, runs 63%-R4 and 0%-R4 are excluded from further discussion. With regard to run 63%-R4, the ARC instrument did not detect the exotherm between 150°C and 240°C. A smoothed plot of the temperature rate determined from the full data series within this region is presented in Fig. 4.4(d). This shows the maximum rate reached was greater, while after 240°C the rate is lower than runs 63%-R1\2\3. As for run 0%-R4, the broken temperature rate plot and the relatively low temperature rate is due to the relatively slow and non-self-sustaining reaction. Hence, similar to the 100% SOC case, only runs R1-R3 are considered for further analysis for both the 63% and 0% SOC cases.

Figure 4.4(b) shows the results of cells at 100% SOC and will be discussed first as a benchmark to compare the results at other SOC. It can be seen from Fig. 4.4(b), that from the onset of self-heating at 95°C, the temperature rate increases up to the maximum temperature rate of 3.7°C/min (value determined from the average of the maximum temperature rates of the three runs) at ~230°C, where after, the temperature rate generally reduces with increasing temperature until the end of the experiment (315°C). A secondary peak of 1.6°C/min is seen at 280°C. From Fig. 4.4(b), we see that the cells' temperature behaviour can be further split into 4 distinct regions, determined by inspection (also depicted in Fig. 4.7 which, for visual clarity, compares a single ARC temperature rate plot from each SOC that is most representative of the average behaviour at each respective SOC): (I) first exotherm - containing self-heating onset to venting; (II) endothermic event - attributed to the expansion of the venting gases cooling the cell (and is seen in the as a break in the data points as the ARC exits exothermic mode); (III) second exotherm - containing the first peak temperature rate; (IV) third exotherm - containing the second peak temperature rate.

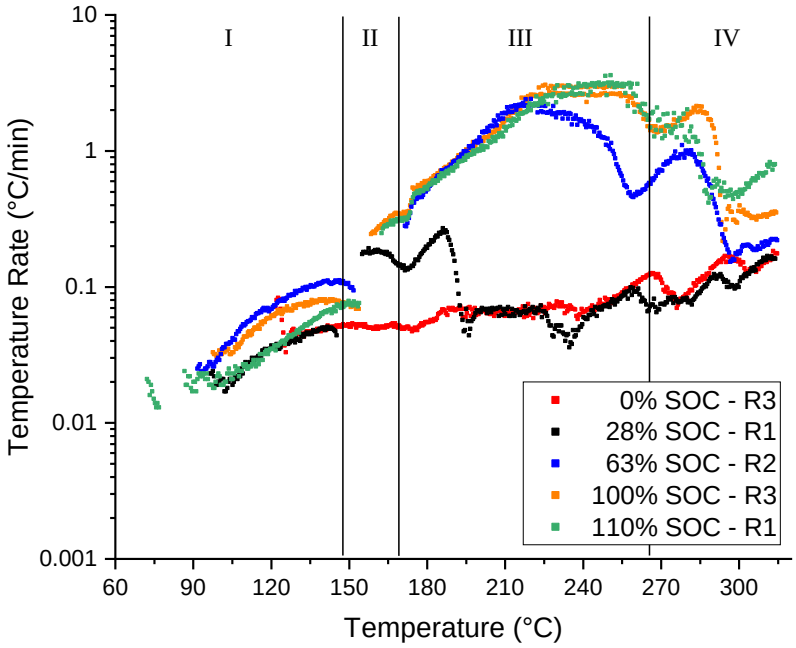

Figure 4.7: Comparison of temperature rate for cells at different SOC under ARC testing. Regions: (I) first exotherm - containing self-heating onset to venting; (II) endothermic event - due to venting; (III) second exotherm - containing the first peak temperature rate; (IV) third exotherm - containing the second peak temperature rate.

From the temperature rate plot in Fig. 4.4(b), and referring to the onset temperature of the individual reactions from the literature (see Table 2.2), relevant reactions can be associated with each region. The first exotherm in region (I), over the range of 95–150°C can largely be attributed to the solid electrolyte interphase (SEI) reaction, with an increasing contribution from the negative electrode-solvent (NE) reaction at higher temperatures. The second exotherm in region (III), over the range of 150–255°C is due to the NE and positive electrode-solvent (PE) reactions. The NE reaction generates the most heat overall, on the scale of an order of magnitude greater than the PE reaction (see Table 2.1), and therefore dominates the temperature rate profile in this region. The final exotherm in region (IV), at >255°C, is due to the increased contribution of the decomposition reaction of the electrolyte with oxygen evolved from the decomposition of the LFP.

From Fig. 4.4(c) and Fig. 4.4(d), it can be seen that the temperature rate profiles at 110% and 63% SOC respectively are similar to that at 100% SOC. However, as can be seen in Fig. 4.7, there are two distinct differences when comparing the results from these three different SOC with regard to regions (III) and (IV): (1) the magnitude and position of the absolute peak temperature rate, and (2) the magnitude and position of the second temperature rate peak.

With regard to Item (1) and referring to Fig. 4.8, which shows the absolute maximum cell temperature rates, the temperature at which the absolute maximum rates occur and self-heating onset temperature for a given SOC (mean and standard deviation of runs 1-3),

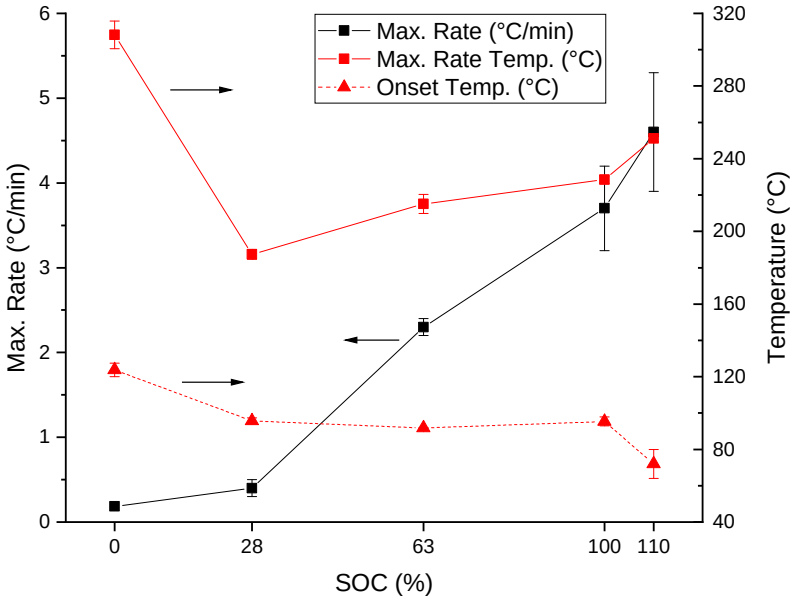

Figure 4.8: Maximum rate at given SOC with the corresponding temperature that the maximum rate occurs at; and onset temperature of first exotherm (Note: error bars are equal to one standard deviation).

it can be seen that as SOC increases the absolute peak temperature rate also increases. This occurs due to the greater amount of energy stored and the resulting increased instability of the electrodes at higher SOC, particularly in the negative electrode due to more lithium being available in the intercalated carbon to react with the binder, filler and electrolyte at higher temperatures [166]. This behaviour can also explain Item (2), as more heat generated by the NE and PE reactions over a larger temperature range at 110% SOC, thus leading to a greater overlap between these two reactions and the electrolyte reaction, and hence a summation of their heat generation rates. This in turn reduces the distinction between the 1st and 2nd peak temperature rates leading to an increase in the overall peak rate. Conversely, at 63% SOC, the increased stability of the electrodes leads to less heat being produced over a smaller temperature range which in turn increases the separation between the 1st and 2nd peak rates. Additionally, the reduction in the 2nd peak temperature rate at 63% SOC compared to that at 100% SOC can be somewhat attributed to (1) the likelihood of less oxygen being available to fuel the electrolyte reaction as the positive electrode will have decomposed less, releasing less oxygen; and (2) the reduced contribution of the NE and PE reactions at higher temperature to the overall heat generated.

Figure 4.4(e) presents the ARC results at 28% SOC and shows the temperature rate increases from onset until a peak at ~190°C whereupon the rate drops. Between 200°C and 225°C, the temperature rate is relatively constant, while after 225°C the temperature rate slowly increases. The behaviour in regions (I) and (II) is comparable to that for the 100% SOC, see Fig. 4.7. However, the peak temperature rate in region (III) for the 28% SOC case occurs at a much lower temperature (~190°C) than at higher SOC and is present

over a smaller temperature range. These characteristics suggest that the NE reaction is the main contributing factor to the self-heating peak, as the NE reaction is more unstable and energetic at lower SOC than the PE reaction. The behaviour beyond 200°C is due to the decomposition of the PE and electrolyte reactions; however, due to the stability of the cathode, these reactions do not occur at a significant rate.

Finally, Fig. 4.4(f) presents the ARC results at 0% SOC and shows the temperature rate is relatively low across all temperatures with a slight trend of increased rate with temperature. The initial heating in region (I) is comparable to that of the other SOCs, see Figure 4.7, with the exception of a delay in the onset temperature. The peak temperature rate at ~190°C that occurs in the 28% SOC is no longer present, while after 200°C the temperature rate is similar to that in the 28% SOC case. The loss of the temperature rate peak at ~190°C is consistent with the electrodes being in their most stable state and, with the negative electrode being fully delithiated, the NE reaction only occurs at a slow rate. As the cell is fully discharged, the heating from the PE electrode will be negligible [126]. Additionally, as the discharged PE electrode will also have released very little O_2, the electrolyte reaction will be limited, but might be facilitated by O_2 entering from the open vent [95]. The factors causing the delayed onset are discussed later.

As stated previously, from Fig. 4.8 we can see that, at increased SOC, the maximum temperature rate during TR is greater. Further, disregarding 0% SOC (because there is no distinct peak in the temperature rate plot of Fig. 4.4(f)), the temperature at which these peak rates occur increases with SOC. However, it can also be seen that the increase in temperature rate is not linear, with a proportionally greater increase in maximum temperature rate over the range of 28%–100% SOC than 0%–28% SOC, and greater still over the range of 100%–110% SOC. Similar behaviour is seen by Refs. [118, 155] in the study of $LiCoO_2$ and $LiMn_2O_4$ cells, as shown in Fig. 4.9. This behaviour is related to the amount of energy stored, the stability of a given reaction at a given SOC and the extent to which reactions occur simultaneously. In other words, as SOC increases there is greater electrochemical potential energy that leads to higher reaction rates and more heat generation, while the resulting greater heat generation leads to larger temperature increases and hence the occurrence of more energetic reactions that only occur at higher temperatures in turn leading to peak reaction rates occurring at higher temperatures. As the maximum temperature rate is directly related to the maximum heat generation rate, it therefore is a good quantity by which to quantify safety, as one can use the maximum temperature rate at different SOC to predict the risk of TR at different SOC.

Figure 4.9 compares the maximum temperature rate at different SOC from the results in this work to that of different chemistries from the literature. Considering the 100% SOC case, it can be clearly seen that LFP cells have a significantly lower maximum temperature rate, of around 3 orders of magnitude lower, and hence are significantly safer than the other chemistries. Indeed, even at low SOC, LFP is significantly less reactive than LCO

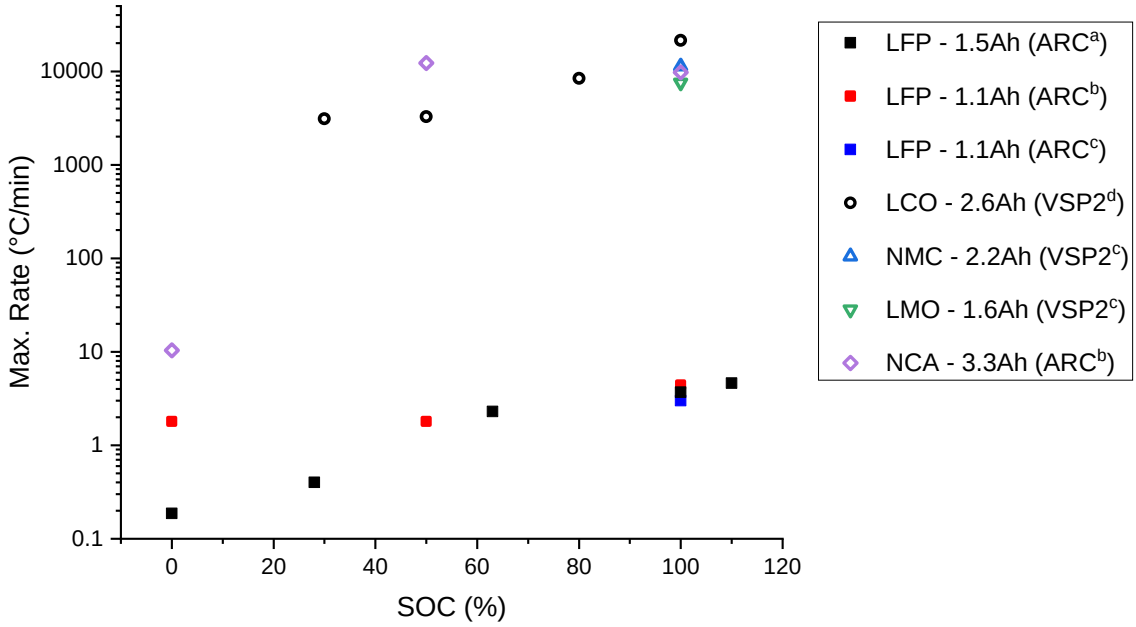

Figure 4.9: A comparison of maximum temperature rates at given SOC for 18650 cells of different chemistries, nominal capacities at 100% SOC are given. [a]This work. [b][88]. [c][171]. [d][118].

cells. Readers should note the different energy densities of the cells compared. The higher energy densities (2.2–3.3 Ah) of the NMC, LCO and NCA cells from the literature makes direct comparison difficult against the LFP (1.5 Ah) studied here. However, as the LMO literature case with a capacity of 1.6 Ah clearly shows, it is not the amount of energy available within a cell that is the major concern for maximum temperature rate, but the cell's chemistry and the resultant reaction rates of its components.

Figure 4.8 also shows the relationship between onset temperature and SOC. Between 28% and 100% SOC, there is little difference in the onset temperature which occurs between 92–96°C. However, at 0% SOC and 110% SOC, there is a significant delay (127°C) to and advance (67°C) of, respectively, the onset temperature. The delay to onset at 0% SOC suggests that there is a reaction other than the SEI decomposition contributing to the onset of self-heating in region (I) of Fig. 4.7 for cells at higher SOC. This is because, once formed, the SEI layer is metastable [209, 261] and hence would decompose and produce the same amount of heat irrespective of SOC. Under the assumption of a four reaction system, this suggests that the lithiation of the negative electrode at SOC $\geq$28% causes a reduction in the onset temperature. To the author's knowledge, this is the first report of the negative electrode to be the trigger of thermal runaway. This offers the opportunity to design batteries where electrodes are thermally decoupled.

The mechanism that advances the onset temperature at 110% SOC is easily identified. Upon overcharge, lithium is irreversibly removed from the cathode and deposited on the surface of the anode. Upon heating, the delithiated cathode and/or the deposited lithium metal leads to reduction of the electrolyte at relatively low temperatures, below that of the

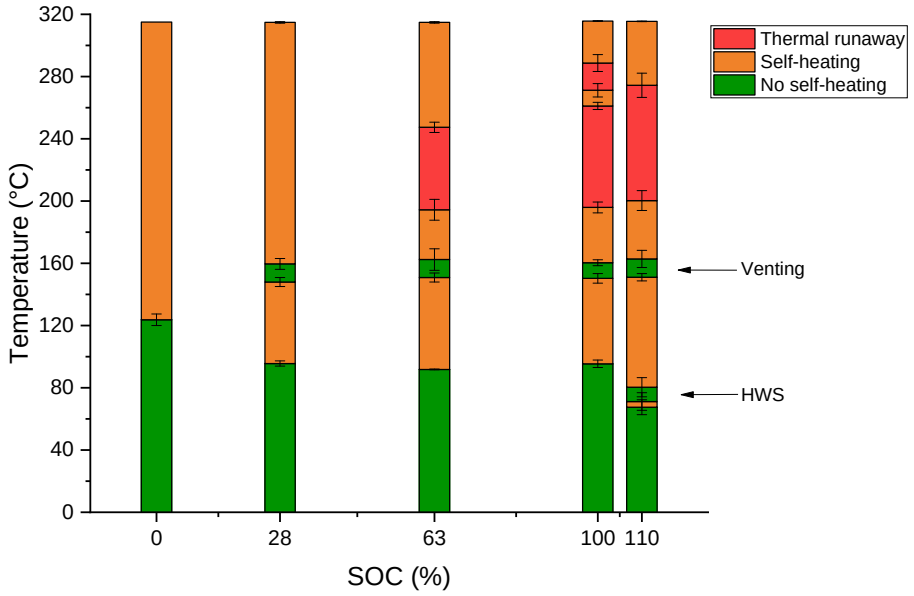

Figure 4.10: Thermal mapping as a function of SOC. No self-heating when temperature rate is <0.02°C/min, self-heating when temperature rate is >0.02°C/min, and thermal runaway when temperature rate is >1°C/min. (Note: error bars are equal to one standard deviation.)

NE or SEI reactions and hence leads to a reduction of the onset temperature of self-heating [92, 176, 262].

Figure 4.10 presents a thermal map of the ARC data from Fig. 4.4 (mean and standard deviation of runs 1-3 for each SOC), and in this format allows for an easier assessment of the TR processes at different SOCs. The green region represents the temperatures over which no detectable self-heating occurs and the ARC is operating in HWS mode. There is an exception at approximately 150°C, due to the cooling of the cell by vented gases which dissipates more heat than is generated by the decomposition reactions. The orange and red regions of Fig. 4.10 relate to when the ARC is in exothermic mode. The orange region indicates when a cell is undergoing detectable self-heating. That is to say, when a cell is increasing in temperature at a rate ≥0.02°C/min and <1°C/min. Where 0.02°C/min is set as the detection limit when carrying out the HWS procedure. The red region indicates when a cell is undergoing TR, i.e. where self-heating leads to temperature rates ≥1°C/min. A cell can go from self-heating to TR and back to a self-heating region as the temperature rates pass through the limits mentioned previously.

As can be seen from Fig. 4.10, the venting of gases at 150°C only occurs in cells of 28–110% SOC, with the exception of run R1 of 0% SOC. It can be assumed that venting does not occur at 0% SOC due the stability of the cell, leading to little decomposition of the electrodes/electrolyte and hence little gas production. Also, once self-heating has been initiated, the reactions are self-sustaining up to the ARC cut off temperature. This is evident of no further HWS procedure being carried out by the ARC from the onset of self-heating until the end of the test. This is excluding the 110% SOC case, where for runs R1 and R2 there is an initial self-heating reaction at ~67°C due to the lithium

plating decomposition reaction [92, 176, 262] before self-sustaining self-heating is initiated at ~75°C. At 110% SOC the onset temperature of self-heating is therefore 75°C. This is still lower than the other SOC cases. Hence, overcharge is still a cause of reduced stability and therefore a safety concern in LFP cells. Analysis of the TR region, indicated in red in Fig. 4.10, shows that at 28% SOC and below TR does not occur, while in all other cases TR occurs at temperatures >200°C. As TR onset occurs at temperatures at approximately 200°C, and the NE reaction onset occurs at temperatures as low as 80°C while the PE reaction onset does not occur until 180°C (see Table 2.2), it implies that the NE reaction is the cause of TR initiation as the PE reaction will only have just initiated and have a negligible heating rate at this point. Hence, if the carbon anode self-heating onset can be postponed, then LFP cells can be stable to greater temperatures.

4.2.3 Oven Test

A record of all oven tests undertaken is presented in Table 4.4, including the cell number to uniquely identify each run, the corresponding oven set temperature, mean oven temperature ($\bar{T}_{oven}$) before and after maximum cell temperature, and observations about the thermocouples (TC) post test. Figure 4.11 presents, on individual sub-plots for each cell, the resulting cell surface temperatures at the positive and negative end of the cell as well as the oven temperature. The figures further present the cell surface temperature rates for each cell thermocouple and annotations indicating the maximum temperatures and temperature rates.

The $\bar{T}_{oven}$ before TR is calculated because, as Fig. 4.11 shows, there is an initial drop in the oven temperature before returning to the oven set temperature sometime later. The temperature drop is due to cooling during oven chamber access. This means that, even though the cells are placed into a preheated oven, the oven set temperature is not precisely the temperature experienced by the cell. However, as the oven temperature is recorded independently, an accurate reading of the oven temperature is obtained and only varies slightly between experimental runs (see Table 4.4). Additionally, as the heating of the cell prior to TR is most important to the behaviour of the TR event, the oven temperature the cell experienced is taken as the average oven temperature up to the occurrence of maximum cell surface temperature. The $\bar{T}_{oven}$ before TR is calculated from the time that the cell temperature rate is greater than 1°C/min up to the time at which the maximum cell temperature. The value of 1°C/min is selected as an indicator of the time at which the cell is put into the oven and started to be heated. This is done because, while the oven is preheated, the cell remains outside. At the point the oven set temperature is reached, the data recorder is set to record, and thereafter the cell placed in the oven. As such the initial data recorded, is of the cell while it is still outside of the oven. The mean temperature after TR is from the time of maximum cell temperature until the end of the test, i.e. at 90 min.

Table 4.4: Record of oven exposure tests.

Cell Nº.	Oven set temperature (°C)	Mean oven temp. before max. cell temp. (°C)	Mean oven temp. after max. cell temp. (°C)	Observation
02	200	190	199	-
03	220	210	219	loose -ve TC
04	180	170	180	-
08	220	-	-	oven TC touching cell
09	220	216	223	-
10	180	181	185	-
12	200	199	205	-
13	200	194	200	loose TCs
14	220	213	219	loose +ve TC
15	180	179	182	-
16	180	180	182	-
17	220	217	223	loose -ve TC
19	180	180	184	-
20	220	213	219	loose -ve TC
21	220	-	-	oven TC touching cell
22	220	217	225	loose -ve TC

After undergoing an oven test, visual inspection of the LFP cells, see Fig. 4.12, show that the cells remain intact even after a TR event has occurred and hence do not present an explosion risk. The only visible difference between the 180°C and 220°C oven temperature cases is that the higher oven temperature leads to a cell that has a greater area of darker discolouration around the cell vents. This is attributed to a greater amount of decomposition/combustible products being produced and expelled through the cell vents.

From the observations made of each cell after testing (see Table 4.4), it was noted that on several occurrences that a TC did not remain firmly attached to, and hence make good contact with, the cell. This occurred in cells 3, 14, 17, 20 and 22, which had 1 loose TC, while for cell 13, both TC came away from the cell surface. As can be seen from Figs. 4.11(b), 4.11(h), 4.11(i), 4.11(l), 4.11(n) and 4.11(p), the occurrence of loose TC leads to difference in temperature readings between the negative and positive TC. As can be seen from the aforementioned figures, the difference in recorded temperature occurs at or just before peak temperatures. Further, it can be seen from Table 4.4 that the instances of loose TC occur at high oven set temperatures (200°C or 220°C), leading to more severe TR events. Indicating that high temperatures can cause the affixed glass cloth tape to deform if not appropriately wound tight enough, and with enough wraps. However, as will be discussed in detail later, analysis can be still undertaken on these cells, focusing on the TC that is still firmly attached. On two occurrences (cells 8 and 21), the TC measuring the oven temperature was in contact with the cell, leading to erroneous readings of oven temperature. In these cases, as the oven temperature was measured inaccurately, as can

be seen from Figs. 4.11(d) and 4.11(o), the mean oven temperature before and after TR could not be calculated, and hence these cells are excluded from further analysis.

Inspecting the negative and positive temperatures for each cell in Fig. 4.11, it can be seen that, additional to the cells identified as having loose TC in Table 4.4, cells 2, 16 and 21 (Figs. 4.11(a), 4.11(k) and 4.11(o) respectively) also present different values between the negative and positive TC. This indicates that a TC also became loose on these cells during the test, however less so than those outlined in Table 4.4, such that it was not visibly noticeable. However, in Figs. 4.11(c), 4.11(d), 4.11(j) and 4.11(m) it can be seen that there is negligible temperature difference between the two thermocouples, this is true even when venting occurs. The uniform temperature over the cells surface is due to the high axial thermal conductivity of the steel cell can and copper and aluminium jelly roll windings. Following this, we can state that under uniform heating the cell has a near uniform surface temperature along its length before, during and after TR. As such, analysis can still be carried out on cells with a loose TC, taking the values recorded by the firmly attached TC as an accurate representation of the overall cell surface temperature. In turn, in all cases, analysis of maximum cell temperature, maximum cell temperature rate, time to maximum values and heat released are calculated for each cell from the TC with the largest maximum temperature reading.

As mentioned above, in the tests of cell 8 and 21, the TC is placed too close to the cell leading to inaccurate recordings of oven temperature. At the end of these tests the oven TC either records temperatures higher than the cell (see Fig. 4.11(d)), or equal to the cell temperature (see Fig. 4.11(o)). In all other cases, except cell 2, the oven temperature remains slightly or very noticeably below the cell temperature at the end of the test. However, in the case of cell 2, the oven temperature is greater than the cell at the end of the test, suggesting an inaccurate recording of the oven temperature.

The temperature rates, plotted in Fig. 4.11, are calculated from the temperature time data, by, first, filtering the data so that consecutive temperature values that are equal to each other are removed. This is done, as on a sampling rate of 100 ms with temperature recorded to an accuracy of two decimals places, there are many equal consecutive values. Hence, when the rate is calculated, these consecutive temperature values lead to zero rate values, while non zero rates are erroneously high. These erroneously high rates are due to fact a change in temperature is recorded over a short time instance (i.e. 100 ms), rather than the whole time period (i.e. >100 ms) from the first instance of a given temperature. From this filtered data the temperature rate is calculated using the "gradient" function in *MATLAB* [263]. The rate calculated herein varies slightly from that determined in Ref. [264]. In Ref. [264] the rate is determined on data down sampled to 1 s, while equal consecutive values are left in and the gradient calculated manually from the difference in consecutive temperature values over the difference in consecutive time values, and assigned to a time halfway between consecutive time values.

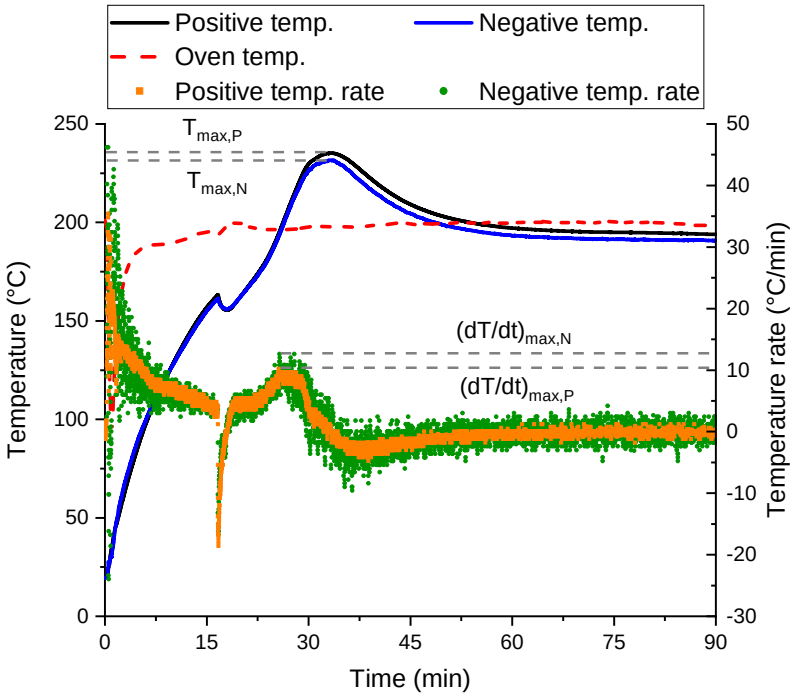

(a) Cell 02

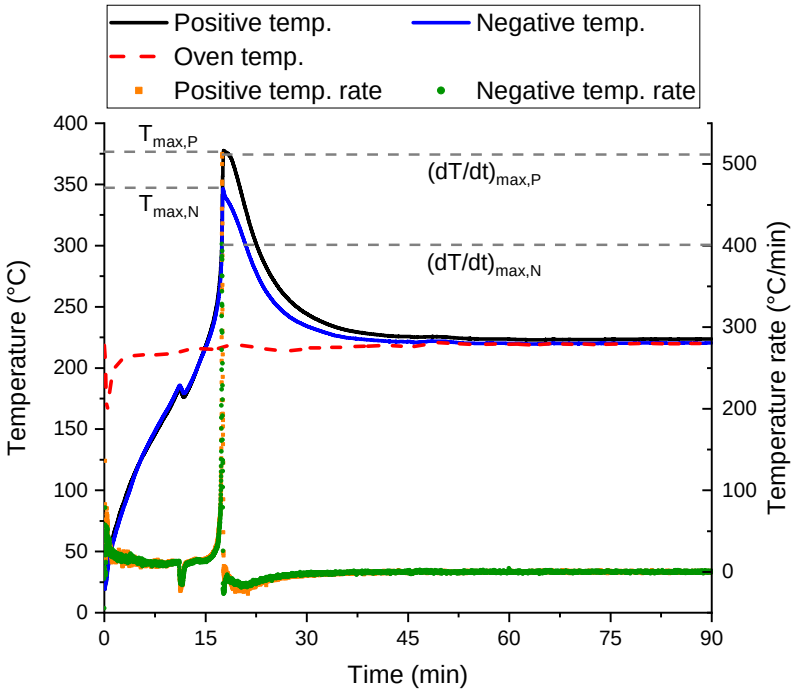

(b) Cell 03

Figure 4.11: Results of oven exposure tests, temperature and temperature rate vs. time, with maximum surface temperatures and maximum surface temperature rates indicated.

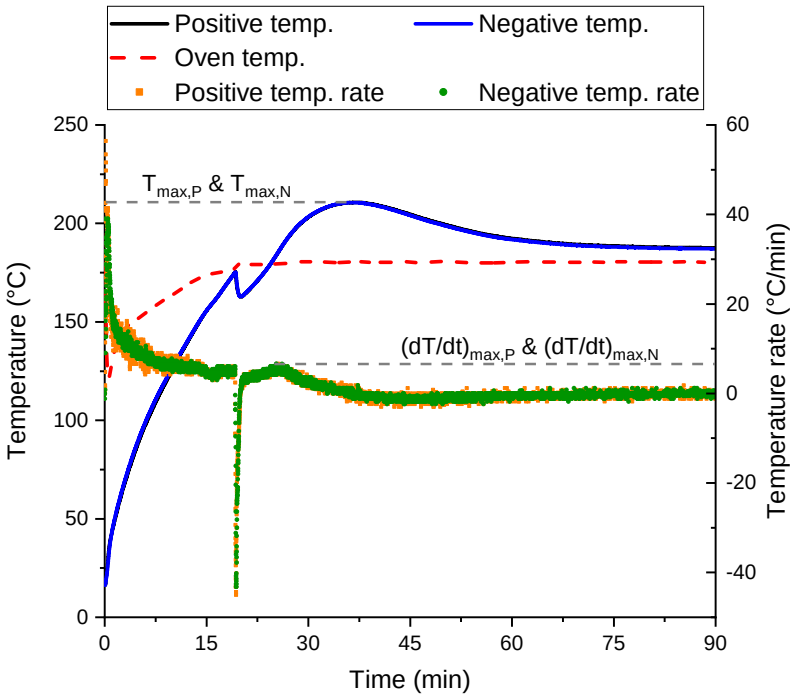

(c) Cell 04

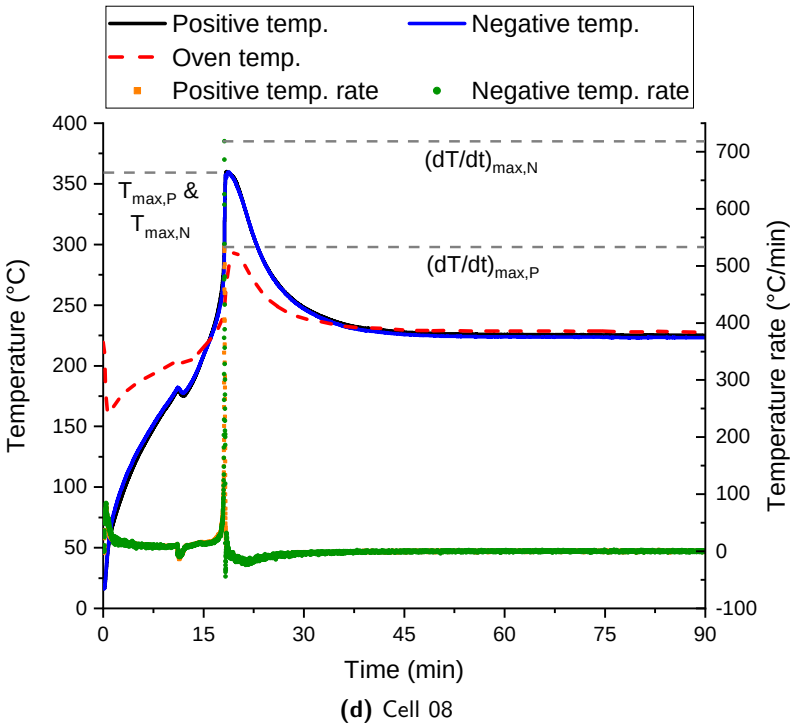

(d) Cell 08

Figure 4.11 (cont.): Results of oven exposure tests, temperature and temperature rate vs. time, with maximum surface temperatures and maximum surface temperature rates indicated.

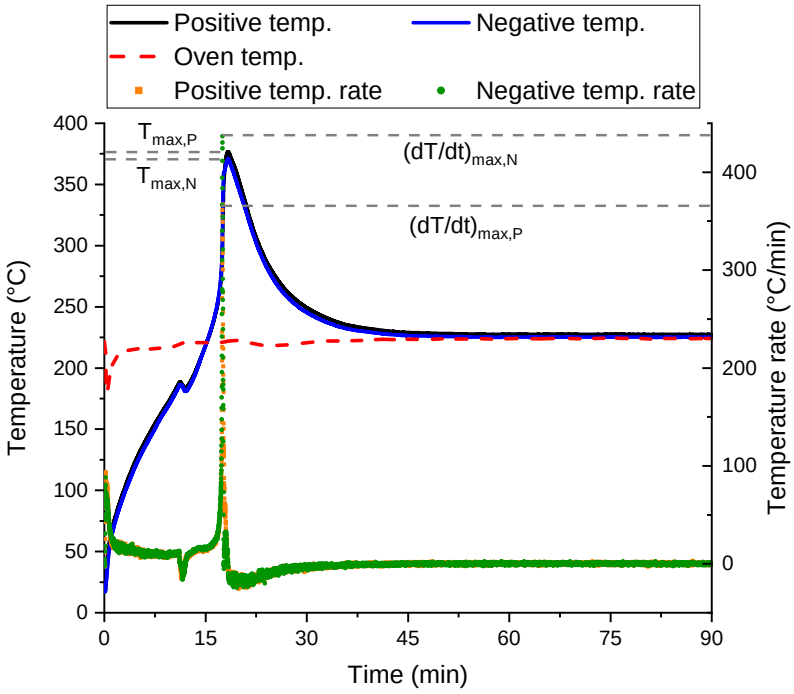

(e) Cell 09

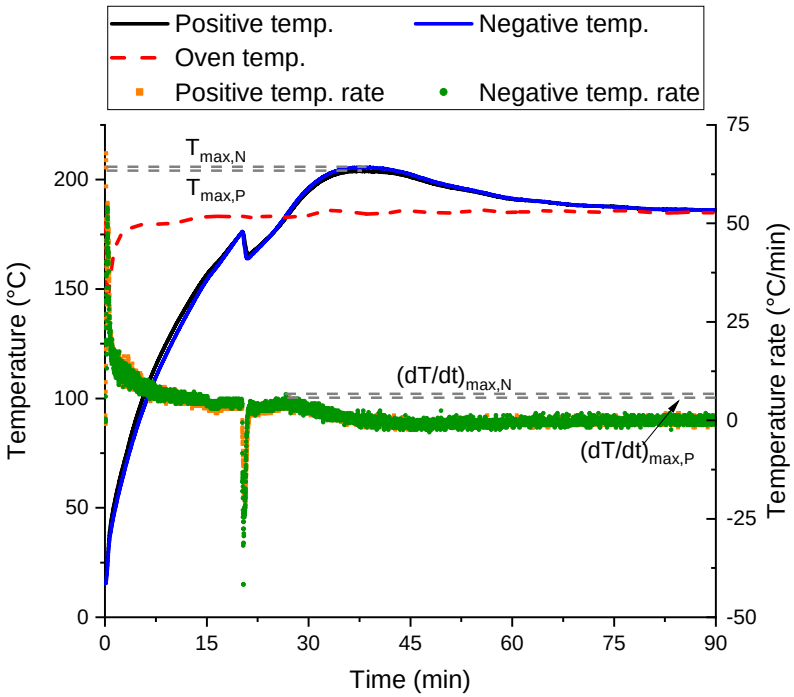

(f) Cell 10

Figure 4.11 (cont.): Results of oven exposure tests, temperature and temperature rate vs. time, with maximum surface temperatures and maximum surface temperature rates indicated.

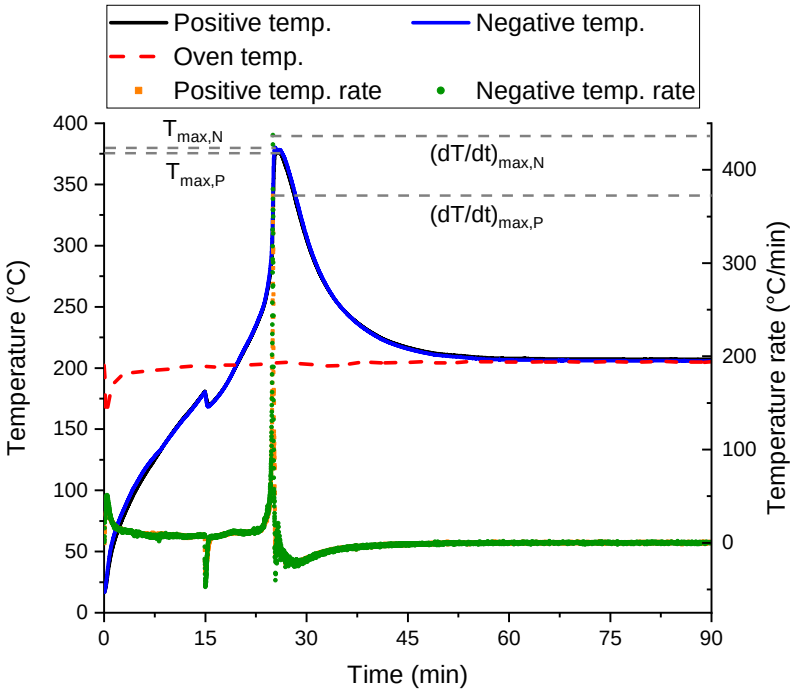

(g) Cell 12

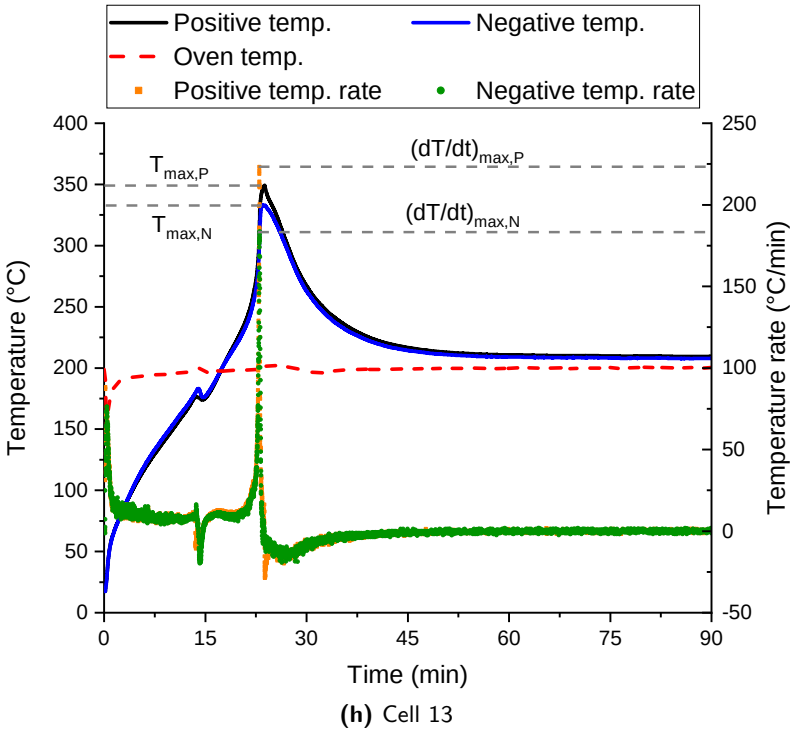

(h) Cell 13

Figure 4.11 (cont.): Results of oven exposure tests, temperature and temperature rate vs. time, with maximum surface temperatures and maximum surface temperature rates indicated.

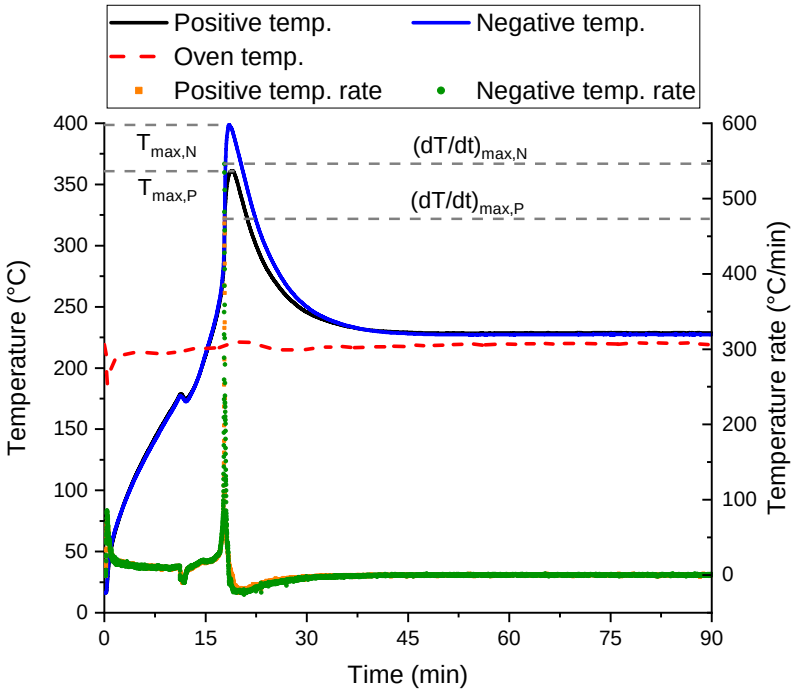

(i) Cell 14

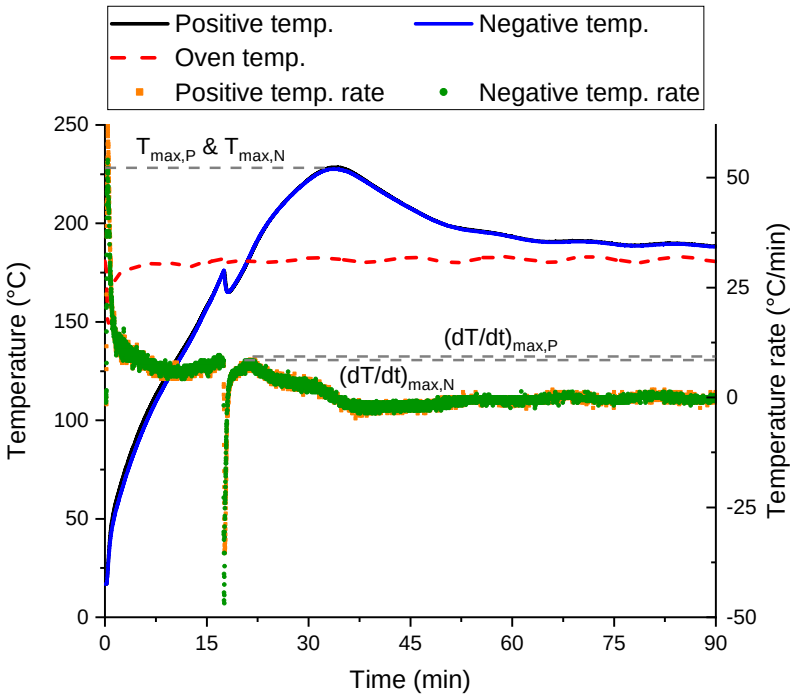

(j) Cell 15

Figure 4.11 (cont.): Results of oven exposure tests, temperature and temperature rate vs. time, with maximum surface temperatures and maximum surface temperature rates indicated.

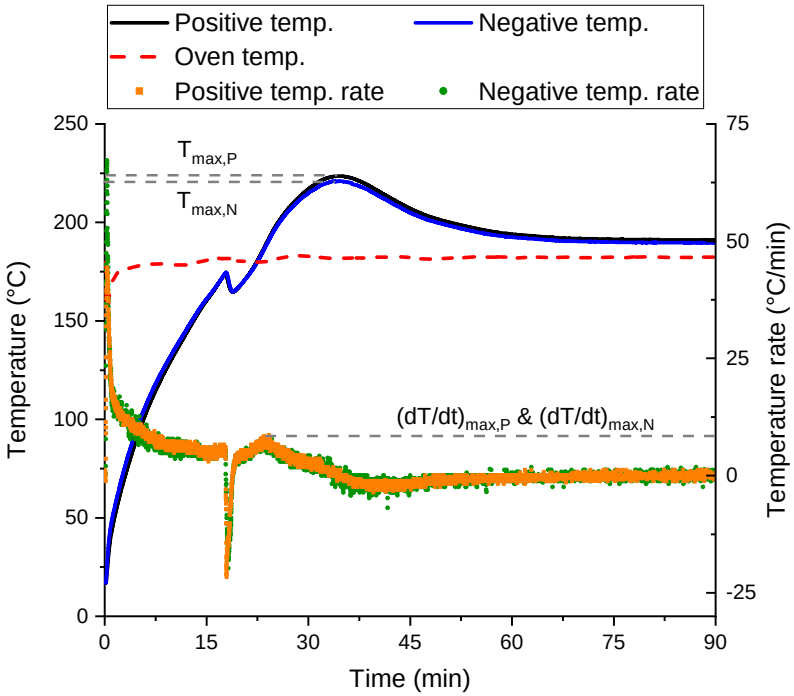

(k) Cell 16

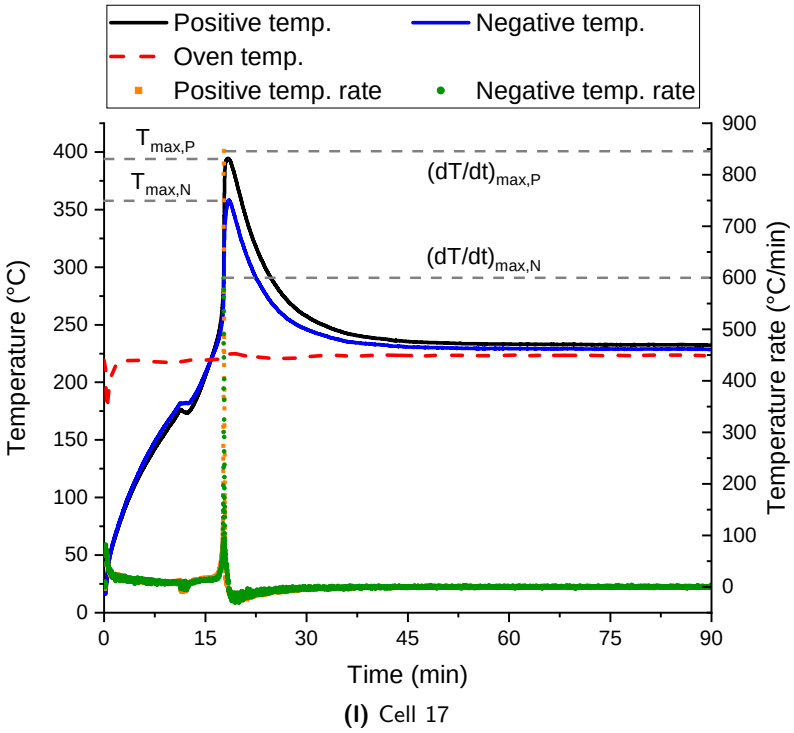

(l) Cell 17

Figure 4.11 (cont.): Results of oven exposure tests, temperature and temperature rate vs. time, with maximum surface temperatures and maximum surface temperature rates indicated.

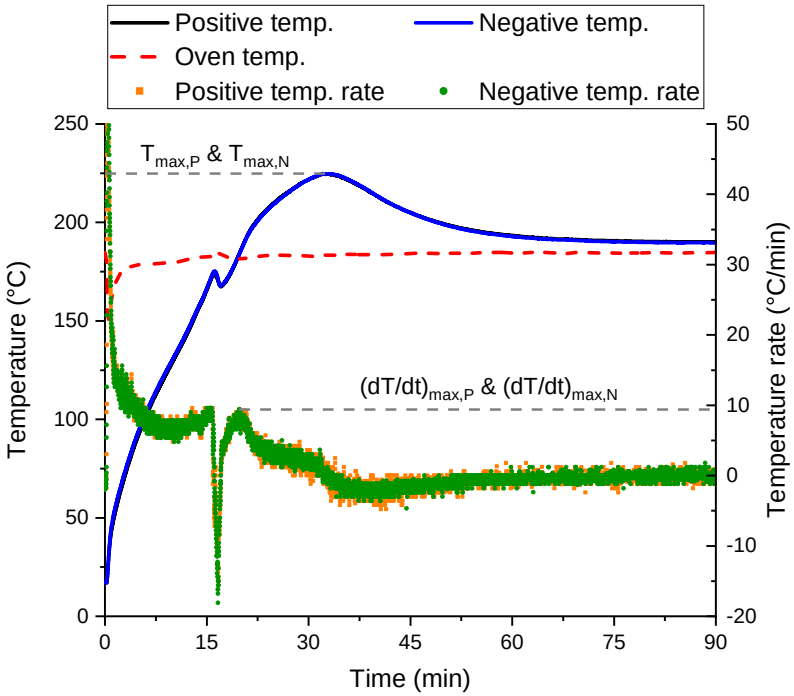

(m) Cell 19

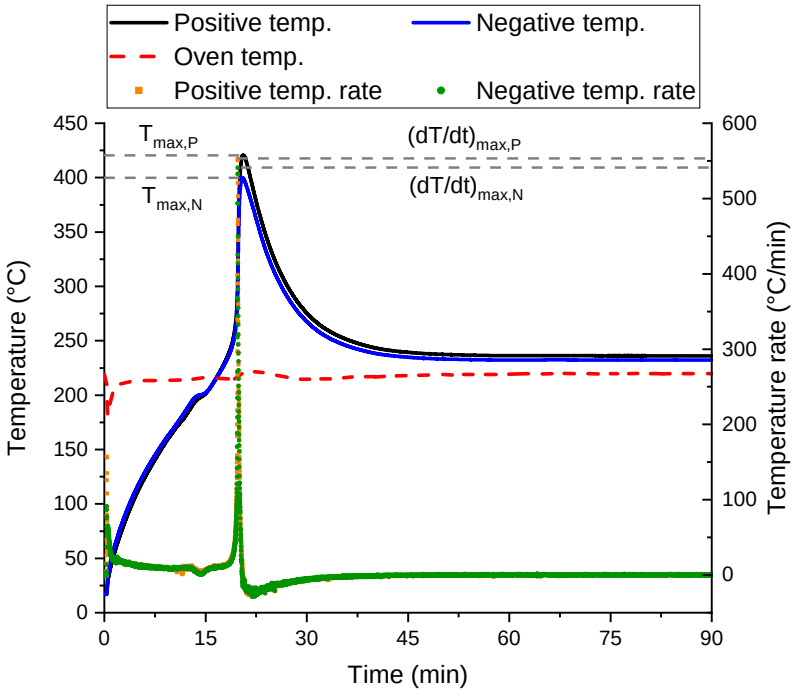

(n) Cell 20

Figure 4.11 (cont.): Results of oven exposure tests, temperature and temperature rate vs. time, with maximum surface temperatures and maximum surface temperature rates indicated.

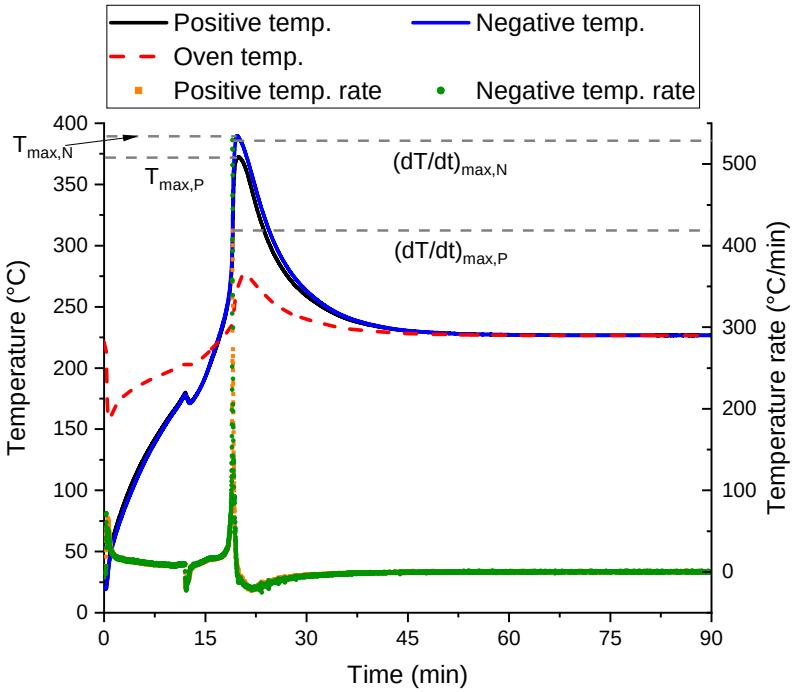

(o) Cell 21

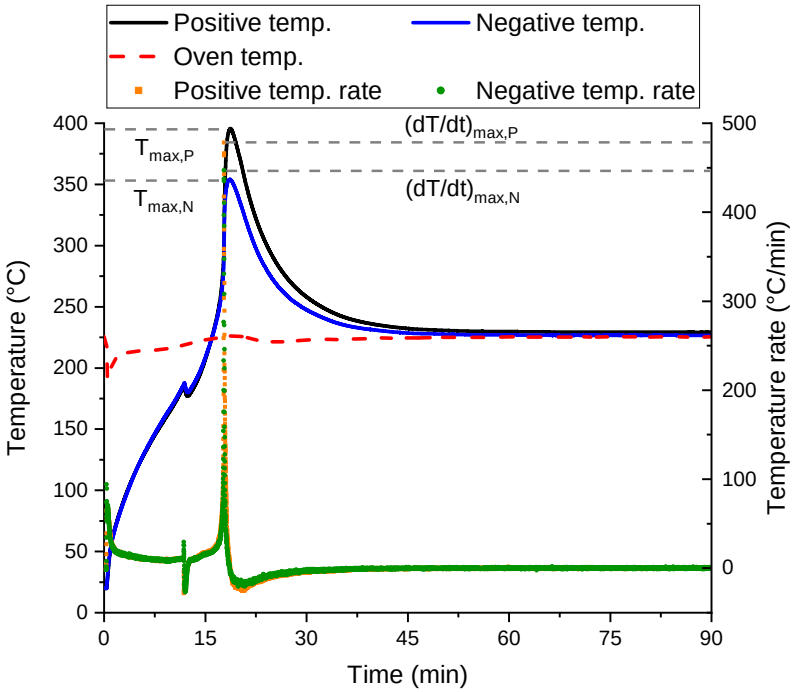

(p) Cell 22

Figure 4.11 (cont.): Results of oven exposure tests, temperature and temperature rate vs. time, with maximum surface temperatures and maximum surface temperature rates indicated.

(a) (b) (c)

Figure 4.12: 18650 $LiFePO_4$ cells. (a) before TR, (b) and (c) post TR after exposure to oven temperatures of 180°C and 220°C respectively.

For comparison of the TR behaviour cells under oven exposure at different oven temperature, the results of individual runs are organised into two groups. Group A consists of cells whose $\bar{T}_{oven}$ before TR lie around 180°C, i.e. cells 10, 15, 16 and 19, while group B consists of cells with a $\bar{T}_{oven}$ before TR approximately 215°C, i.e. cells 3, 9, 14, 17, 20, 22 (see Fig. A.1 for a depiction of cells' $\bar{T}_{oven}$ relative to each other). The temperature profiles of group A and B are presented in Fig. 4.13(a) and Fig. 4.13(c), respectively. Figures 4.13(a) and 4.13(c) also indicate key stages of TR under oven exposure and the location of venting. The period of venting is enlarged in Figs. 4.13(b) and 4.13(d).

The cell surface temperature plots in Fig. 4.11 show, in general, the increase in cell surface temperature from room temperature up to a maximum temperature beyond the oven temperature, before cooling towards the oven temperature. This behaviour can be broken into four regions as depicted in Figs. 4.13(a) and 4.13(c). Region (A) is below a cell surface temperature of 95°C, corresponding to the onset temperature of self-heating reactions determined from the ARC data of a cell at 100% SOC in Section 4.2.2. Region (B) is a period of increasing reaction rates and self-heating over a cell surface temperature range of 95°C to 175–180°C, at which point venting occurs. Region (C) is the period of TR, from venting to peak temperatures. Finally, Region (D) is the period at which the cells cools down trending to the oven temperature after the reactions (are expected to) have finished. In this last region, at times nearing the end of the test, it can be seen from Figs. 4.11(b), 4.11(c), 4.11(e) to 4.11(n) and 4.11(p), that a cell typically does not cool right down to the oven temperature. A temperature offset, with a mean value of ~7°C (with a standard deviation of 4°C), is present. Here, this is attributed to low rate simmering reactions, providing relatively low heating rates, but significant enough to prevent the cells returning all the way to the oven temperature. Also, it can be seen from Figs. 4.13(a) and 4.13(c), that there is a high degree of repeatability for the measured surface temperatures between each experimental run. With regard to this, cells 10 and 20

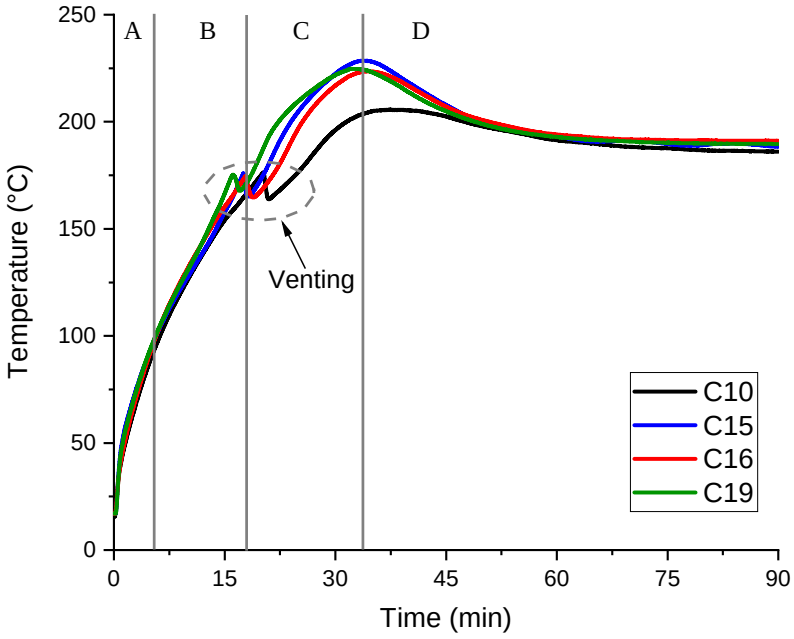

(a) Group A

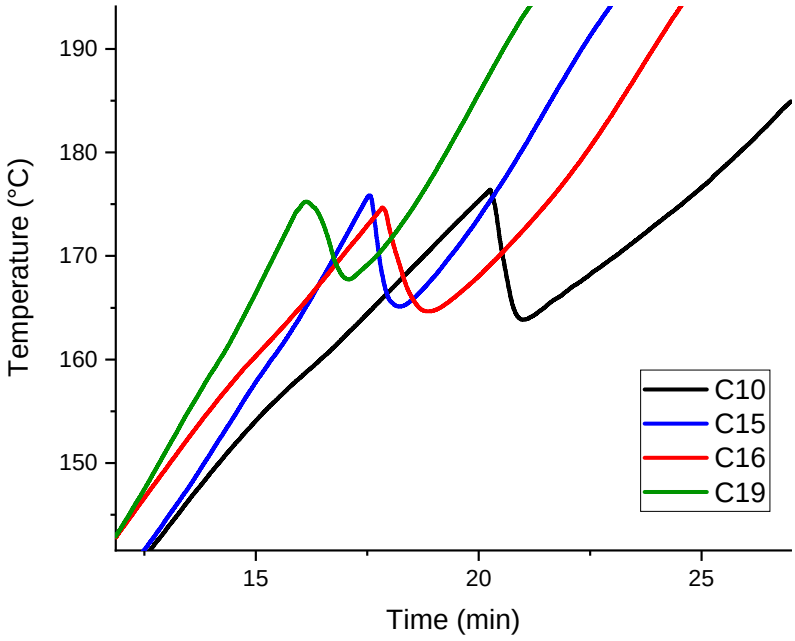

(b) Group A - enlargment of venting

Figure 4.13: Comparison of temperature profiles for cells in Group A and for cells in Group B, with venting highlighted and enlarged in corresponding figures. Regions A, B, C and D indicate key stages of TR under oven exposure (discussed in text).

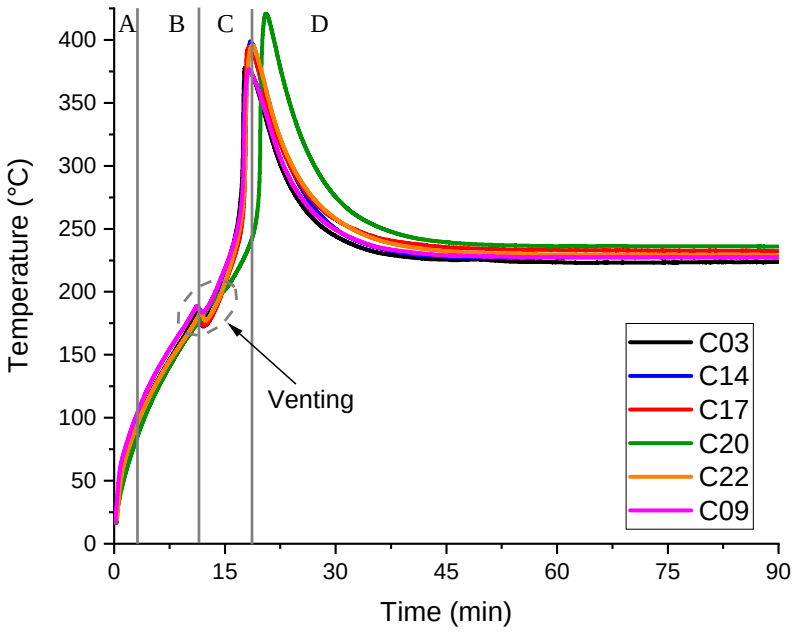

(c) Group B

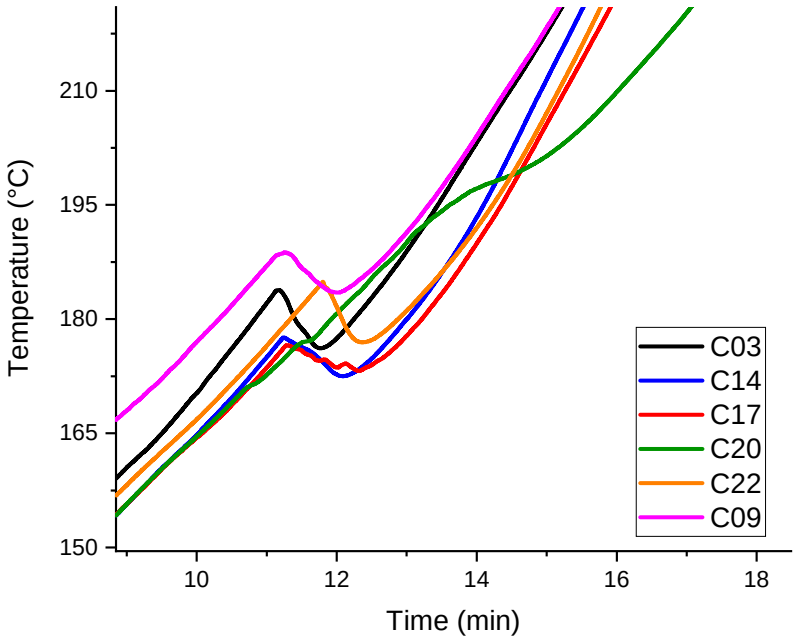

(d) Group B - enlargment of venting

Figure 4.13 (cont.): Comparison of temperature profiles for cells in Group A and for cells in Group B, with venting highlighted and enlarged in corresponding figures. Regions A, B, C and D indicate key stages of TR under oven exposure (discussed in text).

show a significant deviation from the rest of the cells in group A and B respectively. This will be discussed in detail later.

Table 4.5 presents the mean values of important measurements for both oven set temperature groups. This includes the mean calculated oven temperature, maximum cell temperature, maximum temperature rate (after venting) and the time to these two maximums. From this data, it can be seen that these maximum cell surface temperatures relate to a temperature rise of 41°C and 180°C above the mean oven set temperatures of 180°C and 214°C respectively (minor difference, e.g. 4°C relating to maximum temperature, between values here and those in Ref. [264] occur due to sampling data at 100 ms here and 1 s in Ref. [264], and inclusion of a larger data set that leads cells being added to group B in this work). From the data presented here, compared to that from the literature [146, 176], we can see that LFP cells are much safer than LCO cells for a given oven temperature. LFP cells, compared to LCO, are more stable as they go into rapid TR at a higher oven temperature (200°C compared to 155°C), and react less severely leading to lower maximum temperatures (~400°C compared to ~700°C).

As the safety of a battery pack is directly related to the safety of the cells that the pack is constructed of, then the use of LFP cells, such as those studied here which have been shown to be a safer alternative to LCO cells, will in turn improve the safety of a battery pack. This supports the suggestion by MacNeil *et al.* [119] that LFP cells are suited to large format batteries, which have a greater energy capacity and hence safety is a greater concern, especially batteries that would be used in a domestic setting where risk to people is greater, or in harsh environments where the probability of abuse is greater.

Table 4.5 also presents the variation of key measurements for each group of cells. As previously stated, Figs. 4.13(a) and 4.13(c) shows that test have been completed with high repeatability. Table 4.5 quantifies that the calculated oven set temperature of each group has a relative standard deviation (RSD) less than 1.5%. Highlighting the high repeatability of the test conditions. The RSD of the maximum temperature and time to temperature is less than 7% in both groups. However, the RSD of the maximum cell temperature rate is an order of magnitude greater than this. This implies that, while the overall variation of TR severity of a cell is small given a test condition, the rate of reaction is more unpredictable.

Figure 4.11 also shows that, except for cell 20 (see Fig. 4.13(d)), the LFP cells vent at approximately 175°C resulting in a 5–10°C temperature drop at the cell's surface. However, with regard to cell 20 that does not show this temperature drop, there is an inflection in the cell's temperature profile a few minutes after venting for the other cells in group B. This inflection indicates that there is a reduction in the net heat generated, which in-turn implies that the cell's vents opened, but not completely. It is this lack of successful venting, and hence cooling of the cell by the Joule-Thomson effect, to which is attributed the 24°C increase in maximum cell temperature of cell 20 (421°C) compared to the mean maximum

Table 4.5: Mean values of important measurements for each oven set temperature group.

Measurement	Group A		Group B	
	Value	RSD (%)	Value	RSD (%)
Calculated oven temperature (°C)	180	0.49	214	1.32
Max. cell temperature (°C)	221	4.62	394	4.10
Time to max. cell temperature (min)	34	6.33	19	5.18
Max. cell temperature rate (°C/min)	8	14.82	550	29.04
Time to max. cell temp. rate (min)	23	12.64	18	4.83

temperature of group B (394°C). This shows that, although venting is not capable of halting TR, venting does influence the maximum temperature reached.

With regard to cell 10, the cell used in this run had a capacity of 1.49 Ah (see Table 4.2) compared to the mean value of 1.48 Ah for the cells of group A. It was exposed to the highest oven temperature, 181°C compared to the mean of 180°C and had a temperature drop due to venting in the same range as other cells in the group. Such factors can be ruled out as being influential to the temperature difference between cell 10 and the remaining cells in group A. Hence, one can speculate that the cause of this anomaly is due to less heat being produced as a result of decomposition reactions not fully completing. This and the previous paragraph show the importance of considering cell variability when studying the safety of battery modules or packs.

From Table 4.5 we see that these LFP cells under a free convection oven test procedure behave in a similar manner to those of other chemistries in literature [146, 176, 177], i.e. a higher oven set temperature leads to a higher cell TR temperature in a shorter amount of time, as well as reducing the time to venting. Even though the venting occurs sooner at higher oven temperatures (compare Figs. 4.13(a) and 4.13(c)), it occurs at a similar cell temperature for each oven set temperature, see Figs. 4.13(b) and 4.13(d). Therefore, it is assumed here that it relates to cell internal pressure and hence as a result of greater convection heating and of faster reaction rates for the decomposition reactions which in turn leads to gas being produced more quickly.

Additional to the large increase in TR temperature of cells in group B compared to cells of group A, group B shows 2 orders of magnitude greater maximum temperature rate than group A, see Table 4.5. Table 4.5 also shows the maximum temperature rate in group B occurs 1 min before the maximum temperature, while in group A the maximum rate occurs 10 min before the maximum temperature. As the temperature rate of the cell is governed by the heat generation rate, it can be inferred that the maximum reaction rate is much lower in group A than B. From the time difference between maximum rate and maximum temperature, and the breadth of the peak temperature rate (i.e. period over which the rate begins to increase before venting, up to the maximum temperature rate, and onto reducing to zero, see Fig. 4.11) there can be further inferences made about

the reaction rate. Where these two values are greater, while the reaction rate is slower, it proceeds for a longer period of time. This behaviour occurs in group A (cells exposed to relatively lower oven temperatures), where relatively slow reaction rates lead to heat generated over a longer period and a broader peak in temperature, while in group B the reactions occur at a quicker rate but for a relatively short period, so the TR peak is less broad, see Fig. 4.11. This has implications on risk mitigation, in which the reaction rate behaviour of group A requires a thermal management system that can transfer heat away from the cell at a relatively low power for a long time, while conversely, the reaction rate behaviour of group B requires a thermal management system that can transfer heat away at a high flux for a short period of time.

Although the difference in maximum surface temperatures between the two oven temperatures is to be expected, it is interesting to note the large increase in cell surface temperature rate of group B ($\hat{T}_{oven}$ = 214°C). This suggests that between the two $\hat{T}_{oven}$ of group A ($\hat{T}_{oven}$ = 180°C) and B there are additional reactions occurring in group B compared to group A. The analysis of the ARC data for a LFP cell at 100% SOC in Fig. 4.4(b) shows peak reaction rates to be at 228°C, while the decomposition of the LFP electrode has peak reaction rates at temperatures >210°C [115, 119, 126, 164] and heating due to electrolyte decomposition does not occur until >255°C [71, 153]. Therefore, for group A where the cells surface temperature did not reach beyond 230°C, it is clear the cell's internal temperature does not reach a temperature that leads to the onset, or to significant reaction rates, of one or both of the PE and, electrolyte reactions. Most significantly, the cells in group A did not reach the point for the evolution of oxygen and the electrolyte reaction. The absence of these reactions therefore leads to the significantly reduced reaction rate and heat of reaction of the cell for the lower oven temperature.

Furthermore, Fig. 4.14 shows the resulting maximum cell surface temperatures and maximum cell-oven temperature difference (ΔT) occurring at particular $\hat{T}_{oven}$ before TR for all cells. For a definitive understanding of Fig. 4.14 in terms of the overall data of Fig. 4.11, it is reproduced in Appendix A and additionally labelled with corresponding cell numbers (see Fig. A.1). It can be seen from Fig. 4.14 that between 170°C and 190°C, there is a slight increase in maximum cell temperature with oven temperature. Following this, between 190°C and 200°C there is a step increase in maximum cell temperature. Beyond 200°C oven temperature, there again is only a slight increase in maximum cell temperature. The temperature difference (ΔT) is almost flat below 190°C and above 220°C oven temperatures. However, between a (pre-TR average) oven temperature of 190°C and 200°C (denoted by the red highlighted region in Fig. 4.14), there is a significant increase in the observed ΔT. This suggests that in this oven temperature range the cell reaches the critical temperature for the additional (PE, electrolyte) reactions to occur. This indicates that if an LFP cell is maintained below this critical temperature for these reactions, then not only will the overall cell temperature from TR be considerably lower,

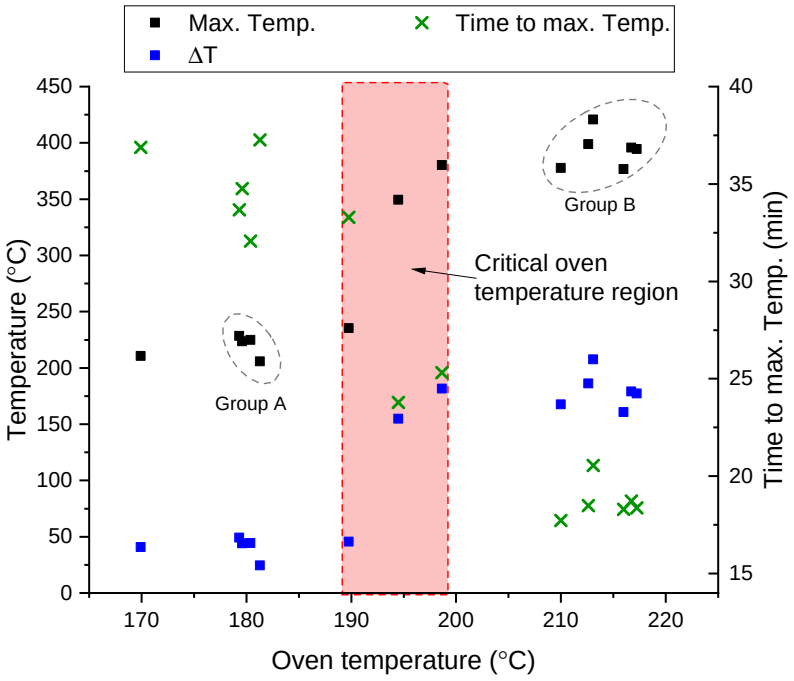

Figure 4.14: Maximum cell surface temperature, temperature difference and time to maximum temperature vs. oven temperature.

but the rate of reaction of the cell will be much lower and therefore the cell much easier and safer to manage.

Also, from Fig. 4.14, it can be seen that the time to maximum cell temperature reduces with increasing oven set temperature, as to be expected [146]. However, while the maximum cell temperature shows a step change around the critical oven temperature region, the time to maximum cell temperature shows linear behaviour inversely proportional to the oven set temperature. Implying that the time to TR is dominated by the oven set temperature and not the proceeding reactions.

The maximum cell temperature rate vs. calculated oven set temperature is presented in Fig. 4.15, along with time to maximum rate. As with the maximum cell temperature of Fig. 4.14, the maximum cell temperature rate shows a step change in severity around the critical oven temperature region. This shows the reaction rate of the cell increases significantlky over a small (10°C) temperature range, and hence the small safety window going from what would be a heating rate that is relevantly easy to manage, to a heating rate that is severe and difficult to manage. However, unlike the time to maximum temperature, the time to maximum temperature rate is not linear with oven set temperature. The time to maximum cell temperature rate remains relatively constant, approximately 25 min, for oven set temperatures between 170°C and 200°C (which is the end of the critical oven set temperature region). After 200°C the time to maximum temperature rate is approximately 18 min. Further, Fig. 4.16 compares the time to maximum temperature and time to maximum temperature rate. This shows the time to maximum rate follows the same linear trend, inversely proportional to oven set temperature, as the time to

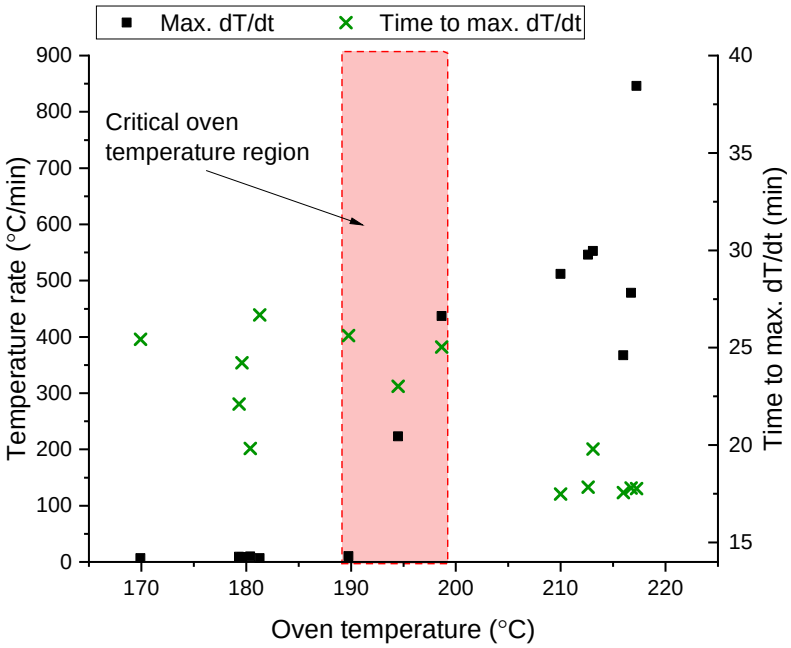

Figure 4.15: Maximum cell surface temperature rate and time to maximum temperature rate vs. oven temperature.

maximum temperature, for oven set temperatures greater than 190°C. However, at and below 190°C this trend is not upheld. On inspection of the relevant plots of Fig. 4.11 for cells 2, 4, 10, 15, 16, 19 (see Fig. A.2 to determine the cell number of cells exposed to oven set temperatures at and below 190°C), it can be seen that the peak temperature rates occur, approximately, at the point at which the oven and cell temperatures are equal. It can be inferred that, due to the low heat generation rate of the cell, the maximum rate occurs when there is effectively no heat loss (as cell and oven temperatures are equal). After this point, with heat generation rates still being relatively low, the temperature rate begins to reduce as the cell temperature is increasingly greater than the oven, in turn heat loss from the cell increases. As a result, this in effect means that the time to maximum temperature rate of cells at and below 190°C is equal to the time for the cell to reach the oven temperature.

A conservative comparison of the oven simulation data from Peng and Jiang [38] to this newly gathered oven experimental data, shows that under simulation there is a large overestimation of the oven temperatures that lead to TR, a large underestimation of cell temperature increase due to TR and an overall disagreement with the qualitative behaviour of the cell surface temperature profile. This outlines the importance of these oven exposure results as a data set for validation of TR models of LFP cells.

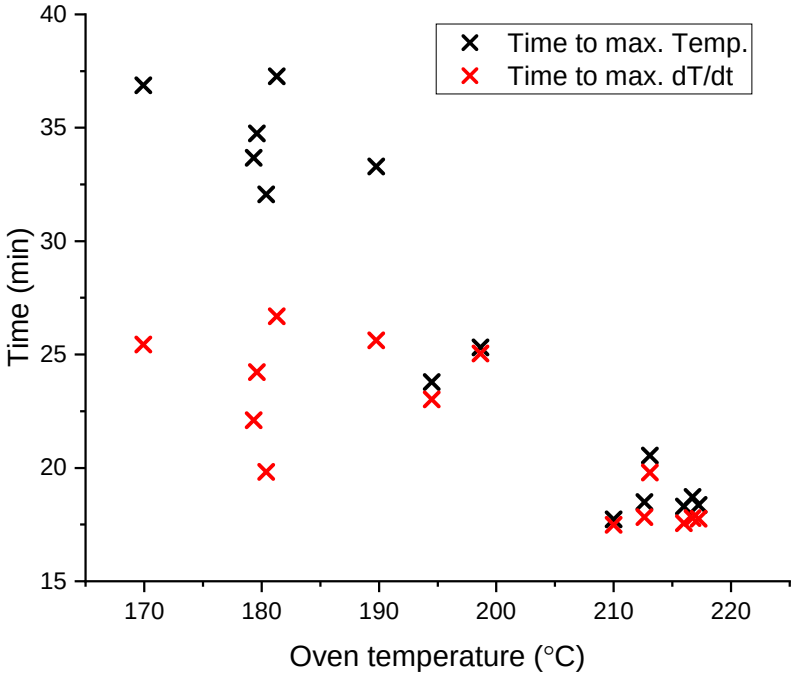

Figure 4.16: Comparison of time to maximum temperature and time to maximum temperature rate.

4.2.4 Comparison of Abuse Methods

By comparing the oven data to the ARC data at 100% SOC, we see that for cells exposed to an oven temperature of approximately 215°C, a more drastic TR event occurs compared to the ARC tests. Similar behaviour is noted by Lei *et al.* [171]. In the oven test, a mean maximum cell surface temperatures of ~394°C is achieved, with a mean maximum temperature rate of 550°C/min (see Table 4.5). In comparison, under ARC tests, the mean maximum cell surface temperature (315°C) and temperature rates (3.7°C/min) are significantly lower, even though there is no heat loss. This can be explained by the contribution of self-heating to cell temperature rise. In the ARC, the temperature rise of the cell is entirely due to the thermal energy generated by self-heating, raising the cell's temperature from 95°C to 315°C. In the oven, however, due to rapid convective heating from the air and conduction through the cell, the cell can reach a higher temperature (up to the oven set temperature) more quickly than that which would occur from the evolution of the reaction rates alone. As the cells (at 100% SOC) are identical in the oven and ARC tests, the amount of energy that can be released during TR will also be the same. However, in the oven test, due to the relatively high temperature rate from convection heating (compared to self-heating in ARC at same temperature), there is a significant increase in temperature before the decomposition reactions can progress. Hence more heat is released at higher temperatures (compared to the ARC), in turn leading to a larger temperature rise overall. Additionally, the compounding of the reaction rates of the four reactions at higher temperatures leads to an overall increase in reaction rate of the cell. Moreover, for the oven at 220°C, it can be seen that TR initiates below the oven set

temperature and occurs so rapidly that the system is effectively adiabatic. This indicates that the severity of TR is increased under rapid heating of the cell and should be taken into account when considering safety, especially in circumstances such as rapid heating of a cell due to short circuit of a neighbouring cell, overheating due to temperature control failure or another source of heat such as fire.

4.2.4.1 Calculation of Heat Released

For further insight into the reactions taking place under the different abuse scenarios, an analysis of the heat released by cells at 100% SOC under ARC and oven testing was undertaken.

Under ARC the thermal energy released can be easily calculated from the adiabatic temperature rise of the cell by Eq. (4.1). In Eq. (4.1), the adiabatic temperature (ΔT) is the difference between the onset and maximum cell temperature, C_p is the average specific heat of the cell and m is the average mass of the cell. The average mass of a cell was measured to be 40.48 g (with shrink wrapping). The C_p value, following the method outlined by [248], was calculated by Eq. (4.2) from the average temperate rate (dT/dt) of a cell in an adiabatic environment subject to a constant heating power (P) at the cells surface, as described in Section 4.2.1. The specific heat of the cell was determined to be 1107 J/kg K. For the cells at 100% SOC under ARC, the average adiabatic temperature rise is approximately 220°C. Therefore, from Equation 4.1, $Q_{ARC} = 9.85$ kJ.

$$Q = \Delta T C_p m \tag{4.1}$$

$$P = \frac{dT}{dt} C_p m \tag{4.2}$$

The determination of the heat released under oven exposure can be estimated from the cell surface temperature rate, Fig. 4.17 shows an example cell surface temperature rate plot from oven exposure. The temperature rate, determined by differentiation of the temperature plot, can be used in conjunction with Eq. (4.2) to determine the heating power at the cells surface for every instance in time. By integration, this in turn can be used to determine the thermal energy released during TR.

As the temperature, and in turn the temperature rate, are both dependent on the heat transfer from the oven as well as the self-heat generation, their contributions to cell heating have to be identified. As discussed in the ARC study, self-heating does not initiate until ~95°C, so at any point in time when the cell surface temperature is <95°C it can

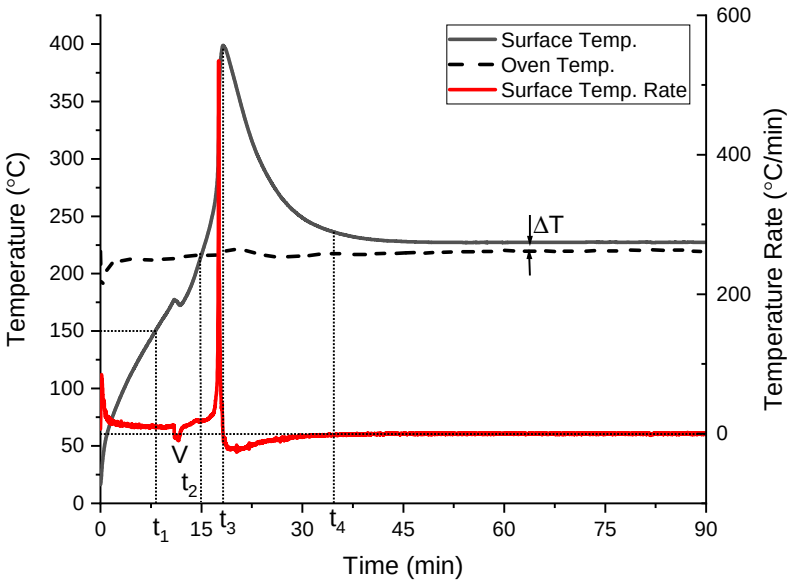

Figure 4.17: Method to calculate heat generated by cell under oven testing, with key time indices annotated.

be confidently said that transfer from the oven dominates. Although a large temperature difference between the cell interior and cell surface can exist during TR due to internal heat generation, at this early stage with no self-heating the surface can be assumed to be hottest [193]. Above this temperature, self-heating will become increasingly important. On inspecting the temperature rate (taking the profile in Fig. 4.17 as an example), it is found that after a plateau in the rate, the rate increases at times coinciding with cell surface temperatures greater than approximately 150°C. Hence, it is assumed that self-heating is not important until surface temperatures are >150°C, at which point it dominates the heat rise of the cell up to the cell's maximum temperature. Beyond the maximum temperature the cell cools. However, this does not mean the decomposition reactions are complete at this point. This is evident from the temperature difference between the cell surface and oven at the end of the test, suggesting low rate reactions are still occurring such that the cell does not equilibrate at the oven temperature.

From this interpretation several key time instances and features can be identified and utilised to estimate the heat generated during TR of a cell under oven exposure. The time instances t_1, t_2, t_3 and t_4, depicted on Fig. 4.17, can be defined as: t_1, the time that self-heating becomes dominant; t_2, the time that the cell becomes hotter than the oven; t_3, the time that the maximum cell temperature occurs and the point the cell begins to cool; and t_4, the point that the cell temperature rate is negligible. Beyond t_4 the temperature difference between the oven and cell surface (from t_4 to the end of the test), due to simmering reactions, is defined as ΔT_{t_i}, at t_i. The negative rate region at point V is due to cooling from the venting gases.

The absolute energy released by self-heating (i.e. considering heat loss due to venting as positive as it inherently originates from self-heating) between t_1 and t_3, $Q_{t_{1-3},Abs}$, can

be determined by integrating the absolute power between t_1 and t_3. In turn the energy lost through venting, Q_V, can be estimated from the difference between $Q_{t_{1-3},Abs}$ and the net energy released between t_1 and t_3, $Q_{t_{1-3},Net}$, i.e. $Q_V = Q_{t_{1-3},Abs} - Q_{t_{1-3},Net}$. If no heat is generated after the peak temperature, it is expected that the heat lost during t_3–t_4, $Q_{t_{3-4},Loss}$ (by the cell cooling down to the oven set temperature), to be equal to the heat that was generated between t_2–t_3, $Q_{t_{2-3}}$. Any difference in these values can be attributed to self-heating as the cell cools. Hence, the heat generated as the cell cools is defined as, $Q_{t_{3-4}} = Q_{t_{2-3}} + Q_{t_{3-4},Loss}$, as $Q_{t_{3-4},Loss}$ is inherently negative. Beyond t_4, where $dT/dt \approx 0$, we can assume steady state conditions. Hence, the self-heating rate, $P_{t_i,SH}$, equals the heat loss rate due to convection and radiation, $P_{t_i,HL}$, at each interval in time t_i between t_4–t_{end}. Radiation is considered because of its importance in convection oven experiments, as Hatchard *et al.* [258] highlights. The heat loss, $P_{t_i,HL}$, is defined by Eq. (4.3), where T_C and T_O are the cell surface and oven temperature respectively, h is the convective heat transfer coefficient, A is the heat transfer area, ε radiative heat transfer coefficient and R is the Stefan-Boltzmann constant. Therefore, the heat generated is determined by Eq. (4.4), where Δt_{t_i} is the time interval between data points. The total heat generated by self-heating is given by Eq. (4.5).

$$P_{t_i,HL} = \left(T_{C,t_i} - T_{O,t_i}\right) h_{conv} A + \left(T_{C,t_i}^4 - T_{O,t_i}^4\right) \varepsilon A R \tag{4.3}$$

$$Q_{t_{4-end}} = \sum_{t_4}^{t_{end}} P_{t_i,HL} \Delta t_{t_i} \tag{4.4}$$

$$Q_{total} = Q_{t_{1-3},Abs} + Q_{t_{3-4}} + Q_{t_{4-end}} \tag{4.5}$$

Following this method, with $h_{conv} = 10\,\mathrm{W/m^2\,K}$ (estimated from [146] from the values for a bare stainless steel cylinder, $12.5\,\mathrm{W/m^2\,K}$, and for a cell with a label, $7.2\,\mathrm{W/m^2\,K}$, h_{conv} for the tested cell is calculated to be the average of these values assuming half of the cell surface area is bare stainless steel, and the remaining surface that is covered in glass cloth tape has the same h_{conv} if was covered in the label), $A = 4.18 \times 10^{-3}\,\mathrm{m^2}$, $\varepsilon = 0.8$ [146] and Δt is the time between temperature readings after consecutive values are removed (as explained earlier, see Page 132), the self-heat generated during TR under oven exposure is calculated.

Table 4.6 presents the calculated heat released for each cell, following the above method, during each of the time periods, including the total heat generated during TR

and heat lost due to venting, as well as the mean values for groups A and B[1]. As a validation of the methodology, the calculated total heat released can be compared to the total electrochemical energy of the cell. For the cells in question, with a capacity of 1.5 Ah at 100% SOC and a nominal voltage of 3.2 V, the total electrochemical energy is $Q_{Elechem} = 17.28\,\text{kJ}$. For cells abused under the highest temperatures, and assuming that all possible decomposition reactions take place in the cells to the fullest extent, then the heat released by these cells can be considered representative of full conversion of electrochemical energy to thermal energy. Hence, by comparing the mean total heat released by group B, $Q_{total,B} = 15.93\,\text{kJ}$, to the electrochemical energy, $Q_{Elechem} = 17.28\,\text{kJ}$, it is shown that the calculated heat released is close to the energy capacity of the cell. As such, the method to calculate heat generation under oven abuse scenarios is valid for the higher oven temperature exposure. Moreover, by comparing the values of $Q_{total,A} = 7.46\,\text{kJ}$ and $Q_{total,B} = 15.93\,\text{kJ}$ estimated here to those predicted by modelling in Section 5.2.3, where $Q_{total,A} = 7.76 - 8.34\,\text{kJ}$ and $Q_{total,B} = 16.04 - 16.64\,\text{kJ}$ (see Table 5.7), it is shown that the numerical method for determining heat generation under oven exposure is close to that predicted computationally in both oven exposure cases, and hence valid for further discussion.

As can be seen from Table 4.6, the heat released (Q_{total}) by the cells exposed to the lower oven temperature is approximately a half of that at the higher oven temperature. This supports the previous statement in the discussion above, that at the higher oven temperature additional reactions, i.e. PE and electrolyte, are taking place. The amount of heat calculated to be released upon venting is greater in the lower oven temperature case. This is thought to be due to, in the higher oven temperature case, greater heat generation rates at the time of venting reducing the overall temperature reduction, in turn reducing the calculated heat loss.

As previously stated, approximately double the heat is released by cells in group B compared to A (see Table 4.6), however the relative change in surface temperature against oven set temperature in group B is 3 times greater than that of group A (see Fig. 4.14). However, inspecting values of $Q_{t_{1\text{-}3},A}$, which corresponds to the heat released from self-heating onset to maximum cell temperature, better relates to the maximum cell tempera-

[1] Values in Table 4.6 differ slightly to those of the corresponding table in Ref. [264]. This is due to 1) the number of cells considered in each group; 2) the temperature rate value at a given time due to the filtering of the data (see Page 132) rather than down sampling to 1 s; and 3) defining that simmering begins when the gradient of the temperature rate is first negative and hence the temperature rate starts to fluctuate about zero, rather than defining simmering to begin when then cooing rate is 10% of the maximum cooling rate. The mean total calculated heat released for group B is similar between the method here and of that of Ref. [264], where there is a 8% difference between the two. However, greater differences occur between the mean total calculated heat released for group A. On inspecting the heat release during the different stages of TR it can be seen that this is mainly due to the calculated heat release in the simmering region. Further, comparison of the heat release calculated from experimental data in Table 4.6 and predicted by simulation in Table 5.7, it can be seen that the estimated heat of the simmering reaction calculated here is close to the predicted values, whereas those in Ref. [264] are not. As such, the calculated heat released during simmering is sensitive to method at which onset is determined, but the method used herein is more accurate that that used in Ref. [264].

tures of Fig. 4.14. As such, from the mean values of $Q_{t_{1\text{-}3},A}$ for each group it can be seen that cells in group B release 2.8 times more heat than group A, almost equivalent to the 3 times increase in temperature. Hence, the methodology to determine heat released during oven exposure is upheld to be valid. Further, from Table 4.6 it can be seen that the heat released due to simmering reactions, $Q_{t_{4-end}}$, is greater, on average, for cells of group B than group A. However, the proportion of simmering heat of the total heat released is larger for group A, with simmering accounting for 34% of the total heat, while for group B, simmering accounts for 24% of the total. The large fraction of simmering heat of the total heat for the mean value of group A leads to the ratio of total heats between group A and B being closer to 2 than 3.

Cell to cell variation is a significant consideration regarding the safety of battery packs. If a cell is less stable or reacts more severely than expected, this may lead to thermal management and safety measures unable to prevent TR propagation. Hence, a large variability in the heat released during TR of commercial cells (which are manufactured to be identical) under exposure to similar abuse conditions can be considered a hindrance to pack safety. However, for the LFP cells in this study, the heat released during the main TR event, $Q_{t_{1\text{-}3},A}$, does not vary by more than 1 kJ from the mean value in both groups, while the variation in total heat released is of the order of the variation in the oven set temperature, see Table 4.6. From Fig. 4.13(a) and Fig. 4.13(c) we can see the variation in $Q_{t_{1\text{-}3},A}$ equates to less than a 25°C difference in maximum cell temperature about the modal maximum temperature of each group. As such, it can be said that the small variation in severity between similar tests shows these cells behave predictably.

When comparing the two abuse methods, ARC and oven exposure, it can be seen that the cells under ARC generate significantly less heat ($Q_{ARC} = 9.85\,\text{kJ}$) than cells exposed to mean oven temperatures of 215°C, which generate $Q_{Oven,215^\circ C} = 15.93\,\text{kJ}$ of heat. The higher temperature oven clearly represents a more complete TR event when compared to the electrochemical energy available, $Q_{Elechem} = 17.28\,\text{kJ}$. It is expected that a cell under adiabatic conditions in the ARC would capture the complete TR process, and hence the heat generated by the cell would be at least equal to that in the higher temperature oven case. As this is not the case, and as the ARC used here only operates up to 315°C, it is apparent that the ARC does not capture the TR event to completion.

4.2.4.2 Recommendations on Abuse Testing Li-ion Cells

In ARC, self-heating is defined when the temperature rate of the cell is >0.02°C/min. Naturally, self-heating can be defined as ending when the temperature rate drops below this value. Returning to the temperature rate plot of from the ARC test (Fig. 4.4(b)), it can be clearly seen that the cell is some way off from this cut-off value. In fact the rate is almost constant from 300°C to the end, again suggesting an incomplete reaction. However, under similar (ARC) conditions but up to higher maximum operating temperatures, i.e.

Table 4.6: Heat released during TR by cells under oven exposure.

Cell Nº.	**Group**	**Calculated oven temp. (°C)**	$\mathbf{Q_{t_{1\text{-}3},A}}$ **(kJ)**	$\mathbf{Q_{t_{1\text{-}3},N}}$ **(kJ)**	$\mathbf{Q_{t_{2\text{-}3}}}$ **(kJ)**	$\mathbf{Q_{t_{3\text{-}4},L}}$ **(kJ)**	$\mathbf{Q_{t_{4\text{-}end}}}$ **(kJ)**	$\mathbf{Q_{total}}$ **(kJ)**	$\mathbf{Q_v}$ **(kJ)**
02	–	190	4.52	3.82	1.74	−1.66	–	4.60	−0.70
03	B	210	10.88	10.19	7.27	−6.59	2.32	13.88	−0.69
04	–	170	3.88	2.72	1.41	−0.10	6.43	11.63	−1.17
08	–	n/a	9.90	9.41	6.25	−5.75	–	10.41	−0.49
09	B	216	10.63	10.15	6.99	−6.34	2.65	13.93	−0.47
10	A	181	3.63	2.49	1.02	−0.28	1.70	6.08	−1.14
12	–	199	11.41	10.31	7.96	−7.59	0.54	12.32	−1.09
13	–	194	9.25	8.93	6.81	−6.04	3.24	13.26	−0.32
14	B	213	11.60	11.14	8.18	−7.57	3.87	16.08	−0.45
15	A	179	4.48	3.52	2.14	−1.34	2.83	8.10	−0.96
16	A	180	4.19	3.29	1.95	−0.95	3.75	8.95	−0.90
17	B	217	11.32	10.95	7.82	−6.49	7.40	20.06	−0.37
19	A	180	4.02	3.35	1.93	−1.21	1.96	6.70	−0.67
20	B	213	12.13	12.13	9.20	−8.18	5.09	18.24	0.00
21	–	n/a	11.42	10.75	7.62	−7.19	–	11.84	−0.67
22	B	217	11.72	11.01	7.70	−7.35	1.36	13.42	−0.71
Group A, ave.		180	4.08	3.16	1.76	−0.94	2.56	7.46	−0.92
Group A, SD		0.88	0.35	0.46	0.50	0.47	0.93	1.31	0.19
Group B, ave.		214	11.38	10.93	7.86	−7.09	3.78	15.93	−0.45
Group B, SD		2.83	0.55	0.73	0.78	0.73	2.20	2.72	0.26

>400°C as this is what is reached in the oven test, it maybe seen that the cell reaches the same maximum temperature and generates the same heat release as in the higher oven temperature case. In fact, assuming the total heat release upon TR to be equal to the electrochemical energy ($Q_{Elechem}$ = 17.28 kJ) and substituting this into Eq. (4.1), with appropriate C_p and mass values for the cells under study, and an onset temperature of 95°C, it is shown that the maximum cell temperature under adiabatic conditions would be 481°C. Also, the ARC being limited to a maximum temperature of 315°C also prevents determining if the cells at different SOC cease self-heating at different temperatures, and hence prevents determination of an accurate heat release for different SOC. As this investigation is beyond the scope of the study here, it is recommended that the self-heating behaviour in an adiabatic environment above 481°C to be made the focus of future work, along with investigation to identify if the discrepancies between ARC and oven tests are true of other cell chemistries.

In contrast, the oven exposure test with a set temperature high enough to induce rapid TR (in this case temperatures >200°C), captures nearly the entirety of the decomposition process within the cell in terms of the proportion of the electrochemical energy released as heat. Also, oven testing is cheaper and more readily accessible as a safety test. Hence, it is concluded that ARC alone could be unsuitable for characterising TR as it does not capture the full severity of TR (in terms of temperature rate). Furthermore, ARC also may not capture maximum achievable cell temperatures. As such, ARC testing should be complimented with oven testing. However, as the temperature measurements are recorded with thermocouples on the cell's surface, there will be a lag between the reactions occurring and the measured temperature. This could have implications on differentiating the individual chemical decompositions reactions compared to ARC, particularly during the high-rate thermal processes that occur during TR. To supplement this, the use of TR abuse modelling could be used to predict the decomposition reaction process and self-heat generated during oven testing, whilst also checking the assumptions of the simple model used here to determine the self-heat generation in the oven test. This is discussed in Chapter 5.

4.3 Statistical Analysis of Experimental Results

For any experimental practice, it is beneficial to quantify how the results obtained from the tested sample represent the population. For the greatest confidence of a sample being representative of a population it is desirable to have a large sample size.

Methods to determine minimum samples size typically require knowing the population standard deviation [265]. In the case of this work, the population standard deviation is not known. However, Mathews [265] show that in such a case a preliminary sample of n = 193 can be used to estimate the population standard deviation (assuming 95%

confidence level and a confidence interval half width of 0.2). Another method, by Cochran [266], calculates sample size given a desired confidence interval and level of variability. From this, a sample size of sample size of 364 is calculated assuming 95% confidence level and maximum variability, for a population of 7000. Where 7000 is the number of 18650 cells used in an EV [267].

It is clear that the sample size in this work, where $n < 10$ for a given set of variables, is small compared to the desired sample sizes suggested above. This means that there is less likelihood that the sample is truly representatives of a population.

Furthermore, to test if a sample is representative of a population the population mean or standard deviation need to be known [268]. This is such that a hypothesis test can be carried out to determine if there is a statistical significance that the sample and population means are equal. As the population mean and standard deviation are not known for this work this can not be implemented.

However, confidence intervals on samples can be calculated without population data. These confidence intervals then give the bounds in which the population mean will likely lie, for a given confidence level. The following section will investigate the confidence intervals, based on this small sample size, for the oven and ARC results.

4.3.1 Confidence Intervals

When the sample size is small, i.e. $n < 30$, the *Student's t Distribution* can be used to compute the confidence intervals for the population mean, assuming the population is normally distributed [269]. This is done using the following equation:

$$\mu = \overline{X} \pm t_{n-1,\alpha/2} \frac{s}{\sqrt{n}} \tag{4.6}$$

where μ is the calculated confidence interval for the population mean, $\overline{X}$ is the sample mean, $t_{n-1,\alpha/2}$ is the Student-t distribution (determined from look up tables [see, for example, 270]), s is the sample standard deviation, n sample size, and α is the confidence internal. For a 95% confidence interval with two tails, $\alpha = 1 - 0.95$.

4.3.1.1 Oven Test Analysis

Eq. (4.6) is used to calculate the 95% confidence interval of the cell temperature at every 0.02 min time instances for the oven abuse test data. The mean cell temperature and confidence intervals are presented in Fig. 4.18.

From Fig. 4.18 it can be seen that the confidence intervals are tight around the mean for both oven temperature tests. But, the confidence intervals grow around the self-heating/

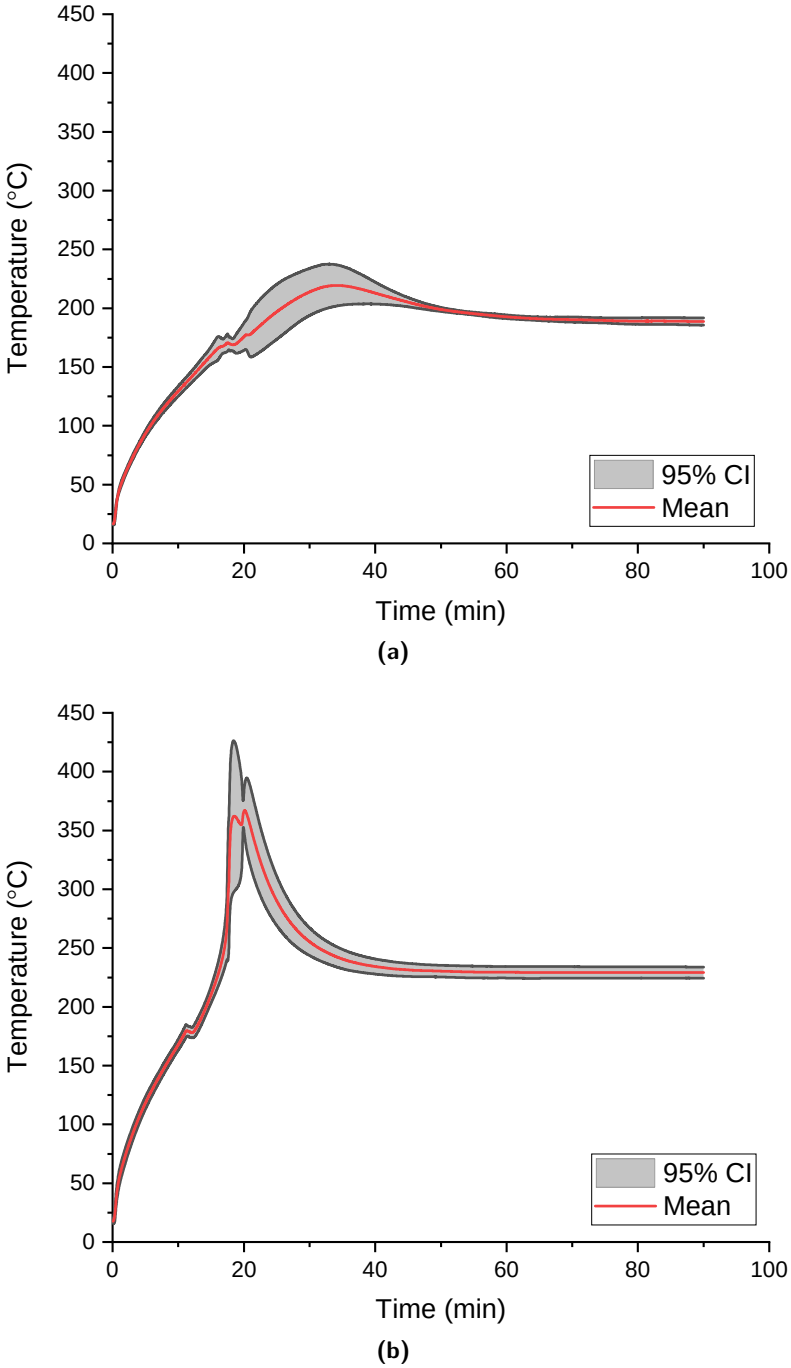

Figure 4.18: Oven exposure test – 95% confidence intervals determined from the Student-t distribution for a) Group A (n=4), and b) Group B (n=6).

TR events (approximately 20 min to 40 min). This highlights the variability of the TR events.

Figure 4.18 also shows that there is a 95% probability that the population mean peak cell temperatures are 203°C $< T_{max,A} <$ 238°C and 352°C $< T_{max,B} <$ 426°C for the respective oven exposure temperatures of 180°C and 214°C.

4.3.1.2 ARC Test Analysis

Eq. (4.6) is also used to calculate the 95% confidence interval of the cell temperature rate given 0.5°C temperature steps for the 100% SOC ARC abuse data. The mean cell temperature rate and confidence intervals are presented in Fig. 4.19.

The data of Fig. 4.19 is split into two sub-sets. One for the data before venting, and one for the data after venting. This is done to facilitate the interpolation of the rate data. As the whole data set can contain more that one record of a given temperature due to the cooling of the cell at venting, as can be seen in the mean temperature rate in Fig. 4.19. Thus making it difficult in interpolate the continuous data series.

As each run of the ARC tests result in different temperatures at which self-heating is onset and venting starts and stops, there is not a constant sample size over the entire temperature range. Table 4.7 presents the sample size used in calculating the confidence interval at each temperature step. Further, form Fig. 4.19 it can be seen that the mean line extends beyond the ends of the confidence interval. This is due to only one sample being recorded at those temperatures, hence the confidence interval cannot be calculated.

It can be seen from Fig. 4.19 that the 95% confidence interval for the temperature rate remains at the magnitude of the mean at a given temperature. However, around the point after venting (i.e. the start of the "after venting" data subset) and of peak temperature rate (above the 1°C TR definition) the relative width of the confidence interval increases. This highlights the variability of the venting and TR behaviour.

Figure 4.19 also shows that there is a 95% probability that the population mean peak cell temperature rate is 1.38°C/min $< T_{rate,max} <$ 4.26°C/min for cells at 100% SOC under ARC exposure.

Further testing would be beneficial to determine the difference in the mean and variance of two sample sets (for given oven exposure temperature, or SOC under ARC testing). This would help determine if they can individually be considered representative of a population. As well as carrying out further testing to identify what sample size can be considered representative of a population.

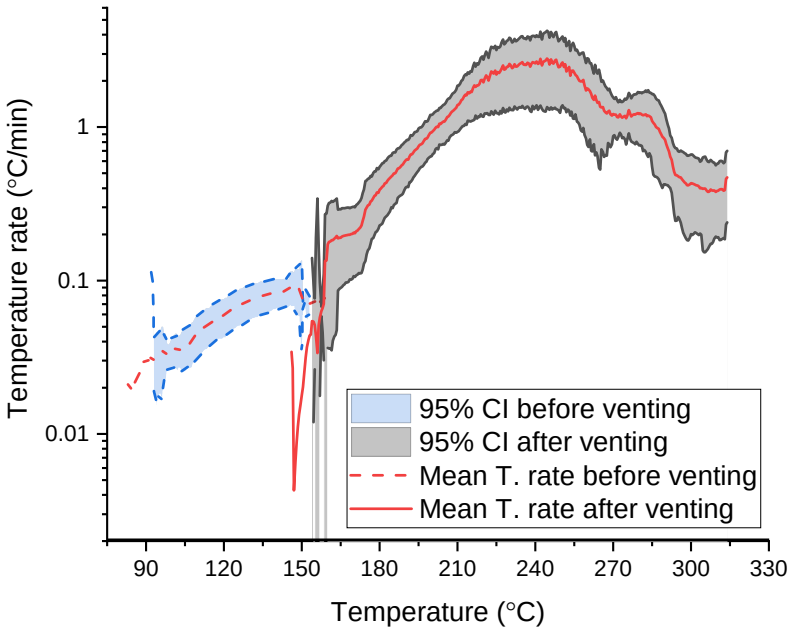

Figure 4.19: 95% confidence intervals determined from the Student-t distribution for the 100% SOC ARC tests. n=7 over the majority of the temperature range. However, due to the variation in the data, at the start and end of the "before venting" and "after venting" sub-sets n varies, see Table 4.7.

Table 4.7: Sample size over temperature range for 100% ARC results.

Before Venting		After Venting	
Temp. Range (°C)	**Sample size, n**	**Temp. Range (°C)**	**Sample size, n**
92.0–92.5	2	154.0–158.5	2
93.0–96.5	3	159.0–159.5	4
97.0–97.5	4	160.0–163.5	5
98.0–101.5	6	164.0–304.0	7
102.0–145.0	7	304.5–313.0	6
145.5–147.0	6	313.5–314.0	5
147.5–149.0	4		
149.5–150.0	3		
150.5–153.0	2		

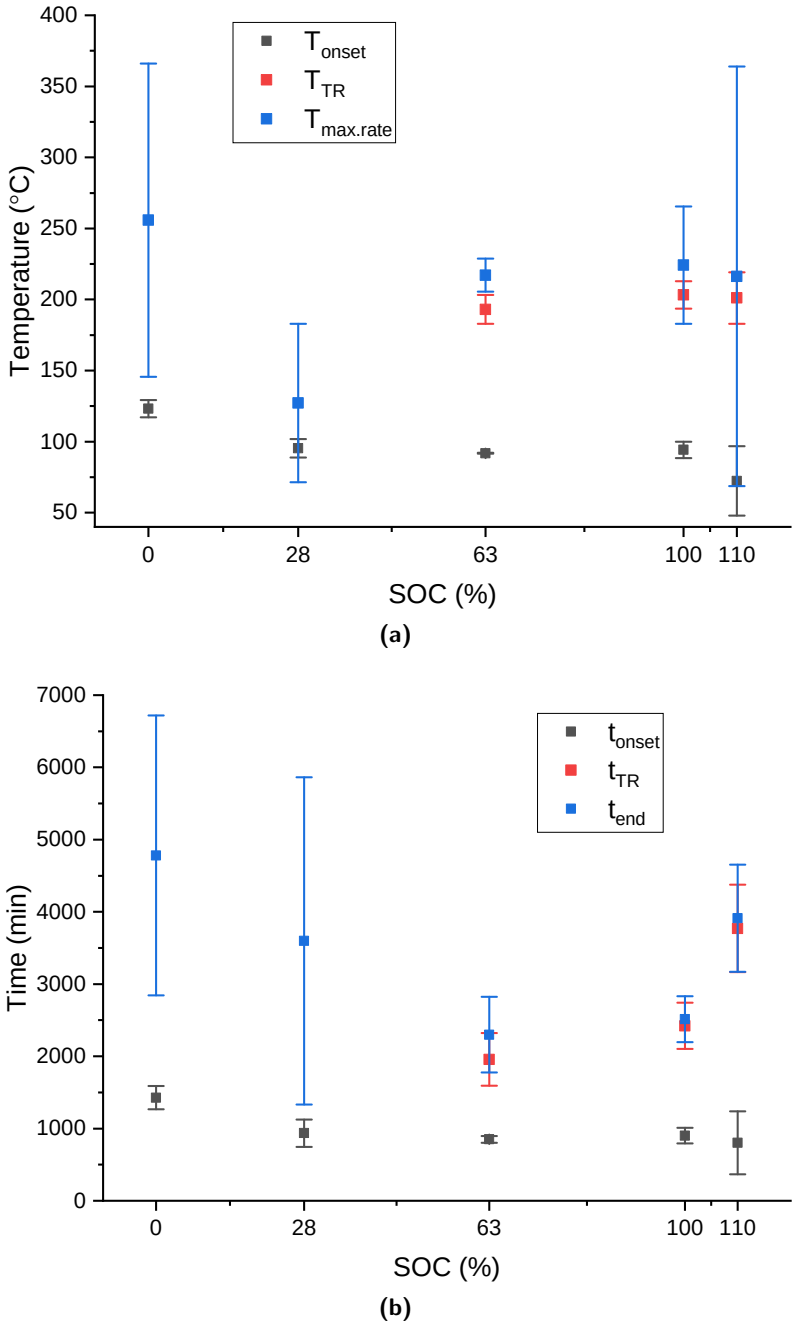

Figure 4.20: Means and 95% confidence intervals (depicted by the error bars) for specific a) temperatures, and b) times, of the ARC experiments for all SOC. n = 4, 3, 4, 7, 3 for SOC of 0%, 28%, 63%, 100%, 110%, respectively. There are no T_{TR} or t_{TR} for the 0% and 28% SOC cases as TR does not occur.

For the ARC experiments, the confidence intervals of key temperature and time points are calculated for a comparison of important stages throughout TR and for analysis of all SOC studied. Figure 4.20(a) presents the mean temperature and confidence intervals for the onset of self-heating, the onset of TR and for the maximum temperaturre rate. Similarly, Fig. 4.20(b) presents the mean time and confidence intervals for the onset of self-heating, the onset of TR and for the time to end of test.

From Fig. 4.20(a) it can be seen that the confidence intervals for the temperature at which self-heating and TR start are relatively narrow and do not overlap (for a given SOC). This means there is a statistical difference between the mean self-heating onset and mean TR onset temperatures [271]. However, the confidence intervals for the temperature at maximum temperature rate is very wide in most cases, except for 63% SOC. In the case of 28%, 100% and 110% SOC, this leads to the confidence intervals of the temperature at maximum rate overlapping the confidence intervals if the self-heating or TR onset temperatures. Similar features are present in the time plot Fig. 4.20(b) for the confidence intervals of time to TR and time to end for the 63%, 100% and 110% SOC cases.

To state that the means are statistically different in the cases were the confidence intervals overlap we first describe a null hypothesis: $\mu_0 = group\ means\ are\ the\ same$. Then, calculate the 95% confidence interval on the difference between 2 group means. If the confidence interval contains 0, then we can accept the null hypothesis and state the means are the same at the $\alpha = 0.05$ level [271]. Otherwise, we reject the null hypotheses and state that there is a difference in group means.

The 95% confidence interval on the difference between 2 group means $(\mu_x - \mu_y)$ can be found from the following equation [269]:

$$(\mu_x - \mu_y) = \left(\overline{X} - \overline{Y}\right) \pm t_{\nu,\alpha/2}\sqrt{\frac{s_X^2}{n_x} + \frac{s_Y^2}{n_Y}} \tag{4.7}$$

where the number of degrees of freedom v (rounded down to the nearest integer) is determined from:

$$\nu = \frac{\left(\frac{s_X^2}{n_x} + \frac{s_Y^2}{n_Y}\right)^2}{\frac{\left(s_X^2/n_X\right)^2}{n_x - 1} + \frac{\left(s_Y^2/n_Y\right)^2}{n_Y - 1}} \tag{4.8}$$

The notation of this equation follows that as in Eq. (4.6), but with X and Y referring to the properties of the two different groups under analysis.

Utilising Eqs. (4.7) to (4.8) the calculation of the confidence interval on the difference between 2 group means is presented in Table 4.8, for the instances where confidence intervals cross over. From Table 4.8 it can be seen that the null hypotheses is accepted in all cases. This is because the confidence interval on the difference between 2 group means

Table 4.8: 95% confidence interval for the difference between 2 group means for variable X and Y.

Variable (X,Y)	SOC	$\overline{X}$	$\overline{Y}$	s_X	s_Y	n_X	n_Y	ν	$t_{\nu,\alpha/2}$	Lower $(\mu_x - \mu_y)$	Upper $(\mu_x - \mu_y)$
T_{TR},T_{rate}	100	203.24	224.21	10.37	44.59	7	7	6.65	2.45	-63.31	21.38
T_{onset},T_{rate}	28	95.26	127.17	2.60	22.47	3	3	2.05	4.30	-88.12	24.29
T_{TR},T_{rate}	110	201.07	216.33	7.31	59.46	3	3	2.06	4.30	-164.08	133.57
T_{onset},T_{rate}	110	72.36	216.33	9.86	59.46	3	3	2.11	4.30	-293.70	5.77
t_{TR},t_{end}	63	1957.78	2299.31	229.30	328.84	4	4	5.36	2.57	-856.87	173.82
t_{TR},t_{end}	100	2422.19	2513.78	346.73	342.38	7	7	12.00	2.18	-492.91	309.73
t_{TR},t_{end}	110	3770.42	3911.80	243.79	298.04	3	3	3.85	3.18	-848.76	566.00

includes 0 in all cases. Hence, we can not say the means are different within the tested groups, e.g between T_{TR} and $T_{max,rate}$ for 100% SOC.

Intuitively, in the 100% and 110% SOC cases one would expect, for the population, the mean temperature of maximum rate to be different to (and greater than) the mean temperature of TR onset. Hence, it would be beneficial to increase the sample size to determine if the variation, and confidence intervals, reduce in size, particularly for the temperature at maximum rate, time to TR and time to end. Hence, with a greater sample size improve predictions and determine if the means of the temperature at maximum rate and TR onset are different.

4.4 Conclusion

ARC and free convection oven experiments were undertaken to investigate the stability and severity of TR in LFP cells. In both experiments, all cells remained intact, showing the that LFP cells are likely to present no explosion risk.

ARC was carried out on LFP 18650 cells at various states of charge, including overcharge. It was found that as SOC increases, so does TR severity whilst cell stability reduces. From the resulting exothermic data, the contribution of the four decomposition reactions to the thermal runaway potential of the cell for each different SOC was discussed. To date, analysis of this type has not been presented in the literature. It was found that at higher states of charge, there was an increasing overlap in the occurrence of the NE, PE and electrolyte reactions leading to an overall increase in maximum temperature rate. Also, the main contributions to TR at SOC of 100% and 110% were the negative and positive electrode reactions, while at lower SOC TR is dominated by the negative electrode reaction. At SOC greater than 0%, the negative electrode reaction is a significant contributor to self-heating onset temperature and at 110% SOC, the lithium plating reaction reduces the onset temperature. At and below 28%, SOC thermal runaway did not occur and hence is most suitable for the storage and transport of LFP cells, while for cells above 28% SOC the onset of TR occurs at approximately 200°C, at which point TR onset was due to the NE reaction. In comparison to other chemistries studied in the literature, LFP

cells have a reaction rate 3 orders of magnitude lower, even at low SOC, due to the limited oxygen production.

Oven tests were carried out to analyse the TR response of LFP 18650 cells at 100% SOC to understand how the cells respond under rapid heating, and to compare effects of the two different thermal abuse techniques on the severity of TR. It was shown that for higher oven temperatures the LFP cell had a more extreme TR event. Results indicate that if the cell temperature remains below the critical temperature (190–200°C) for cathode decomposition and electrolyte/O_2 reactions to occur, there is a significant reduction in maximum cell temperature and cell reaction rate. Hence, there is an improved ability to manage the temperature rise of the cell which in turn increasing overall safety. Compared against the literature, the LFP cells studied here are safer at a given oven temperature than other chemistries, with TR onset occurring at a higher oven temperature whilst reaching a lower maximum temperature. In oven tests, higher cell temperatures and temperature rates can be achieved than in ARC, showing how failure accelerated by external heating (where decomposition reactions are compounded) leads to more severe TR.

By comparing the heat released in both ARC and oven tests, it is shown that ARC (at temperatures up to 315°C) does not capture the full decomposition process of a cell during TR. Hence, care should be taken when determining safety from ARC results. As such it is recommended complimenting ARC with oven testing, as oven testing presents a more severe TR event. As a result, a more complete picture of TR and cell safety can be obtained.

The work of this chapter was, in part, motivated by the need of well-defined abuse conditions and an accurate record of the thermal response of cells for model development and validation. Extensive data of this kind was not available for LFP cells, a cell chemistry which is also not accurately modelled. Hence, considering the complexity of Li-ion cell TR and the level of data required (to characterise TR response under various thermal abuse conditions), this work provides an essential data set for the development of accurate LFP TR models and will be used in the following Chapter 5.

Chapter 5

Development of an Advanced Thermal Abuse Model for LFP Cells

Aims & Objectives

The aim of this chapter is to develop an extended TR abuse model, referred to as the advanced abuse model (AAM), and validate it for LFP cells. Within this, the objectives are to:

(1) show that the classical abuse model and literature parameters are not valid for LFP cells;

(2) validate the novel BPV method that describes cell pressurisation;

(3) parametrise the AAM, that includes the BPV method and simmering reactions, for an LFP cell; and

(4) investigate the effects that the governing pressure method and the inclusion of simmering reactions has on model parameterisation.

5.1 Introduction

In this chapter, the development and assessment of the novel AAM is undertaken to address points highlighted by the Literature Review in Section 2.2. Specifically, addressing the lack of accuracy of classical TR models representing LFP cells (e.g. Refs. [38, 132]), apparent when comparing the predictions of Refs. [38, 132] to the experimental work in

Chapter 4. In turn, as highlighted by Abada *et al.* [272], there is a low confidence in the parameter values used for LFP TR modelling. Further, previous work does not account for cell venting in parameterising LFP cells, which, for other chemistries, is shown to improve predictions [199]. However, the PPV method used previously to calculate internal cell pressure is uncommon for similar systems. In other words, calculating the pressure of a multiphase (liquid and vapour), multi component (e.g. electrolyte and decomposition gases) fluid is more commonly done under the bubble point assumption [200], hence the development of the novel BPV methodology (see Section 3.2.3.2).

Section 5.2, presents the results of several studies to address the points and objectives highlighted above. First, a classical TR model with literature abuse parameters is used to highlight the inaccuracies of the literature method and the behaviour that is responsible for said inaccuracies. This highlights the caution that should be taken when using parameter values quoted in the literature for the reaction kinetics. Then, the BPV method is validated against the PPV method for appropriateness of predicting cell pressurisation in TR modelling. After, the AAM (outlined in Section 3.2) is parameterised for different assumed cell composition on burst pressures. From which, the improvements of the AAM over the classical TR are shown, while affects of assumed parameters are discussed. Finally, Section 5.3 concludes the chapter, this highlights cautions that should be taken in TR model development, outlines the improvements the AAM has over the classical model, and summarises the link between reaction parameters and venting behaviour.

Throughout this chapter TR model development and parameterisation is carried out against experimental data of LFP 18650 (1.5 Ah) cells under oven exposure at 180°C and 218°C from Section 4.2.3. Parameter estimation is carried out, using heuristic fitting methods where reactions are progressively introduced to the model, and their parameters estimated to fit the model to a larger proportion of the experimental data (as discussed in Section 5.2.1). Further, throughout this work the cells' thermo-physical and heat transfer properties, as well as the initial values of the dependent variable within the decomposition reactions and the constants m_x and n_x, are kept the same between investigations. These general parameters are given in Table 5.1.

Table 5.1: General Parameters.

Parameter	Value	Source/ notes
Specific heat capacity of cell, C_p (J/kg K)	1107	measured [264]
Thickness of cell can, d_{can} (mm)	0.3	[123]
Surface emissivity of cell, ε (-)	0.8	[146]
Convection coefficient, h_{conv} (W/m^2 K)	12.5	[146]
Height of cell, h_{cell} (mm)	65	measured
Height of jelly roll, h_{jelly} (mm)	57.3	[123]
Radial conductivity of cell, κ (W/m K)	0.5	estimated
Mass of cell, m_{cell} (g)	39.9	measured
Radius of cell, r_{batt} (mm)	9	measured
Radius of mandrel, r_{man} (mm)	2	[123]
Density of cell, ρ (kg/m^3)	2418	measured [264]
Initial cell temperature, T_{init} (°C)	16.5	See note[a]
Oven set temperature, T_{oven} (°C)	180, 218	See note[a]
Simulation length, t_{length} (min)	90	See note[a]
Abuse parameters		
Initial species concentration SEI, $C_{sei,0}$ (-)	0.15	[99]
Initial species concentration NE, $C_{ne,0}$ (-)	0.75	[99]
Initial SEI thickness, $t_{sei,0}$ (-)	0.33	[99]
Initial species concentration PE, $C_{pe,0}$ (-)	0.04	[99]
Initial species concentration E, $C_{e,0}$ (-)	1	[99]
m_{sei} (-)	1	[99]
n_{sei} (-)	0	[99]
m_{ne} (-)	1	[99]
n_{ne} (-)	0	[99]
m_{pe} (-)	1	[99]
n_{pe} (-)	1	[99]
m_{ele} (-)	1	[99]
n_{ele} (-)	0	[99]

[a]set to match experimental conditions.

5.2 Results and Discussion

The *Results and Discussion* is organised as follows: Section 5.2.1 presents preliminary work on using the classical model showing its inadequacy and outlining the affect of using different assumed cell mass compositions. Section 5.2.2 validates the BPV methodology. Section 5.2.3 discusses the AAM predictions against experimental data and classical TR model results. Finally, Section 5.2.4 validates the TR predictions beyond the oven set temperatures the model was parameterised against (i.e. 180°C and 218°C) and discusses LFP cell TR behaviour beyond experimental findings.

5.2.1 Preliminary Findings - Using the Classical Abuse Model

Preliminary oven abuse simulations were carried out using a classical abuse model (i.e. without simmering reactions or venting accounted for) with literature decomposition reaction parameters (see initial values in Table 5.2 and Table 5.3). Fig. 5.1 shows the Temperature vs. Time plots of these simulations for different oven set temperatures, and compares them to experimental data from Section 4.2.3 .

From Fig. 5.1, it can be clearly seen that the simulation vastly over-predicts TR severity while under predicting time to TR. From this, the high TR temperatures suggest that the heat within this reaction model is too large. I.e. the specific mass of reactant(s) or the heat of reaction(s) are too large. Further, the early occurrence of TR suggests the onset of (at least some of) the reactions occur at too low a temperature, i.e. the activation energies are, in general, too low. Hence, the reaction parameters ($E_{a,x}$, A_x, W_x and H_x) are of interest, and an investigation should be carried out to determine their appropriate values.

Abada *et al.* [272] has shown the importance of the values of specific masses. The specific mass of a jelly roll component can be derived from the mass of a given component within a cell divided by the jelly roll volume, V_{jelly} (here this takes a value of $\text{V}_{\text{jelly}} = 1.29 \times 10^{-5}\,\text{m}^3$, calculated from Eq. (5.1)). Several references give the mass composition of Li-ion cells, with [65] and [273] giving values for LFP 18650 cells specifically, which are presented in Table 5.4. The relative masses from Table 5.4 allow for the estimation of two cell compositions of the cells studied here (also presented in Table 5.4), providing two case studies, referred to as Cell A and Cell B. Cell A is derived from the mass ratios of [65], while Cell B is derived from the mass ratios of [273]. The calculated respective specific masses for each component in each case are presented in Table 5.5.

$$V_{jelly} = \pi h_{jelly} \left((r_{batt} - d_{can})^2 - r_{mandrel}^2 \right) \tag{5.1}$$

Comparing Table 5.5, showing the calculated specific masses, and Table 5.3, showing literature values, clearly presents that there significant differences between the two.

Table 5.2: Abuse parameters for LFP cells, from literature and estimated parameters in terms of a factor of original value, which were used in preliminary studies.

Parameter	Absolute value Initial Case (from [38])	Scaling factor Case A	Case B
E_{a_ne} (J/mol)	1.3508×10^5	1.05	1.06
E_{a_sei} (J/mol)	1.3508×10^5	1.1	1.115
E_{a_pe} (J/mol)	1.03×10^5	0.935	0.965
E_{a_e} (J/mol)	2.74×10^5	1.1	1.05
A_{ne} (1/s)	2.5×10^{13}	1.0	1.0
A_{sei} (1/s)	1.667×10^{15}	1.0	1.0
A_{pe} (1/s)	2×10^8	1.0	1.0
A_e (1/s)	5.14×10^{25}	1.0	1.0
H_{ne} (J/g)	1714	2.0	1.65
H_{sei} (J/g)	257	2.249	2.249
H_{pe} (J/g)	194.7	1.24	1.0
H_e (J/g)	155	2.2	1.9

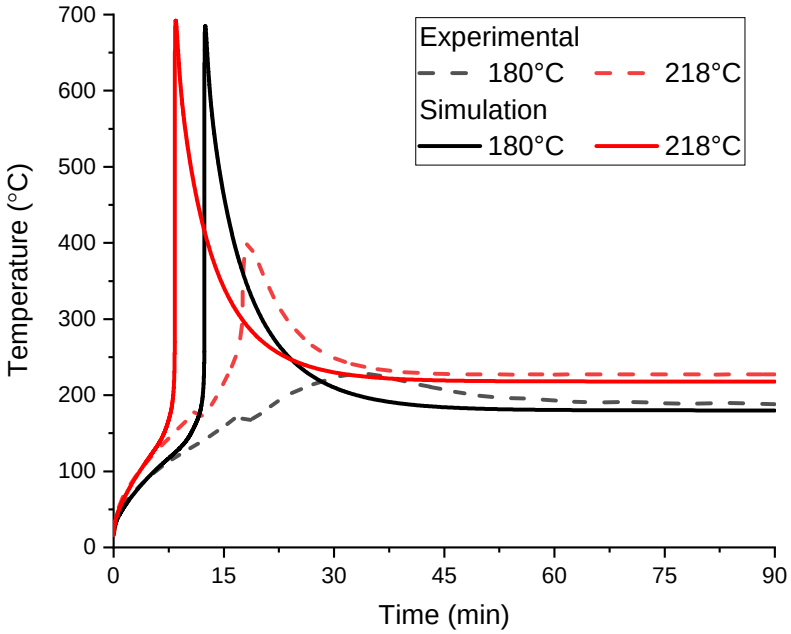

Figure 5.1: Preliminary results employing classical thermal runaway model simulating oven exposure using literature parameters (see initial values Table 5.2 and Table 5.3).

Table 5.3: Range of specific masses used in the modelling of TR (PE specifically for LFP cells), and values used by Peng and Jiang [38] which are used in the initial simulations in this work. *Values taken from references [38, 78, 82, 99, 190].

Specific Mass	Range*	Initial Values
W_{ne} (kg/m^3)	610-1700	1700
W_{pe} (kg/m^3)	960	960
W_e (kg/m^3)	407-500	500

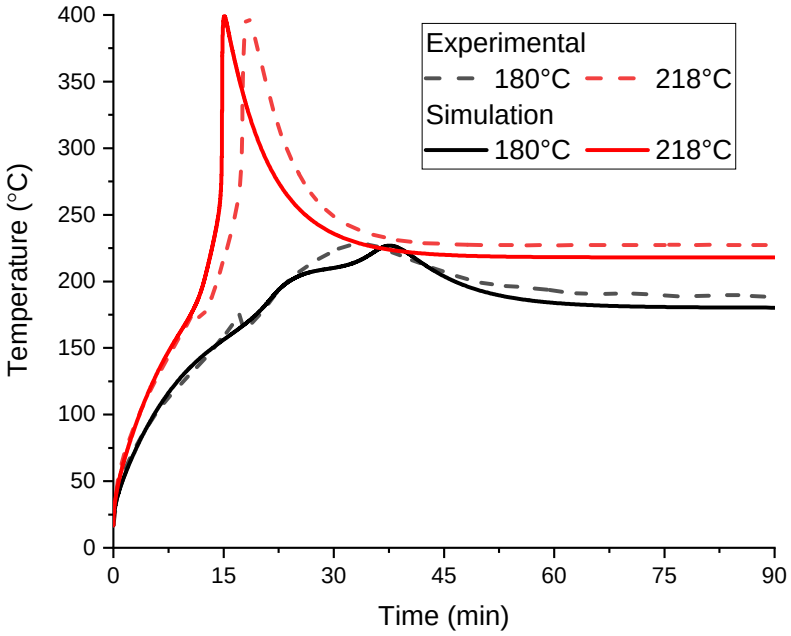

(a)

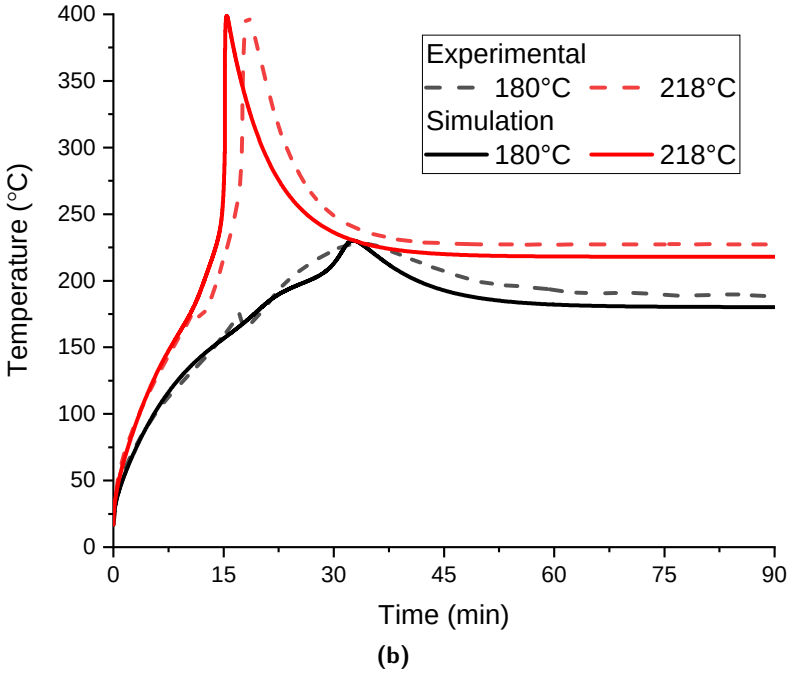

(b)

Figure 5.2: Preliminary results employing classical thermal runaway model simulating oven exposure: (a) and (b) fit of abuse parameters given the specific masses (of Table 5.5) for case A and B, respectively.

Table 5.4: Cell composition by mass from literature and estimates for the cell under study.

	Ref. [65]		**Ref. [273]**		**Estimates for cell under study**	
Capacity (Ah)	1.1		n/a		1.5	
	g	%	g	%	Cell A (g)	Cell B (g)
Cell Total	38.87		45.00		39.90	39.90
Cathode, active	7.73	19.90	14.22	31.60	7.94	12.61
Cathode, other	1.93	4.97	1.94	4.31	1.98	1.72
Anode, active	4.84	12.46	8.15	18.11	4.97	7.23
Anode, other	0.34	0.88	0.90	2.00	0.35	0.80
Electrolyte	6.41	16.50	2.20	4.89	6.58	1.95
Separator	1.15	2.96	2.00	4.44	1.18	1.77
Case	10.45	26.90	10.09	22.42	10.73	8.95
Foil	6.00	15.44	5.50	12.22	6.16	4.88

Table 5.5: Calculated specific masses for cell mass compositions of Case A and B.

	Case A		**Case B**	
	g	kg/m^3	g	kg/m^3
Anode, active	4.97	385	7.23	560
Cathode, active	7.94	615	12.61	977
Electrolyte	6.58	510	1.95	151

Also, there is a large difference in the ratios of specific masses between the two cases (Table 5.5). This highlights the uncertainty in the literature regarding appropriate values of specific mass of reactants. In turn, this makes it a necessity to evaluate the effect of the specific mass values on determining the remaining abuse parameters through parameter estimation.

With the specific masses set to those from Table 5.5, parameter estimation on the abuse parameters ($E_{a,x}$, A_x and H_x) was carried out using the classical TR model. Using the classical TR model and the specific masses of Table 5.5, three stages of parameter estimation were carried out. Where each stage was developed on the findings of the previous. Stage 1 utilised the (initial) kinetic parameters of Table 5.2. Stage 2 required updating the upper bounds of the heat of reaction of the SEI and electrolyte reactions to be that of the upper values used in the literature ($H_{sei,max}$ = 578J/g , $H_{e,max}$ = 645J/g). Then, within these bounds, parameter estimation was carrying out on the SEI and electrolyte heats of reaction and on the activation energies for all reactions. Finally, Stage 3 required increasing the upper bounds on the heats of reaction for the NE and PE reactions, see Table 2.1. Then, again, carrying out parameter estimation on all activation energies and heats of reaction. Following this procedure, the resulting prediction of cells undergoing TR during oven testing is presented in Fig. 5.2(a) and Fig. 5.2(b), for case A and B respectively.

From the results presented in Fig. 5.2(a) and Fig. 5.2(b), it can be seen the severity of TR has been be predicted accurately, significantly improving predictions over those using the initial values used in Table 5.2. However, the shape of the temperature profiles compared to the experimental data differ in agreement depending on the oven set temperature. For both cases A and B, at the higher oven temperature the cell surface temperature profile resembles that of the experimental data well. Further, for the lower oven temperature (180°C) case, while the peak temperature is predicted accurately, the smooth temperature profile is not reproduced. At the higher oven temperature (218°C), without the occurrence of venting (investigated in Section 5.2.2) the TR incident occurs sooner than that in the experiment. For each oven temperature, the model does not simulate any simmering reactions (investigated in Section 5.2.3), causing the discrepancies, seen at later times between, the simulation and experimental results.

Table 5.2 presents the estimated parameters used to produce the predictions of Fig. 5.2(a) and Fig. 5.2(b). From this table, it is shown that to meet the TR maximum temperature the model requires significant changes, from initial values, of the heat of reaction of the reactions.

5.2.2 Vent Sub-Model Development

A reproduction of the work by Coman *et al.* [199] for predicting internal cell pressure and venting behaviour is first presented for validation. Then, a comparison between the PPV method and the BPV method is made.

The reproduction of the predicted pressures vs. average cell temperature by the partial pressure model is presented in Fig. 5.3, along with the original data from Coman *et al.* [199] for comparison. The original data is titled "Literature" in the legend, while the title "Reproduction" refers to the results of this work. It can be seen from Fig. 5.3 that the overall prediction of cell pressure P_{tot} is reproduced well, although there is an under prediction of P_{tot} over the entire temperature range up to the point of venting. The cause of this under prediction is discussed below.

The total pressure, as defined by Eq. (3.41), is the sum of the saturation and gas pressures. The saturation pressure is governed by the same empirical formula in both modelling approaches, hence is exactly reproduced in Fig. 5.3. Then, rationally, it is clear that it is the prediction of the gas pressure that is leading to the discrepancies in the total pressure. This can be seen from the differences in the gas pressure plots of Fig. 5.3. The gas pressure, P_g, of the reproduction does not begin to deviate from the initially linear pressure increase until a higher temperature of approximately 115°C. At this point, the increase of pressure with temperature is slow compared with the literature data. At approximately 130°C, the gradient of pressure with temperature of the reproduction begins to become steeper than the literature. This continues to increase in gradient up to the

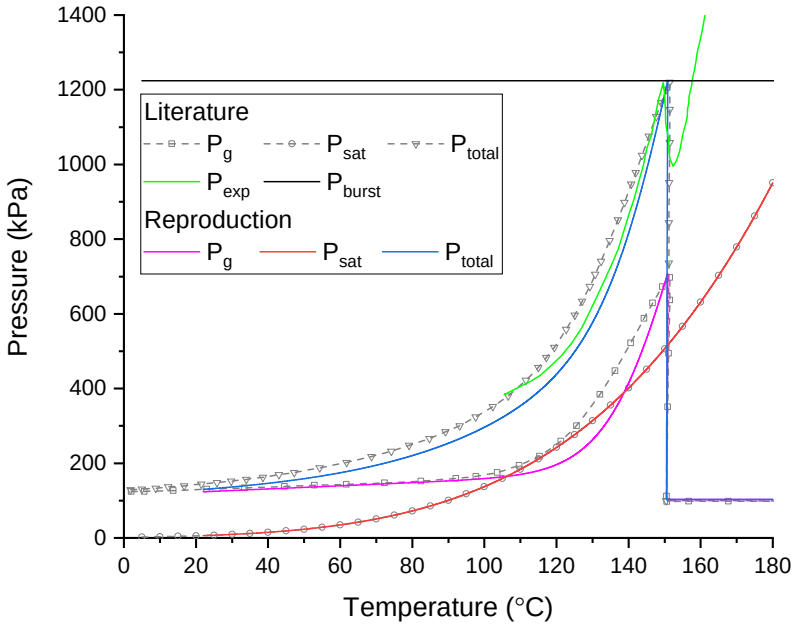

Figure 5.3: Validation of the reproduced PPV method. Literature from [199].

point of venting. Thus leading to the temperature of venting in the reproduction to be the same as in the literature.

As sated in the methodology (Section 3.2.3), the gas pressure is governed, in part, by the SEI reaction species. However, due to the slight differences in the formulation of the SEI decomposition equation in this work and in the work by Coman *et al.* [199], there is a difference in the fitted value of the SEI reaction activation energy. However, the implementation here of the partial pressure model is deemed acceptable. This is because the temperature at which venting is predicted is reproduced correctly, and the fact that the deviation of the reproduction from the experimental plot in Fig. 5.3 is of the same magnitude as the deviation of the literature prediction from the experimental.

A comparison between the current method (i.e. the PPV method by Coman *et al.* [199]) and the new BPV method is now presented. In both cases the following parameters are used: the general properties from Table 5.1, the specific masses of Cell A from Table 5.5, the abuse parameters corresponding to column A of Table 5.2 and a burst pressure (P_{burst}) of 1224 kPa.

Figure 5.4(a) shows the surface temperature of a cell under oven abuse simulations considering both venting methodologies. This data is presented for two oven set temperatures, and is further compared with experimental results. The venting methodology has little effect on the overall predicted temperature profile and TR behaviour. The most significant difference between the methodologies is the temperature at which venting is predicted. As can be seen in Fig. 5.4(b), the BPV method predicts venting at a later time/ higher temperature and is closer to the experimental data.

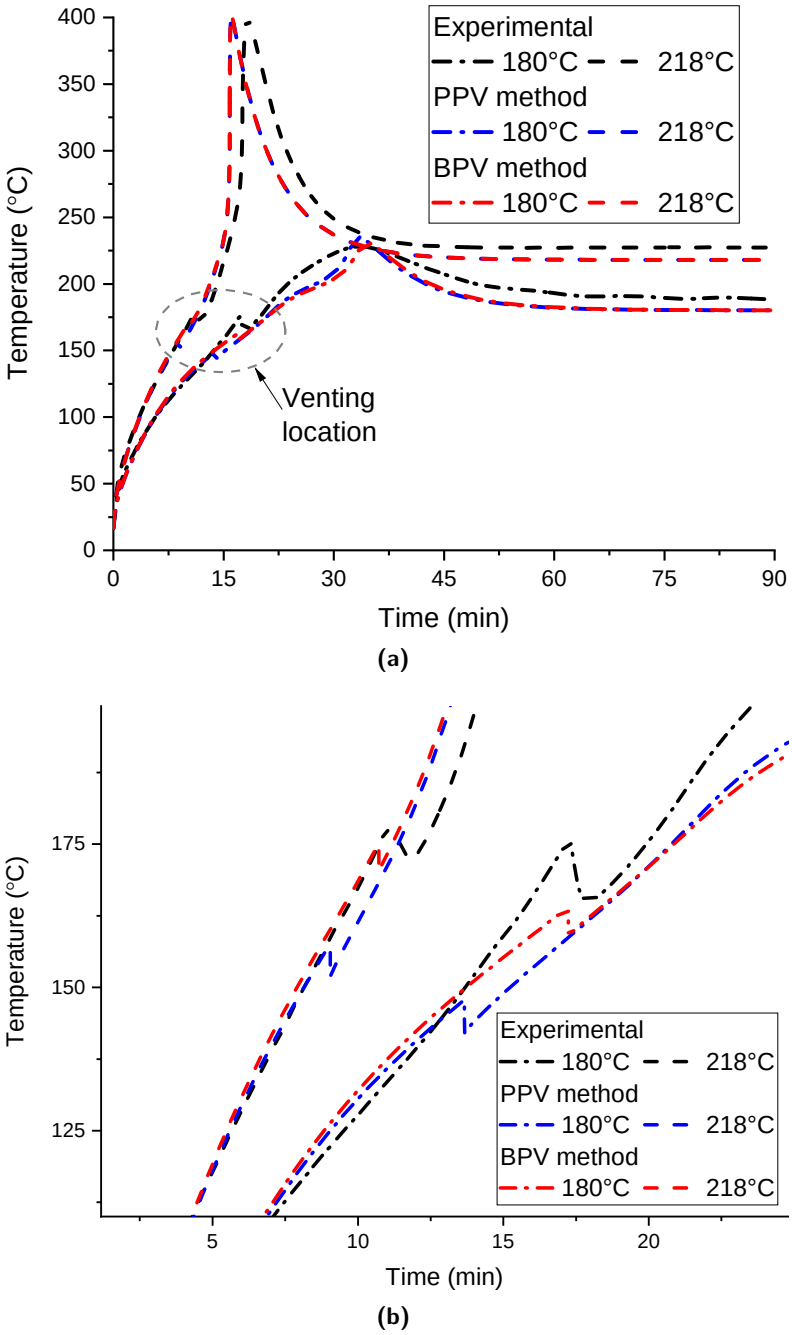

Figure 5.4: Oven abuse simulations for both internal pressure methods (a) whole time frame (b) enlargement of venting location.

The location of venting predicted by the BPV method can be further analysed by looking at the pressure vs. surface temperature plots in Fig. 5.5(a). Firstly, it is important to note that, following the bubble point assumption, there should only exist a single electrolyte temperature for a given pressure and bulk mole fraction, this is not the case for the surface temperature. Unlike the PPV method, which predicts a steady increase in pressure due to the saturation and gas pressures, the BPV method predicts little pressure increase until approximately 110°C, at which point the pressure increases steeply. The sudden pressure increase in the BPV method simulation is because the cell is initially at a pressure of 0.1 MPa, which, for temperatures below 110°C and a mole fraction near the initial value, is greater than the bubble pressure. Hence, the pressure remains constant until temperatures greater than 110°C, at which point the bubble pressure is greater than 0.1 MPa and the pressure increases according to Eq. (3.57). Further, as the mole fraction remains relatively constant up to 125°C (see Fig. 5.5(b)), it is clear that the increase in pressure up to approximately 125°C is predominantly determined by temperature.

As discussed above, the pressure predictions at lower cell temperatures are significantly different between methods. However, once the mole fraction within the BPV method starts to increase, i.e. when gas begins to be generated, then the pressure prediction of the BPV method resembles that of the PPV method. Although, the pressure profiles between methods are somewhat offset along the temperature axis.

As stated above, there is a difference in the predicted temperature at which venting occurs between the two methods. However, one must consider that the literature, i.e. [199], fits the point of venting in simulations to experimental data by altering the SEI reaction activation energy. Hence, it is conceivable that either method could be used to predict venting in TR modelling, although each would require different reaction parameters to provide the same location of venting. However, the BPV method is, the author believes, more representative of the system under study as it accounts for the phase equilibria of the mixture, unlike the PPV model which assumes the CO_2 generated is entirely in the gaseous phase. Therefore, the BPV method will be used in the remainder of this work.

Further, one can see in Fig. 5.4 that the BPV model predicts venting closer to the experimental data for the given parameter set. However, if the assumed burst pressure were to be higher (as in [221]) then the point of venting for both methods would be at a higher temperature. Hence, it can be clearly recognised that the assumed burst pressure can have an indirect influence on the abuse parameters through the need to accurately fit the location of venting. This will be systematically investigated as part of Section 5.2.3.

5.2.3 Advanced Abuse Model Investigation

This section discusses the results of the AAM, which includes venting phenomena and a reaction to describe simmering reactions. This is to address the suggested improvements

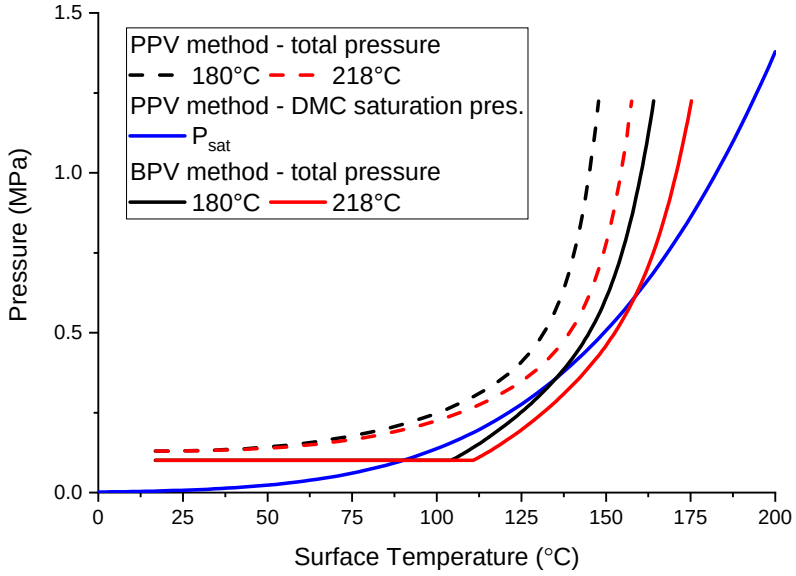

Figure 5.5: Comparison of (a) Pressure vs. temperature (b) vapour or mixture fraction vs. temperature, from oven abuse simulations for both internal pressure methods.

in Section 5.2.1, along with a study of the effects of assumed burst pressure on estimated abuse parameters.

Figure 5.6 shows the resulting temperature plots of oven simulations for the two different mass fractions (see Table 5.5) and for two different burst pressures ($P_{burst,Low}$ = 1224 kPa and $P_{burst,High}$ = 2158 kPa). It can be clearly seen from Fig. 5.6(a) and Fig. 5.6(b) that the AAM predicts TR very accurately for the higher oven temperature exposure when compared to the experimental data, and vastly improves predictions when compared the classical abuse model, see Fig. 5.2(a) and Fig. 5.2(b). Specifically, the implementation of the venting behaviour delays TR noticeably, such that the peak temperatures of the simulation occur at a closer time to the experimental peak than the predictions of the classical model. Additionally, under the lower oven temperature abuse scenario the shape of the temperature profile better resembles the experimental results when using the AAM when compared with the classical model.

From Fig. 5.6(a) and Fig. 5.6(b) it can be seen for the lower oven temperature exposure case the peak temperature and time to peak temperature are under predicted. Through the parameter estimation process, it was found that to accurately predict the peak temperature for the 180°C oven exposure case one of two conditions needed to be met:

1. the heat of reaction of the NE reaction needed to be increased. However, this lead to TR occurring too soon under the higher oven temperature exposure case. Or,

2. lowering of the onset of the PE reaction. However, this also lead to TR occurring too soon under the higher oven temperature exposure case. Additionally, this also lead to "deforming" of the temperature profile for the lower oven exposure case (such that it does not resemble the experimental data) due to the faster rate of the PE reaction compared to the NE reaction.

Hence, it is suspected that there are secondary or interdependent reactions that are of a similar reaction rate to the NE reaction but are most important to consider at lower oven exposure temperatures. These additional reactions are thought to be SEI reformation/decomposition and/or secondary NE dependent reactions.

Inspection of the temperature profile upon venting shows that the predicted temperature drop occurs more rapidly than in the experimental data, see Fig. 5.6(c) and Fig. 5.6(d). Clearly, if the venting behaviour was predicted to occur over a greater time period, then the peak temperature would, in turn, be predicted later and more accurately when compared with the experimental data. Hence, while the venting methodology used here significantly improves predictions, it also identifies that there are some important phenomena missing. It is hypothesised that this could be due to a disequilibrium between phases [274], as, upon venting of the vapour, there is a rapid pressure drop. When there is a pressure drop, for the liquid to remain in equilibrium, it has to cool accordingly. If

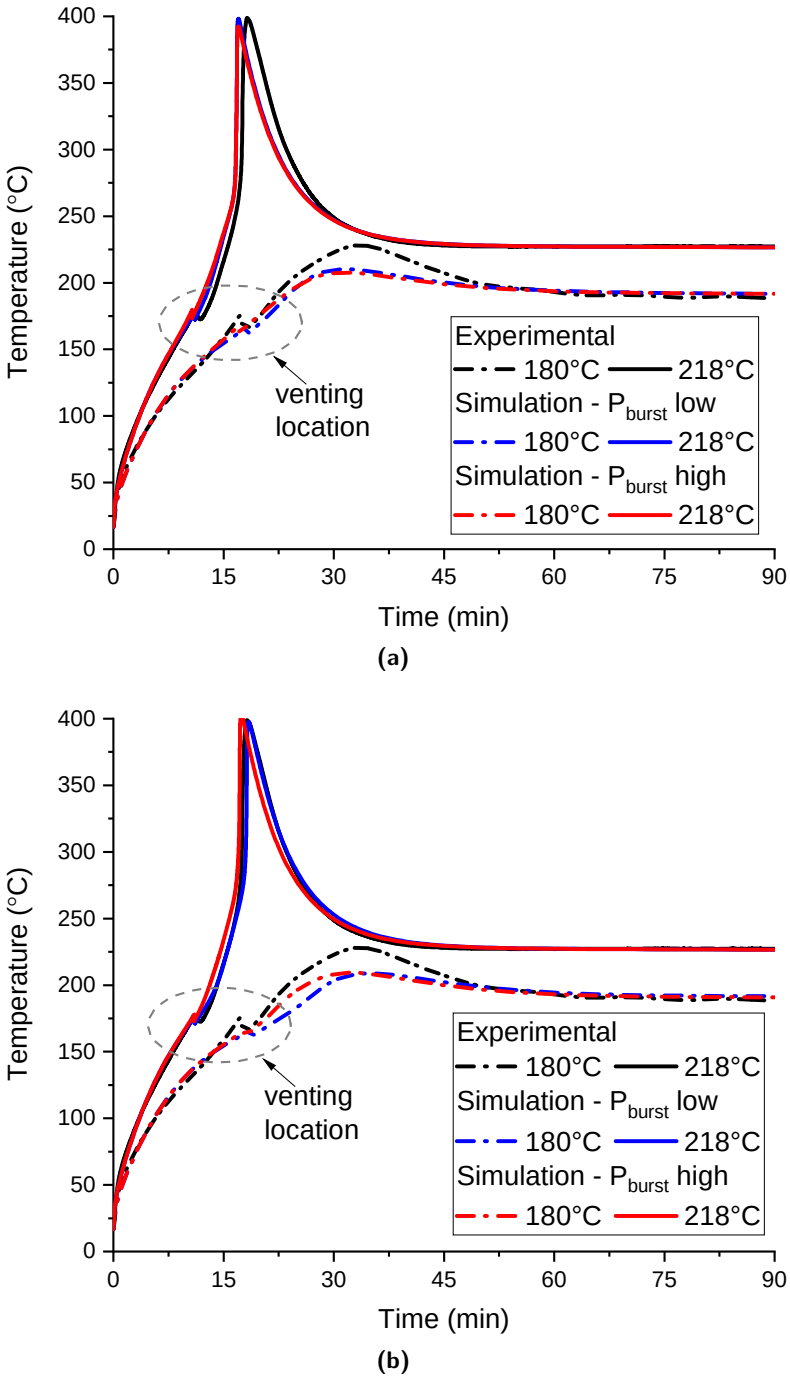

Figure 5.6: Temperature plots for oven abuse simulations for parametrised advanced abuse model (a) mass composition A (b) mass composition B (c) enlargement of venting location mass composition A and (d) enlargement of venting location mass composition B.

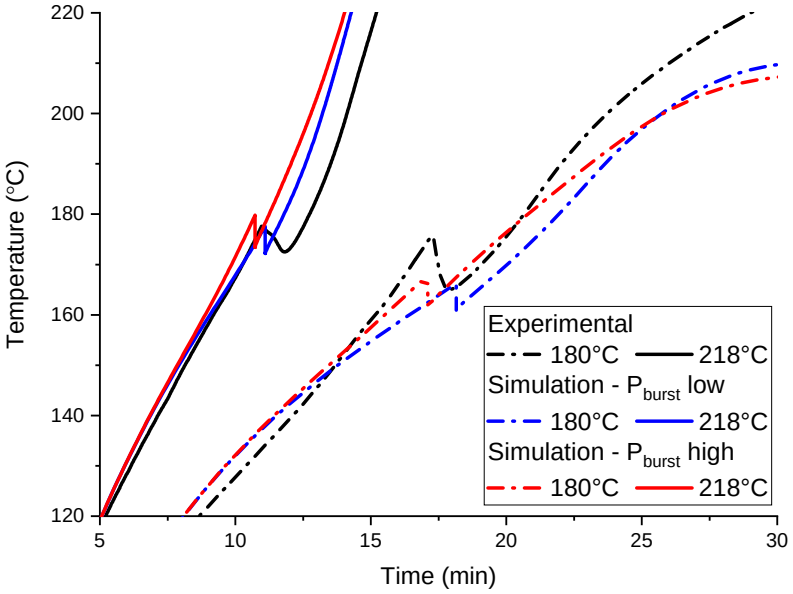

(c)

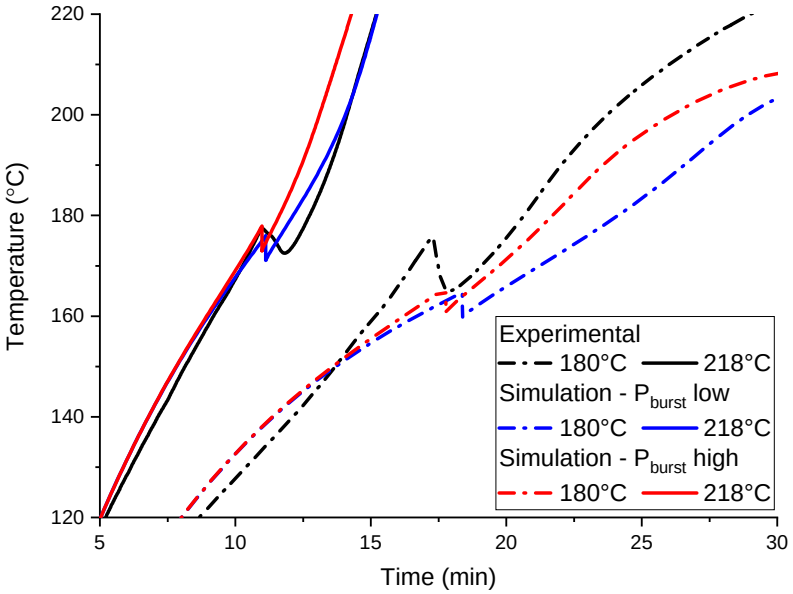

(d)

Figure 5.6 (cont.): Temperature plots for oven abuse simulations for parametrised advanced abuse model (a) mass composition A (b) mass composition B (c) enlargement of venting location mass composition A and (d) enlargement of venting location mass composition B.

the liquid does not cool at a rate quickly enough for the rate of pressure drop, this leads to superheated liquid, as has been seen elsewhere (see for example [275]). Equilibrium is re-established after some time as the liquid evaporates/ flashes, during which the depressurisation rate is reduced because the pressure starts to recover due to the volume increase of evaporation. Further, the inclusion of the simmering reaction improves the predictions after the TR event, showing its importance to the AAM.

On inspection of the estimated parameters for the AAM (see Table 5.6) it can be seen that the values of the SEI, PE and electrolyte heats of reaction lie within the bounds presented in the literature (see Table 2.1). However, of most interest is the estimated values of the NE heat of reaction, which are somewhat larger than the upper bound in Table 2.1. This is a direct result of the value of the specific masses of carbon used, as the heat generated is directly related to the product of specific mass and heat of reaction for a given reaction. As can be seen from Table 5.5, the value of specific mass of carbon used in the AAM (385–560 $\mathrm{kg/m^3}$) is much smaller than that used in the literature, i.e. 1700 $\mathrm{kg/m^3}$ (see Table 5.3). Further, for the case in which the specific mass of carbon is lowest, i.e. cases A, the value of H_{ne} is highest. The values of H_{ne} are relatively high, i.e. 3771 J/g for case A and 2914 J/g for case B see Table 5.6, compared to the initial case, 1714 J/g see Table 5.2. However, in case B the value of H_{ne} is not significantly larger than the upper values found in the literature (see Table 2.1). The value of H_{ne} is closer to literature bounds for the simulation utilising mass composition B than with A. This suggests that the mass ratio used in case B is a better representation of the mass composition of the cell under study.

As the largest discrepancy in temperature predictions is for the lower oven temperature case, see Fig. 5.6, where the PE reaction does not occur, both improving the prediction at lower oven temperature and reducing the estimated value of H_{ne} could be addressed by the inclusion of additional reactions. With this, it is suggested that other reaction(s), such as possible secondary and tertiary decomposition of active materials, decomposition of the reaction products and reactions involving the binder, should be accounted for, concurring with comments and findings made by Hatchard *et al.* [146] and Ping *et al.* [86].

Table 5.7 presents the heat generated by each reaction over the entire 90 min simulation, and also the heat generated by each reaction over the time only up to the point of maximum cell temperature. This table shows that the model predicts that, under the high oven temperature exposure, approximately 16 kJ of heat is produced. It should be noted that this is almost equal to the 17 kJ of electrochemically stored energy of the cell [264]. For the entire time period, under both oven set temperatures, the majority of this heat is produced by the NE reaction and the simmering reaction. However, up to the point of maximum cell temperature, it is the NE reaction that dominates the total heat generated, with a considerable contribution from the PE reaction at higher oven abuse temperatures.

Table 5.6: Advanced abuse model parameters.

Parameters	A.Pl	A.Ph	B.Pl	B.Ph	Source/ note
Abuse sub model					
W_{carbon} (kg/m^3)	385.12	385.12	560.24	560.24	estimated, see Table 5.5
W_{pos} (kg/m^3)	615.26	615.26	977.13	977.13	estimated, see Table 5.5
W_e (kg/m^3)	m_e/V_{jelly}				-
$m_{e,0}$ (g)	6.58	6.58	1.95	1.95	estimated, see Table 5.5
$E_{a,ne}$ (J/mol)	1.4183×10^5	1.4042×10^5	1.4751×10^5	1.4325×10^5	fit
$E_{a,sei}$ (J/mol)	1.5007×10^5	1.4413×10^5	1.5453×10^5	1.5007×10^5	fit
$E_{a,pe}$ (J/mol)	1.0197×10^5	1.0197×10^5	1.0197×10^5	1.03×10^5	fit
$E_{a,e}$ (J/mol)	2.877×10^5	2.877×10^5	2.877×10^5	2.877×10^5	fit
A_{ne} (1/s)	2.0×10^{13}	1.75×10^{13}	2.25×10^{13}	1.25×10^{13}	fit
A_{sei} (1/s)	1.667×10^{15}	1.667×10^{15}	1.667×10^{15}	1.667×10^{15}	fit
A_{pe} (1/s)	1.4×10^8	1.4×10^8	1.2×10^8	1.4×10^8	fit
A_e (1/s)	3.598×10^{25}	3.598×10^{25}	5.14×10^{25}	5.14×10^{25}	fit
H_{ne} (J/g)	3771	3771	2914	2914	fit
H_{sei} (J/g)	578	578	578	578	fit
H_{pe} (J/g)	292	292	204	224	fit
H_e (J/g)	170	170	164	178	fit
Venting sub model					
$m_{vented,0}$ (g)	0.8	0.8	0.7	0.7	fit
P_{burst} (kPa)	1224 [a]	2158 [b]	1224 [a]	2158 [b]	[a][199], [b][221]
A_v (m^2)	8.9×10^{-6}				[221]
γ (-)	1.4				[199]
k_b (J/K)	1.38×10^{-23}				[199]
M_{DMC} (g/mol)	90				[199]
M_g (g/mol)	44.01				CO_2
$m_{g,rxn}$ (g)	0.88				[65]
P_0 (kPa)	130				[199]
P_{amb} (kPa)	101				[199]
R_{DMC} (J/kg K)	92.38				[199]
R_g (J/kg K)	188.9				CO_2
V_{cell} (m^3)	1.654×10^{-5}				[199]
V_h (m^3)	$0.07*V_{cell}$				[199]
$X_{mixture,0}$ (-)	8.2308×10^{-4}				Calculated from [199]

From the above discussion, for the LFP cell under study, it can be said that TR is dominated by the heat from NE reaction, followed by the PE (at higher oven temperatures), until the point of maximum temperature. After this point, the heat generated is dominated by the simmering reaction followed by NE reaction, while for lower oven temperature the PE reaction contributes. As such, the greatest improvement to the safety of LFP cells can be made through cell developments that lead to a reduced heat of reaction of the NE reaction, for example, by electrolyte additives [276] or anode structure [277]. Further, while it has been shown that the heat lost through venting is important to improve temperature predictions, its value is small in comparison to the total energy released by decomposition reactions before the maximum cell temperature. Hence, the exclusion of such behaviour would only lead to small errors in the predicted total heat generated.

5.2.3.1 Venting Behaviour

This section discusses the venting behaviour in further detail. Assessing the influence of assumed burst pressure on model prediction and parameterisation. Identifying the reaction(s) that lead to venting and discussing the causes of discrepancies within the temperature drop of the cell at venting.

Table 5.7: Heat released for different mass compositions and burst pressure scenarios under oven test simulations. (The values in brackets represent the heat released up to the point in time that maximum cell temperature occurs).

	Heat (kJ)							
	Mass composition A				Mass composition B			
	T_{oven}=180°C		T_{oven}=218°C		T_{oven}=180°C		T_{oven}=218°C	
	$P_{burst,low}$	$P_{burst,high}$	$P_{burst,low}$	$P_{burst,high}$	$P_{burst,low}$	$P_{burst,high}$	$P_{burst,low}$	$P_{burst,high}$
SEI	0.43 (0.43)	0.43 (0.43)	0.43 (0.43)	0.43 (0.43)	0.63 (0.63)	0.63 (0.63)	0.63 (0.63)	0.63 (0.63)
NE	3.09 (2.19)	3.16 (2.26)	7.62 (6.24)	7.56 (6.17)	2.57 (1.65)	2.89 (1.95)	8.07 (6.54)	8.26 (6.73)
PE	1.25 (0.09)	1.14 (0.08)	2.23 (2.23)	2.23 (2.23)	1.07 (0.09)	0.89 (0.08)	2.71 (2.71)	2.71 (2.71)
Electrolyte	0.01 (0.00)	0.00 (0.00)	1.01 (1.01)	1.01 (1.01)	0.00 (0.00)	0.00 (0.00)	0.24 (0.24)	0.24 (0.24)
Simmering	3.57 (0.66)	3.58 (0.70)	4.79 (0.32)	4.81 (0.35)	3.50 (0.78)	3.54 (0.71)	4.76 (0.39)	4.79 (0.36)
Total	**8.34 (3.37)**	**8.31 (3.47)**	**16.06 (10.22)**	**16.04 (10.18)**	**7.76 (3.14)**	**7.95 (3.37)**	**16.41 (10.51)**	**16.64 (10.67)**
Venting	-0.14	-0.13	-0.14	-0.13	-0.12	-0.11	-0.11	-0.10

Returning to Fig. 5.6, it can be seen that the choice of burst pressure has little effect on overall TR predictions. However, venting is predicted to occur at slightly later times and lower temperatures for a lower burst pressure than compared with higher burst pressures. This can be explained by further looking at the fitted abuse parameters (see Table 5.6) and the plots of reaction species with time (Fig. 5.7). By comparing the activation energies of the reactions for the two burst pressure cases (see Table 5.6), it can be seen that at the higher burst pressure the model requires lowering of the activation energies of the SEI and NE reaction slightly (by 1% to 4%), compared with the lower burst pressure limit. This is due to more gas being required to be generated to meet the higher pressure limit while at the same temperature limit of experimental data. As such, the reaction(s) have start earlier at lower temperatures. This can be seen by the dashed lines in Fig. 5.7. As the reactions start earlier, heat is generated earlier and the cells reach higher temperatures earlier. Hence, the time to venting is shorter but it occurs at slightly higher temperatures. However, this shows that by lowering the activation energy of the reactions, the temperature at which venting occurs can be controlled for different assumed burst pressures.

Table 5.8 presents the degree of conversion of each reaction just prior to venting. This table shows that the SEI reaction is the only reaction to undergo a significant degree of conversion, while the NE reaction contributes slightly to the overall decomposition and gas generation. Hence, under the assumption that the mass of gas is dependent on the equal weighting of the four decomposition reactions (see Eq. (3.46)), gas generation from the SEI and NE reactions are the main contributors to initial gas generation and cell pressurisation up to the cell burst pressure of the experimental results. However, due to the large mass difference between the anode and the SEI it is logical that the NE reaction would produce more gas than the SEI reaction (when fully decomposed). As such, even though the NE reaction is much slower than the SEI it may have a greater influence (than calculated here) on gas generation up to the point of venting. This implies it would be beneficial, in further work, to separate out the gas generation terms for each reaction to identify the amount of gas produced by each reaction through TR.

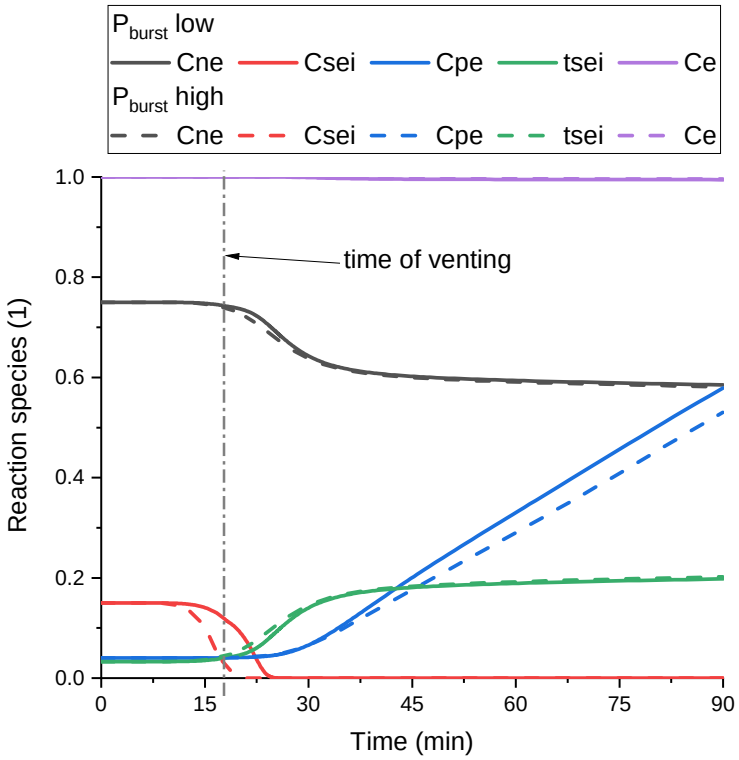

(a)

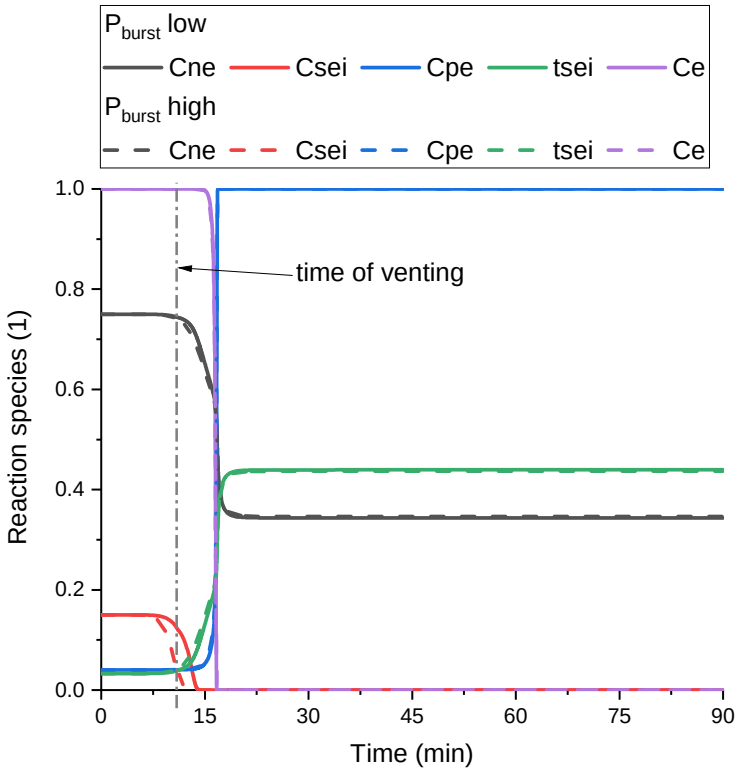

(b)

Figure 5.7: Plots of the cell decomposition species vs. time at different oven temperature, cell mass compositions and burst pressure limits. Sub-figures: (a) oven at 180°C, mass composition A; (b) oven at 218°C, mass composition A; (c) oven at 180°C, mass composition B; (d) oven at 218°C, mass composition B, for high and low burst pressures. Time of venting is average of both the high and low burst cases (as, on the time scale shown, individual lines for each pressure limit are indistinguishable).

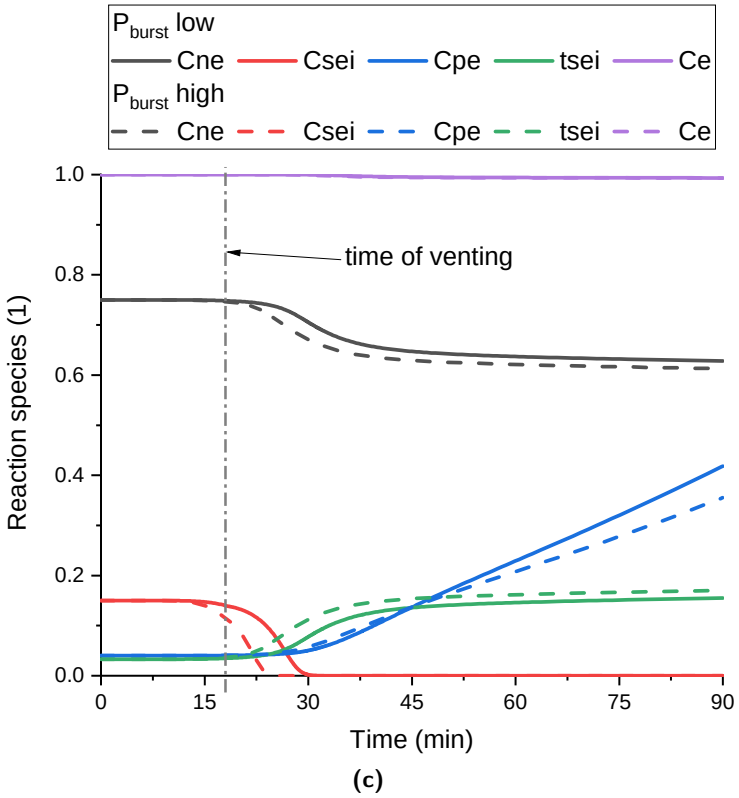

(c)

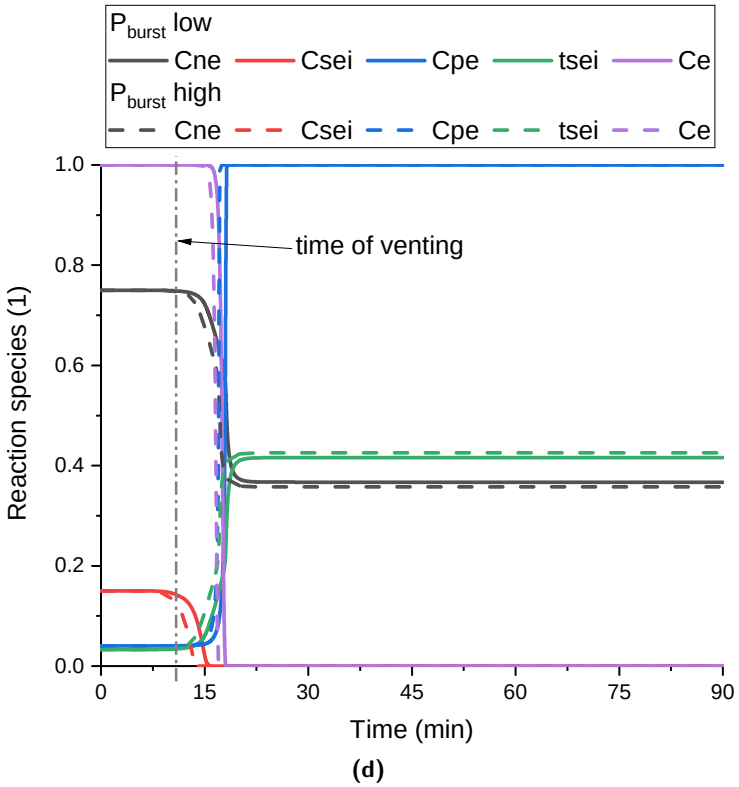

(d)

Figure 5.7 (cont.): Plots of the cell decomposition species vs. time at different oven temperature, cell mass compositions and burst pressure limits. Sub-figures: (a) oven at 180°C, mass composition A; (b) oven at 218°C, mass composition A; (c) oven at 180°C, mass composition B; (d) oven at 218°C, mass composition B, for high and low burst pressures. Time of venting is average of both the high and low burst cases (as, on the time scale shown, individual lines for each pressure limit are indistinguishable).

Table 5.8: Percentage degree of conversion for each reaction at the point just prior to venting for different mass compositions and burst pressure scenarios.

	Degree of conversion (%)							
	Mass composition A				**Mass composition B**			
	T_{oven}=180°C		**T_{oven}=218°C**		**T_{oven}=180°C**		**T_{oven}=218°C**	
	$P_{burst,low}$	**$P_{burst,high}$**	**$P_{burst,low}$**	**$P_{burst,high}$**	**$P_{burst,low}$**	**$P_{burst,high}$**	**$P_{burst,low}$**	**$P_{burst,high}$**
C_{sei}	23.87	72.79	19.95	66.17	7.50	22.34	6.25	20.24
C_{ne}	1.07	1.24	0.87	1.10	0.27	0.45	0.22	0.40
C_{pe}	0.07	0.06	0.05	0.05	0.06	0.05	0.04	0.04
C_e	0.00	0.00	0.00	0.00	0.00	0.00	0.00	0.00

Table 5.9: Amount of gas generated and average decomposition of cell at the instant before venting.

Mass composition at oven set temperature	**P_b=1224 kPa**		**P_b=2158 kPa**		**Mass ratio**
	m_g (g) $\times 10^{-2}$	**C_{ave} (-)**	**m_g (g) $\times 10^{-2}$**	**C_{ave} (-)**	
A, 180°C	5.76	0.9375	16.6	0.8148	2.88
B, 180°C	1.80	0.9804	5.10	0.9429	2.83
A, 218°C	4.85	0.9478	15.1	0.8317	3.11
B, 218°C	1.51	0.9837	4.63	0.9483	3.07

Considering the large burst pressure range investigated (1224 kPa to 2185 kPa), there is only a small change to the $E_{a,sei}$ and $E_{a,ne}$ parameters, while predictions are almost identical. The value of the burst pressure is therefore not critical to TR model parameterisation. Conversely, if the value of the burst pressure is exactly known then it would help in parameterisation. This is because it would be required of the model to accurately predict the internal cell pressure, in addition to the predictions of temperature.

The time to venting is predicted accurately under both oven exposure temperatures and the temperature that venting occurs in the higher oven exposure is accurate (see Fig. 5.6(c) and Fig. 5.6(d)). However, the temperature at which venting is predicted in the 180°C oven is noticeably lower than in the experiment. Hence, the discrepancy between the temperature at which venting occurs in the 180°C simulation and experiment highlights that the AAM, while significantly improving predictions, lacks some features that influence the complex pressure behaviour.

Table 5.9 also shows the ratio of gas generation between the high and low burst limit simulation from which it can be seen that, at the higher burst limit, three times more gas is produced prior to venting. Also, the magnitude of gas generated prior to venting is on the order of, or two orders lower, that the total measured, e.g 0.79 g to 1.4 g [65, 114, 278], depending on the assumed burst pressure.

For simplicity, the bubble pressure is determined from the bulk mole fraction. For fluids that are very similar to each other and along the bubble point line, this is similar to the mole fraction of each phase. However, for dissimilar fluids, as is the case here, the mole fraction of each phase can be very different (this can be seen specifically for the CO_2/DMC from the data in Ref. [253]). Hence, with respect to the bubble point

of a mixture, the possible cause of the temperature of venting discrepancy is the lack of calculation of the overall vapour/ liquid ratio of the mixture and the lack of calculation of the composition (i.e. CO_2/DMC ratio) of the liquid and vapour phases. The bulk mole fraction assumption may be inaccurate for a complete description of venting. However, for the purpose of validating the BPV model (as is the objective of this work) as a way to govern internal pressure rather than using the PPV model, it is believed that it is acceptable for proving that new model is valid. Further development beyond the scope of this work is required to incorporate the compositions of each phase.

5.2.4 Validation

Further validation of the estimated parameters for the AAM can be achieved by simulating the oven experiment over a range of values below and above those so far discussed. Figure 5.8 presents the maximum cell temperature and maximum change in cell temperature compared with the oven set temperature, both plotted against the oven set temperature. This provides a useful data set to compare with experimental results. From Fig. 5.8, it is clear the model predictions are in good agreement with the experimental data. Hence, the model can be used to investigate cell abuse beyond the experimental temperature range. However, from Fig. 5.8, over the range that experimental data is presented, the predicted temperatures are somewhat lower at oven set temperatures below 180°C and between 195°C–205°C. At the critical point at 195°C, where there is a step change in the TR severity of the experimental data, the model predicts the step change but does not predict the correct magnitude of temperature increase. Below is discussed possible contributing factors that lead to the discrepancies in predictions of Fig. 5.8.

The under prediction of maximum cell surface temperature at oven set temperatures below 180°C in Fig. 5.8 are attributed to a lack of representation of additional SEI reformation/decomposition and/or secondary NE dependent reactions. This is previously discussed in Section 5.2.3 of simulations made at oven exposure temperatures of 180°C. The discrepancies at oven set temperatures of 195°C–205°C are thought to be linked to the under prediction of step change at the oven set temperature of 195°C. A possibility of sudden increase in heat generation that leads to the step change in cell surface temperature could occur due to the internal short of the cell when the separator melts. However, typical layered polyethylene-polypropylene separators used in common Li-ion cells melt at approximately 165°C–170°C [96, 97]. As this melting temperature is significantly below the step increase, where cell temperatures are approximately 230°C, it can be ruled out as a contributing factor to the step increase in surface temperature of the experimental data that is not accounted for in the AAM. As previously stated, it is suspected that additional SEI decomposition and secondary NE dependent reactions may occur that are not represented in the model. These reactions at higher temperatures may contribute to the sudden increase in reactivity at 195°C. It is also possible that interdependent reactions,

which are not considered, are the cause of the step increase in surface temperature. For example, electrolyte solvents (with flash points between 17°C to 160°C [83]) can combust in the presence of on O_2 [26, 148]. O_2 becomes available within a cell when released by cathode decomposition [71]. As Table 2.2 shows, PE decomposition of LFP cathode begins at 180°C–250°C. As such, the step change in experimental data, which occurs at cell surface temperatures of approximately 230°C, maybe caused by combustion of the electrolyte upon availability of O_2. Further investigation, beyond the scope of this work, would be required to identify the probable cause of under prediction of the cell temperature.

The model allows assessment of TR behaviour beyond the scope of experimental testing. At an oven set temperature of 140°C, the maximum cell temperature is equal to that of the oven set temperature. Hence, from these predictions the LFP cells in question are shown to be stable up to 140°C oven exposure. From 140°C to 185°C oven set temperature there is a steady increase in severity following a linear trend. The magnitude of severity is small, i.e. ΔT below 50°C. Between 185°C and 220°C oven set temperature there is a significant increase in severity, with ΔT equal to 150°C at 218°C oven set temperature. Most interestingly, however, beyond an oven set temperature of 218°C, there is little increase in severity in relative terms to the oven set temperature; in fact, beyond 230°C, there is a slight decrease in relative severity.

From the above, it has been shown that the use of this AAM has enabled the prediction of cell TR severity outside the experimental oven set temperature range. In turn, showing that cells abuse beyond 190°C could lead to the same hazard at any oven temperature, i.e. $\Delta T = 150$°C. However, if the cells are kept below 185°C, to avoid the onset of the PE and electrolyte reactions and also avoiding significant heat generation from the NE reaction, then the hazard the cells pose is small. A hazard on this scale would be manageable by traditional thermal management techniques for battery packs. This is because the maximum heat generated at this abuse temperature is under 5 W, which is on the scale of the heat generated (up to 2.6 W [279]) by a high rate discharge of a similar cell.

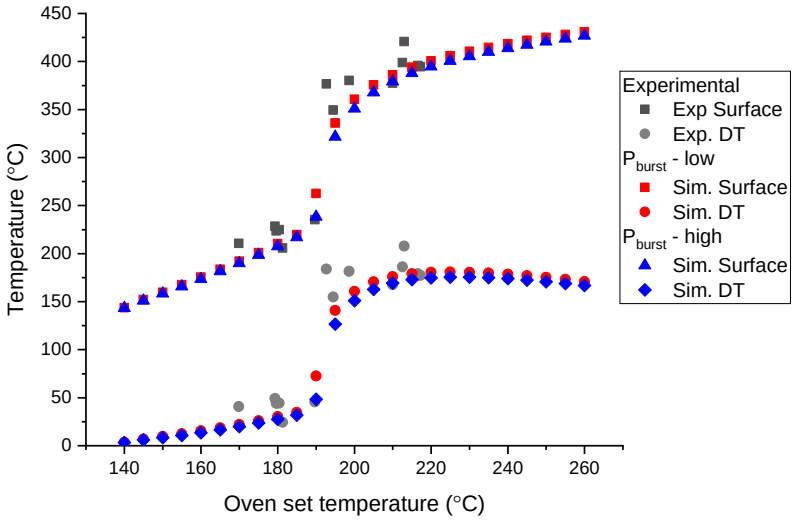

(a)

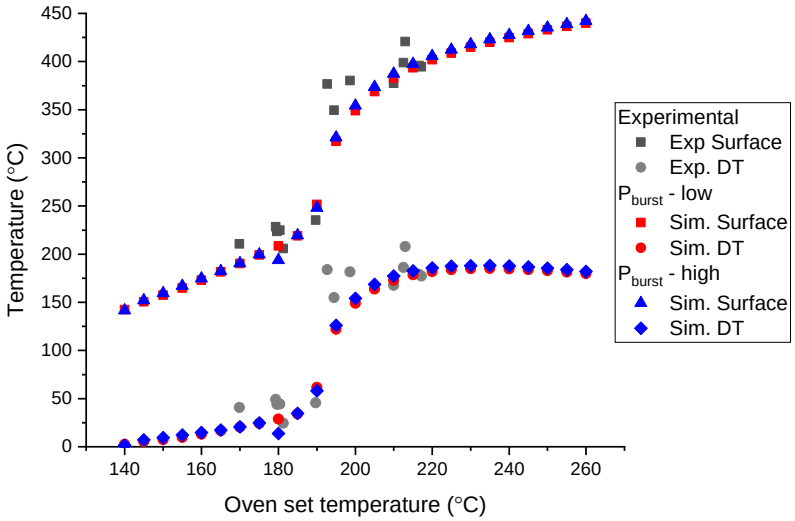

(b)

Figure 5.8: Simulated thermal runaway severity vs. oven abuse temperature (a) mass composition A (b) mass composition B, compared to experimental data.

5.3 Conclusion

In this chapter, through the development of the AAM, the performance of current TR models has been shown to be inadequate for LFP cells. This is because, when using existing models, TR is predicted too early as venting is not accounted for. Also, accuracy after TR is poor when using existing models due to their lack of representation of the simmering reaction. Further, parameters values used in the literature are shown to be inappropriate, leading to vast over predictions of TR severity. From this, the need for parameter estimation of reaction kinetics is shown. However, the variation in the mass fractions of cell components available in the literature leads to estimation of different reaction kinetic parameters that lead to similar TR predictions. Highlighting the non unique nature of parameterising the TR phenomenon.

The AAM model is shown to outperform the classical TR models due to its inclusion of novel venting behaviour and simmering reactions. The venting behaviour, based on a bubble-point assumption, is a more accurate description of a multiphase, multicomponent system like a cell under TR. The AAM leads to accurate predictions of time to venting, magnitude of heat loss at venting and time to maximum TR temperature. The inclusion of simmering reactions improves predictions of temperature after a TR, and hence is essential for LFP cells.

From parameterising the AAM, accurate knowledge of the burst pressure is required for determining accurate reaction parameters. The time of venting is most dependent on the decomposition of the SEI reaction, and slightly on the NE reaction. For higher burst pressures, the activation energies for the SEI and the NE reactions must be reduced, to allow the pressure increase by the time that venting should occur.

The work here aids the wider Li-ion battery community and the development of advanced batteries. The AAM, with its predictions of internal cell pressure, is a development enabling two pressure dependent phenomena to be modelled. The first, the prediction of battery state-of-health through pressure sensors in state-of-the-art battery management systems. The second, the modelling of the ejecta process and with it the complex heat transfer process of ejecta flow in a battery pack.

Three main points are outlined for future work regarding the development of LIB TR models:

1. consideration of secondary and interdependent reactions;
2. improved phase-equilibria of the liquid-vapour mixture for an improved prediction of pressure during the venting process, through accounting for the liquid-vapour fraction and mole fraction in each phase, expansion of vapour phase and re-equilibrium; and

3. focus on developing an intelligent computational aided method for model parameterisation to enable a statistical analysis of the appropriateness of parameters values.

Chapter 6

Thermal Runaway Propagation Potential Studies

Aims & Objectives

The aim of this chapter is to determine the safety and thermal runaway propagation (TRP) potential of LFP battery packs. The objectives are:

(1) simulate a battery pack constructed of 18650 LFP cells under a worst case scenario to determine the TRP potential of the pack and how individual decomposition reactions contribute;

(2) determine how estimated parameters affect predictions of TRP behaviour; and

(3) investigate the importance of heat transfer pathways, most significantly that of radiation, on TRP potential.

6.1 Introduction

In this chapter an investigation of the safety of LFP battery packs is made. Such studies are important because, as has been discussed in Chapter 2, when cells are assembled into modules and packs the potential hazards are more severe [90, 222]. This is due to the fact that the TR of a single cell presents a serious hazard to the surrounding cells. This occurs as the heat released by a single cell will dissipate to the neighbouring cells, which can in turn lead to these surrounding cells to heat up to the point that they themselves go into TR. Thus, this can be the start of a chain reaction of TR from cell-to-cell occurring throughout the entire module, known as TRP. Hence, here the aim is to determine the potential of TRP in LFP packs.

The motivation for studying the TRP of LFP packs is that, even though LFP cells are the safest Li-ion chemistry available, LFP batteries, including those in EV buses, have been reported to undergo TR [54, 114–116]. Hence, it is important to develop the current limited research on LFP cell safety. To the author's knowledge, only one study has been carried out on LFP packs, in which a module of pouch cells is studied [228]. Evidently, there is a need to expand the understanding of the TR behaviour of LFP packs when abused, to facilitate their wider adoption.

To investigate the TRP of LFP battery packs, a small lab scale battery pack is modelled based on the parameterised single cell model of Chapter 5. Further, a worst case scenario is considered, assuming extreme environmental temperatures and the most severe abuse condition i.e. total internal short circuit. In modelling the pack, the estimated abuse parameters determined in Chapter 5 are used.

Further, considering the previous finding identifying the importance of radiative heat transfer [27, 146, 222, 243], the effect of emissivity on the TRP of packs has not been studied. To address this, the pack model developed here is used to quantify the importance of radiative heat transfer on TRP for various cell surface emissivity and cell spacing values.

The remainder of this chapter is arranged as follows: Section 6.2 presents a summary of the results of two preliminary studies. The first of which investigates the effect of cell geometrical dimensionality, due to increasing the dimensionality from 1D, for the parameterised model of Chapter 5, to a 3D model representative of the cell in the pack. The second is a mesh analysis study for a single cell, to be used as a proxy mesh analysis for the pack due to computational limitations restricting the ability to undertake mesh analysis on the pack. Section 6.3 describe the main studies undertaken to investigate the TRP of LFP packs, the effects of model parameters and the importance of radiative heat transfer. Section 6.4 presents the results and discussion of the pack study presenting the results of the abuse of a small LFP battery pack under worst case scenario, commenting on the TRP potential of the LFP battery pack and the influence of parameters. Within this, Section 6.4.5 discusses the importance of radiative heat transfer pathways in packs. Finally, Section 6.5 concludes the chapter.

6.2 Summary of Preliminary Findings

Two preliminary studies (see Sections 3.3.1.1 and 3.3.1.3) were undertaken to investigate the effect of model dimensionality, and the effect of model mesh density on predictions. The key findings are summarized here.

The results of the dimensionality study, Section 3.3.1.2, show that there is a slight under estimate of TR severity by the 3D-HT/1D-abuse model compared to the 1D-HT-abuse model. This is due to the more accurate, but smaller, volume of jelly roll in the 3D-

HT/1D-abuse model. As decomposition heat generation is dependent on jelly roll volume, heat generation is proportionately smaller in the 3D-HT/1D-abuse model. Further there is a slight delay in maximum temperature using the 3D-HT/1D-abuse model, for the same reason. With this in mind, the pack study can be undertaken considering propagation may be postponed due to the delayed TR event of a cell or, if propagation is boarder-line, cautious assessments of safety should be made considering the under prediction of severity.

The results of the mesh study, Section 3.3.1.4, show that the relative errors of key values (e.g. *time to venting*, *maximum cell temperature* and *time to maximum cell temperature*) for the coarsest mesh (comparable to the one used in the pack study) are less than 1% (compared to the finest mesh). As such, the use of a coarse mesh (i.e. M1) is suitable for the pack study.

6.3 TRP Studies

To investigate the TRP potential of LFP cells assembled in a pack the model geometry presented in Fig. 3.10 is used with $d_{cc} = 0\,\text{mm}$, with environmental and abuse conditions as stated in Section 3.3. Further, the study considers four AAM parameter sets as estimated in Table 5.6. These parameter sets, consisting of reaction kinetics, mass composition and vent burst pressure limits, are referred to by the abbreviations MAH, MAL, MBH and MBL. The abbreviations respectively stand for (and relate to the parameters of) *mass composition A, with high burst pressure limit*; *mass composition A, with low burst pressure limit*; *mass composition B, with high burst pressure limit*; and *mass composition B, with low burst pressure limit*, respectively. Note, cell surface emissivity used in this study is 0.8.

For the study of cell surface emissivity effects on TRP potential the same model is used as above, with the exception that only the AAM parameters set MAH is considered for cell surface emissivity values of 0, 0.27, 0.54, 0.8 and 1, with d_{cc} values of 0 mm, 1 mm, 2 mm and 4 mm.

6.4 Results and Discussion

The values of average cell temperature, average cell decomposition and accumulated cell decomposition energy for each of the 9 cells in the simulated pack, utilising parameters for case MAH, are presented in Figs. 6.1 to 6.3, respectively. Case MAH is selected, as an example, to discuss, in Section 6.4.1, the general behaviour of the pack under abuse. The results of the pack abuse for each (mass composition/burst pressure) case are presented in Figs. B.1 to B.3 of the Supplementary Figures and Tables of Heat Transfer Pathway Study (Appendix B.1), which shows the behaviour in the pack is similar in each case,

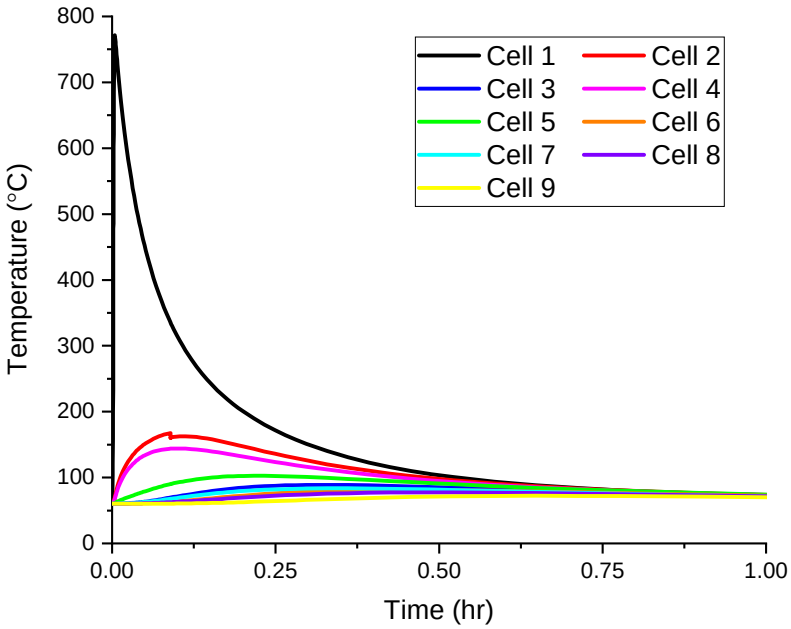

Figure 6.1: Average cell temperature within pack where Cell 1 is abused by short circuit for case MAH.

allowing for the general discussion. A more detailed discussion of key features on the response of the abused pack is presented in Sections 6.4.2 and 6.4.3 respectively for the temperature rise of Cell 1 and the decomposition of Cells 1, 2 and 4. A comparison of the different parameter cases is presented in Section 6.4.4. Finally, Section 6.4.5 discusses the importance of different heat transfer pathways.

6.4.1 Overview of Pack Behaviour Under Abuse

Although the simulation was solved for a 2 h period, for Figs. 6.1 to 6.3, only the first hour is shown as all quantities reach a stable value by this point. The plot of average cell temperature, Fig. 6.1, shows that Cell 1, the abused cell, heats up rapidly at the point when the short circuit occurs, and reaches a maximum temperature of almost 800°C. Note, for Cell 1, the maximum surface temperature is similar to the maximum of the average cell temperature. The rapid heating is due to the heat from the short circuit, over the small period of 10 s, leading to TR and the near complete decomposition of Cell 1, see Fig. 6.2, and a release of approximately 16 kJ of heat, see Fig. 6.3.

Following the large and rapid temperature rise of Cell 1, Cells 2 and 4, which are in contact with cell 1, heat up the most out of the remaining cells in the pack, see Fig. 6.1. Cells 2 and Cell 4 reach maximum average temperatures of 167°C and 144°C, respectively. Cells 2 and 4 undergo self-heating, as seen by the decomposition and energy release of Figs. 6.2 and 6.3, but not to a great extent. Compared to the near full decomposition of cell 1 and the ~16 kJ heat released, Cell 2 only decomposes by 25%, releasing ~1.1 kJ of

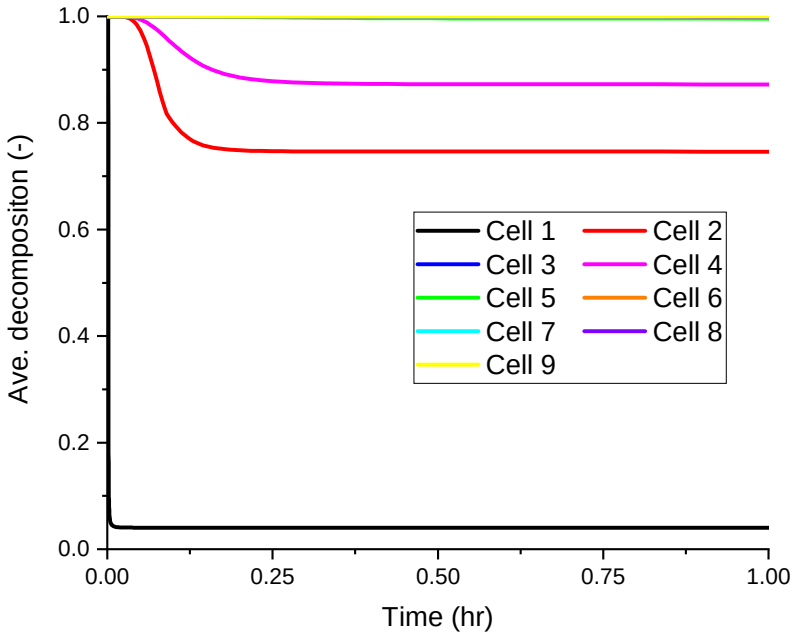

Figure 6.2: Average cell decomposition within pack where Cell 1 is abused by short circuit for case MAH.

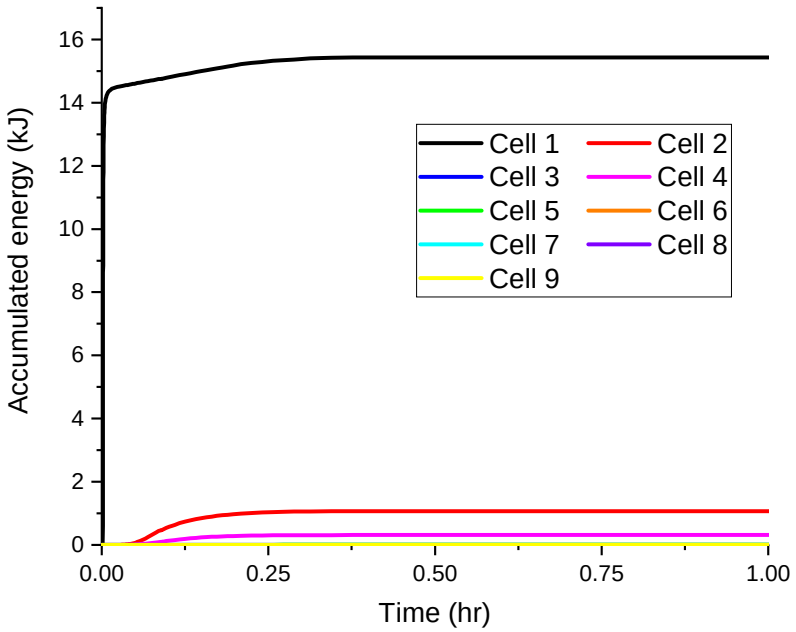

Figure 6.3: Accumulated energy from decomposition within pack where Cell 1 is abused by short circuit for case MAH.

heat, while cell 4 decomposes by 10%, releasing less than 0.5 kJ of heat.[1] Although Cells 2 and 4 are located in similar locations relative to the rest of the cells (see Fig. 3.10), Cell 2 reaches a slightly higher average temperature, and at a greater rate, than Cell 4. The positioning of Cell 2 and 4 means that they experience comparable heat transfer paths, excluding that through the tabs. From Fig. 3.10(b) it can be seen that Cell 2 has the additional heat transfer path through the tabs that directly connects Cells 1 and 2, while Cell 4 is not connected to Cell 1 by the tabs. As such, as has been found elsewhere [222, 225], the tabs have been shown to be an important heat transfer path.

The remaining Cells (3 and 5 to 9) heat up relatively slowly, with little difference between temperature plots of Cells 6 to 9. From Figs. 6.2 and 6.3, it can be seen Cells 3 and 5 to 9 shown negligible decomposition and thermal energy release. This indicates that the temperature rise of the cell is due to energy from Cells 1, 2 and 4 being transferred through the pack. At later times (approximately >0.5 h), all cells are in the processes of cooling down, tending to 60°C (the environmental temperature), while the pack remains stable as it does not show any TRP behaviour. Hence, after the TR of Cell 1, self-heating, but not TR, of Cells 2 and 4 occurs, while the remainder of the cells undergo no self-heating. As such, under this study, a battery pack constructed of LFP cells is shown to be very resilient to TRP, even under extreme circumstances, and highlights the abuse resilience and potential for uses in harsh environments of the LFP battery pack. This finding is substantiated by the work from Said *et al.* [247], which required an attached heater to provide a constant power of 115 W over the length of the experiment, providing 10–24 times more energy than the electrochemical energy stored in one cell, to induce cell-to-cell propagation. Here, however, the fact that there is an underestimate of heat generation by the 0D abuse model, requires that this statement should be further corroborated by analysing the heat released of individual reactions, and assessing if the additional heat would lead to any further cells going into TR.

6.4.2 Discussion of Cell 1 Temperature Rise

As stated in Section 6.4.1, the maximum surface temperature of Cell 1 reached ~800°C. Which, compared to the maximum surface temperatures of 400°C under oven exposure, from the experimental work of Chapter 4 (see Fig. 4.11), is relativity high. Further, as shown by Huang *et al.* [280], short circuit by nail penetration of a cell similar to those studied here leads to maximum cell TR temperatures less than 140°C.

[1] The percentage decomposition refers to averaged decomposition value, and hence the overall decomposition of the cell. As such, it does not strictly represent the percentage of total heat released by the cell, which on complete decomposition, is mostly from the NE, PE and simmering reactions, as discussed in Section 5.2.3, see Table 5.7. For example, for Cell 2 in MAH, the 25% decomposition is primarily due to the entire decomposition of the SEI reaction (1 of 4 reactions), while the heat released is due to the SEI (417 J), NE (414 J) and simmering (230 J) reactions, see Table 6.2. In which, the NE produces a similar amount of heat to the SEI reaction even though it has no developed significantly because the NE reaction as a much greater heat of reaction.

This overestimate of initiation cell maximum temperature is due to the fact that the cell's thermal energy potential has been accounted for twice, once through the short circuit and once through the decomposition behaviour. The decomposition of a single LFP cell at 100% releases approximately the same energy as the cell is electrically rated (see Chapter 4). This inherently occurs due to:

1. the simplification of omitting the electrochemical behaviour, as such there is no description of cell SOC change under discharge; and
2. as there is a lack of parameterisation of the abuse model as a function of SOC it is not possible to couple the cell decomposition model and cell SOC due to discharge when shorting.

However, since the electrical capacity and decomposition energies are similar for the cells studied, it can be cautiously assumed here that Cell 1 is heated approximately twice as much as what may occur in reality, explaining the maximum temperatures predicted that are double experimental oven tests.

In comparing the maximum surface temperatures from these two different abuse scenarios, the fact they are both rapid allows the assumption of pseudo-adiabatic conditions, and hence the ability to compare temperatures. The fact that there is an over estimate of energy released from cell 1, and hence the initial abuse condition, is not a significant concern to the study of the LFP pack, as it only further highlights the abuse resilience of the LFP pack.

6.4.3 Discussion of Individual Reactions of Cells 1, 2 and 4

As stated previously, while Cell 1 undergoes near complete decomposition, Cells 2 and 4 only undergo a small fraction of decomposition and a low amount of self-heating. To further explore the discrete reactions that have occurred in these cells, Fig. 6.4 presents the individual species decomposition values for Cells 1, 2 and 4 for the first 0.5 h of results form case MAH, in Figs. 6.4(a) to 6.4(c) respectively, while Fig. 6.4(d) shows an enlargement of the rapid decomposition behaviour of Cell 1. From Fig. 6.4 (and Fig. 6.4(d)) it can be seen that all reactions quickly (in ~3 s) run to completion, besides the NE reaction, which has some active species remaining after the TR event. However, for Cell 2, Fig. 6.4(b) shows only the SEI reaction completes, while there is a small reduction in the NE active species from 0.75 to 0.73. For Cell 4, see Fig. 6.4(c), the SEI again shows the largest change, while no discernible change is seen in the species of the other reactions.

Further to the individual decomposition species for each reaction of the Cells 1, 2 and 4, Fig. 6.5 presents the individual accumulated energy released for each reaction in each cell (of Cells 1, 2 and 4). From Fig. 6.5(a), it is shown that the NE reaction contributes

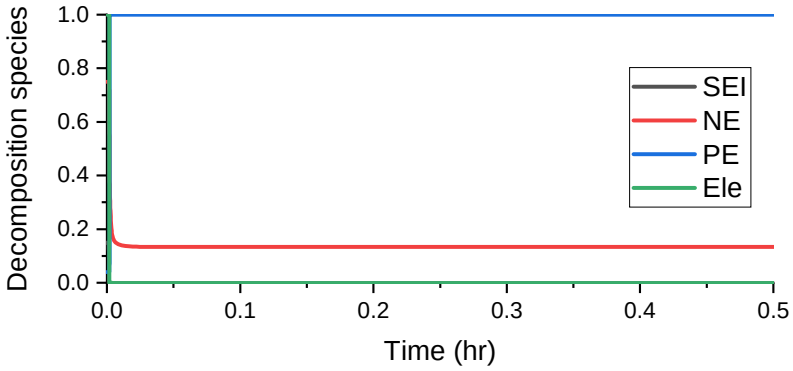

(a) Cell 1

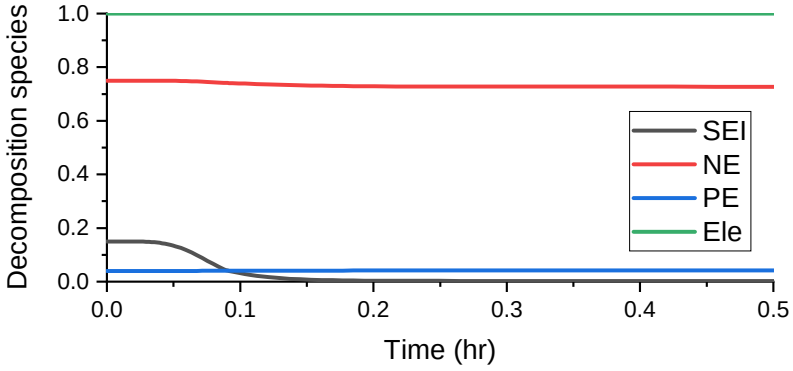

(b) Cell 2

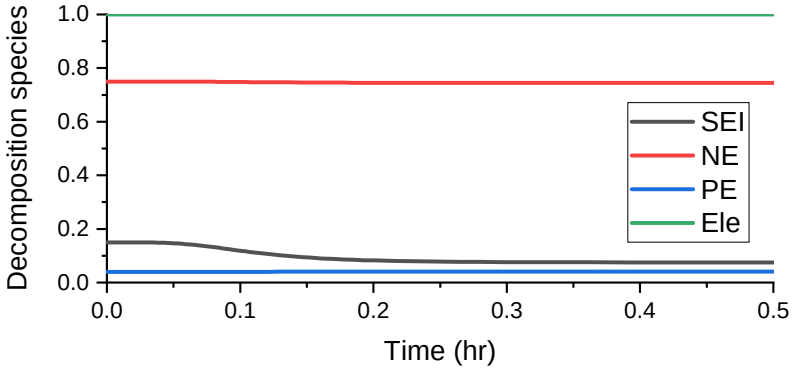

(c) Cell 4

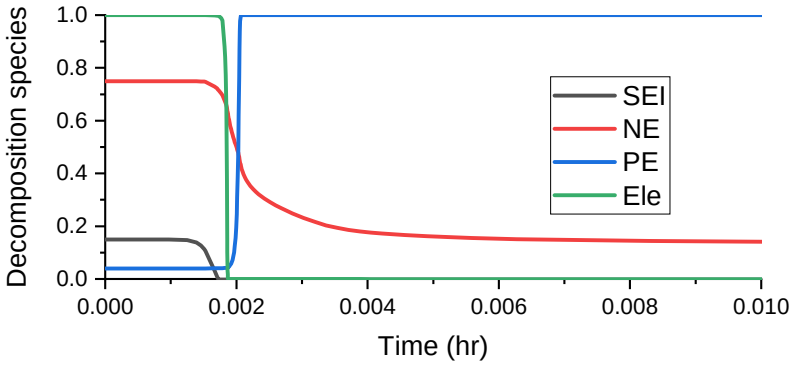

(d) Cell 1, enlargment of time period when short occurs

Figure 6.4: Decomposition species of individual reactions for cells 1, 2 and 4 (parameters set MAH).

the most heat (~11 kJ) of the decomposition reactions to the heating of Cell 1, while the PE reaction and the sum of the SEI, electrolyte and simmering reactions contribute approximately 2.2 kJ of heat each. This is comparable to the heat released under high temperature oven exposure (see Table 5.7), with the difference that under short abuse in the pack, Cell 1 reaches higher temperatures than the oven abused cell, leading to greater NE decomposition and hence more NE heat release in Cell 1. Whereas the heat released by the simmering reaction in Cell 1, in the pack, generates less heat due to the low temperature (<120°C) of Cell 1 for the majority of the time after venting. Hence, due to the temperature dependence of the simmering reaction, the predicted heat is lower in Cell 1 than the oven abuse of cells, as under oven abuse the cells remain at high temperatures after venting.

For cell 2, Fig. 6.5(b) shows that the heat generated by the decomposition reactions is dominated by the SEI and NE reactions, which generate approximately 400 J of heat each, while the simmering reaction generates half as much as either of these. For Cell 4, see Fig. 6.5(c), which reaches a lower temperature than Cell 2 and in which venting does not occur, the heat generated is dominated by the SEI reaction, which releases ~200 J of heat, while the NE reaction on generates ~100 J and simmering does not occur as the vents have not opened.

The behaviour described above is similar for all cases, which can be seen in Figs. B.4 to B.9, while discrete differences between all cases are highlighted through the values of the decomposition species and energy released, for each reaction of Cells 1, 2 and 4 at the end of the simulations, in Tables 6.1 and 6.2, respectively. From Table 6.1 it can be seen that the SEI reaction undergoes more decomposition in the cases for mass composition A than that for mass composition B. Considering that the activation energy of the SEI reaction is lower for mass composition A (for given a burst Pressure), see Table 5.6, it is to be expected that for a similar temperature rise the SEI reaction will start sooner and develop further than for mass composition B. The same is true for the NE reaction between mass composition cases, and the SEI reaction between pressure cases for mass composition B.

As previously stated, the SEI reaction of mass composition A decomposes more than B, leading to more heat release in Cells 2 and 4. However, for Cell 1 in which SEI reaction completes in both mass compositions, interestingly more heat is released by the SEI reaction of mass composition B. From Table 5.6, it is clear the SEI reaction of mass composition B has more potential to generate heat as the specific mass of carbon is greater for mass composition B, while the heat of reaction of the SEI reaction is the same for both mass compositions. More heat is generated by the SEI and NE reactions, given mass composition, by the higher burst pressure cases, due to the lower activation energies of reactions in these cases, as explained in Section 5.2.3.1. The energy released by the PE and simmering reactions are, for each reaction, the same between cases. For mass composition

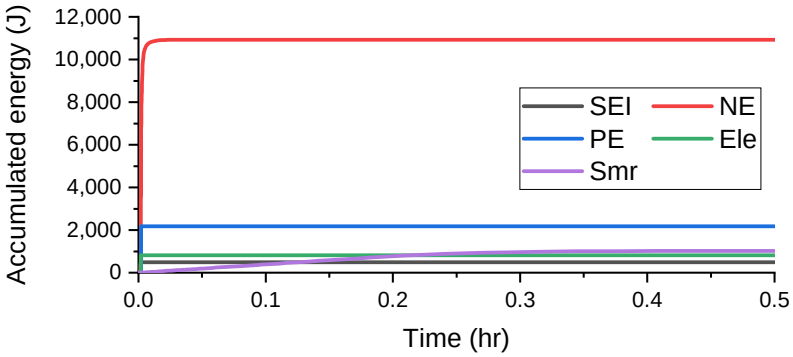

(a) Cell 1

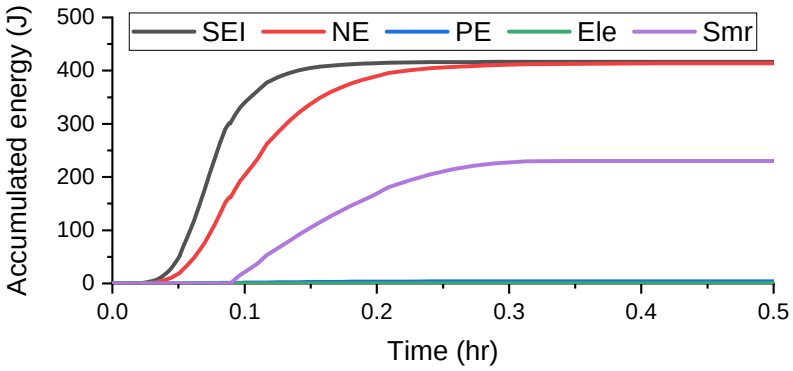

(b) Cell 2

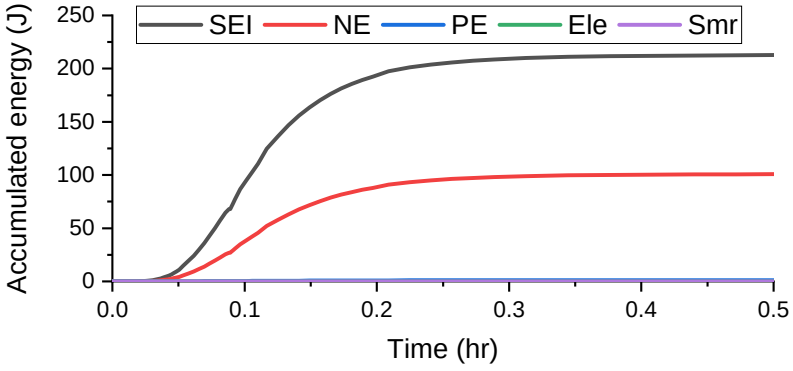

(c) Cell 4

Figure 6.5: Accumulated energy of individual reactions for cells 1, 2 and 4 (parameters set MAH).

Table 6.1: Decomposition species value at the end of simulation for cells 1, 2 and 4.

		Decomposition species			
Case	**Cell**	**SEI**	**NE**	**PE**	**Ele**
MAL	Cell 1	0.00	0.13	1.00	0.00
	Cell 2	0.00	0.73	0.04	1.00
	Cell 4	0.07	0.74	0.04	1.00
MAH	Cell 1	0.00	0.13	1.00	0.00
	Cell 2	0.00	0.73	0.04	1.00
	Cell 4	0.07	0.74	0.04	1.00
MBL	Cell 1	0.00	0.14	1.00	0.00
	Cell 2	0.12	0.74	0.04	1.00
	Cell 4	0.14	0.75	0.04	1.00
MBH	Cell 1	0.00	0.14	1.00	0.00
	Cell 2	0.06	0.74	0.04	1.00
	Cell 4	0.13	0.75	0.04	1.00

Note: Initial values of SEI, NE, PE and Ele decomposition values are 0.15, 0.75, 0.04 and 1, respectively.

B, relative to A, the energy released by the electrolyte reaction is less due to the smaller mass of electrolyte available, especially after venting, as explained in Section 5.2.3, while the energy from the NE reaction is greater due to the significantly larger NE mass and NE heat of reaction in mass composition B.

As shown in Section 6.4.1, the average cell values, such as decomposition and accumulated energy, allows one to understand the overall behaviour of the pack. However, to properly inform of the TRP potential, the values of these quantities has to be presented and analysed on a single reaction basis to understand the potential of high energy reactions occurring. Also, from Tables 6.1 and 6.2, while the NE reaction shows little change from its initial decomposition value in Cells 2 and 4, similar amounts of energy are released as the SEI reaction. Hence, it is important to consider more than the average or individual decomposition values when discussing the TR behaviour of a cell in a pack, as the values of energy provide more information to temperature rise and TRP potential.

From the above discussion, it has been shown that the shorted cell decomposition reactions generate heat in a similar manner to cells abused at high oven temperatures. However, in the neighbouring cells, Cells 2 and 4, there is lack of decomposition of the energetic NE reaction, as well as the PE and electrolyte reactions. Due to the stability of the LFP cell chemistry, and the lack of heat transferred into the neighbouring cells of the shorted cell minimising the heating of Cells 2 and 4, the positive TR feed back loop (Fig. 1.6) does not develop in Cells 2 and 4 as the energetic decomposition reactions have not developed. Considering that there is an underestimate of heat produced by the 0D abuse model (detailed in Section 3.3.1.1), the significant lack of development of the NE and PE reactions suggests that even for the larger heat generation of the 1D model TRP

Table 6.2: Accumulated energy at the end of simulation for cells 1, 2 and 4.

		Accumulated energy (J)				
Case	**Cell**	**SEI**	**NE**	**PE**	**Ele**	**Smr**
MAL	Cell 1	388	10,953	2,196	805	1,001
	Cell 2	187	280	3	0	183
	Cell 4	43	69	1	0	0
MAH	Cell 1	486	10,931	2,177	820	1,015
	Cell 2	417	414	4	0	230
	Cell 4	213	101	1	0	0
MBL	Cell 1	521	12,388	2,261	200	1,021
	Cell 2	113	103	4	0	223
	Cell 4	23	22	1	0	0
MBH	Cell 1	488	12,165	2,564	176	1,029
	Cell 2	374	224	4	0	262
	Cell 4	87	46	1	0	0

would still not occur. Hence, it is clearly shown that within this pack there is no potential of TRP due to the stability and lack of severity of the LFP cells.

6.4.4 Comparing the Effects of Different Mass Compositions and Burst Pressures

As stated previously, the overall behaviour of an abused pack in each case study is similar. Here, however, the finer details of the results are discussed to understand the affects the different parameters have on the resulting abuse of the pack. Figure 6.6 compares, for Cells 1, 2 and 4, cells which undergo the largest changes, the temperature results between cases which use different masses with the same cell burst pressure, and between cases that use different cell burst pressures for the same mass. Similarly, Figs. 6.7 and 6.8 undertake this comparison but for the average decomposition and accumulated energy parameters, respectively.

As can be seen from Figs. 6.6(a) and 6.6(b), mass composition B leads to slightly greater temperatures than mass composition A. For Cell 1, this increase in temperature is approximately 25°C. This temperature difference is due to the greater energy released by mass composition B (16.4 kJ for MBH vs. 15.4 kJ for MAH), see Figs. 6.8(a) and 6.8(b), which has been discussed in Section 6.4.3, where it was shown that the NE reaction is the cause of the additional heat. Further, Figs. 6.6(c) and 6.6(d) compare the resulting cell temperatures for abused packs of each burst pressure for mass composition A and B, respectively. From these figures it can be seen that, given a mass composition, the value of cell burst pressure has little effect on overall temperatures.

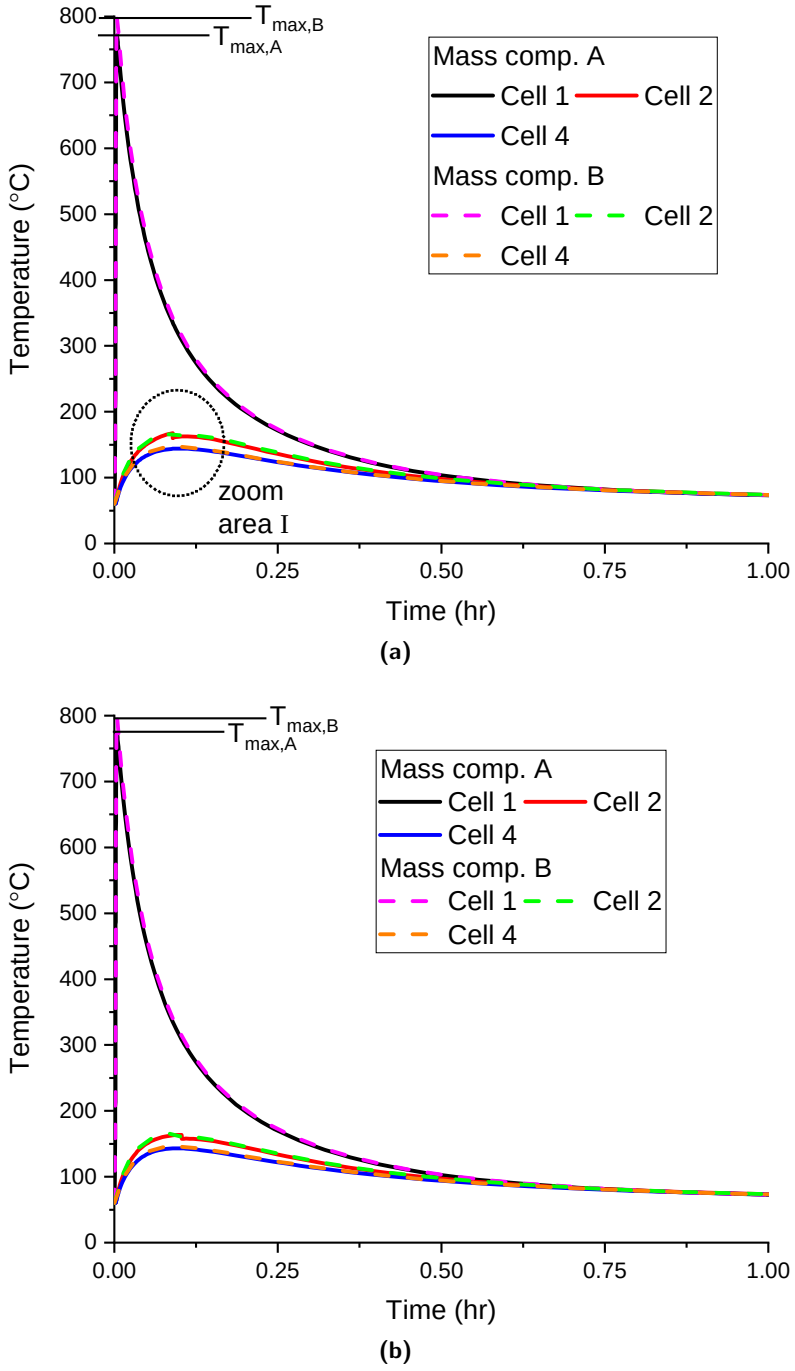

Figure 6.6: Effect of different mass compositions and burst pressures on temperature. (a) Comparison of different mass compositions for a high burst pressure (for *zoom area I* see Fig. 6.9(a)), (b) comparison of different mass compositions for a low burst pressure, (c) comparison of different burst pressures for mass composition A (for *zoom area II* see Fig. 6.9(b)), and (d) comparison of different burst pressures for mass composition B.

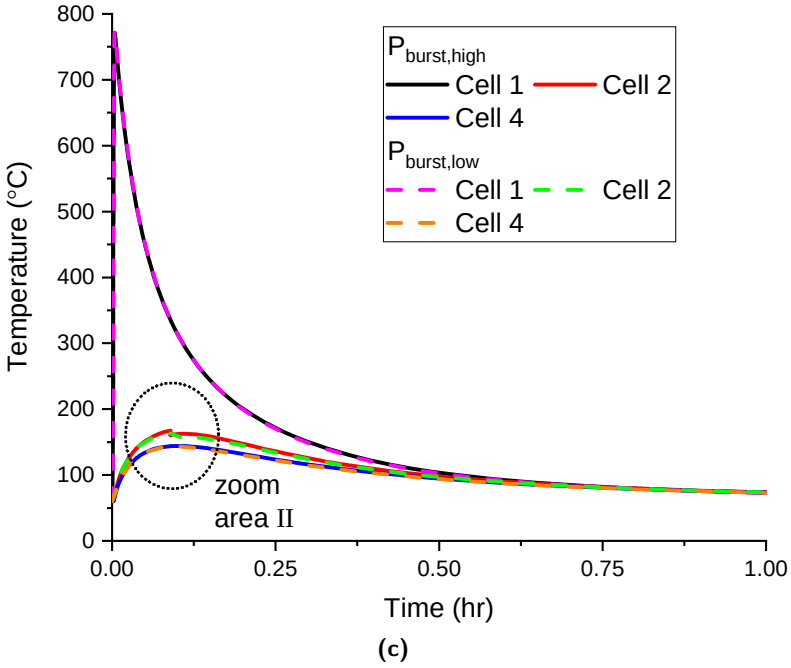

(c)

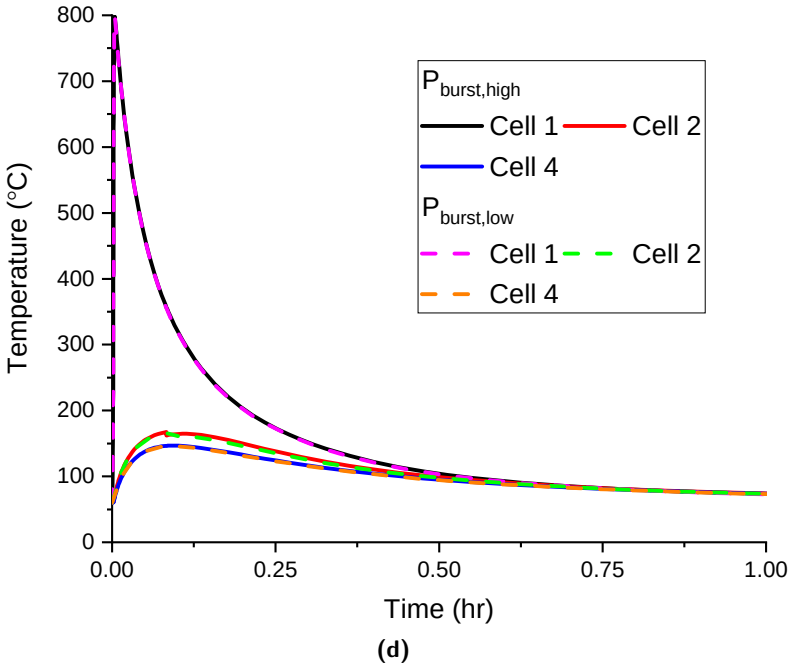

(d)

Figure 6.6 (cont.): Effect of different mass compositions and burst pressures on temperature. (a) Comparison of different mass compositions for a high burst pressure (for *zoom area I* see Fig. 6.9(a)), (b) comparison of different mass compositions for a low burst pressure, (c) comparison of different burst pressures for mass composition A (for *zoom area II* see Fig. 6.9(b)), and (d) comparison of different burst pressures for mass composition B.

From the comparison of average decomposition species plots, Figs. 6.7(a) and 6.7(b), it can be seen that for a given cell, those of mass composition A decompose quicker than B. From Fig. 6.4 and Figs. B.4 to B.6 it can see that this is due to the earlier onset and decomposition of the SEI reaction. Which, as can be seen from the values of the activation energies (see Table 5.6) where for mass composition A for a given pressure they are lower, is to be expected. Similarly, for cases with a higher cell burst pressure the cells decompose quicker, see Figs. 6.7(c) and 6.7(d). Again, the lower activation energies of the SEI and NE reactions, in the higher burst pressure cases, leads to sooner decomposition over cases with lower burst pressure. Furthermore, the heat generation's, and hence, accumulated energy's, are intrinsically dependenent on the reaction species change for a given mass composition. Inherently, mass composition B cases and the lower cell burst pressure cases lead to less accumulated energy (see Fig. 6.8) due to the higher activation energies of the SEI and NE reactions, while the temperature rise is driven by heat from Cell 1. This is apparent in all cells besides cell 1, which has undergone equal decomposition between cell burst pressure cases due to the abuse condition on Cell 1.

In Figs. 6.6(a) and 6.6(c) the point of venting of Cell 2 is highlighted, referred to as *zoom area I* and *zoom area II*, respectively. For Figs. 6.6(a) and 6.6(c), these *zoom areas* are enlarged and presented in Figs. 6.9(a) and 6.9(b), respectively. From Fig. 6.9(a), it can be seen that venting is predicted earlier for mass composition B, while from Fig. 6.9(b) it can be seen that for a lower burst pressure venting is predicted later, which is also seen in the oven simulations of Section 5.2.3.1. To explain the advance and lag of venting, Figs. 6.10 and 6.11 present the pressure, temperature, mole fraction, gas generation rate and average decomposition value for Cell 2, in comparing case MAH to MBH, and MAH to MAL, respectively.

Differences between cases MAH and MBH in Fig. 6.10 will be discussed in reference to annotations I, II and III.

- Referring to **point I** in Fig. 6.10, by 20 s the temperature of Cell 2 in MBH is greater than that of Cell 2 in MAH. Considering the lack of decomposition in either case until >100 s, due to the greater amount of energy released by cells of mass composition B, the additional heat from Cell 1 in MBH over that of MAH leads to greater heat transfer to Cell 2 in case MBH.

- Hence, over the period of **region II** in Fig. 6.10 there is a higher temperature of Cell 2 in case MBH over case MAH. Further, over this period it can be seen that MBH has a slightly greater cell pressure than MAH, see the top panel of Fig. 6.10. However, from the bottom panel of Fig. 6.10, it can be seen that the mole fractions between the cases are indistinguishable over the same period. Hence, as the (cell) bubble pressure is known to be more sensitive to temperature than mole fraction, see Fig. 5.5, the difference in pressure between cases MAH and MBH over the first 230 s can be attributed to the higher temperature of the cell in the case of MBH.

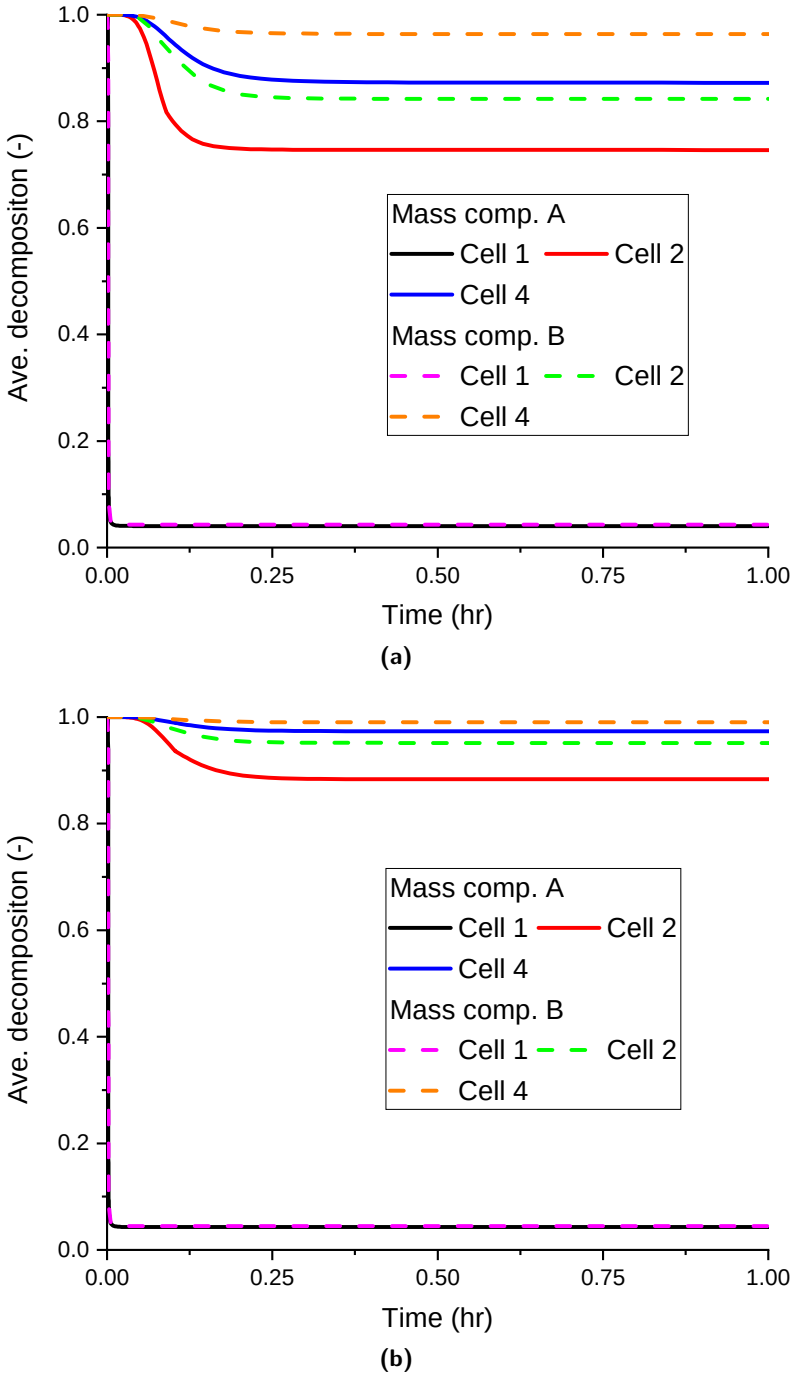

Figure 6.7: Effect of different mass compositions and burst pressures on average decomposition species. (a) Comparison of different mass compositions for a high burst pressure, (b) comparison of different mass compositions for a low burst pressure, (c) comparison of different burst pressures for mass composition A, and (d) comparison of different burst pressures for mass composition B.

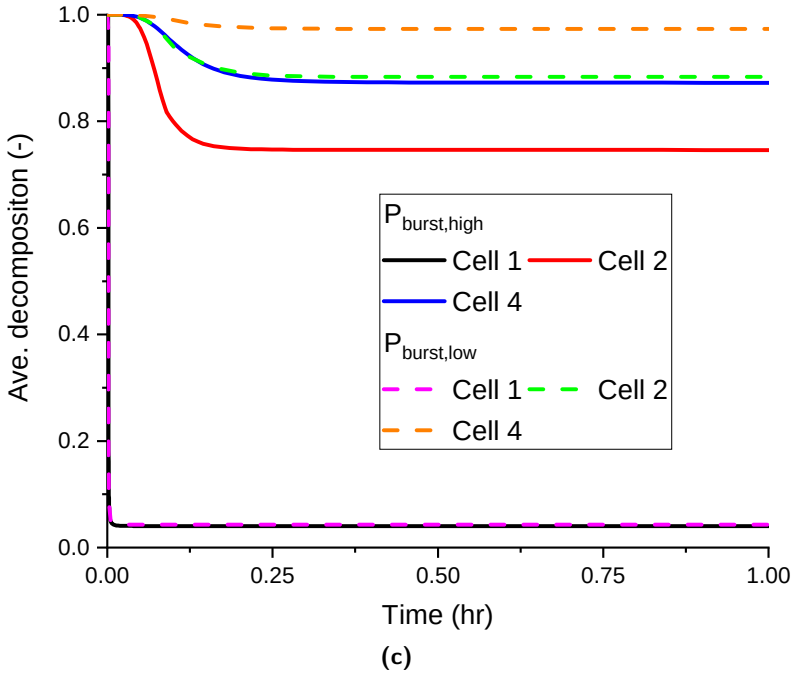

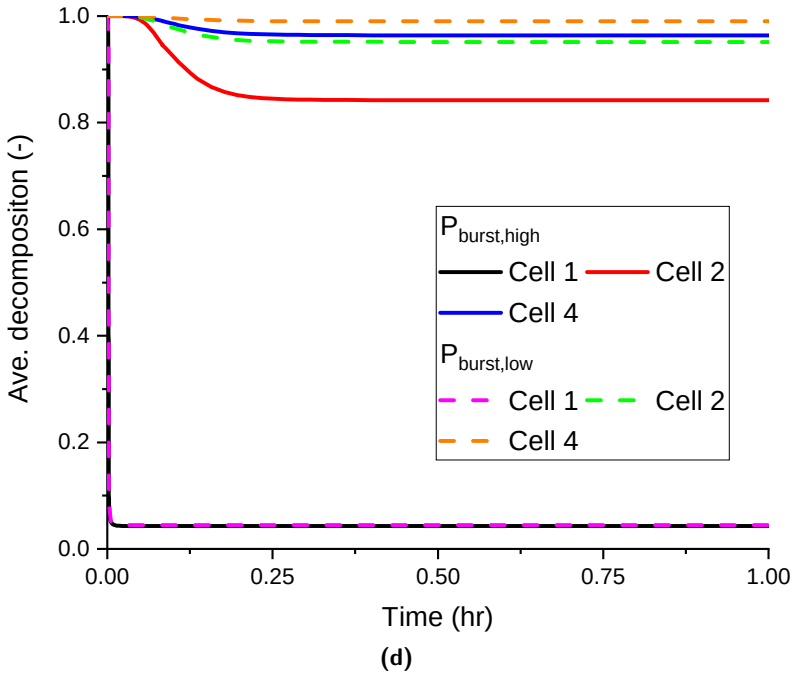

Figure 6.7 (cont.): Effect of different mass compositions and burst pressures on average decomposition species. (a) Comparison of different mass compositions for a high burst pressure, (b) comparison of different mass compositions for a low burst pressure, (c) comparison of different burst pressures for mass composition A, and (d) comparison of different burst pressures for mass composition B.

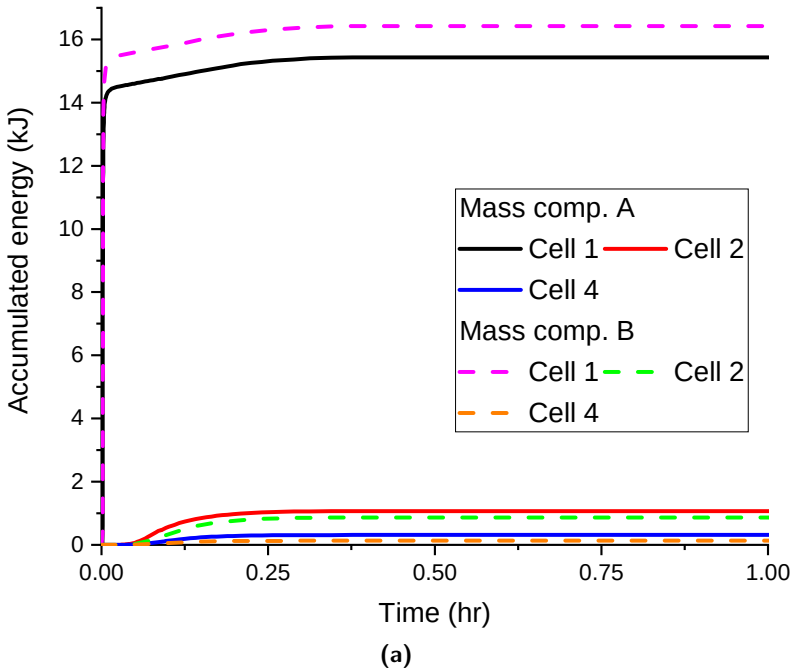

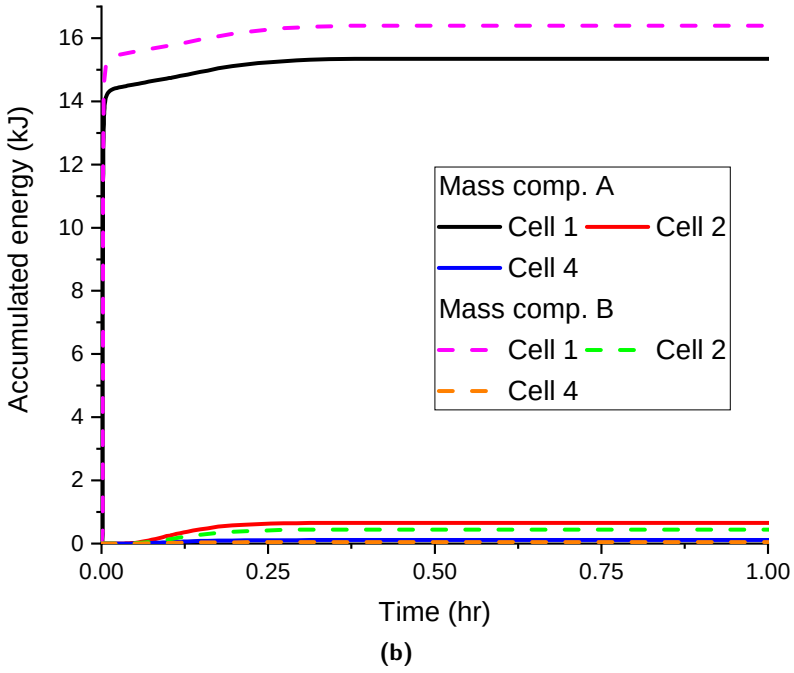

Figure 6.8: Effect of different mass compositions and burst pressures on accumulated energy. (a) Comparison of different mass compositions for a high burst pressure, (b) comparison of different mass compositions for a low burst pressure, (c) comparison of different burst pressures for mass composition A, and (d) comparison of different burst pressures for mass composition B.

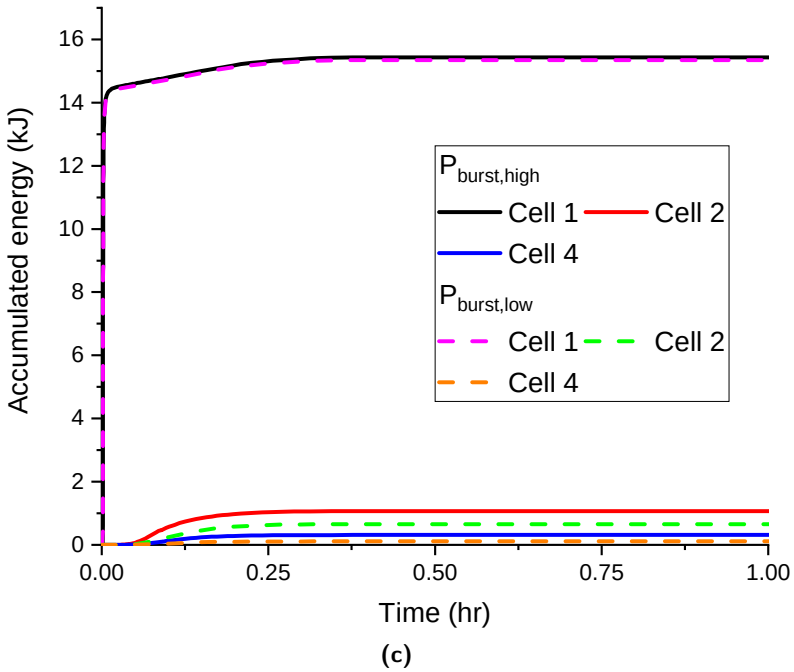

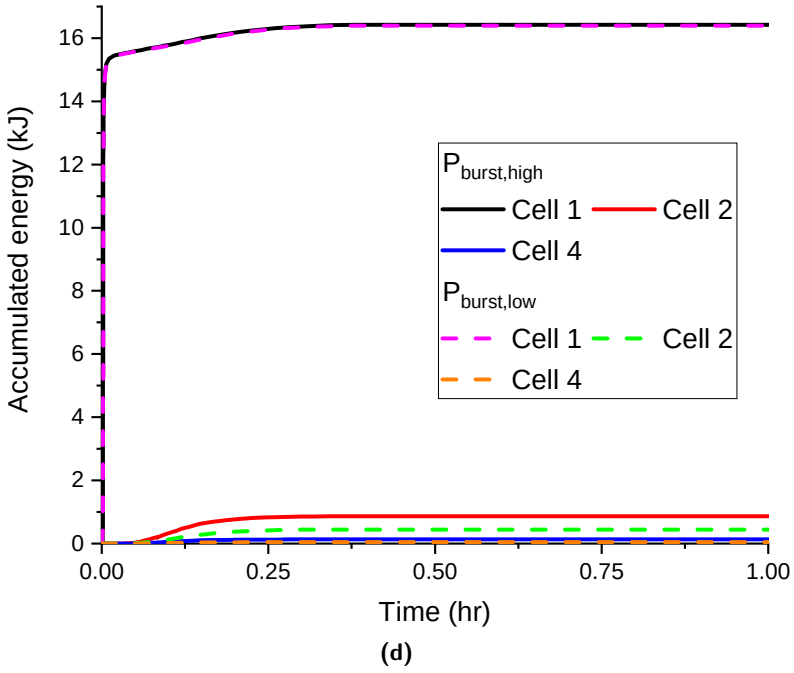

Figure 6.8 (cont.): Effect of different mass compositions and burst pressures on accumulated energy. (a) Comparison of different mass compositions for a high burst pressure, (b) comparison of different mass compositions for a low burst pressure, (c) comparison of different burst pressures for mass composition A, and (d) comparison of different burst pressures for mass composition B.

- After this period, at **point III** in Fig. 6.10, it can be seen that the pressure of the cell in case MBH rises more rapidly than in MAH (see top panel of Fig. 6.10). Which, from (the bottom panel of) Fig. 6.10, can be seen to be due to the increase in mole fraction of MBH compared to MAH. Interestingly, the mole fraction of MBH increases quicker at point III than for case MAH, although MAH decomposes more rapidly.

However, considering Eq. (3.57), which governs the mole fraction as a function of the variable mass of gas and the fixed value of mass of electrolyte (up to the point before venting), then, for a given profile of gas mass increase, the system that has a lower mass of electrolyte will lead to larger values of mole fraction for a given mass of gas. Hence, as MBH has a lower mass of electrolyte, 1.95 g compared to MAH with 6.58 g of electrolyte, it has a greater mole faction, even though less decomposition has occurred. Further, the deviation occurs because the production of gas in MAH slows at point II, and shortly after reaches a peak so the slope of mole fraction for MAH lessens, while in MBH the production is still to reach a maximum and the gradient of mole fraction remains relatively steep. As such, even though the SEI and NE reactions are delayed in MBH, the lower amount of electrolyte amplifies the gas's contribution to increasing the mole fraction, and the earlier occurrence of venting.

From Fig. 6.11, it can be seen that case MAH vents before MAL as the cell in case MAH reaches its pressure limit sooner. Interestingly, this occurs even though the pressure limit is higher in case MAH. As above, from Eq. (3.56) we see that the internal cell's pressure is governed by the average cell temperature and mole fraction of the mixture. In the cases of MAH and MAL, the temperatures of the cells remain equal up to approximately 175 s, refer to I of Fig. 6.11. However, the pressure starts to increase in MAH much before this, at approximately 120 s (see point II of Fig. 6.11), and deviates away from the pressure in MAL. It can be seen from Fig. 6.11 (bottom panel) that this deviation coincides with the more rapid increase in mole fraction of MAH compared to MAL, see point III of Fig. 6.11. The mole fraction is governed by the mass of gas produced, see Eq. (3.57), which in turn is governed by the decomposition rate, see Eq. (3.45). From this, it can be seen that the greater gas production rate of MAH, see IV of Fig. 6.11, leads to the increased cell pressurisation over MAL. This in turn is due to the lower activation energies of the SEI and NE reactions of the MAH case. As such, while the burst pressure is higher, the limit is reached sooner as the reactions start earlier in the MAH case.

Here, due to the stability of the LFP cells, the variation in parameters between cases lead to insignificant changes in TRP hazards. However, it has been shown how assumptions on cell mass composition and cell pressure limit affects the nature of decomposition in a cell, and hence, between cells in a pack. Specifically, the selection of cell burst pressure affects the parametrisation of the SEI and NE reactions most significantly. This, in turn can effect the time to severe TR reactions. For example, the higher burst pressure leads

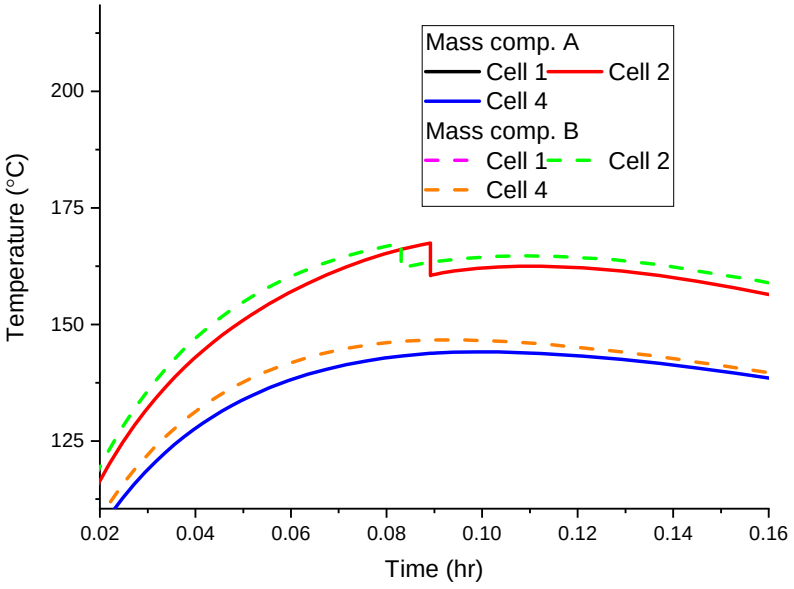

(a)

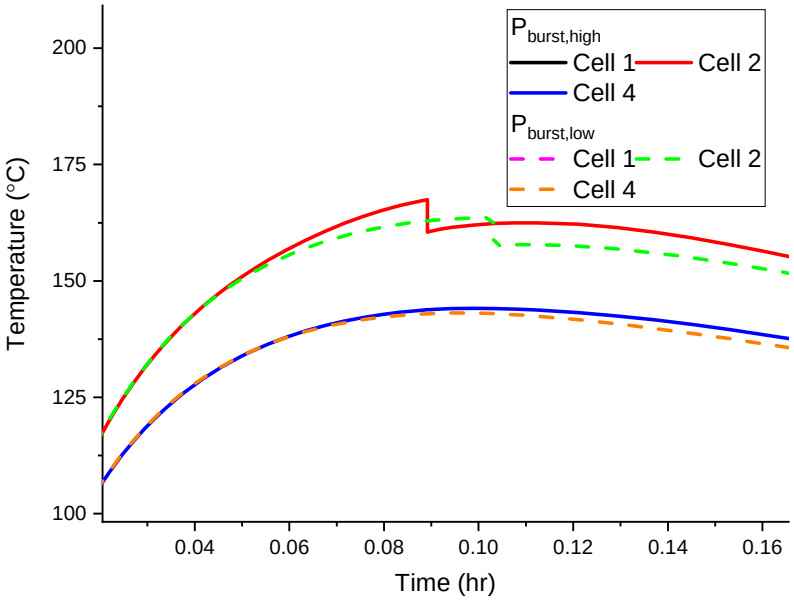

(b)

Figure 6.9: Effect of different mass compositions and burst pressures on vent behaviour. (a) different mass compositions for a high burst pressure, an enlargement of zoom area I of Fig. 6.6(a), and (b) different burst pressures for mass composition A, an enlargement of zoom area II of Fig. 6.6(c).

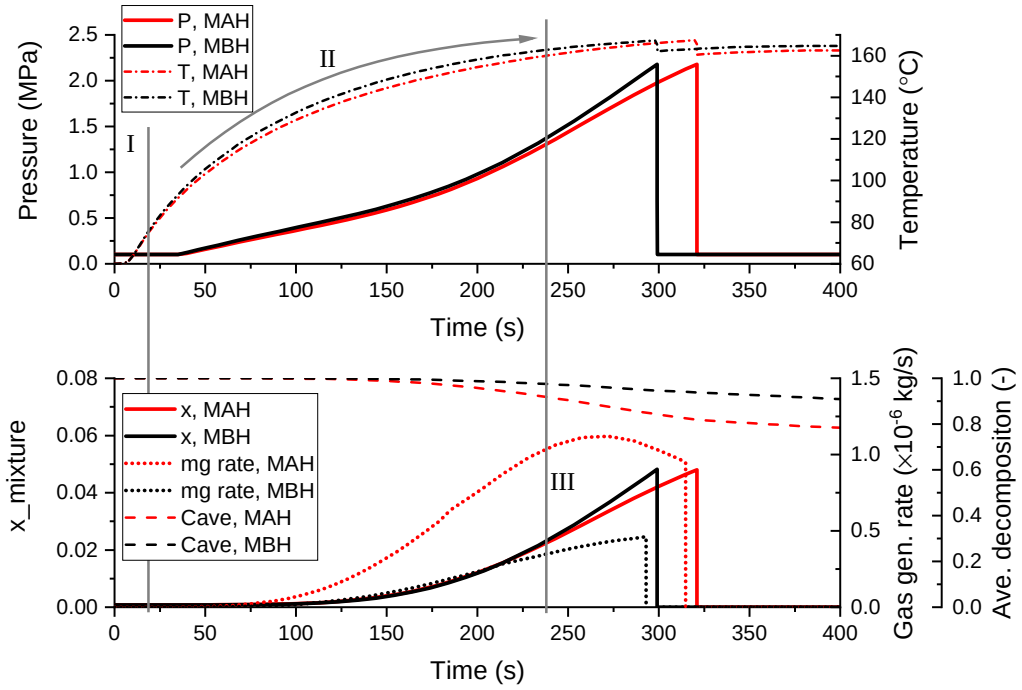

Figure 6.10: Comparison of key values related to the venting of Cell 2 for cases MAH and MBH (x is mole fraction of mixture, mg rate is mass of gas rate).

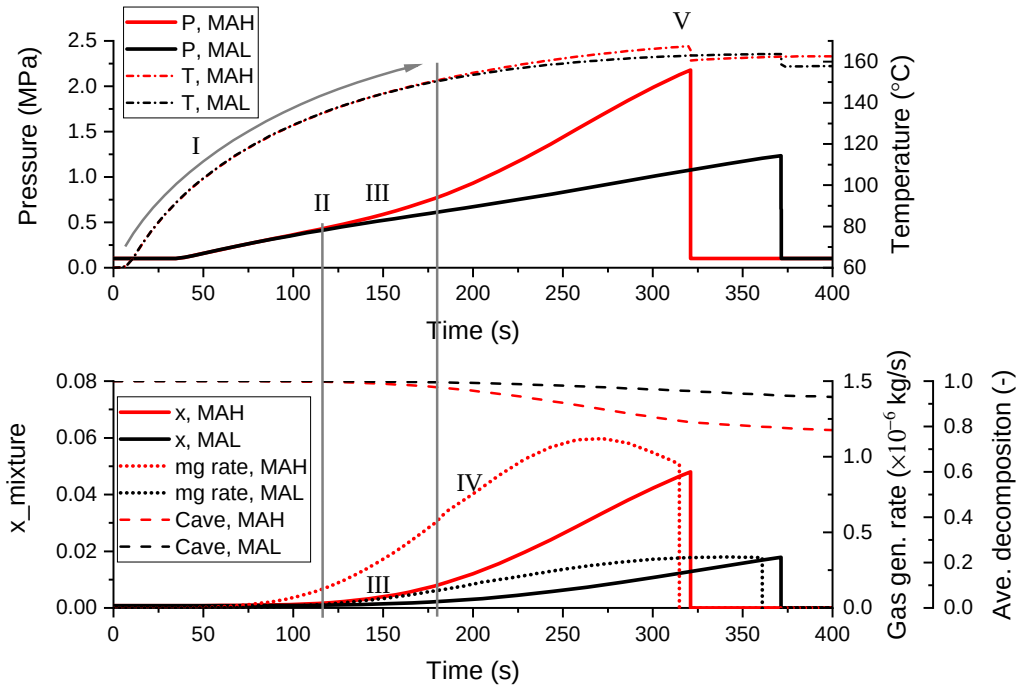

Figure 6.11: Comparison of key values related to the venting of Cell 2 for cases MAH and MAL (x is mole fraction of mixture, mg rate is mass of gas rate).

to lower activation energies for the SEI and NE reactions, which lead to them occurring sooner. Here, this has no effect of TRP as the cells are stable. However, for cells that are more unstable with more energetic self-heating reactions, which could in turn go into TR, one can expect that TR would occur sooner, and TRP faster than cells that are parameterised assuming a lower burst pressure. This highlights the importance of looking at the sensitivity and range of parameters that are first representative of an oven simulation in parameter estimation development, and the effect it can have on TRP prediction.

6.4.5 Importance of Heat Transfer Pathways

As Fig. 6.1 shows, Cells 1, 2, 4 and 5 undergo the most significant changes in the pack when abused. Hence, they are the focus of analysis on the affect cell surface emisivity, ε_{cell}, and cell spacing, d_{cc}, have on maximum cell temperatures and decomposition heat released. With this, Figure 6.12 presents the maximum mean cell temperature at given emissivity and cell spacing values for Cell 1 (Fig. 6.12(a)) and Cells 2, 4 and 5 (Fig. 6.12(b)) which surround Cell 1. Similarly, Figure 6.13 presents the total decomposition heat generated for Cells 1, 2, 4 and 5 at various emissivity and cell spacing values. To study the heat transfer pathways Tables B.1 to B.4 presents the net heat transfer to a cell by radiation, surface conduction, tab conduction and the total sum, for each ε_{cell} up to the time of maximum cell temperature for inter-cell spacings of 0 mm, 1 mm, 2 mm and 4 mm, respectively. Further, Tables B.5 and B.6 presents the net heat transfer from maximum cell temperatures to the end time of simulation for inter-cell spacings of 0 mm and 4 mm, respectively. With regard to Tables B.1 to B.6, positive values indicate that over the time period in question the overall heat transfer is into a cell, while for negative values the opposite is true.

6.4.5.1 Tab Heat transfer

It was stated in Section 6.4.1 that the heat transfer through the tabs causes the heating of Cell 2, which is connected to Cell 1 by the tabs, more greatly than Cell 4, which is not connected to cell 1 by the tabs. The significance of the tabs as a heat transfer pathway can be quantified through Tables B.1 to B.4.

Comparing the heat transfer for Cell 2 and 4 in Table B.1, which presents data for the same cell spacing as in Section 6.4.1, it can be seen the total heat transfer to cell 2 (4295 kJ) is greater than to Cell 4 (3553 kJ). In which, the heat transfer by radiation and surface conduction is greater in Cell 4 (accumulatively 3830 kJ) than Cell 2 (accumulatively 2922 kJ). However, Cell 4 loses heat by tab conduction (−277 kJ), compared to Cell 2 witch gains significant heat by tab conduction (1374 kJ) from Cell 1. Hence, the highly thermal conductive tabs between Cell 1 and 2, and not between 1 and 4, clearly is the cause of the temperature difference between Cell 2 and 4.

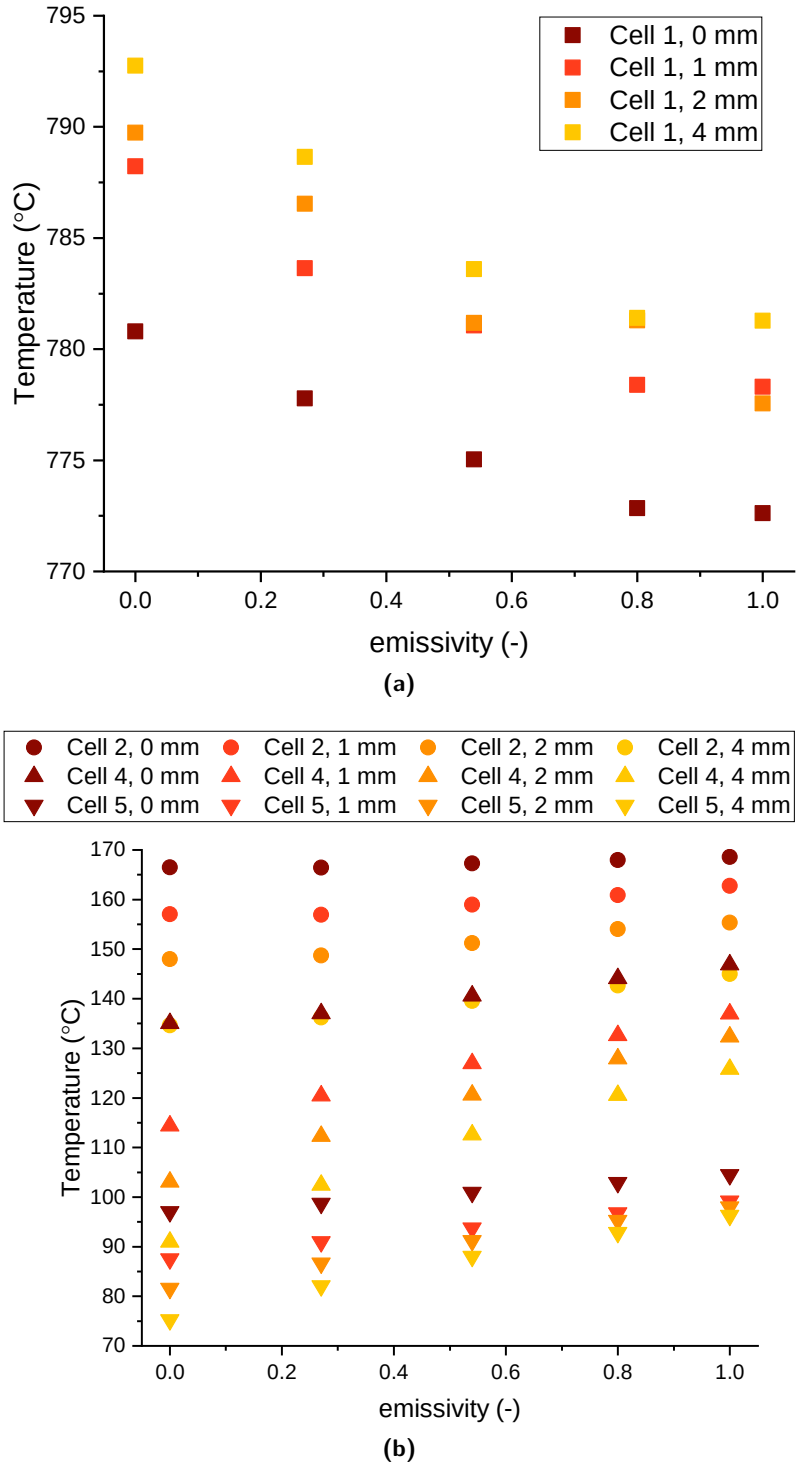

Figure 6.12: Maximum mean temperature reached at various ε_{cell} and d_{cc} values. Sub-figures (a) and (b) present cell 1 and cells 2, 4 and 5 respectively.

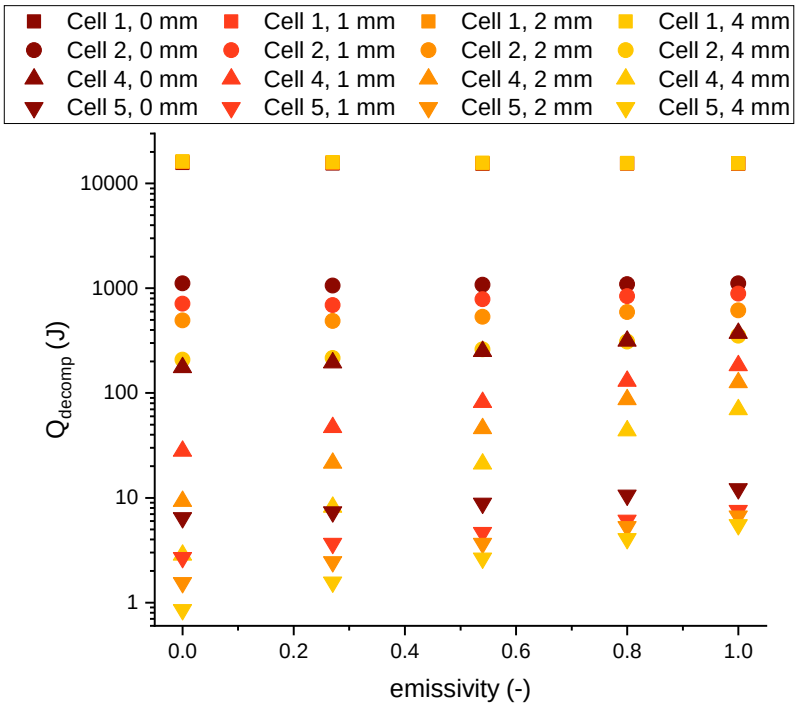

Figure 6.13: Accumulated decomposition energy for cells 1, 2, 4 and 5 at various ε_{cell} and d_{cc} values.

6.4.5.2 Effect of ε_{cell} and d_{cc} on Maximum Cell Temperature

For cell 1, from Fig. 6.12(a), it can be seen that at a given cell-to-cell spacing as ε_{cell} increases the maximum cell temperature reduces. From $\varepsilon_{cell} = 0$ to $\varepsilon_{cell} = 1$ the temperature reduces by 8–12°C, irrespective of d_{cc}. For a given emissivity the maximum temperature increases as d_{cc} increases. From 0 mm to 1 mm the temperature increases by approximately 6°C, while for further increases in d_{cc} the increase in temperature is generally lower. This shows that the severity of TR in a cell under TR is worsened by lower cell surface emissivity and greater cell-to-cell spacing, however only slightly.

For the cells adjacent to Cell 1 (i.e. Cells 2, 4, and 5) the trends in maximum temperature with emissivity and cell spacing are opposite to that observed for Cell 1. That is to say, as emissivity increases and cell spacing is reduced maximum cell temperature increases, see Figure 6.12(b). As such, it is apparent that to reduce the TRP potential by reducing heat transfer through increased cell spacing and reducing cell surface emissivity there is an inherent increase in the severity of the initiation cell.

For Cell 2, when $d_{cc} = 0$ mm there is little change (2°C) in the maximum temperature reached in the cell over the range of $\varepsilon_{cell} = 0$ to $\varepsilon_{cell} = 1$. Over this range the heat transfer to the cell only increases by 107 J, while radiation accounts for 36% of the heat transfer up to the point of maximum cell temperature when $\varepsilon_{cell} = 1$ (see Table B.1). However, at $d_{cc} = 4$ mm there is a greater temperature increase, 10°C, and a greater dependence of maximum temperature on emissivity value. This is due to an increase in heat transfer, by 384 J, between cases with $\varepsilon_{cell} = 0$ and $\varepsilon_{cell} = 1$ (see Table B.4), while radiation is more

dominant (in general) at any given ε_{cell} at larger d_{cc} compared to small d_{cc}, see Tables B.1 to B.4. For comparison, when $\varepsilon_{cell} = 1$ radiation accounts for 62% of the heat transfer up to maximum temperature of cell 2 when $d_{cc} = 4\,\text{mm}$.

A similar trend, whereby there is a greater increase in maximum mean cell temperature over the studied ε_{cell} range at larger d_{cc} compared to lower d_{cc}, is observed in cells 4 and 5, see Fig. 6.12(b). However, the magnitude of this behaviour for a given d_{cc} is greater in Cells 4 and 5 compared to Cell 2. Further more, Cell 4 is more sensitive to ε_{cell} than Cell 5, even though a larger fraction of heat transfer to Cell 5 is by radiation than compared to Cell 4. As can be seen from Tables B.1 to B.4, this is due to the greater relative increase in radiative heat transfer at each increment of ε_{cell} from the last, for Cell 4 compared to 5. As the perpendicular distance to the dominant heat source (i.e. cell 1) is greater to Cell 5 (i.e. $d_{\perp} = \sqrt{2}\,(d_{cc} + 2r_{cell}) - 2r_{cell}$) than Cell 4 (i.e. $d_{\perp} = d_{cc}$), then due to the dependence of radiative flux on the inverse of the squared distance, then the heat transfer by radiation to Cell 5 is lower by a proportional $(1/\sqrt{2})$ amount (approximately) and as such further increases are proportionally lower.

Figure 6.12(b) also shows that at a given emissivity value, as d_{cc} increases the maximum temperature reduces in cells adjacent to Cell 1, as shown elsewhere [e.g. 222]. However, this effect is greater for lower ε_{cell} values. As can be seen from Tables B.1 to B.4, at lower ε_{cell} a larger proportion of heat transfer is by conduction and the overall heat transfer up to the time of maximum cell is reduced for smaller ε_{cell}, while as d_{cc} increases heat transfer is increasingly dependent on radiation. Further, for cells not connected to the failed cell by the busbar (i.e. Cells 4 and 5) the greatest reduction in maximum temperature between incremental increases in d_{cc} is by increasing d_{cc} from 0 mm to 1 mm. This is due to the removal of contact heat transfer between cells and the insulation air provides between cells [225, 227]. As such, the TRP potential of any pack can be reduced by reducing the cell surface emissivity for any given cell spacing, while a minimum spacing is beneficial to remove contact heat transfer.

Section 6.4.1 showed LFP packs are highly resilient to TRP with typical cell surface emissivities. Further, under the parameter sweep of ε_{cell} and d_{cc}, Fig. 6.12(b) shows that even under the conditions that heat transfer is greatest, i.e. $d_{cc} = 0\,\text{mm}$ and $\varepsilon_{cell} = 1$, the maximum temperatures of adjacent cells remain below 170°C. The accumulated decomposition energy also remains relatively low for cells 2, 4 and 5 (following similar trends with ε_{cell} and d_{cc} to that of maximum temperature of Fig. 6.12(b)), see Fig. 6.13, due to the dependence of Q_{decomp} on temperature. Hence, under these extreme abuse and environmental conditions LFP packs can be stated to be highly resilient to TRP at any cell spacing and cell surface emissivity value.

6.4.5.3 Importance of Radiation Heat Transfer in Pack at Key Time Instances

The heat transfer behaviour of cells in the pack can be analysed for the cell under TR, referred to as the *initiation* cell, for the cells adjacent to the initiation cell, termed *primary* cells, and for cells adjacent to the primary cells, termed *secondary* cells. The initiation cell is Cell 1, the primary cells are Cells 2, 4 and 5, and the secondary cells are Cells 3, 6, 7–9. The heat transfer over two important time instances is discussed. The first is up to the time of each individual cell's maximum temperature, and the second is the period from the individual cell's maximum temperature to the end time of simulation, a.k.a the cool down period.

The heat transfer up to an individual cells' maximum temperature is first discussed. For the initiation cell the magnitude of total heat transfer from the cell up to the maximum cell temperature generally increases with larger ε_{cell}. Between $\varepsilon_{cell} = 0$ and $\varepsilon_{cell} = 1$ at a $d_{cc} = 0\,\text{mm}$ the magnitude of heat loss increases by 105 J (see Table B.1), while at a $d_{cc} = 4\,\text{mm}$ the magnitude of heat loss increases by 203 J (see Table B.4). The heat transfer by surface conduction is greater than that by conduction through the tabs, due to the small surface area of the tabs compared to the cell surface area. As ε_{cell} increases a greater proportion of heat transfer is by radiation and the proportion by surface conduction reduces, while that by conduction through the tabs remains relativity constant. For example at $d_{cc} = 0\,\text{mm}$ (see Table B.1) the fraction of heat transfer that is by radiation increases from 0% to 30% over the range of $\varepsilon_{cell} = 0$ to $\varepsilon_{cell} = 1$, while heat transfer by surface conduction and tab conduction reduce from 80% to 54% and 20% to 15%, respectively. At larger d_{cc} the magnitude of total heat transfer is less (see Tables B.1 to B.4), for example at $d_{cc} = 0\,\text{mm}$ compared to $d_{cc} = 4\,\text{mm}$ when $\varepsilon_{cell} = 0.8$ the total heat loss is $-1136\,\text{J}$ compared to $-832\,\text{J}$, see Table B.1 and Table B.4 respectively. However, for the same ε_{cell}, a greater amount of this total is by radiation, e.g. 44% at $d_{cc} = 4\,\text{mm}$ compared to 26% at $d_{cc} = 0\,\text{mm}$. Reduction in overall heat transfer is due to the lower values of conduction, dominated by lower cell surface conduction values, while tab condition reduces less at larger d_{cc} due to the high thermal conductivity of the nickel busbar.

Similar to the initiation cell, both the primary and secondary cells have increased total heat transfer with increased ε_{cell}, and reduced total heat transfer with increased d_{cc} as Tables B.1 to B.4 show. Also, as with the initiation cell, there is an increased proportion of heat transfer by radiation with increased ε_{cell} and increased d_{cc}. This shows that TRP potential of the pack can be reduced by lowering ε_{cell} without any reduction in pack volumetric or gravimetric energy density that would occur through increased cell spacing or the use of conductive intra-pack materials such as aluminium or composite PCMs.

The magnitude of heat transfer over the time to maximum cell temperature in the primary cells is greater than in the initiation cell. This is due to the fact that the initiation

cell's temperature rise is driven by rapid internal heat generation, while the primary cells' inward heat transfer is driven by the large temperature difference between the initiation and primary cells, leading to a greater period of heat transfer before peak temperature in the primary cells. Furthermore, the magnitude of heat transfer to the secondary cells is less than to the primary cells. This is due to the smaller temperature difference driving heat transfer between the primary and secondary cells compared to the initiation and primary cells.

In general, radiation accounts for a greater portion of heat transfer in the primary cells compared to secondary cells due to the greater temperature difference between initiation and primary cells and the dependence of radiative heat transfer on $T_2^4 - T_1^4$. For example at $\varepsilon_{cell} = 0.8$ and $d_{cc} = 0\,\text{mm}$ Table B.1 shows that radiation, on average, accounts for 45% of the heat transfer up to the maximum temperatures of the primary cells, while for the secondary cells radiation accounts for only 29% of total heat transfer on average. Comparatively, at $d_{cc} = 4\,\text{mm}$ Table B.4 shows that radiation, on average, accounts for 81% and 61% of total heat transfer in primary and secondary cells, respectively. Cell 2 is the exception, where radiative heat transfer accounts for a similar fraction of heat transfer as in secondary cells, due to the large amount of heat transfer by the direct connection with the initiation cell through the busbar. At $d_{cc} = 0\,\text{mm}$ when $\varepsilon_{cell} = 0.8$ radiation accounts for 30% of total heat transfer compared to the 44% and 62% for cells 4 and 5 respectively.

The heat transfer over the cool down period is now discussed. Above it has been shown that radiation can be important in the heating of cells adjacent to a cell in TR. However, as Tables B.5 and B.6 show, the heat transfer as the cells cool (i.e. from the time of maximum cell to end time of simulations) is dominated by surface conduction in all cells. However, this is due to the fact that heat transfer after maximum cell temperatures is calculated over a longer period of time of which cell temperatures are similar for the majority (approximately 80%) of the cooling time, see Fig. 6.1. Hence, the heat transfer benefits of radiation and tab conduction at large temperature differences are not influential. In primary cells tab conduction is the second larger contributor, while radiation and tab conduction play a larger role in the cooling of primary cells than secondary cells. This occurs as the primary cells have slightly longer periods of larger temperature differences than secondary cells.

The magnitude of total heat loss from cell 1, summing corresponding values in Table B.1 and Table B.5, is an order of magnitude greater than the next highest cells. However, this is due to the heat generated by short circuit (17.28 kJ) and decomposition (15.4–16.2 kJ see Fig. 6.13) of the cell being large, which in turn approximately equals the 31.5–32.0 kJ of heat lost from cell 1.

As above, increased ε_{cell} and smaller d_{cc} increases heat transfer, as such, cells cool more effectively under these conditions. Hence, there is the competing effects of increasing heat

transfer from a cell to reduce its TR potential, which improves heat transfer to adjacent cells and hence increases TRP potential. As TRP did not occur in this pack, due to the intrinsic stability of LFP cells, it is difficult to make confident conclusions on the effect cell emissivity has on TRP potential. It is shown that radiation and tab heat transfer are important at large temperature differences, present when a cell is under TR, and a lower emissivity reduces heat transfer to neighbouring cells, which in turn may reduce TRP potential. However, if more unstable and energetic cells are used, then reducing cell surface emissivity may only postpone TRP by increasing the time it takes for heat to be transferred to adjacent cells. This may lead to more severe TR as more heat can accumulate [70]. As such, further work would assist the study of the effect of cell surface emissivity on pack constructed more cells of different chemistries.

6.5 Conclusion

In this chapter a computational investigation into the safety of LFP battery packs has been undertaken. The aim was to establish the potential of pack TRP under extreme environmental temperatures when a single cell had undergone short circuit. To achieve this, a small 9-by-9 cell battery pack was modelled in 3D (a.k.a. 3D transfer model, 3D-HT), utilising the AAM, developed in Chapter 5 for a single LFP cell, solved in 0D (a.k.a 0D-AAM) for each cell.

First, to evaluate the suitability of the 0D abuse model assumption, and the use of a relatively coarse mesh due to computational limitations, 3D-HT/0D-AAM single cell simulations were carried out. This showed that the use of the 3D-HT/0D-AAM model leads to quicker heating of the cell from the environment, however this only leads to a slight advance of the cell temperature, e.g. by 1 min. Further, the 3D-HT/0D-AAM leads to an underestimate of energy released from cell decomposition. A reduction of 25°C in maximum temperature using the 3D-HT/0D-AAM compared to the 1D parametrised model is apparent. This due to the smaller jelly roll in the 3D model compared to the 1D parametrised model of Chapter 5. In turn, this also leads to a later occurrence of TR. Although differences are apparent between the 3D-HT/0D-AAM and 1D models, they are quantified and, overall, small. Hence, the 3D-HT/0D-AAM was deemed appropriate for full pack studies.

The use of a relatively coarse mesh was shown to have little effect on the prediction of key TR values, i.e. time to venting, time to maximum temperature and maximum temperature. There was less than 1% deference between the coarsest and finest meshes. Hence, the coarse mesh was deemed suitable for the pack study.

From the LFP pack simulation, it was shown that under the abuse of short-circuiting of one cell, there is not enough energy available to heat the neighbouring cells up to the

temperature at which significant self-heating reactions occur. Particularly, the NE reaction does not develop by any significant amount in cells neighbouring the abused cell, as such TR is not present in the neighbouring cells and TRP does not occur. Therefore, it is clear that LFP cell lead to battery pack that are greatly resilient to TRP.

The influence of differences between the parametrised single cell model are negligible to the overall prediction of pack TRP potential in this case study. However, effects of the parameterised model give rise to important considerations when analysing pack behaviour, particularly in respect to the inclusion of venting behaviour. Mass composition B, which has a greater carbon and LFP content, leads to a greater temperature in the shorted cell, but cooler temperatures in the neighbouring cells, compared to the respective cells of mass composition A. The choice of burst pressure does not affect the resulting temperatures. The temperature rise in the cells adjacent to the shorted cell is driven by the heat from the shorted cell, as self heating reaction do not evolve significantly until higher temperatures that are not reached. For this reason, the greater heat in mass composition B in the shorted cell, over mass composition A, leads to cell venting sooner in the neighbouring cell, as the higher temperatures lead to higher pressure evolution sooner, as the bubble pressure is more dependent on temperature than mole fraction. Further, for a given gas production rate, a system with less electrolyte present leads to a greater increase in mole fraction, considering all else is equal. Hence, even in the case where activation energies of the NE and SEI reactions are higher, with less electrolyte present in the system the mole fraction increases to greater values sooner, leading to venting sooner. Given comparable masses, lower activation energies leads to venting sooner. Here, between case studies, the difference in venting and heating is small for different burst pressures given a mass composition. However, considering high rate and energy reactions of other Li-ion chemistries, the assumed burst pressure may have a greater influence on the advance/ delay of heating and hence TRP predictions, where higher assumed burst pressure (leading to lower parameterised activation energies) leads to heating and TRP sooner.

The importance of radiative heat transfer and cell surface emissivity on heat transfer within a pack was also studied. It was shown that radiation is more important at larger cell spacings and for greater surface emissivity values. At any cell spacing TRP potential of cells adjacent to a cell under TR can be reduced by lowering cell surface emissivity, which lowers overall heat transfer between cells. As such, it is recommended to lower cell surface emissivity to reduce pack TRP potential without any loss in overall pack volumetric or gravimetric energy density.

This work is important in the larger scope of LIB packs, as through novel investigation of cell surface emissivity on heat transfer within a pack, it enables the design of lighter battery packs that are resilient to TRP through simple alterations of cell surface to reduce emissivity value.

It has been shown that, considering only decomposition phenomena, LFP packs are resilient against TRP. Although cell electrochemistry (EC), and hence pack voltage, have not been considered, if one assume cells are connected in series then the LFP pack would be safe, while EC would have to be included to accurately state if the pack is safe under parallel arrangement. Hence, future work should include the modelling of EC to account for the additional ohmic heating that may lead to significant temperature rise and additional cell TR events. Future work should also consider the heat transfer by vent debris and vent gas combustion. TRP resilient batteries, such as those constructed of LFP cells, provide a safety advantage over other batteries, especially in uses such as home storage or extreme environments. Hence, further studies should develop on this work to consider larger batteries, suitable for these applications, to understand their resilience considering their larger battery capacity and electrical influences. It is also important that the TR field of study takes account of the affect venting has on parametrisation of models, and it turn the effects on TRP predictions. Finally, further work is recommended to corroborate these findings by investigating the effect of cell surface emissivity in LIB pack of cells of greater TR severity and accounting for electrical discharge between cells in parallel connections.

Chapter 7

Conclusions and Future Work

This thesis has introduced the TR hazard of Li-ion cells and the safety benefits of using an LFP chemistry in applicable applications. The aim of this work was to carry out an in-depth analysis of the TR hazard of LFP cells by experimental and computational methods, while further developing the theory and understanding of Li-ion TR models. From this, the following novel contributions have been made to the study of LIB TR:

- the first assessment of TR in LFP cells at various SOC under ARC and oven testing;
- the recommendation that ARC may not capture the full severity of TR and, hence, should be complemented by oven testing;
- development of a novel TR model referred to as the AAM, in which the assumption of cell pressurisation occurring at the bubble point of the electrolyte/ gas mixture is validated, and the use of the AAM is shown to considerably improve TR predictions of the LFP cells;
- using the parametrised LFP AAM, predictions of TR severity beyond the experimental studies were made, this showed that even at significantly higher temperatures beyond a critical oven set temperature the relative TR severity did not increase further;
- LFP packs are resilient to TRP under severe environmental and abuse scenarios even without any thermal management system in place;
- in packs where cells are closely packed radiation can account for up to 30% of heat transfer, while TRP potential can be reduced by lowering cell surface emissivity.

The findings of this work have been published in peer reviewed journals (see "List of Publications" on Page v). The following paragraphs summarise each chapter of the thesis.

The rapidly growing installed capacity of LIBs to facilitate renewable energy generation and enable EVs is motivation to study TR in Li-ion cells. Further, the potential and real dangers of TR at various battery scales has been shown through examples of past incidents. The TR process is known to be complex due to the many reactions occurring simultaneously. TR is also known to be hazardous due to the positive feedback loop that leads to vast amounts of heat generation, toxic and flammable gases, and the risk of explosion. Also, the LFP Li-ion chemistry is understood to be the safest chemistry available, whilst having additional benefits of being non-toxic and relatively low cost. As such the LFP chemistry has a substantial potential for utilisation at larger scales. However, TR incidents of LFP LIBs have still been recorded in the real world, viz. in EV buses. This highlights the need to further understand the complicated TR process so that it can be better prevented and, specifically, aid the utilisation of LFP LIBs as they provided environmental benefits over other Li-ion chemistries.

From undertaking a literature review, it was shown that the abuse scenarios of adiabatic calorimetry (which leads to zero heat loss from the cell and hence considered a worst case scenario) and oven testing are fundamental to TR analysis. From which, it was apparent that there was a lack of literature regarding detailed analysis of LFP cells. Further, the literature review discussed the modelling of TR in Li-ion cells, where it was shown that the calorimetry approach, based on Arrhenius formulae, was the most appropriate method for representing the TR reactions. However, regarding LFP cells, there was a lack of literature modelling LFP cells that had been validated. Additionally, the literature had shown that accounting for cell venting was important for accurate TR predictions. In other areas, such as a pressurised vessels representative of a system similar to Li-ion cells, a more detailed consideration of the thermodynamics usually requires that the system is at the bubble point. As such, the partial pressure method used in the literature is an over-simplification of cell pressurisation.

The literature also highlighted that investigations should be carried out upon battery packs. This is to understand a cell's safety under conditions that can lead to the more hazardous TRP event. To prevent TRP several thermal management techniques were reported in the literature. However, none had quantified the importance of cell-to-cell heat transfer by radiation.

LFP cells were chosen for investigations to assess the highlighted gaps in the literature regarding LFP specifically and Li-ion cell models generally as there is a lack of experimental testing and validated abuse models for LFP cells. Greater understanding of LFP cells will increase their accessibility in battery markets, providing a safer and less toxic Li-ion alternative, while advanced TR models will aid the development of safer LIBs.

The experimental thermal abuse of cells in this work was undertaken under ARC (specifically *Thermal Hazard Technology ARC EV+*) and oven testing. Further, a test to determine the cells' specific heat capacity, which is a key parameter to the TR models,

was undertaken. Modelling studies were carried out utilising the novel AAM TR model. The AAM considers cell pressurisation at bubble point, as highlighted by the literature review, and also a simmering reaction, identified in the experimental results.

ARC and oven testing was carried out to analyse the TR behaviour of 18650 LFP at various SOC under thermal abuse. From ARC testing it was found that TR only occurred at SOC greater than 28%, and in these cases was initiated at approximately 200°C, while maximum temperature rates where low (below 10°C/min). Hence, the overall safety of LFP cells at any SOC is greater than other chemistries. In fact, the maximum temperature rate of LFP cells is 3 to 4 orders of magnitude less than LMO, LCO, NMC and NCA cells at SOC of 30% and above. Further, it was concluded that NE reaction was the main cause of self-heating and the onset of TR. Therefore, improvements to the negative electrode are of primary importance to enhance the safety of LFP cells. From oven testing it was shown that there is a critical oven set temperature, at which there is a step change in TR severity of the cell. However, below this critical temperature, the heat generated by TR is at a rate on the same order of magnitude as high discharge operation, and hence manageable by typical thermal management systems.

A novel numerical method for estimating the heat generated by TR under oven exposure was presented, and shown to provide suitable estimates when compared to computational predictions. Utilising this and comparing the heat generated by cell TR under ARC and oven exposure for cells at 100% SOC, it was shown that the heat generated under ARC testing was less than that under abuse by oven exposure at 218°C oven set temperature. As ARC analysis is considered to be a worst case scenario, this highlights that the ARC analysis may not capture the full decomposition processes and hence should be complimented by oven analysis for a fuller picture of a cell's TR behaviour and safety.

In developing the AAM, it was shown that a classical TR model could not be parameterised such that the TR response of LFP cells under oven exposure could be reproduced accurately. Also, the bubble point assumption determining cell pressurisation through the BPV method in the AAM was tested, and proven valid by comparison with a previous methodology in the literature. The AAM was shown to greatly outperform the classical TR model due to the inclusion of the venting and simmering reactions. Although similar TR predictions can be made for the different mass compositions and pressure limit values, defining the exact reaction kinetics is difficult without precise knowledge of these parameters. This highlights the presence of valid but non-unique reaction kinetics, which brings to attention the caution needed when applying the same kinetic parameters across different cell mass compositions.

The AAM also allowed simulation of oven tests at oven set temperatures beyond those studied experimentally. From this, the same step change in severity at the critical oven temperature was predicted as seen in the experimental results. It was also shown that at oven temperatures significantly above this critical temperature there is no further increase

in relative TR severity. The AAM aids the battery community as accurate predictions of cell pressurisation help the development of safer batteries through aiding the development of advanced BMS, accounting for pressure measurements, and being an enabling step towards modelling vent ejecta and their associated heat transfer.

Considering a 18650 LFP battery pack in extreme environmental temperatures experiencing a severe internal short circuit, it was shown that the pack did not undergo TRP. This was attributed to the high stability of the LFP cells, as the heat released from the failed cell was not sufficient to heat the neighbouring cell to the temperatures that lead to significant progression of the energetic NE reaction. It was also shown that any of the parameterised models, which lead to similar single cell TR predictions in all cases, had little effect on the results of pack simulations. However, it was noted that in cases with larger NE masses there was a slight increase in temperatures of neighbouring cells due to the disproportionate influence of the NE reaction on the overall heat generated owing to the energetic nature of the NE reaction and its low onset temperature. Finally, it was shown that radiation is more important at greater cell spacings, while overall heat transfer can be reduced by lowering cell surface emissivity value. Hence, it is recommended to design battery packs with lower cell surface emissivities, through simple surface alterations, in order to design safer and lighter LIBs.

7.1 Future Work

From the work carried out in this thesis several opportunities for future work are brought to the attention of the reader.

7.1.1 Abuse Model Governing Theory Development

In parameterising the AAM for the LFP cell, errors in predictions at lower oven set temperatures and at the critical oven set temperature highlight further points for investigation. Additionally, under the assumed four reaction system of TR modelling, at lower oven temperatures, peak TR temperature could not be met while still maintaining accurate predictions. Hence, secondary and interdependent reactions, which are stated to occur in the literature but generally not accounted for in modelling, are recommended for consideration in future work.

While the BPV method of cell pressurisation was validated, the behaviour of the temperature drop at venting was seen to occur too rapidly. Therefore an improved representation of the phase equilibrium of the liquid-vapour mixture is needed. This requires the development the governing equation away from the dependence of the bulk mole fraction of the electrolyte/DMC mixture, to one that considers vapour fraction and mole fraction

in each phase to improve pressure calculation. Also, this allows for the expansion and re-equilibrium of the mixture as the cell cools during venting which is thought to slow the rate pressure drop of the cell and in turn the temperature rate over venting. Furthermore, developing on this, there should be work on predicting the vent gas flow and combustion behaviour, as it is known to be a significant fire hazard.

7.1.2 Abuse Model Parameterisation Methodology

Parameterising an abuse model is difficult and slow due to the complex reactions' behaviours. Hence, there needs to be development of a computationally aided and intelligent method of parametrisation, such as using Gaussian Processes or deep learning techniques. Thus, parameterisation could be undertaken more rapidly, allowing for statistical analysis and for greater detailed models, making it more useful to industry. Model detail can be increased by intelligent parameterisation as it can be used to aid parameterisation of individual reactions dependent on SOC, which is important for battery packs under operation where SOC is time variant. Further, it can allow for a black box model approach, considering a reaction database, that can be used to perform reaction pathway analysis to determine the likely reactions occurring in individual cell chemistries. This will enable the determination and utilisation of interdependent and secondary reactions highlighted as important in Section 7.1.1.

7.1.3 LIB Pack Studies

In this work only the decomposition heat generation was accounted for in the LFP pack studies. However, it is known that ohmic heating through failed cells is important in parallel connected cells. Hence, there is a need for further work on assessing the TRP potential of the LFP pack studied, considering the electrical behaviour alongside validation against experimental data. Further, building on the developments of cell pressurisation and the further work mentioned in Section 7.1.1, there should be work including vent gas flow and combustion, as it is shown to be important to TRP under experimental tests. Finally, for the LFP cells studied, it was shown that lower cell surface emissivities reduced overall heat transfer to cells adjacent to the abused cell and in turn lead to reduced decomposition of said cells. However, these findings should be corroborated for packs of cells of chemistries that are more prone to TRP to determine if this is true in all cases.

References

[1] M.R. Allen and O.P. Dube and W. Solecki and F. Aragn-Durand and W. Cramer, S. Humphreys and M. Kainuma and J. Kala and N. Mahowald and Y. Mulugetta and R. Perez and M. Wairiu and K. Zickfeld, "Framing and Context." 2018, In: *Global Warming of 1.5˚C. An IPCC Special Report on the impacts of global warming of 1.5˚C above pre-industrial levels and related global greenhouse gas emission pathways, in the context of strengthening the global response to the threat of climate change, sustainable development, and efforts to eradicate poverty.* [V. Masson-Delmotte, P. Zhai, H.-O. Prtner, D. Roberts, J. Skea, P.R. Shukla, A. Pirani, W. Moufouma-Okia, C. Pan, R. Pidcock, S. Connors, J.B.R. Matthews, Y. Chen, X. Zhou, M.I. Gomis, E. Lonnoy, T. Maycock, M. Tignor, and T. Waterfield (eds.)].

[2] United States Environmental Protection Agency, "Global Greenhouse Gas Emissions Data," [online] Available at: https://www.epa.gov/ghgemissions/global-greenhouse-gas-emissions-data [Accessed 23 September 2019].

[3] J. Rogelj and D. Shindell and K. Jiang and S. Fifita and P. Forster and V. Ginzburg and C. Handa and H. Kheshgi and S. Kobayashi and E. Kriegler and L. Mundaca and R. Sfrian and M.V.Vilario, "Mitigation Pathways Compatible with 1.5°C in the Context of Sustainable Development." 2018, In: *Global Warming of 1.5˚C. An IPCC Special Report on the impacts of global warming of 1.5˚C above pre-industrial levels and related global greenhouse gas emission pathways, in the context of strengthening the global response to the threat of climate change, sustainable development, and efforts to eradicate poverty.* [V. Masson-Delmotte, P. Zhai, H.-O. Prtner, D. Roberts, J. Skea, P.R. Shukla, A. Pirani, W. Moufouma-Okia, C. Pan, R. Pidcock, S. Connors, J.B.R. Matthews, Y. Chen, X. Zhou, M.I. Gomis, E. Lonnoy, T. Maycock, M. Tignor, and T. Waterfield (eds.)].

[4] M. I. Hoffert, K. Caldeira, G. Benford, D. R. Criswell, C. Green, H. Herzog, A. K. Jain, H. S. Kheshgi, K. S. Lackner, J. S. Lewis, H. D. Lightfoot, W. Manheimer, J. C. Mankins, M. E. Mauel, L. J. Perkins, M. E. Schlesinger, T. Volk, and T. M. L. Wigley, "Advanced Technology Paths to Global Climate Stability: Energy for a Greenhouse Planet," *Science*, vol. 298, no. 5595, pp. 981–987, 2002.

[5] International Energy Agency, "Global EV Outlook 2016: Beyond one million electric cars," Paris, Tech. Rep., 2016. [Online]. Available: Availableat:https://www.iea.org/publications/freepublications/publication/Global_EV_Outlook_2016.pdf [accessed 2 August 2016].

[6] B. Diouf and R. Pode, "Potential of lithium-ion batteries in renewable energy," *Renewable Energy*, vol. 76, pp. 375 – 380, 2015.

[7] J. M. Tarascon, "Key challenges in future li-battery research," *Philosophical Transactions of the Royal Society*, vol. 369, no. 1923, p. 32273241, 2010.

[8] T.-H. Kim, J.-S. Park, S. K. Chang, S. Choi, J. H. Ryu, and H.-K. Song, "The Current Move of Lithium Ion Batteries Towards the Next Phase," *Advanced Energy Materials*, vol. 2, no. 7, pp. 860–872, 2012.

[9] T. Placke, R. Kloepsch, S. Dühnen, and M. Winter, "Lithium ion, lithium metal, and alternative rechargeable battery technologies: the odyssey for high energy density," *Journal of Solid State Electrochemistry*, vol. 21, no. 7, pp. 1939–1964, 2017.

[10] Deutsche Bank, "Electric Cars: Plugged In 2," 2009, [online] Available at: http://www.libralato.co.uk/docs/Electric%20Cars%20Plugged%20In%202%20Deutsche%20Bank%202009.pdf [Accessed 23 September 2019].

[11] J.-M. Tarascon and M. Armand, "Issues and challenges facing rechargeable lithium batteries," *Nature*, vol. 414, no. 6861, pp. 359–367, 2001.

[12] DUKES, "Renewable sources of energy: Chapter 6, Digest of United Kingdom Energy Statistics," London, Tech. Rep., 2016. [Online]. Available: https://www.gov.uk/government/statistics/renewable-sources-of-energy-chapter-6-digest-of-united-kingdom-energy-statistics-dukes [accessed 2 August 2016].

[13] BP, "Wind energy," 2015. [Online]. Available: http://www.bp.com/en/global/corporate/energy-economics/statistical-review-of-world-energy/renewable-energy/wind-energy.html [accessed 22 September 2016].

[14] ——, "Solar Energy," 2015. [Online]. Available: http://www.bp.com/en/global/corporate/energy-economics/statistical-review-of-world-energy/renewable-energy/solar-energy.html [accessed 22 September 2016].

[15] Global Wind Energy Council, "Global Wind Report Annual Market Update 2015," Tech. Rep., 2015. [Online]. Available: http://www.gwec.net/publications/global-wind-report-2/global-wind-report-2015-annual-market-update/ [accessed 22 September 2016].

[16] IRENA and IEA-ETSAP, "Technology Brief - Electricity Storage," Tech. Rep. April, 2012. [Online]. Available: https://www.irena.org/DocumentDownloads/Publications/IRENA-ETSAP%20Tech%20Brief%20E18%20Electricity-Storage.pdf [accessed 22 September 2016].

[17] X. Luo, J. Wang, M. Dooner, and J. Clarke, "Overview of current development in electrical energy storage technologies and the application potential in power system operation," *Applied Energy*, vol. 137, pp. 511 – 536, 2015.

[18] U.S. Department of Energy and Sandia National Laboratories, "DOE Global Energy Storage Database," 2016. [Online]. Available: http://www.energystorageexchange.org/projects [accessed 22 September 2016].

[19] A. Hirtenstein, "Batteries Win Biggest Energy Storage Competition of the Year," 2016. [Online]. Available: http://www.renewableenergyworld.com/articles/2016/08/batteries-win-biggest-energy-storage-competition-of-the-year.html [accessed 22 September 2016].

[20] O. Palizban and K. Kauhaniemi, "Energy storage systems in modern grids Matrix of technologies and applications," *Journal of Energy Storage*, vol. 6, pp. 248–259, 2016.

[21] J. Leadbetter and L. G. Swan, "Selection of battery technology to support grid-integrated renewable electricity," *Journal of Power Sources*, vol. 216, pp. 376–386, 2012.

[22] B. Dunn, H. Kamath, and J.-M. Tarascon, "Electrical energy storage for the grid: A battery of choices," *Science*, vol. 334, no. 6058, pp. 928–935, 2011.

[23] D. Doughty and E. P. Roth, "A General Discussion of Li Ion Battery Safety," *The Electrochemical Society Interface*, vol. 21, no. 2, pp. 37–44, 2012.

[24] M. Steen, N. Lebedeva, F. Di Persio, and L. Boon-Brett, "EU Competitiveness in Advanced Li-ion Batteries for E-Mobility and Stationary Storage Applications Opportunities and Actions," European Commission's Joint Research Centre, Tech. Rep., 2017. [Online]. Available: http://publications.jrc.ec.europa.eu/repository/bitstream/JRC108043/kjna28837enn.pdf [accessed 1 September 2018].

[25] D. Linden and T. B. Reddy, Eds., *Handbook of Batteries*, 3rd ed. New York: McGraw-Hill, 2001.

[26] Q. Wang, P. Ping, X. Zhao, G. Chu, J. Sun, and C. Chen, "Thermal runaway caused fire and explosion of lithium ion battery," *Journal of Power Sources*, vol. 208, pp. 210–224, 2012.

[27] S.-C. Chen, Y.-Y. Wang, and C.-C. Wan, "Thermal Analysis of Spirally Wound Lithium Batteries," *Journal of The Electrochemical Society*, vol. 154, no. 4, pp. A637–A648, 2006.

[28] C. Daniel, "Materials and processing for lithium-ion batteries," *JOM*, vol. 60, no. 9, pp. 43–48, 2008.

[29] S. C. Chen, C. C. Wan, and Y. Y. Wang, "Thermal analysis of lithium-ion batteries," *Journal of Power Sources*, vol. 140, no. 1, pp. 111–124, 2005.

[30] K. Smith and C.-Y. Wang, "Power and thermal characterization of a lithium-ion battery pack for hybrid-electric vehicles," *Journal of Power Sources*, vol. 160, no. 1, pp. 662–673, 2006.

[31] T. F. Fuller, M. Doyle, and J. Newman, "Simulation and Optimization of the Dual Lithium Ion Insertion Cell," *Journal of The Electrochemical Society*, vol. 141, no. 1, pp. 1–10, 1994.

[32] G. Liu, H. Zheng, X. Song, and V. S. Battaglia, "Particles and Polymer Binder Interaction: A Controlling Factor in Lithium-Ion Electrode Performance," *Journal of The Electrochemical Society*, vol. 159, no. 3, pp. 214–221, 2012.

[33] H. Zheng, R. Yang, G. Liu, X. Song, and V. S. Battaglia, "Cooperation between Active Material, Polymeric Binder and Conductive Carbon Additive in Lithium Ion Battery Cathode," *The Journal of Physical Chemistry*, vol. 116, no. 7, pp. 4875–4882, 2012.

[34] P. Arora and Z. J. Zhang, "Battery Separators," *Chemical Reviews*, vol. 104, no. 10, pp. 4419–4462, 2004.

[35] W. Bohnstedt, "Separators," in *Handbook of Battery Materials*, 2nd ed., C. Daniel and J. O. Besenhard, Eds. Weinheim: Wiley-VCH, 2011, ch. 11, p. 285.

[36] N. Tanaka and W. G. Bessler, "Numerical investigation of kinetic mechanism for runaway thermo-electrochemistry in lithium-ion cells," *Solid State Ionics*, vol. 262, pp. 70–73, 2014.

[37] S. Abada, G. Marlair, A. Lecocq, M. Petit, V. Sauvant-Moynot, and F. Huet, "Safety focused modeling of lithium-ion batteries: A review," *Journal of Power Sources*, vol. 306, pp. 178–192, 2016.

[38] P. Peng and F. Jiang, "Thermal safety of lithium-ion batteries with various cathode materials: A numerical study," *International Journal of Heat and Mass Transfer*, vol. 103, pp. 1008–1016, 2016.

[39] I. Buchmann, *Batteries in a Portable World*, 4th ed. Cadex Electronics Inc., 2016, ch. 2 - Battery Types, pp. 63–69.

[40] H. U. Escobar-Hernandez, R. M. Gustafson, M. I. Papadaki, S. Sachdeva, and M. S. Mannan, "Thermal Runaway in Lithium-Ion Batteries: Incidents, Kinetics of the Runaway and Assessment of Factors Affecting Its Initiation," *Journal of The Electrochemical Society*, vol. 163, no. 13, pp. A2691–A2701, 2016.

[41] K. Bullis, "Are Electric Vehicles a Fire Hazard?" 2013, [online] Available at: https://www.technologyreview.com/s/521976/are-electric-vehicles-a-fire-hazard/ [Accessed 18 August 2017].

[42] R. Campbell, "Electronic Cigarette Explosions and Fires: The 2015 Experience," Tech. Rep., 2016, [online] Available at: http://www.nfpa.org/news-and-research/fire-statistics-and-reports/fire-statistics/fire-causes/electrical-and-consumer-electronics/electronic-cigarette-explosions-and-fires-the-2015-experience [Accessed 18 August 2017].

[43] S. Hollister, "Here are the reasons why so many hoverboards are catching fire," 2016, [online] Available at: https://www.cnet.com/uk/news/why-are-hoverboards-exploding-and-catching-fire/ [Accessed 18 August 2017].

[44] Jukin Media, "No smoke without fire: e-cigarette explodes in mans pocket video," 2016. [Online]. Available: https://www.theguardian.com/society/video/2016/nov/04/no-smoke-without-fire-e-cigarette-explodes-in-mans-pocket-video [accessed 19 September 2018].

[45] U.S. Department of Health and Human Services, "E-Cigarette Use Among Youth and Young Adults: A Report of the Surgeon General," 2016. [Online]. Available: https://e-cigarettes.surgeongeneral.gov/documents/2016_sgr_full_report_non-508.pdf [accessed 19 September 2018].

[46] A. Griffin, "Samsung Galaxy Note 7: Company Issues Unprecedented Statement Offering Returns After Phones Explode," 2016. [Online]. Available: https://www.independent.co.uk/life-style/gadgets-and-tech/news/samsung-galaxy-note-7-company-issues-unprecedented-statement-offering-returns-after-phones-explode-a7221466.html [accessed 19 September 2018].

[47] BBC, "Samsung confirms battery faults as cause of Note 7 fires," 2017. [Online]. Available: https://www.bbc.co.uk/news/business-38714461 [accessed 19 September 2018].

[48] Chappaqua Fire Department, "Holiday Gift Explodes and Catches Fire," 2015. [Online]. Available: http://www.chappaquafd.org/LatestNewsStory.php?nSI=1333812519 [accessed 19 September 2018].

[49] National Transportation Safety Board, "Investigative Update of Battery Fire Japan Airlines B-787 - Jan 7, 2013," 2013. [Online]. Available: https://www.ntsb.gov/news/events/Documents/2013_Lithium_Batteries_FRM-Pres1.pdf [accessed 19 September 2018].

[50] N. Williard, W. He, C. Hendricks, and M. Pecht, "Lessons Learned from the 787 Dreamliner Issue on Lithium-Ion Battery Reliability," *Energies*, vol. 6, no. 9, pp. 4682–4695, 2013.

[51] A. Gill, "Tesla car on fire," 2013. [Online]. Available: https://www.youtube.com/watch?v=q0kjI08n4fg [accessed 19 September 2018].

[52] B. Klayman and B. Woodall, "UPDATE 5-Tesla reports third fire involving Model S electric car," 2013. [Online]. Available: https://www.reuters.com/article/autos-tesla-fire-idUSL2N0IS0TL20131107 [accessed 19 September 2018].

[53] L. Xin, "[Responding to new energy bus fires: battery pack active safety design is essential]," 2015. [Online]. Available: http://www.diandong.com/news/5310.html [accessed 19 September 2018] (In Chinese).

[54] "[Shenzhen Wuzhoulong electric bus burning and explosion, BYD issued an announcement to clarify]," 2015. [Online]. Available: http://nev.ofweek.com/2015-04/ART-71008-8120-28951921.html [accessed 19 September 2018] (In Chinese).

[55] N. S. Spinner, K. M. Hinnant, R. Mazurick, A. Brandon, S. L. Rose-pehrsson, and S. G. Tuttle, "Novel 18650 lithium-ion battery surrogate cell design with anisotropic thermophysical properties for studying failure events," *Journal of Power Sources*, vol. 312, pp. 1–11, 2016.

[56] FAA, "Lithium Battereies & Lithium battery-Powered Devices: Events Involving Smoke, Fire, Extreme Heat or Explosion Involving Lithium Batteries," 2019, [online] Available at: https://www.faa.gov/hazmat/resources/lithium_batteries/media/Battery_incident_chart.pdf [Accessed 26 September 2019].

[57] S. Saxena, L. Kong, and M. G. Pecht, "Exploding e-cigarettes: A battery safety issue," *IEEE Access*, vol. 6, pp. 21 442–21 466, 2018.

[58] X. Feng, M. Ouyang, X. Liu, L. Lu, Y. Xia, and X. He, "Thermal runaway mechanism of lithium ion battery for electric vehicles: A review," *Energy Storage Materials*, vol. 10, pp. 246 – 267, 2018.

[59] National Transportation Safety Board, "Preliminary Report Highway HWY18FH011," Tech. Rep., 2018. [Online]. Available: https://ntsb.gov/investigations/AccidentReports/Reports/HWY18FH011-preliminary.pdf [accssesd 18 September 2018].

[60] L. Greenemeier, "Could Chevy Volt Lithium-Ion Battery Fires Burn Out Interest in EVs and Hybrids?" 2011, [online] Available at: https://blogs.scientificamerican.com/observations/could-chevy-volt-lithium-ion-battery-fires-burn-out-interest-in-evs-and-hybrids/ [Accessed 26 September 2019].

[61] Advanced Propulsion Centre UK, "The Roadmap Report Towards 2040: A Guide To Automotive Propulsion Technologies," 2018, [online] Available at: https://www.apcuk.co.uk/app/uploads/2018/06/roadmap-report-26-6-18.pdf [Accessed 26 September 2019].

[62] Viridor, "Lithium ion battery warning issued after landfill site fire," 2019, [online] Available at: https://www.viridor.co.uk/who-we-are/latest-news/2019-news/lithium-ion-battery-warning-issued-after-landfill-site-fire/ [Accessed 26 September 2019].

[63] W. Date, "Fire extinguished at Viridors St Helens WEEE plant," 2019, [online] Available at: https://www.letsrecycle.com/news/latest-news/fire-extinguished-at-viridors-st-helens-weee-plant/ [Accessed 26 September 2019].

[64] S. Binks, "Lead, lithium recycling mix: a clear and present danger," *Batteries International*, vol. Spring, pp. 12–13, 2015. [online] Available at: https://www.ila-lead.org/UserFiles/File/Newsletter%20files/Lithium%20battery%20safety%20-%20Batteries%20International.pdf [Accessed 26 September 2019].

[65] A. W. Golubkov, S. Scheikl, R. Planteu, G. Voitic, H. Wiltsche, C. Stangl, G. Fauler, A. Thaler, and V. Hacker, "Thermal runaway of commercial 18650 Li-ion batteries with LFP and NCA cathodes - impact of state of charge and overcharge," *RSC Adv.*, vol. 5, no. 70, pp. 57 171–57 186, 2015.

[66] J. Wen, Y. Yu, and C. Chen, "A Review on Lithium-Ion Batteries Safety Issues: Existing Problems and Possible Solutions," *Materials Express*, vol. 2, no. 3, pp. 197–212, 2012.

[67] E. P. Roth and C. J. Orendorff, "How electrolytes influence battery safety," *The Electrochemical Society Interface*, vol. 21, no. 2, pp. 45–49, 2012.

[68] Q. Wang, J. Sun, and G. Chu, "Lithium Ion Battery Fire and Explosion," in *Fire Safety Science Proceedings of the Eighth International Symposium International Association for Fire Safety Science*, Beijing, 2005, pp. 375–382.

[69] Q. Wang, P. Ping, and J. Sun, "Catastrophe analysis of cylindrical lithium ion battery," *Nonlinear Dynamics*, vol. 61, no. 4, pp. 763–772, 2010.

[70] X. Feng, X. He, M. Ouyang, L. Lu, P. Wu, C. Kulp, and S. Prasser, "Thermal runaway propagation model for designing a safer battery pack with 25Ah $LiNi_xCo_yMn_zO_2$ large format lithium ion battery," *Applied Energy*, vol. 154, pp. 74–91, 2015.

[71] G. Chen and T. J. Richardson, "Thermal instability of Olivine-type $LiMnPO_4$ cathodes," *Journal of Power Sources*, vol. 195, no. 4, pp. 1221–1224, 2010.

[72] Federal Aviation Administration, "SAFO09013SUP: Fighting Fires Caused By Lithium Type Batteries in Portable Electronic Devices," 2009. [Online]. Available: https://www.faa.gov/other_visit/aviation_industry/airline_operators/airline_safety/safo/all_safos/media/2009/SAFO09013SUP.pdf [accessed 18 August 2017].

[73] R. T. Long Jr., A. F. Blum, T. J. Bress, and B. R. Cotts, "Battery Testing - Best Practices for Responding to Emergency Incidents in Plug-in Electric Vehicles (EV)," The Fire Protection Research Foundation, Tech. Rep., 2013. [Online]. Available: https://energy.gov/sites/prod/files/2014/02/f8/final_report_nfpa.pdf [accessed 18 August 2017].

[74] Hazard Control Technologies Inc., "Fire Suppression for Hybrid and Electric Vehicles," Tech. Rep., 2013. [Online]. Available: http://www.hct-world.com/wp-content/uploads/2013/08/Articles/CH_F5_AUT_Fire%20Suppression%20for%20Hybrid%20and%20Electric%20Vehicles-Compiled.pdf [accessed 18 August 2017].

[75] N. N. Semenov, *Some Problems of Chemical Kinetics and Reactivity.* London: Pergamon Press, 1959, vol. 2, translated from Russian by J. E. S. Bradley.

[76] D. A. Frank-Kamenetskii, *Diffusion and Heat Transfer in Chemical Kinetics*, 2nd ed. New York-London: Plenum Press, 1969, translated from Russian by J. P. Appleton.

[77] T. Kotoyori, *Critical Temperatures for the Thermal Explosion of Chemicals.* Amsterdam - San Diego - Oxford - London: Elsevier, 2005, vol. 7, ch. Chapter 1 An approach to the thermal explosion theory, pp. 1–17.

[78] R. Spotnitz and J. Franklin, "Abuse behavior of high-power, lithium-ion cells," *Journal of Power Sources*, vol. 113, no. 1, pp. 81–100, 2003.

[79] D. H. Doughty, P. C. Butler, R. G. Jungst, and E. P. Roth, "Lithium battery thermal models," *Journal of Power Sources*, vol. 110, no. 2, pp. 357–363, 2002.

[80] M. N. Richard and J. R. Dahn, "Accelerating Rate Calorimetry Study on the Thermal Stability of Lithium Intercalated Graphite in Electrolyte I. Experimental," *Journal of The Electrochemical Society*, vol. 146, no. 6, pp. 2068–2077, 1999.

[81] ——, "Accelerating Rate Calorimetry Study on the Thermal Stability of Lithium Intercalated Graphite in Electrolyte. II. Modeling the Results and Predicting Differential Scanning Calorimeter Curves," *Journal of The Electrochemical Society*, vol. 146, no. 6, pp. 2078–2084, 1999.

[82] A. Melcher, C. Ziebert, M. Rohde, and H. J. Seifert, "Modeling and simulation of the thermal runaway behavior of cylindrical Li-ion cells-computing of critical parameters," *Energies*, vol. 9, no. 4, pp. 1–19, 2016.

[83] M. J. Loveridge, G. Remy, N. Kourra, R. Genieser, A. Barai, M. J. Lain, Y. Guo, M. Amor-segan, M. A. Williams, T. Amietszajew, M. Ellis, R. Bhagat, and D. Greenwood, "Looking Deeper into the Galaxy (Note 7)," *Batteries*, vol. 4, no. 1, pp. 1–11, 2018.

[84] D. P. Abraham, E. P. Roth, R. Kostecki, K. McCarthy, S. MacLaren, and D. H. Doughty, "Diagnostic examination of thermally abused high-power lithium-ion cells," *Journal of Power Sources*, vol. 161, no. 1, pp. 648–657, 2006.

[85] S. Al Hallaj, H. Maleki, J. Hong, and J. Selman, "Thermal modeling and design considerations of lithium-ion batteries," *Journal of Power Sources*, vol. 83, no. 1-2, pp. 1–8, 1999.

[86] P. Ping, Q. Wang, P. Huang, J. Sun, and C. Chen, "Thermal behaviour analysis of lithium-ion battery at elevated temperature using deconvolution method," *Applied Energy*, vol. 129, pp. 261–273, 2014.

[87] X. Feng, M. Fang, X. He, M. Ouyang, L. Lu, H. Wang, and M. Zhang, "Thermal runaway features of large format prismatic lithium ion battery using extended volume accelerating rate calorimetry," *Journal of Power Sources*, vol. 255, pp. 294–301, 2014.

[88] A. Kvasha, C. Gutirrez, U. Osa, I. de Meatza, J. A. Blazquez, H. Macicior, and I. Urdampilleta, "A comparative study of thermal runaway of commercial lithium ion cells," *Energy*, vol. 159, pp. 547 – 557, 2018.

[89] S. Wilke, B. Schweitzer, S. Khateeb, and S. Al-hallaj, "Preventing thermal runaway propagation in lithium ion battery packs using a phase change composite material: An experimental study," *Journal of Power Sources*, vol. 340, pp. 51–59, 2017.

[90] J. Lamb, C. J. Orendorff, L. A. M. Steele, and S. W. Spangler, "Failure propagation in multi-cell lithium ion batteries," *Journal of Power Sources*, vol. 283, pp. 517–523, 2015.

[91] Q. Wang, B. Mao, S. I. Stoliarov, and J. Sun, "A review of lithium ion battery failure mechanisms and fire prevention strategies," *Progress in Energy and Combustion Science*, vol. 73, pp. 95–131, 2019.

[92] T. Ohsaki, T. Kishi, T. Kuboki, N. Takami, N. Shimura, Y. Sato, M. Sekino, and A. Satoh, "Overcharge reaction of lithium-ion batteries," *Journal of Power Sources*, vol. 146, no. 1-2, pp. 97–100, 2005.

[93] P. G. Balakrishnan, R. Ramesh, and T. P. Kumar, "Safety mechanisms in lithium-ion batteries," *Journal of Power*, vol. 155, pp. 401–414, 2006.

[94] Z. An, L. Jia, Y. Ding, C. Dang, and X. Li, "A review on lithium-ion power battery thermal management technologies and thermal safety," *Journal of Thermal Science*, vol. 26, no. 5, pp. 391–412, Oct 2017.

[95] D. Belov and M.-H. Yang, "Failure mechanism of Li-ion battery at overcharge conditions," *Journal of Solid State Electrochemistry*, vol. 12, no. 7-8, pp. 885–894, 2008.

[96] G. Venugopal, J. Moore, J. Howard, and S. Pendalwar, "Characterization of microporous separators for lithium-ion batteries," *Journal of Power Sources*, vol. 77, no. 1, pp. 34–41, 1999.

[97] S. S. Zhang, "A review on the separators of liquid electrolyte Li-ion batteries," *Journal of Power Sources*, vol. 164, no. 1, pp. 351–364, 2007.

[98] X. Feng, J. Sun, M. Ouyang, F. Wang, X. He, L. Lu, and H. Peng, "Characterization of penetration induced thermal runaway propagation process within a large format lithium ion battery module," *Journal of Power Sources*, vol. 275, pp. 261–273, 2015.

[99] G. H. Kim, A. Pesaran, and R. Spotnitz, "A three-dimensional thermal abuse model for lithium-ion cells," *Journal of Power Sources*, vol. 170, no. 2, pp. 476–489, 2007.

[100] Underwriters Laboratory, "Safety Issues for Lithium-Ion Batteries," Tech. Rep., 2012. [Online]. Available: http://europe-ul.com/portfolio-items/safety-issues-for-lithium-ion-batteries/ [accessed 21 August 2017].

[101] Battery Standards, "General overview on test standards for Li-ion batteries, part 1 (H)EV," [online] Available at: https://www.batterystandards.info/sites/batterystandards.info/files/general_overview_part1.pdf [Accessed 27 September 2019].

[102] ——, "General overview on test standards for Li-ion batteries, part 2," [online] Available at: https://www.batterystandards.info/sites/batterystandards.info/files/general_overview_part2.pdf [Accessed 27 September 2019].

[103] SAE, "SAE J2464- Electric and Hybrid Electric Vehicle Rechargeable Energy Storage System (RESS) Safety and Abuse Testing ," SAE, Tech. Rep., Nov. 2009. [Online]. Available: https://www.sae.org/standards/content/j2464_200911/

[104] ——, "SAE J2929 - Safety Standard for Electric and Hybrid Vehicle Propulsion Battery Systems Utilizing Lithium-based Rechargeable Cells," SAE, Tech. Rep., Nov. 2013. [Online]. Available: https://www.sae.org/standards/content/j2929_201302/

[105] ISO, "ISO 6469-1:2019 - Electrically propelled road vehicles Safety specifications Part 1: Rechargeable energy storage system (RESS)," ISO, Tech. Rep., 2019. [Online]. Available: https://www.iso.org/standard/68665.html

[106] IEC, "IEC 62660-2:2018 - Secondary lithium-ion cells for the propulsion of electric road vehicles - Part 2: Reliability and abuse testing," IEC, Tech. Rep., 2018. [Online]. Available: https://webstore.iec.ch/publication/25737

[107] ——, "IEC 62660-3:2016 Secondary lithium-ion cells for the propulsion of electric road vehicles - Part 3: Safety requirements," IEC, Tech. Rep., 2018. [Online]. Available: https://webstore.iec.ch/publication/27387

[108] EU/ECE, "Regulation No 100 of the Economic Commission for Europe of the United Nations (UNECE) Uniform provisions concerning the approval of vehicles with regard to specific requirements for the electric power train," EU/ECE,

Tech. Rep., 2015. [Online]. Available: https://op.europa.eu/en/publication-detail/-/publication/fd8e6b47-d767-11e4-9de8-01aa75ed71a1/language-en

[109] UL, "UL2580 - Batteries for Use In Electric Vehicles," Underwriters Laboratories, Tech. Rep., 2020. [Online]. Available: https://standardscatalog.ul.com/ProductDetail.aspx?productId=UL2580

[110] T. Unkelhaeuser and D. Smallwood, "USABC - Electrochemical Storage System Abuse Test Procedure Manual," United States Advanced Battery Consortium, Tech. Rep., 1999. [Online]. Available: https://www.uscar.org/guest/article_view.php?articles_id=86

[111] J. L. Christopher J. Orendorff and L. A. M. Steele, "SAND2017-6925 - Recommended Practices for Abuse Testing Rechargeable Energy Storage Systems (RESSs)," Sandia National Laboratories, Tech. Rep., 2017. [Online]. Available: https://www.sandia.gov/ess-ssl/wp-content/uploads/2019/05/SNL-Abuse-Testing-Manual_July2017_FINAL.pdf

[112] The Automotive Industry Standard of India, "Battery Operated Vehicles - Safety Requirements of Traction Batteries," The Automotive Industry Standard of India, Tech. Rep., 2009. [Online]. Available: https://emobility.araiindia.com/wp-content/uploads/2018/06/AIS-048.pdf

[113] The National Development and Reform Committee, "QC/T731 - Li-ion Batteries for Electric Vehicles," Industry Standard of The People's Reublic of China, Tech. Rep., 2006. [Online]. Available: https://www.chinesestandard.net/PDF.aspx/QCT743-2006

[114] A. W. Golubkov, D. Fuchs, J. Wagner, H. Wiltsche, C. Stangl, G. Fauler, G. Voitic, A. Thaler, and V. Hacker, "Thermal-runaway experiments on consumer Li-ion batteries with metal-oxide and olivin-type cathodes," *RSC Advances*, no. 4, pp. 3633–3642, 2014.

[115] J. Jiang and J. R. Dahn, "ARC studies of the thermal stability of three different cathode materials: $LiCoO_2$; $Li[Ni_{0.1}Co_{0.8}Mn_{0.1}]O_2$; and $LiFePO_4$, in $LiPF_6$ and LiBoB EC/DEC electrolytes," *Electrochemistry Communications*, vol. 6, no. 1, pp. 39–43, 2004.

[116] X. Liu, Z. Wu, S. I. Stoliarov, M. Denlinger, A. Masias, and K. Snyder, "Heat release during thermally-induced failure of a lithium ion battery: Impact of cathode composition," *Fire Safety Journal*, vol. 85, pp. 10–22, 2016.

[117] T.-Y. Lu, C.-C. Chiang, S.-H. Wu, K.-C. Chen, S.-J. Lin, C.-Y. Wen, and C.-M. Shu, "Thermal hazard evaluations of 18650 lithium-ion batteries by an adiabatic calorimeter," *Journal of Thermal Analysis and Calorimetry*, vol. 114, no. 3, pp. 1083–1088, 2013.

[118] W. C. Chen, J. D. Li, C. M. Shu, and Y. W. Wang, "Effects of thermal hazard on 18650 lithium-ion battery under different states of charge," *Journal of Thermal Analysis and Calorimetry*, vol. 121, no. 1, pp. 525–531, 2015.

[119] D. D. MacNeil, Z. Lu, Z. Chen, and J. R. Dahn, "A comparison of the electrode/electrolyte reaction at elevated temperatures for various Li-ion battery cathodes," *Journal of Power Sources*, vol. 108, no. 1-2, pp. 8–14, 2002.

[120] P. Röder, N. Baba, K. A. Friedrich, and H. Wiemhöfer, "Impact of delithiated Li_0FePO_4 on the decomposition of $LiPF_6$-based electrolyte studied by accelerating rate calorimetry," *Journal of Power Sources*, vol. 236, pp. 151–157, 2013.

[121] J. W. Fergus, "Recent developments in cathode materials for lithium ion batteries," *Journal of Power Sources*, vol. 195, no. 4, pp. 939–954, 2010.

[122] C.-Y. Wen, C.-Y. Jhu, Y.-W. Wang, C.-C. Chiang, and C.-M. Shu, "Thermal runaway features of 18650 lithium-ion batteries for $LiFePO_4$ cathode material by DSC and VSP2," *Journal of Thermal Analysis and Calorimetry*, vol. 109, no. 3, pp. 1297–1302, 2012.

[123] L. H. Saw, Y. Ye, and A. A. O. Tay, "Electrochemical thermal analysis of 18650 Lithium Iron Phosphate cell," *Energy Conversion and Management*, vol. 75, pp. 162–174, 2013.

[124] K. Zaghib, M. Dontigny, A. Guerfi, P. Charest, I. Rodrigues, A. Mauger, and C. M. Julien, "Safe and fast-charging Li-ion battery with long shelf life for power applications," *Journal of Power Sources*, vol. 196, no. 8, pp. 3949–3954, 2011.

[125] D. A. H. McCleary, J. P. Meyers, and B. Kim, "Three-Dimensional Modeling of Electrochemical Performance and Heat Generation of Spirally and Prismatically Wound Lithium-Ion Batteries," *Journal of The Electrochemical Society*, vol. 160, no. 11, pp. A1931–A1943, 2013.

[126] M. Takahashi, S.-i. Tobishima, K. Takei, and Y. Sakurai, "Reaction behavior of $LiFePO_4$ as a cathode material for rechargeable lithium batteries," *Solid State Ionics*, vol. 148, no. 3-4, pp. 283–289, 2002.

[127] F. Larsson, P. Andersson, P. Blomqvist, and B.-e. Mellander, "Characteristics of lithium-ion batteries during fire tests," *Journal of Power Sources*, vol. 271, pp. 414–420, 2014.

[128] S. Wang, L. Lu, and X. Liu, "A simulation on safety of $LiFePO_4$/C cell using electrochemical-thermal coupling model," *Journal of Power Sources*, vol. 244, pp. 101–108, 2013.

[129] U.S. Department of Energy, "Global Energy Storage Database," 2017. [Online]. Available: http://www.energystorageexchange.org/ [accessed 20 August 2017].

[130] D. Anseán, M. González, V. M. García, J. C. Viera, J. C. Alvarez, and C. Blanco, "Evaluation of $LiFePO_4$ Batteries for Electric Vehicle Applications," *EEE Transactions on Industry Applications*, vol. 51, no. 2, pp. 1855–1863, 2015.

[131] M. Klippenstein, "Tesla Is Playing Catch-Up With Chinas BYD in Nearly Every Business Category," 2016. [Online]. Available: https://www.greentechmedia.com/articles/read/tesla-is-playing-catch-up-with-chinas-byd#gs.OSOWYSo [accessed 14 November 2018].

[132] G. Guo, B. Long, B. Cheng, S. Zhou, P. Xu, and B. Cao, "Three-dimensional thermal finite element modelling of lithium-ion battery in thermal abuse application," *Journal of Power Sources*, vol. 195, no. 8, pp. 2393–2398, 2010.

[133] D. Ren, X. Feng, L. Lu, M. Ouyang, S. Zheng, J. Li, and X. He, "An electrochemical-thermal coupled overcharge-to-thermal-runaway model for lithium ion battery," *Journal of Power Sources*, vol. 364, pp. 328–340, 2017.

[134] D. Ren, X. Liu, X. Feng, L. Lu, M. Ouyang, J. Li, and X. He, "Model-based thermal runaway prediction of lithium-ion batteries from kinetics analysis of cell components," *Applied Energy*, vol. 228, pp. 633–644, 2018.

[135] P. T. Coman, E. C. Darcy, C. T. Veje, and R. E. White, "Modelling Li-Ion Cell Thermal Runaway Triggered by an Internal Short Circuit Device Using an Efficiency Factor and Arrhenius Formulations," *Journal of The Electrochemical Society*, vol. 164, no. 4, pp. A587–A593, 2017.

[136] Z. An, K. Shah, L. Jia, and Y. Ma, "Modeling and analysis of thermal runaway in li-ion cell," *Applied Thermal Engineering*, vol. 160, p. 113960, 2019.

[137] K. Shah and A. Jain, "Prediction of thermal runaway and thermal management requirements in cylindrical li-ion cells in realistic scenarios," *International Journal of Energy Research*, vol. 43, no. 5, pp. 1827–1838, 2019.

[138] M. Chen, Q. Sun, Y. Li, K. Wu, B. Liu, P. Peng, and Q. Wang, "A thermal runaway simulation on a lithium titanate battery and the battery module," *Energies*, vol. 8, no. 1, pp. 490–500, 2015.

[139] X. Feng, L. Lu, M. Ouyang, J. Li, and X. He, "A 3D thermal runaway propagation model for a large format lithium ion battery module," *Energy*, vol. 115, pp. 194–208, 2016.

[140] W. Wu, W. Wu, and S. Wang, "Thermal optimization of composite PCM based large-format lithium-ion battery modules under extreme operating conditions," *Energy Conversion and Management*, vol. 153, pp. 22–33, 2017.

[141] J. Xu, C. Lan, Y. Qiao, and Y. Ma, "Prevent thermal runaway of lithium-ion batteries with minichannel cooling," *Applied Thermal Engineering*, vol. 110, pp. 883–890, 2017.

[142] B. Coleman, J. Ostanek, and J. Heinzel, "Reducing cell-to-cell spacing for large-format lithium ion battery modules with aluminum or PCM heat sinks under failure conditions," *Applied Energy*, vol. 180, pp. 14–26, 2016.

[143] P. T. Coman, S. Rayman, and R. E. White, "A lumped model of venting during thermal runaway in a cylindrical Lithium Cobalt Oxide lithium-ion cell," *Journal of Power Sources*, vol. 307, pp. 56–62, 2016.

[144] T. Yamanaka, Y. Takagishi, Y. Tozuka, and T. Yamaue, "Modeling lithium ion battery nail penetration tests and quantitative evaluation of the degree of combustion risk," *Journal of Power Sources*, vol. 416, pp. 132–140, 2019.

[145] Y. Fu, S. Lu, L. Shi, X. Cheng, and H. Zhang, "Ignition and combustion characteristics of lithium ion batteries under low atmospheric pressure," *Energy*, vol. 161, pp. 38–45, 2018.

[146] T. D. Hatchard, D. D. MacNeil, A. Basu, and J. R. Dahn, "Thermal Model of Cylindrical and Prismatic Lithium-Ion Cells," *Journal of The Electrochemical Society*, vol. 148, no. 7, pp. A755–A761, 2001.

[147] K.-C. Chiu, C.-H. Lin, S.-F. Yeh, Y.-H. Lin, and K.-C. Chen, "An electrochemical modeling of lithium-ion battery nail penetration," *Journal of Power Sources*, vol. 251, pp. 254–263, 2014.

[148] C. F. Lopez, J. A. Jeevarajan, and P. P. Mukherjee, "Characterization of Lithium-Ion Battery Thermal Abuse Behavior Using Experimental and Computational Analysis," *Journal of The Electrochemical Society*, vol. 162, no. 10, pp. A2163–A2173, 2015.

[149] D. Lisbona and T. Snee, "A review of hazards associated with primary lithium and lithium-ion batteries," *Process Safety and Environmental Protection*, vol. 89, no. 6, pp. 434–442, 2011.

[150] J. C. Leung, "Simplified Vent Sizing Equations for Emergency Relief Requirements in Reactors and Storage Vessels," *AIChE Journal*, vol. 32, no. 10, pp. 1622–1634, 1986.

[151] V. S. Smitha, M. Surianarayanan, H. Seshadri, N. V. Lakshman, and A. B. Mandal, "Reactive thermal hazards of tributyl phosphate with nitric acid," *Industrial & Engineering Chemistry Research*, vol. 51, no. 21, pp. 7205–7210, 2012.

[152] C. Y. Jhu, Y. W. Wang, C. Y. Wen, C. C. Chiang, and C. M. Shu, "Self-reactive rating of thermal runaway hazards on 18650 lithium-ion batteries," *Journal of Thermal Analysis and Calorimetry*, vol. 106, no. 1, pp. 159–163, 2011.

[153] A. Ben Mayza, M. Ramanathan, R. Radhakrishnan, S. Ha, V. Ramani, J. Prakash, and K. Zaghib, "Thermal Characterization of $LiFePO_4$ Cathode in Lithium Ion Cells," *ECS Transactions*, vol. 35, no. 34, pp. 177–183, 2011.

[154] H. Ishikawa, O. Mendoza, Y. Sone, and M. Umeda, "Study of thermal deterioration of lithium-ion secondary cell using an accelerated rate calorimeter (ARC) and AC impedance method," *Journal of Power Sources*, vol. 198, pp. 236–242, 2012.

[155] O. S. Mendoza-Hernandez, H. Ishikawa, Y. Nishikawa, Y. Maruyama, and M. Umeda, "Cathode material comparison of thermal runaway behavior of Li-ion cells at different state of charges including over charge," *Journal of Power Sources*, vol. 280, pp. 499–504, 2015.

[156] C. Y. Jhu, Y. W. Wang, C. Y. Wen, and C. M. Shu, "Thermal runaway potential of $LiCoO_2$ and $Li(Ni_{1/3}Co_{1/3}Mn_{1/3})O_2$ batteries determined with adiabatic calorimetry methodology," *Applied Energy*, vol. 100, pp. 127–131, 2012.

[157] X. Liu, S. I. Stoliarov, M. Denlinger, A. Masias, and K. Snyder, "Comprehensive calorimetry of the thermally-induced failure of a lithium ion battery," *Journal of Power Sources*, vol. 280, pp. 516 – 525, 2015.

[158] D. Townsend and J. Tou, "Thermal hazard evaluation by an accelerating rate calorimeter," *Thermochimica Acta*, vol. 37, no. 1, pp. 1–30, 1980.

[159] C. F. Askonas, J. P. Burelbach, and J. C. Leung, "The versatile vsp2: A tool for adiabatic thermal analysis and vent sizing applications," 2000.

[160] C. Askonas and Fauske & Associates, LLC (FAI), "Vent Sizing (VSP2) User Forum Optimizing Temperature Measurement," 2014, [online] Available at: https://www.fauske.com/blog/vent-sizing-vsp2-user-forum-optimizing-temperature-measurement [Accessed 30 January 2019].

[161] W.-C. Chen, Y.-W. Wang, and C.-M. Shu, "Adiabatic calorimetry test of the reaction kinetics and self-heating model for 18650 li-ion cells in various states of charge," *Journal of Power Sources*, vol. 318, pp. 200–209, 2016.

[162] I. Uchida, H. Ishikawa, M. Mohamedi, and M. Umeda, "AC-impedance measurements during thermal runaway process in several lithium/polymer batteries," *Journal of Power Sources*, vol. 119-121, pp. 821–825, 2003.

[163] S. Zheng, L. Wang, X. Feng, and X. He, "Probing the heat sources during thermal runaway process by thermal analysis of di ff erent battery chemistries," *Journal of Power Sources*, vol. 378, pp. 527–536, 2018.

[164] A. Yamada, S. C. Chung, and K. Hinokuma, "Optimized $LiFePO_4$ for Lithium Battery Cathodes," *Journal of Electroanalytical Society*, vol. 148, no. 3, pp. 224–229, 2001.

[165] F. Larsson and B.-E. Mellander, "Abuse by External Heating , Overcharge and Short Circuiting of Commercial Lithium-Ion Battery Cells," *Journal of The Electrochemical Society*, vol. 161, no. 10, pp. A1611–A1617, 2014.

[166] E. P. Roth and D. H. Doughty, "Thermal abuse performance of high-power 18650 Li-ion cells," *Journal of Power Sources*, vol. 128, no. 2, pp. 308–318, 2004.

[167] I. Belharouak, Y.-K. Sun, W. Lu, and K. Amine, "On the Safety of the $Li_4Ti_5O_{12}\backslash LiMn_2O_4$ Lithium-Ion Battery System," *Journal of The Electrochemical Society*, vol. 154, no. 12, p. A1083, 2007.

[168] D. D. MacNeil, L. Christensen, J. Landucci, J. M. Paulsen, and J. R. Dahn, "An Autocatalytic Mechanism for the Reaction of Li_xCoO_2 in Electrolyte at Elevated Temperature," *Journal of The Electrochemical Society*, vol. 147, no. 3, pp. 970–979, 2000.

[169] J. Jiang and J. R. Dahn, "ARC studies of the reaction between $LiFePO_4$ and $LiPF_6$ or LiBOB EC/DEC electrolytes," *Electrochemistry Communications*, vol. 6, no. 7, pp. 724–728, 2004.

[170] S. E. Khakani, D. Rochefort, and D. D. MacNeil, "Arc study of lifepo4 with different morphologies prepared via three synthetic routes," *Journal of The Electrochemical Society*, vol. 163, no. 7, pp. A1311–A1316, 2016.

[171] B. Lei, W. Zhao, C. Ziebert, N. Uhlmann, M. Rohde, and H. Seifert, "Experimental Analysis of Thermal Runaway in 18650 Cylindrical Li-Ion Cells Using an Accelerating Rate Calorimeter," *Batteries*, vol. 3, no. 2, p. 14, 2017.

[172] A. Perea, A. Paolella, J. Dub, D. Champagne, A. Mauger, and K. Zaghib, "State of charge influence on thermal reactions and abuse tests in commercial lithium-ion cells," *Journal of Power Sources*, vol. 399, pp. 392–397, 2018.

[173] M. Chen, D. Zhou, X. Chen, W. Zhang, J. Liu, R. Yuen, and J. Wang, "Investigation on the thermal hazards of 18650 lithium ion batteries by fire calorimeter," *Journal of Thermal Analysis and Calorimetry*, vol. 122, no. 2, pp. 755–763, 2015.

[174] H. M. Barkholtz, Y. Preger, S. Ivanov, J. Langendorf, L. Torres-Castro, J. Lamb, B. Chalamala, and S. R. Ferreira, "Multi-scale thermal stability study of commercial lithium-ion batteries as a function of cathode chemistry and state-of-charge," *Journal of Power Sources*, vol. 435, p. 226777, 2019.

[175] C. H. Lee, S. J. Bae, and M. Jang, "A study on effect of lithium ion battery design variables upon features of thermal-runaway using mathematical model and simulation," *Journal of Power Sources*, vol. 293, pp. 498–510, 2015.

[176] S.-i. Tobishima and J.-i. Yamaki, "A consideration of lithium cell safety," *Journal of Power Sources*, vol. 81-82, pp. 882–886, 1999.

[177] J. Jiang, H. Fortier, J. N. Reimers, and J. R. Dahn, "Thermal Stability of 18650 Size Li-Ion Cells Containing LiBOB Electrolyte Salt," *Journal of The Electrochemical Society*, vol. 151, no. 4, pp. A609–A613, 2004.

[178] F. Larsson, P. Andersson, and B.-E. Mellander, "Lithium-Ion Battery Aspects on Fires in Electrified Vehicles on the Basis of Experimental Abuse Tests," *Batteries*, vol. 2, no. 2, pp. 9–13, 2016.

[179] Y. S. Duh, M. T. Tsai, and C. S. Kao, "Characterization on the thermal runaway of commercial 18650 lithium-ion batteries used in electric vehicle," *Journal of Thermal Analysis and Calorimetry*, vol. 127, no. 1, pp. 983–993, 2017.

[180] X. Liu, Z. Wu, S. I. Stoliarov, M. Denlinger, A. Masias, and K. Snyder, "A Thermo-Kinetic Model of Thermally-Induced Failure of a Lithium Ion Battery: Development, Validation and Application," *Journal of Electroanalytical Society*, vol. 165, no. 11, pp. A2909–A2918, 2018.

[181] U. von Sacken, E. Nodwell, A. Sundher, and J. Dahn, "Comparative thermal stability of carbon intercalation anodes and lithium metal anodes for rechargeable lithium batteries," *Journal of Power Sources*, vol. 54, no. 2, pp. 240–245, 1995.

[182] D. D. MacNeil, T. D. Hatchard, and J. R. Dahn, "A Comparison Between the High Temperature Electrode/Electrolyte Reactions of Li_xCoO_2 and $Li_xMn_2O_4$," *Journal of The Electrochemical Society*, vol. 148, no. 7, pp. A663–A667, 2001.

[183] D. D. MacNeil and J. R. Dahn, "Test of Reaction Kinetics Using Both Differential Scanning and Accelerating Rate Calorimetries As Applied to the Reaction of Li_xCoO_2 in Non-aqueous Electrolyte," *The Journal of Physical Chemistry A*, vol. 105, no. 18, pp. 4430–4439, 2001.

[184] Y. Nishiyama, T. Tanaka, and K. Nakajima, "Numerical simulations of thermal behavior in relation with safety improvement of li-ion battery," *ECS Meeting Abstracts*, vol. MA2006-02, no. 5, p. 329, 2006.

[185] J. Gustin, "Thermal stability screening and reaction calorimetry. application to runaway reaction hazard assessment and process safety management," *Journal of Loss Prevention in the Process Industries*, vol. 6, no. 5, pp. 275 – 291, 1993.

[186] B. Shi, H. Zhang, Y. Qi, and L. Yang, "Calculation Model of Effective Thermal Conductivity of a Spiral-wound Lithium Ion Battery," *Journal of Thermal Science*, vol. 27, no. 6, pp. 572–579, 2018.

[187] P. Peng, Y. Sun, and F. Jiang, "Thermal analyses of $LiCoO_2$ lithium-ion battery during oven tests," *Heat Mass Transfer*, vol. 50, no. 10, pp. 1405–1416, 2014.

[188] C. Kupper, S. Spitznagel, H. Dring, M. A. Danzer, C. Gutierrez, A. Kvasha, and W. G. Bessler, "Combined modeling and experimental study of the high-temperature behavior of a lithium-ion cell: Differential scanning calorimetry, accelerating rate calorimetry and external short circuit," *Electrochimica Acta*, vol. 306, pp. 209–219, 2019.

[189] P. Ping, Q. Wang, Y. Chung, and J. Wen, "Modelling electro-thermal response of lithium-ion batteries from normal to abuse conditions," *Applied Energy*, vol. 205, pp. 1327–1344, 2017.

[190] T. Dong, P. Peng, and F. Jiang, "Numerical modeling and analysis of the thermal behavior of NCM lithium-ion batteries subjected to very high C-rate discharge/charge operations," *International Journal of Heat and Mass Transfer*, vol. 117, pp. 261–272, 2018.

[191] T. G. Zavalis, M. Behm, and G. Lindbergh, "Investigation of Short-Circuit Scenarios in a Lithium-Ion Battery Cell," *Journal of The Electrochemical Society*, vol. 159, no. 6, pp. A848–A859, 2012.

[192] L. Zhang, P. Zhao, M. Xu, and X. Wang, "Computational identification of the safety regime of li-ion battery thermal runaway," *Applied Energy*, vol. 261, p. 114440, 2020.

[193] M. Parhizi, M. B. Ahmed, and A. Jain, "Determination of the core temperature of a Li-ion cell during thermal runaway," *Journal of Power Sources*, vol. 370, pp. 27–35, 2017.

[194] M. S. Rad, D. Danilov, M. Baghalha, M. Kazemeini, and P. Notten, "Adaptive thermal modeling of li-ion batteries," *Electrochimica Acta*, vol. 102, pp. 183 – 195, 2013.

[195] P. Huang, H. Chen, A. Verma, Q. Wang, P. Mukherjee, and J. Sun, "Non-dimensional analysis of the criticality of li-ion battery thermal runaway behavior," *Journal of Hazardous Materials*, vol. 369, pp. 268–278, 2019.

[196] I. Esho, K. Shah, and A. Jain, "Measurements and modeling to determine the critical temperature for preventing thermal runaway in Li-ion cells," *Applied Thermal Engineering*, vol. 145, pp. 287–294, 2018.

[197] K. Shah, D. Chalise, and A. Jain, "Experimental and theoretical analysis of a method to predict thermal runaway in Li-ion cells," *Journal of Power Sources*, vol. 330, pp. 167–174, 2016.

[198] E. Cabrera-Castillo, F. Niedermeier, and A. Jossen, "Calculation of the state of safety (sos) for lithium ion batteries," *Journal of Power Sources*, vol. 324, pp. 509 –520, 2016.

[199] P. T. Coman, M. Stefan, C. T. Veje, and R. E. White, "Modeling Vaporization, Gas Generation and Venting in Li-Ion Battery Cells with a Dimethyl Carbonate Electrolyte," *Journal of The Electrochemical Society*, vol. 164, no. 9, pp. 1858–1865, 2017.

[200] R. M. Felder and R. W. Rousseau, *Elementary Principles of Chemical Processes*, 3rd ed. John Wiley & Sons, Inc., 2005.

[201] B. Wang, C. Ji, S. Wang, and S. Pan, "A detailed finite element model of internal short circuit and venting during thermal runaway in a 32650 lithium-ion battery," *Fire Technology*, 2020.

[202] J. K. Ostanek, W. Li, P. P. Mukherjee, K. Crompton, and C. Hacker, "Simulating onset and evolution of thermal runaway in li-ion cells using a coupled thermal and venting model," *Applied Energy*, vol. 268, p. 114972, 2020.

[203] I. H. Bell, J. Wronski, S. Quoilin, and V. Lemort, "Pure and pseudo-pure fluid thermophysical property evaluation and the open-source thermophysical property library coolprop," *Industrial & Engineering Chemistry Research*, vol. 53, no. 6, pp. 2498–2508, 2014, pMID: 24623957.

[204] T. Cai, A. G. Stefanopoulou, and J. B. Siegel, "Modeling li-ion battery temperature and expansion force during the early stages of thermal runaway triggered by internal shorts," *Journal of The Electrochemical Society*, vol. 166, no. 12, pp. A2431–A2443, 2019.

[205] R. Srinivasan, M. E. Thomas, M. B. Airola, B. G. Carkhuff, L. J. Frizzell-Makowski, H. Alkandry, J. G. Reuster, H. N. Oguz, P. W. Green, J. L. Favors, L. J. Currano, and P. A. Demirev, "Preventing Cell-to-Cell Propagation of Thermal Runaway in Lithium-Ion Batteries," *Journal of The Electrochemical Society*, vol. 167, no. 2, p. 020559, feb 2020.

[206] A. R. Baird, E. J. Archibald, K. C. Marr, and O. A. Ezekoye, "Explosion hazards from lithium-ion battery vent gas," *Journal of Power Sources*, vol. 446, p. 227257, 2020.

[207] Y. Fu, S. Lu, L. Shi, X. Cheng, and H. Zhang, "Combustion Characteristics of Electrolyte Pool Fires for Lithium Ion Batteries," *Journal of The Electrochemical Society*, vol. 163, no. 9, pp. A2022–A2028, 2016.

[208] G. G. Eshetu, S. Gudeon, S. Laruelle, S. Boyanov, A. Lecocq, J.-P. Bertrand, and G. Marlair, "In-depth safety-focused analysis of solvents used in electrolytes for large scale lithium ion batteries," *Physical Chemistry Chemical Physics*, vol. 15, pp. 9145–9155, 2013.

[209] S. J. An, J. Li, C. Daniel, D. Mohanty, S. Nagpure, and D. L. Wood, "The state of understanding of the lithium-ion-battery graphite solid electrolyte interphase (SEI) and its relationship to formation cycling," *Carbon*, vol. 105, pp. 52–76, 2016.

[210] L. Zhao, I. Watanabe, T. Doi, S. Okada, and J.-i. Yamaki, "TG-MS analysis of solid electrolyte interphase (SEI) on graphite negative-electrode in lithium-ion batteries," *Journal of Power Sources*, vol. 161, no. 2, pp. 1275–1280, 2006.

[211] K. Tasaki, A. Goldberg, J.-J. Lian, M. Walker, A. Timmons, and S. J. Harris, "Solubility of Lithium Salts Formed on the Lithium-Ion Battery Negative Electrode Surface in Organic Solvents," *Journal of The Electrochemical Society*, vol. 156, no. 12, pp. A1019–A1027, 2009.

[212] Y. Nan, S. Li, B. Li, and S. Yang, "An artificial TiO 2/lithium n-butoxide hybrid SEI layer with facilitated lithium-ion transportation ability for stable lithium anodes," *Nanoscale*, vol. 11, no. 5, pp. 2194–2201, 2019.

[213] H. Yang, H. Bang, K. Amine, and J. Prakash, "Investigations of the Exothermic Reactions of Natural Graphite Anode for Li-Ion Batteries during Thermal Runaway," *Journal of The Electrochemical Society*, vol. 152, no. 1, pp. A73–A79, 2005.

[214] D. Aurbach, A. Zaban, Y. Ein-Eli, I. Weissman, O. Chusid, B. Markovsky, M. Levi, E. Levi, A. Schechter, and E. Granot, "Recent studies on the correlation between surface chemistry, morphology, three-dimensional structures and performance of Li and Li-C intercalation anodes in several important electrolyte systems," *Journal of Power Sources*, vol. 68, no. 1, pp. 91–98, 1997.

[215] P. Ping, Q. S. Wang, P. F. Huang, K. Li, J. H. Sun, D. P. Kong, and C. H. Chen, "Study of the fire behavior of high-energy lithium-ion batteries with full-scale burning test," *Journal of Power Sources*, vol. 285, pp. 80–89, 2015.

[216] A. Du Pasquier, T. Bowmer, A. S. Gozdz, G. Amatucci, and J.-M. Tarascon, "Differential Scanning Calorimetry Study of the Reactivity of Carbon Anodes in Plastic Li-Ion Batteries," *Journal of The Electrochemical Society*, vol. 145, no. 2, pp. 472–477, 1998.

[217] H. Yang, G. V. Zhuang, and P. N. Ross, "Thermal stability of $LiPF_6$ salt and Li-ion battery electrolytes containing $LiPF_6$," *Journal of Power Sources*, vol. 161, no. 1, pp. 573–579, 2006.

[218] T. Kawamura, S. Okada, and J. ichi Yamaki, "Decomposition reaction of $LiPF_6$-based electrolytes for lithium ion cells," *Journal of Power Sources*, vol. 156, no. 2, pp. 547–554, 2006.

[219] G. G. Eshetu, J.-P. Bertrand, A. Lecocq, S. Grugeon, S. Laruelle, M. Armand, and G. Marlair, "Fire behavior of carbonates-based electrolytes used in Li-ion rechargeable batteries with a focus on the role of the $LiPF_6$ and LiFSI salts," *Journal of Power Sources*, vol. 269, pp. 804–811, 2014.

[220] D. Ouyang, J. Liu, M. Chen, and J. Wang, "Investigation into the fire hazards of lithium-ion batteries under overcharging," *Applied Sciences*, vol. 7, no. 12, pp. 1–20, 2017.

[221] F. A. Mier, M. J. Hargather, and S. R. Ferreira, "Experimental Quantification of Vent Mechanism Flow Parameters in 18650 Format Lithium Ion Batteries," *Journal of Fluids Engineering*, vol. 141, no. 6, pp. 061 403-1–061 403-11, 2019.

[222] C. F. Lopez, J. A. Jeevarajan, and P. P. Mukherjee, "Experimental Analysis of Thermal Runaway and Propagation in Lithium-Ion Battery Modules," *Journal of The Electrochemical Society*, vol. 162, no. 9, pp. 1905–1915, 2015.

[223] N. S. Spinner, C. R. Field, M. H. Hammond, B. A. Williams, K. M. Myers, A. L. Lubrano, S. L. Rose-pehrsson, and S. G. Tuttle, "Physical and chemical analysis of lithium-ion battery cell-to-cell failure events inside custom fi re chamber," *Journal of Power Sources*, vol. 279, pp. 713–721, 2015.

[224] P. Huang, P. Ping, K. Li, H. Chen, Q. Wang, J. Wen, and J. Sun, "Experimental and modeling analysis of thermal runaway propagation over the large format energy storage battery module with $Li_4Ti_5O_{12}$ anode," *Applied Energy*, vol. 183, pp. 659–673, 2016.

[225] R. Kizilel, R. Sabbah, J. R. Selman, and S. Al-Hallaj, "An alternative cooling system to enhance the safety of Li-ion battery packs," *Journal of Power Sources*, vol. 194, no. 2, pp. 1105–1112, 2009.

[226] G.-H. K. Kim, A. Pesaran, and K. Smith, "Thermal Abuse Modeling of Li-Ion Cells and Propagation in Modules," *The 4th International Symposium on Large Lithium Ion Battery Technology and Application*, pp. 1–37, 2008.

[227] P. T. Coman, E. C. Darcy, C. T. Veje, and R. E. White, "Numerical analysis of heat propagation in a battery pack using a novel technology for triggering thermal runaway," *Applied Energy*, vol. 203, pp. 189–200, 2017.

[228] F. Larsson, J. Anderson, P. Andersson, and B.-E. Mellander, "Thermal Modelling of Cell-to-Cell Fire Propagation and Cascading Thermal Runaway Failure Effects for Lithium-Ion Battery Cells and Modules Using Fire Walls," *Journal of The Electrochemical Society*, vol. 163, no. 14, pp. A2854–A2865, 2016.

[229] K. F. Yeow and H. Teng, "Characterizing Thermal Runaway of Lithium-ion Cells in a Battery System Using Finite Element Analysis Approach," *SAE International Journal of Alternative Powertrains*, vol. 2, no. 1, pp. 179–186, 2013.

[230] R. M. Spotnitz, J. Weaver, G. Yeduvaka, D. H. Doughty, and E. P. Roth, "Simulation of abuse tolerance of lithium-ion battery packs," *Journal of Power Sources*, vol. 163, no. 2, pp. 1080–1086, 2007.

[231] P. Shack, C. Iannello, S. Rickman, and R. Button, "NASA Perspective and Modeling of Thermal Runaway Propagation Mitigation in Aerospace Batteries," 2014.

[232] S. Arora, A. Kapoor, and W. Shen, "A novel thermal management system for improving discharge/charge performance of Li-ion battery packs under abuse," *Journal of Power Sources*, vol. 378, pp. 759–775, 2018.

[233] R. Zhao, S. Zhang, J. Gu, J. Liu, S. Carkner, and E. Lanoue, "An experimental study of lithium ion battery thermal management using flexible hydrogel films," *Journal of Power Sources*, vol. 255, pp. 29–36, 2014.

[234] K. S. Kshetrimayum, Y.-G. Yoon, H.-R. Gye, and C.-J. Lee, "Preventing heat propagation and thermal runaway in electric vehicle battery modules using integrated pcm and micro-channel plate cooling system," *Applied Thermal Engineering*, vol. 159, p. 113797, 2019.

[235] Q. Li, C. Yang, S. Santhanagopalan, K. Smith, J. Lamb, L. A. Steele, and L. Torres-Castro, "Numerical investigation of thermal runaway mitigation through a passive thermal management system," *Journal of Power Sources*, vol. 429, pp. 80 – 88, 2019.

[236] G. Zhong, H. Li, C. Wang, K. Xu, and Q. Wang, "Experimental Analysis of Thermal Runaway Propagation Risk within 18650 Lithium-Ion Battery Modules," *Journal of The Electrochemical Society*, vol. 165, no. 9, pp. A1925–A1934, 2018.

[237] H. Li, Q. Duan, C. Zhao, Z. Huang, and Q. Wang, "Experimental investigation on the thermal runaway and its propagation in the large format battery module with $Li(Ni_{1/3}Co_{1/3}Mn_{1/3})O_2$ as cathode," *Journal of Hazardous Materials*, vol. 375, pp. 241–254, 2019.

[238] S. Gao, X. Feng, L. Lu, N. Kamyab, J. Du, P. Coman, R. E. White, and M. Ouyang, "An experimental and analytical study of thermal runaway propagation in a large format lithium ion battery module with ncm pouch-cells in parallel," *International Journal of Heat and Mass Transfer*, vol. 135, pp. 93–103, 2019.

[239] M. Chen, O. Dongxu, J. Liu, and J. Wang, "Investigation on thermal and fire propagation behaviors of multiple lithium-ion batteries within the package," *Applied Thermal Engineering*, vol. 157, p. 113750, 2019.

[240] D. Ouyang, J. Weng, J. Hu, M. Chen, Q. Huang, and J. Wang, "Experimental investigation of thermal failure propagation in typical lithium-ion battery modules," *Thermochimica Acta*, vol. 676, pp. 205 – 213, 2019.

[241] D. Ouyang, M. Chen, R. Wei, Z. Wang, and J. Wang, "A study on the fire behaviors of 18650 battery and batteries pack under discharge," *Journal of Thermal Analysis and Calorimetry*, vol. 136, no. 5, pp. 1915–1926, 2019.

[242] D. Ouyang, J. Liu, M. Chen, J. Weng, and J. Wang, "An Experimental Study on the Thermal Failure Propagation in Lithium-Ion Battery Pack," *Journal of The Electrochemical Society*, vol. 165, no. 10, pp. A2184–A2193, 2018.

[243] Z. Tang, A. Song, S. Wang, J. Cheng, and C. Tao, "Numerical Analysis of Heat Transfer Mechanism of Thermal Runaway Propagation for Cylindrical Lithium-ion Cells in Battery Module," *Energies*, vol. 13, no. 4, 2020.

[244] J. A. Jeevarajan, "Hazards Associated with High Voltage High Capacity Lithium-ion Batteries," *ECS Transactions*, vol. 33, no. 22, pp. 1–6, 2011.

[245] C. Tao, G. Li, J. Zhao, G. Chen, Z. Wang, Y. Qian, X. Cheng, and X. Liu, "The investigation of thermal runaway propagation of lithium-ion batteries under different vertical distances," *Journal of Thermal Analysis and Calorimetry*, Jan 2020.

[246] S. Koch, A. Fill, K. Kelesiadou, and K. P. Birke, "Discharge by Short Circuit Currents of Parallel-Connected Lithium-Ion Cells in Thermal Propagation," *Batteries*, vol. 5, no. 1, 2019.

[247] A. O. Said, C. Lee, and S. I. Stoliarov, "Experimental investigation of cascading failure in 18650 lithium ion cell arrays: Impact of cathode chemistry," *Journal of Power Sources*, vol. 446, pp. 227–347, 2020.

[248] T. S. Bryden, B. Dimitrov, G. Hilton, C. P. D. León, P. Bugryniec, S. Brown, D. Cumming, and A. Cruden, "Methodology to determine the heat capacity of lithium-ion cells," *Journal of Power Sources*, vol. 395, pp. 369–378, 2018.

[249] The University of Warwick, *Engineering Data Book*, 6th ed., 2010, p. 30.

[250] P. J. Bugryniec, J. N. Davidson, and S. F. Brown, "Advanced abuse modelling of Li-ion cells A novel description of cell pressurisation and simmering reactions," *Journal of Power Sources*, vol. 474, p. 228396, 2020.

[251] G. Thorncroft, J. S. Patton, and R. Gordon, "Modeling Compressible Air Flow In A Charging Or Discharging Vessel And Assessment Of Polytropic Exponent," in *ASEE Annual Conference & Exposition*, 2007, pp. 12.1075.1 – 12.1075.18.

[252] X. Feng, S. Zheng, D. Ren, X. He, L. Wang, H. Cui, X. Liu, C. Jin, F. Zhang, C. Xu, H. Hsu, S. Gao, T. Chen, Y. Li, T. Wang, H. Wang, M. Li, and M. Ouyang, "Investigating the thermal runaway mechanisms of lithium-ion batteries based on thermal analysis database," *Applied Energy*, vol. 246, pp. 53 – 64, 2019.

[253] E. W. Lemmon, I. H. Bell, M. L. Huber, and M. O. McLinden, "NIST Standard Reference Database 23: Reference Fluid Thermodynamic and Transport Properties-REFPROP, Version 10.0, National Institute of Standards and Technology," 2018.

[254] R. Akasaka, T. Yamaguchi, and T. Ito, "Practical and direct expressions of the heat of vaporization for mixtures," *Chemical Energy Science*, vol. 60, pp. 4369–4376, 2005.

[255] COMSOL Multiphysics®V5.2a, www.comsol.com. COMSOL AB, Stockholm, Sweden.

[256] D. K. Smith, *Chemistry Data Book*. The University of York, 2011.

[257] M. Ashby, *Material property data for engineering materials*, 4th ed. Cambridge University, Engineering Department and Granta Design, 2016.

[258] T. D. Hatchard, D. D. Macneil, D. A. Stevens, L. Christensen, and J. R. Dahn, "Importance of Heat Transfer by Radiation in Li-Ion Batteries during Thermal Abuse," *Electrochemical and Solid-Stae Letters*, vol. 3, no. 7, pp. 305–308, 2000.

[259] ENIX Energies, "18650 $LiFePO_4$ Battery 1500mAh 3.2V Data Sheet," 2014, [online] Available at: http://www.enix-energies.co.uk/media/pdf/ACL9011_UK.pdf [Accessed 13 June 2017].

[260] W. Q. Walker, J. J. Darst, D. P. Finegan, G. A. Bayles, K. L. Johnson, E. C. Darcy, and S. L. Rickman, "Decoupling of heat generated from ejected and non-ejected contents of 18650-format lithium-ion cells using statistical methods," *Journal of Power Sources*, vol. 415, pp. 207–218, 2019.

[261] P. Verma, P. Maire, and P. Novák, "A review of the features and analyses of the solid electrolyte interphase in Li-ion batteries," *Electrochimica Acta*, vol. 55, no. 22, pp. 6332–6341, 2010.

[262] S. S. Zhang, "Insight into the Gassing Problem of Li-ion Battery," *Frontiers in Energy Research*, vol. 2, pp. 1–4, 2014.

[263] MathWorks Inc., "Symbolic Math Toolbox - MATLAB R2018b," 2018.

[264] P. J. Bugryniec, J. N. Davidson, D. J. Cumming, and S. F. Brown, "Pursuing safer batteries: Thermal abuse of $LiFePO_4$ cells," *Journal of Power Sources*, vol. 414, pp. 557–568, 2019.

[265] P. Mathews, *Sample Size Calculations: Practical Methods for Engineers and Scientists*. Mathews Malnar and Bailey, Inc, 2010, ch. Chapter 1, pp. 13–16.

[266] W. G. Cochran, *Sampling Techniques*, 2nd ed. New York: John Wiley and Sons, Inc, 1963.

[267] M. Kuipers, F. Hust, S. Meier, and D. U. Sauer, "An in-depth View into the Tesla Model S ModulePart Two: Module Characterization and Comparison to Other State of the Art EV Battery Systems," in *Battery Power Conference*, 2017. [Online]. Available: https://juser.fz-juelich.de/record/844988/files/MKU_Kraftwerk_Batterie_2017_Tesla_Modul_Part2_Poster_final_v2.pdf

[268] W. Navidi, *Statistics for Engineers and Scientists*, 3rd ed. New York: McGraw-Hill, 2010, ch. 6 Hypothesis Testing, pp. 369–504.

[269] ——, *Statistics for Engineers and Scientists*, 3rd ed. New York: McGraw-Hill, 2010, ch. 5 Confidence Intervals, pp. 334–395.

[270] ——, *Statistics for Engineers and Scientists*, 3rd ed. New York: McGraw-Hill, 2010, ch. Table A.3 Upper percentage points for the Student's t distribution, p. 912.

[271] Cornell Statistical Consulting Unit, "Overlapping Confidence Intervals and Statistical Significance," online, 2020. [Online]. Available: https://www.cscu.cornell.edu/news/statnews/73_ci.pdf [accessed 02 March 2021].

[272] S. Abada, M. Petit, A. Lecocq, G. Marlair, V. Sauvant-Moynot, and F. Huet, "Combined experimental and modeling approaches of the thermal runaway of fresh and aged lithium-ion batteries," *Journal of Power Sources*, vol. 399, pp. 264–273, 2018.

[273] B. Streipert, K. Krämer, L. Terborg, V. Kraft, J. Menzel, D. Gallus, I. Cekic-Laskovic, S. Nowak, T. Placke, and M. Winter, "Vernachlässigt, vergessen oder unwichtig? - Inaktivmaterialien für Lithium-Ionen Batterien," 2016, [online] Available at: https://www.gdch.de/fileadmin/downloads/Netzwerk_und_Strukturen/Fachgruppen/Seniorexperten/PDF/Tagungen/6_SEC_Jahrestreffen/Winter02.pdf [accessed 22 March 2019].

[274] F. L. H. Rajiwate, "Investigation of Compressible Fluid Behaviour in a Vent Pipe during Blowdown," Ph.D. dissertation, Curtin University, 2011.

[275] S. Brown, S. Martynov, H. Mahgerefteh, S. Chen, and Y. Zhang, "Modelling the non-equilibrium two-phase flow during depressurisation of co2 pipelines," *International Journal of Greenhouse Gas Control*, vol. 30, pp. 9 – 18, 2014.

[276] A. M. Haregewoin, A. S. Wotango, and B.-J. Hwang, "Electrolyte additives for lithium ion battery electrodes: progress and perspectives," *Energy & Environmental Science*, vol. 9, pp. 1955–1988, 2016.

[277] P. Sehrawat, C. Julien, and S. Islam, "Carbon nanotubes in Li-ion batteries: A review," *Materials Science and Engineering: B*, vol. 213, pp. 12 – 40, 2016, li-ion batteries.

[278] Y. Fernandes, A. Bry, and S. de Persis, "Identification and quantification of gases emitted during abuse tests by overcharge of a commercial li-ion battery," *Journal of Power Sources*, vol. 389, pp. 106–119, 2018.

[279] T. M. Bandhauer, S. Garimella, and T. F. Fuller, "Temperature-dependent electrochemical heat generation in a commercial lithium-ion battery," *Journal of Power Sources*, vol. 247, pp. 618–628, 2014.

[280] Z. Huang, H. Li, W. Mei, C. Zhao, J. Sun, and Q. Wang, "Thermal runaway behavior of lithium iron phosphate battery during penetration," *Fire Technology*, Feb. 2020.

Appendix A

Supplementary Figures of Oven Test Data

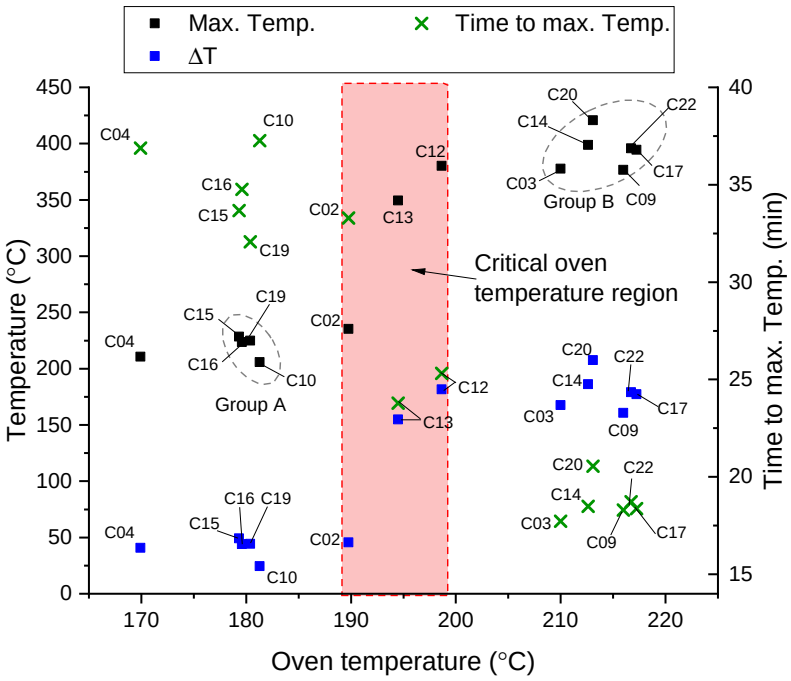

Figure A.1: Maximum cell surface temperature, temperature difference and time to maximum temperature vs. oven temperature with cell annotation.

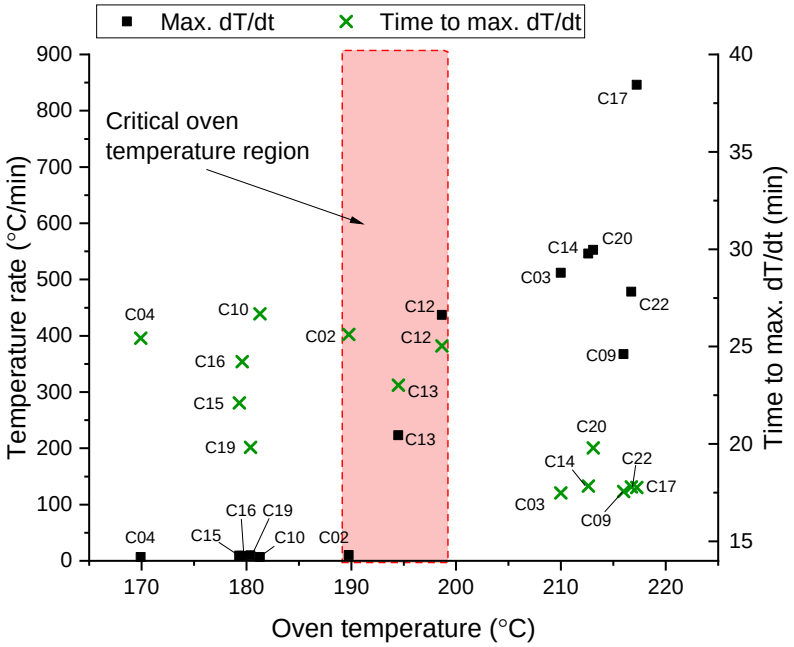

Figure A.2: Maximum cell surface temperature rate and time to maximum temperature rate vs. oven temperature with cell annotation.

Appendix B

Supplementary Pack Study Data

B.1 Supplementary Figures and Tables of Heat Transfer Pathway Study

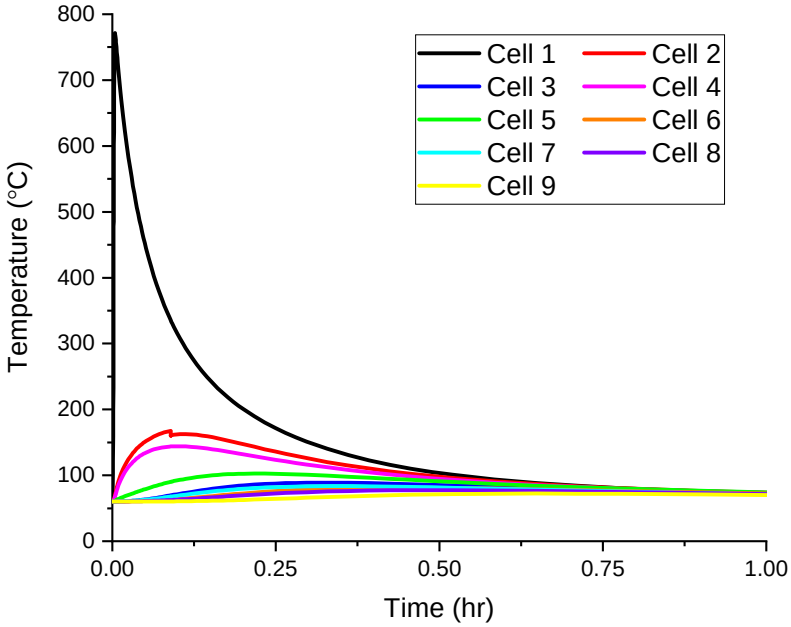

(a)

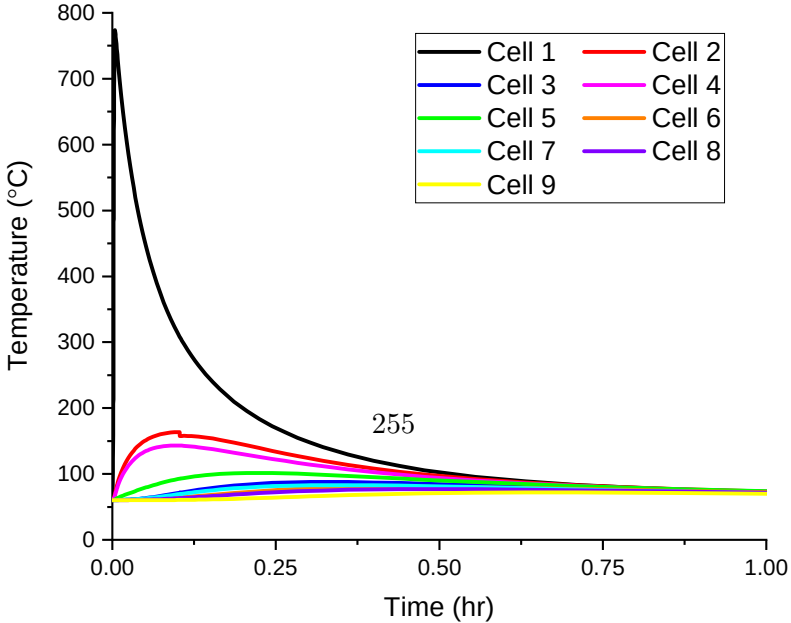

Table B.1: Heat transfer to/from (positive/negative value) individual cells up to the respective times of maximum cell temperatures with inter-cell spacing $d_{cc} = 0\,\text{mm}$.

Heat transfer	**Cell**								
(J)	**1**	**2**	**3**	**4**	**5**	**6**	**7**	**8**	**9**
				$\varepsilon_{cell} = 0$					
Radiation	0	0	0	0	0	0	0	0	0
Surface conduction	-805	2413	587	3601	1377	337	309	623	344
Tab conduction	-203	1803	634	-376	239	499	573	21	113
Total	-1008	4216	1221	3226	1616	836	882	645	457
				$\varepsilon_{cell} = 0.27$					
Radiation	-107	460	127	524	460	107	111	98	49
Surface conduction	-680	2117	491	3101	1032	285	248	560	317
Tab conduction	-181	1635	607	-322	198	468	557	16	112
Total	-968	4213	1224	3303	1689	860	916	675	477
				$\varepsilon_{cell} = 0.54$					
Radiation	-206	916	224	1084	835	177	228	180	95
Surface conduction	-676	1849	452	2642	785	273	200	531	299
Tab conduction	-183	1490	572	-291	161	444	540	5	112
Total	-1065	4256	1247	3435	1781	894	967	717	505
				$\varepsilon_{cell} = 0.8$					
Radiation	-296	1296	315	1576	1160	251	348	268	148
Surface conduction	-658	1626	395	2254	571	235	162	490	275
Tab conduction	-182	1374	556	-277	136	438	511	0	112
Total	-1136	4295	1266	3553	1867	925	1021	758	534
				$\varepsilon_{cell} = 1$					
Radiation	-336	1554	392	1915	1400	317	450	348	200
Surface conduction	-605	1476	358	1978	414	208	124	451	246
Tab conduction	-171	1293	535	-248	123	425	491	-7	112
Total	-1113	4323	1284	3646	1937	951	1066	792	558

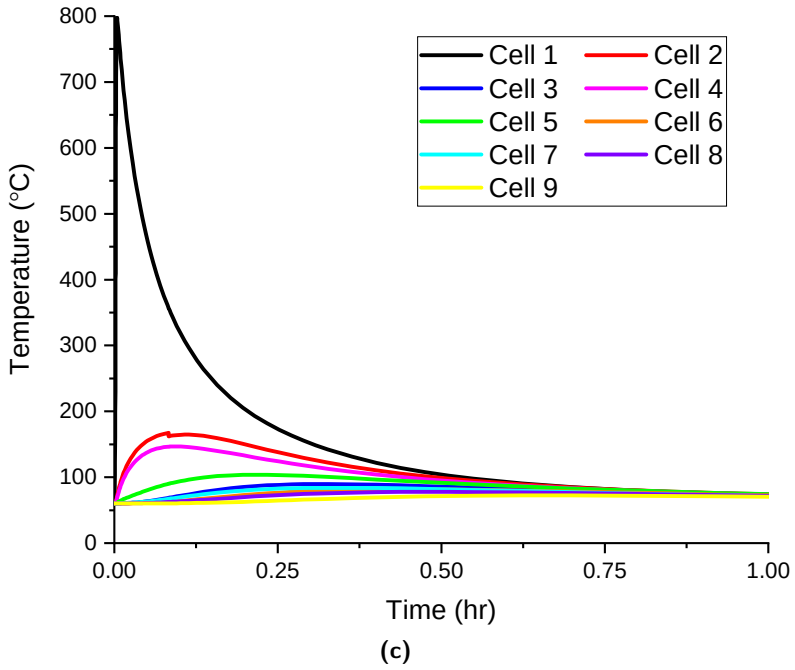

(c)

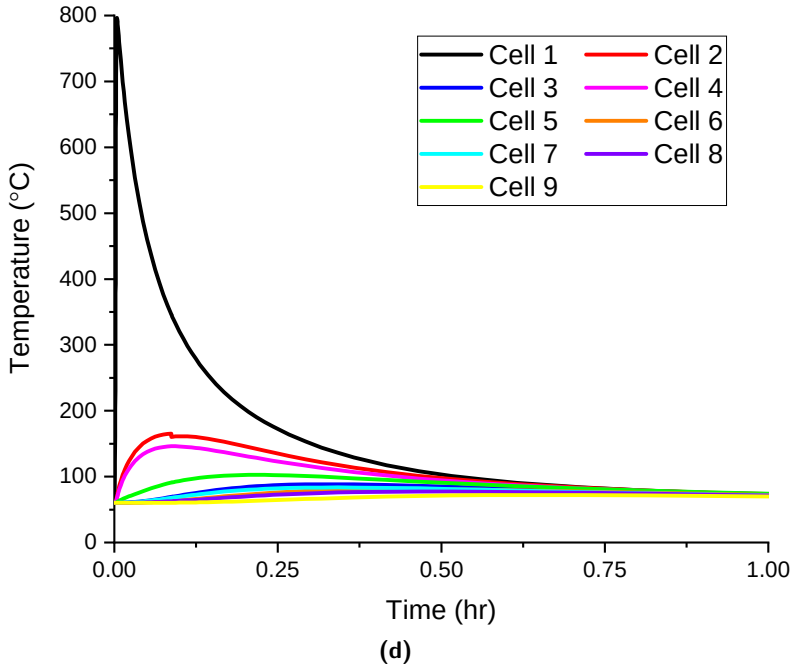

(d)

Figure B.1 (cont.): Average cell temperatures within pack where Cell 1 is abused by short circuit. Sub-figures are for models utilising different abuse parameters and burst pressures - (a) MAH, (b) MAL, (c) MBH, (d) MBL.

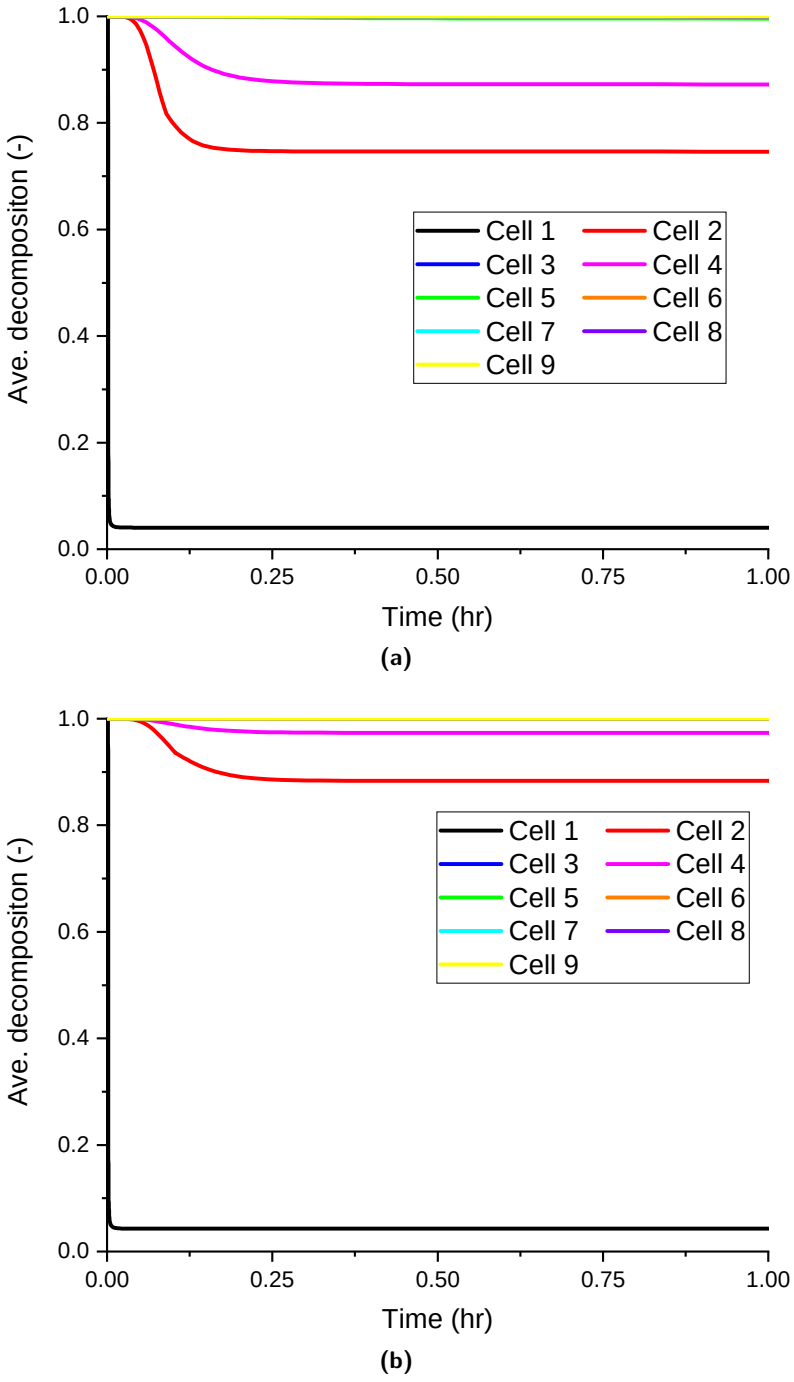

Figure B.2: Average cell decomposition within pack where Cell 1 is abused by short circuit. Sub-figures are for models utilising different abuse parameters and burst pressures - (a) MAH, (b) MAL, (c) MBH, (d) MBL.

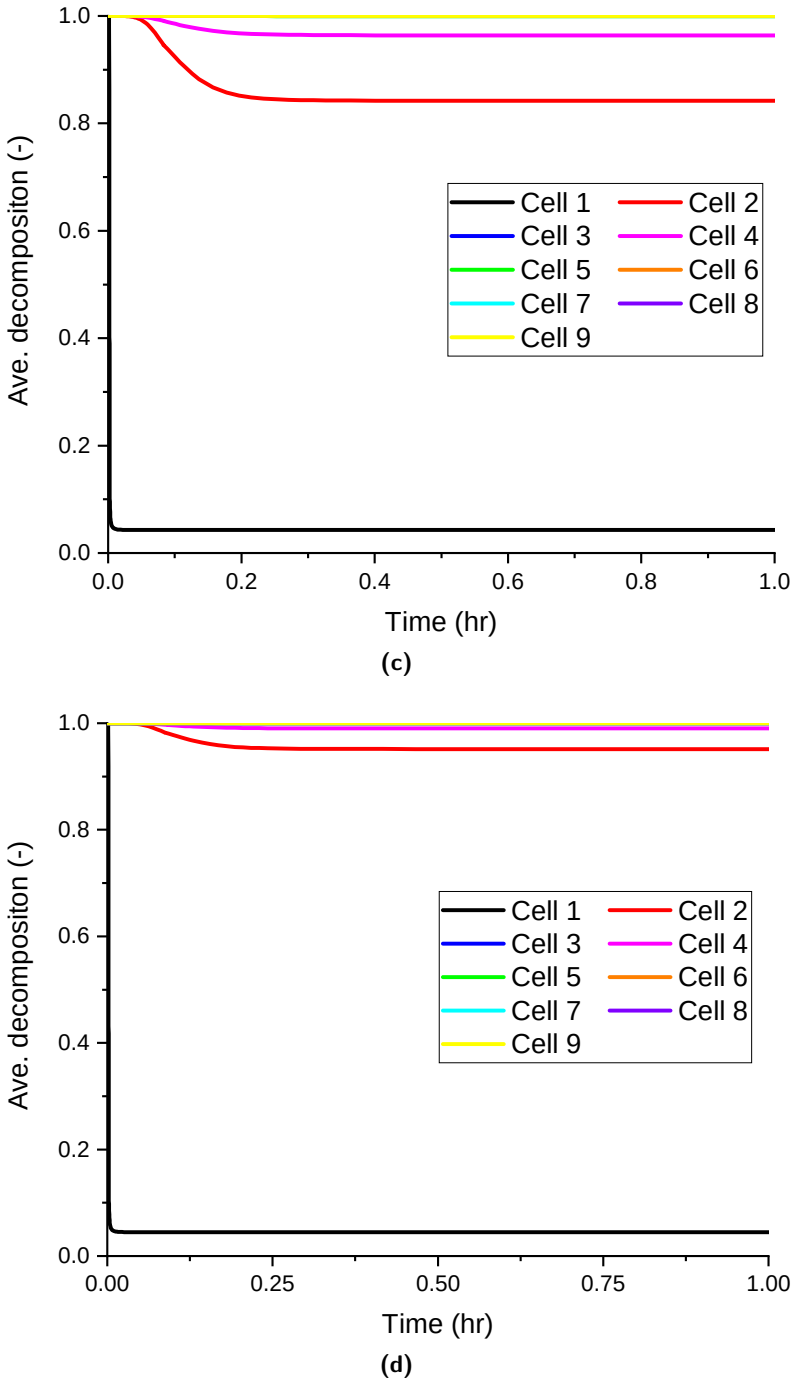

Figure B.2 (cont.): Average cell decomposition within pack where Cell 1 is abused by short circuit. Sub-figures are for models utilising different abuse parameters and burst pressures - (a) MAH, (b) MAL, (c) MBH, (d) MBL.

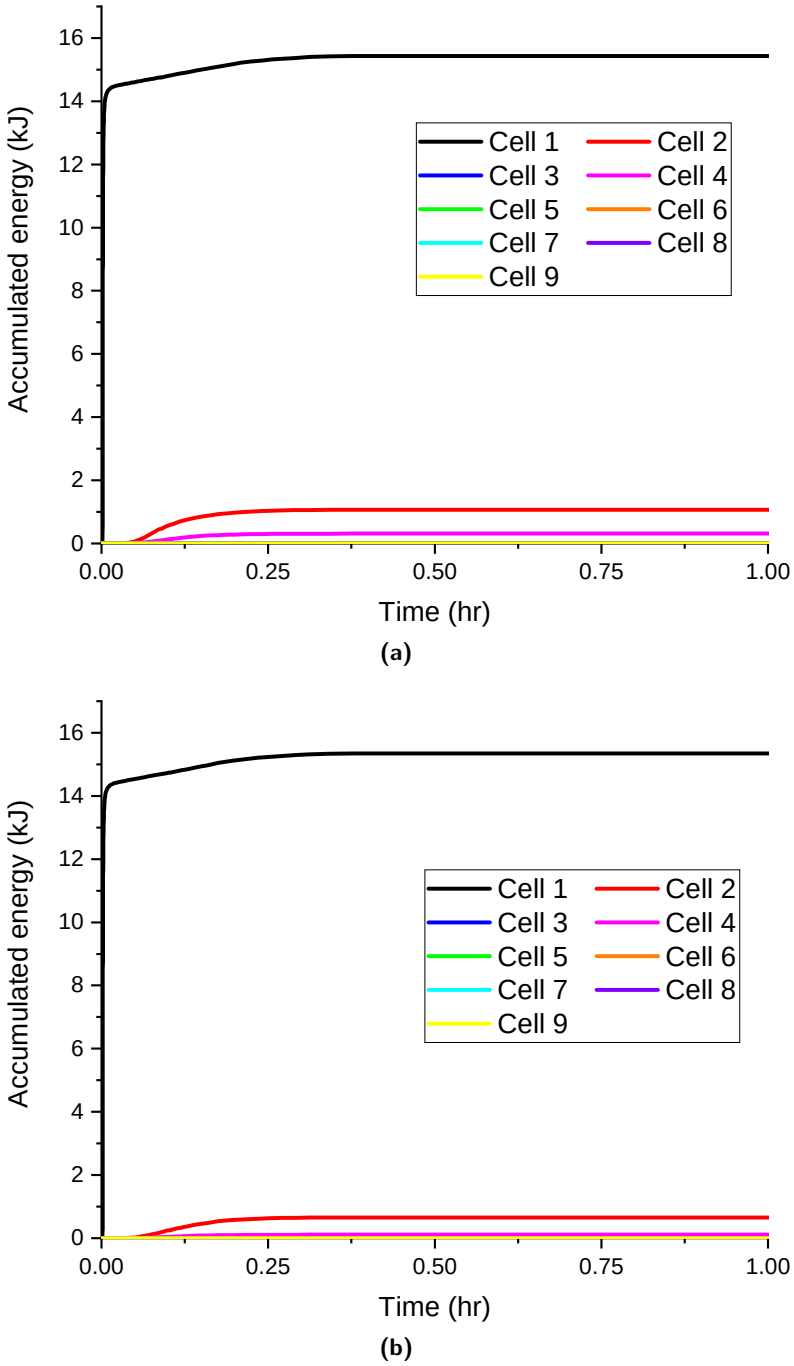

Figure B.3: Accumulated energy from decomposition for each cell within pack, where Cell 1 is abused by short circuit. Sub-figures are for models utilising different abuse parameters and burst pressures - (a) MAH, (b) MAL, (c) MBH, (d) MBL.

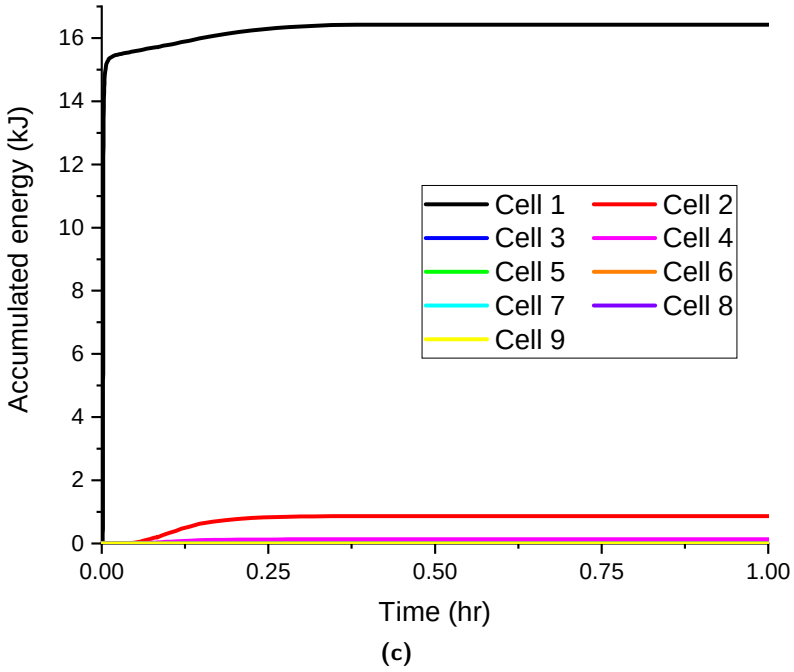

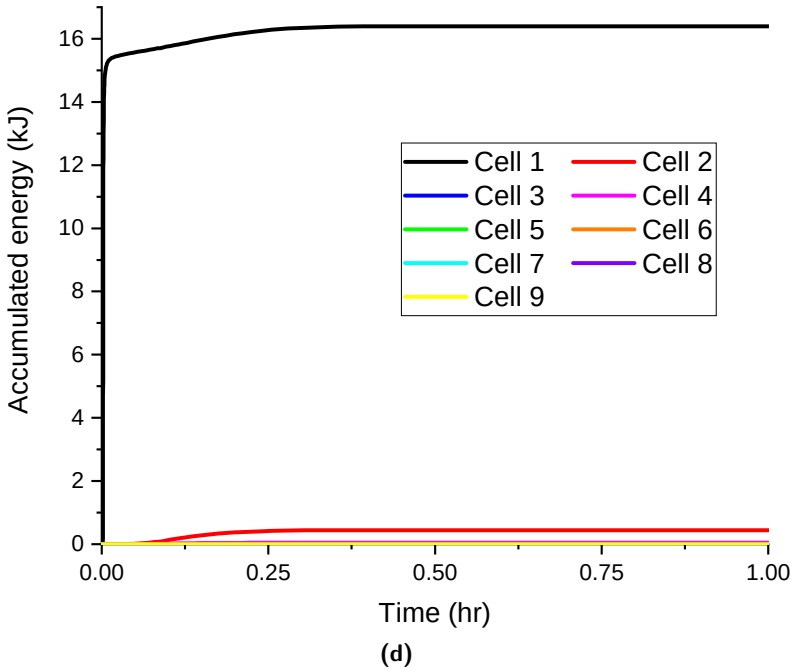

Figure B.3 (cont.): Accumulated energy from decomposition for each cell within pack, where Cell 1 is abused by short circuit. Sub-figures are for models utilising different abuse parameters and burst pressures - (a) MAH, (b) MAL, (c) MBH, (d) MBL.

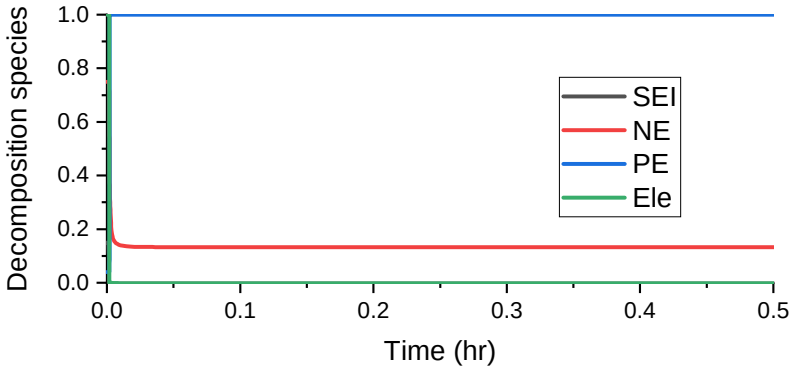

(a) Cell 1

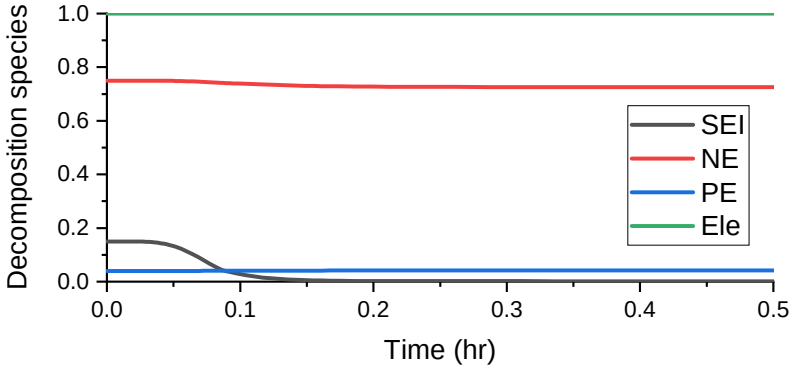

(b) Cell 2

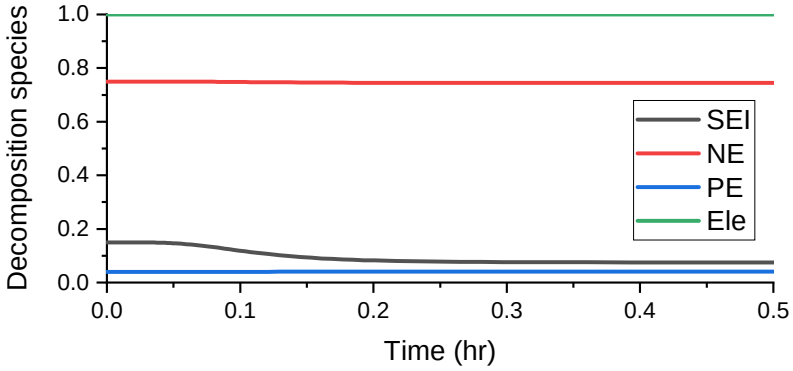

(c) Cell 4

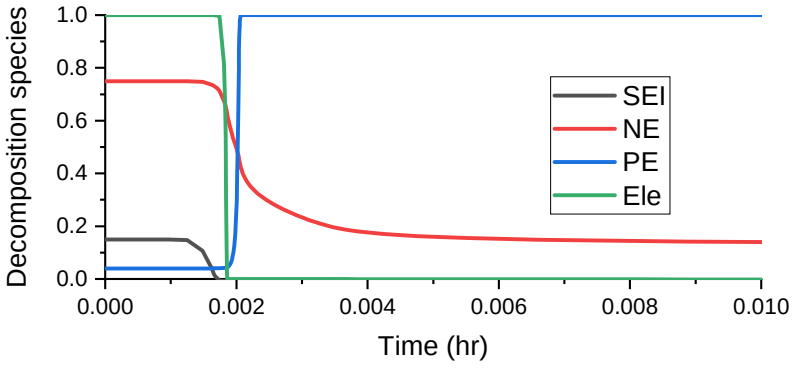

(d) Cell 1, enlargment of time period when short occurs

Figure B.4: Decomposition species of individual reactions for cells 1, 2 and 4 (parameter set MAL).

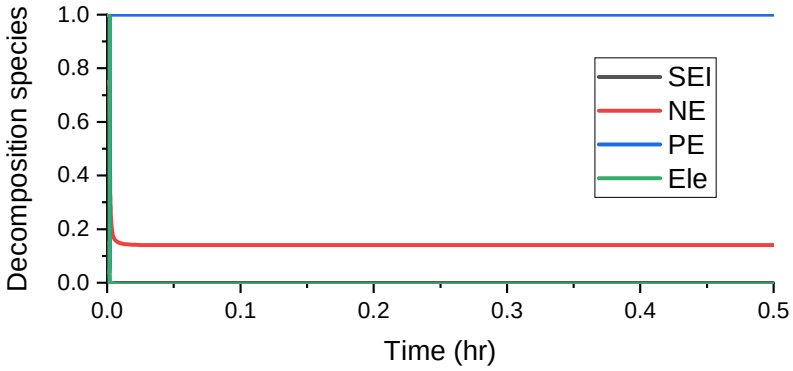

(a) Cell 1

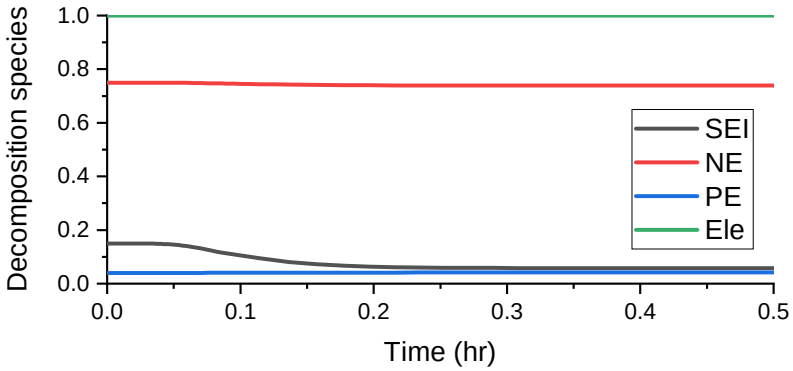

(b) Cell 2

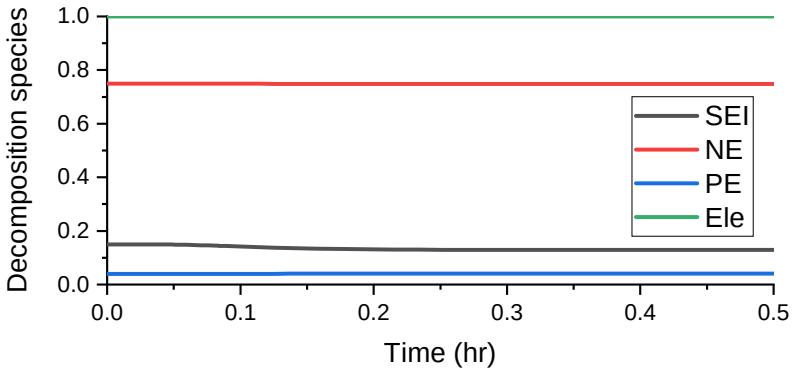

(c) Cell 4

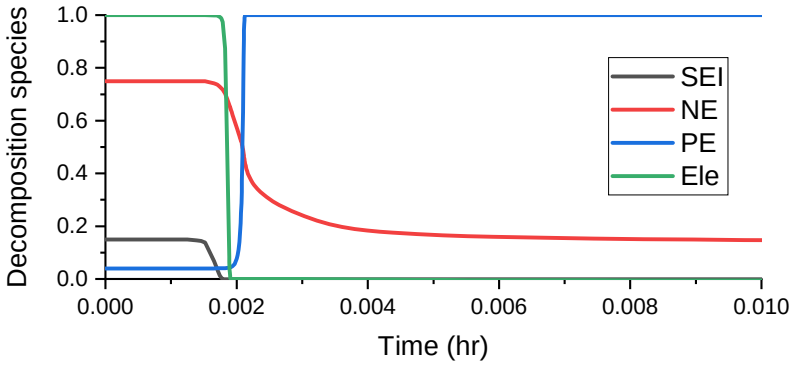

(d) Cell 1, enlargment of time period when short occurs

Figure B.5: Decomposition species of individual reactions for cells 1, 2 and 4 (parameter set MBH).

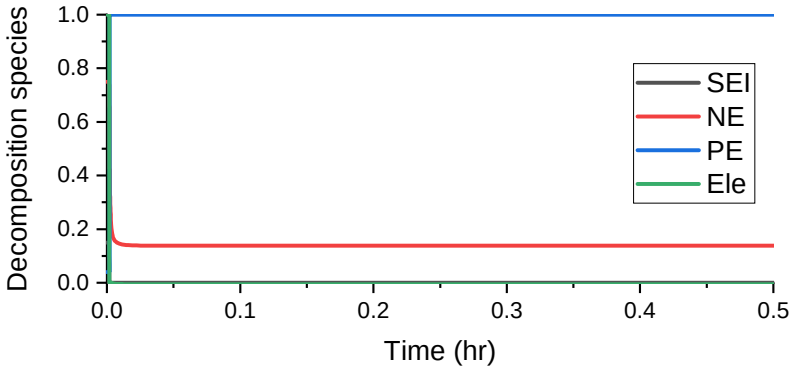

(a) Cell 1

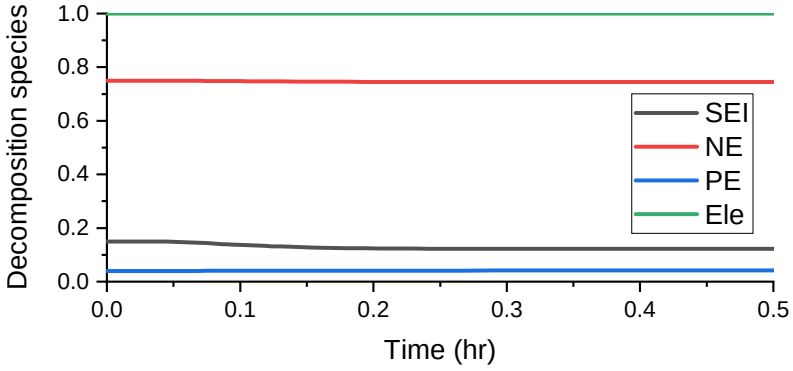

(b) Cell 2

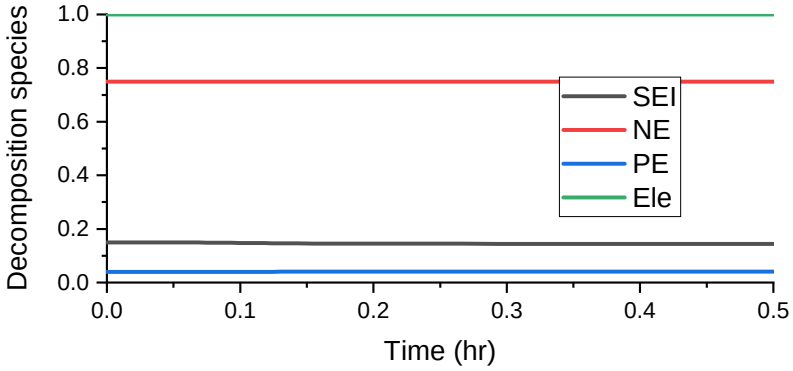

(c) Cell 4

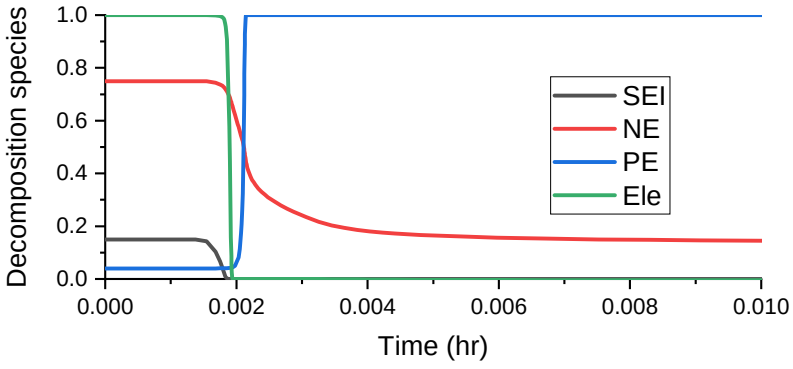

(d) Cell 1, enlargment of time period when short occurs

Figure B.6: Decomposition species of individual reactions for cells 1, 2 and 4 (parameter set MBL).

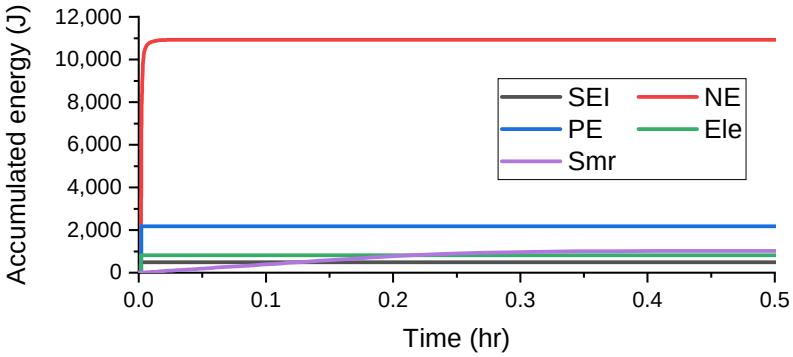

(a) Cell 1

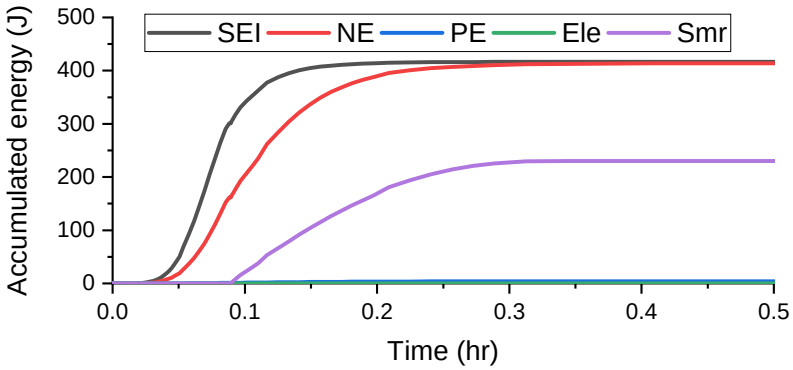

(b) Cell 2

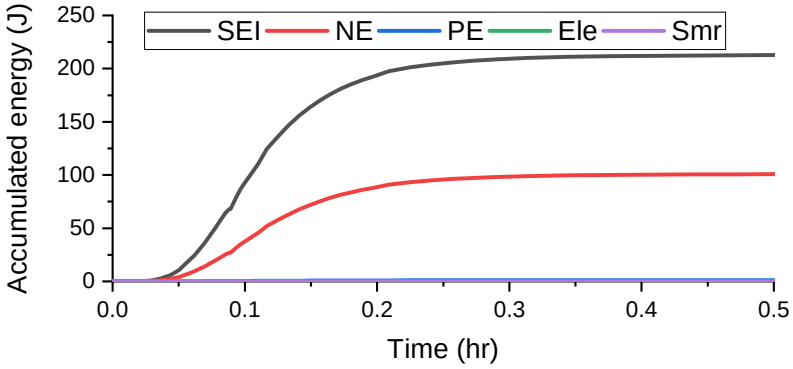

(c) Cell 4

Figure B.7: Accumulated energy of individual reactions for cells 1, 2 and 4 (parameter set MAL).

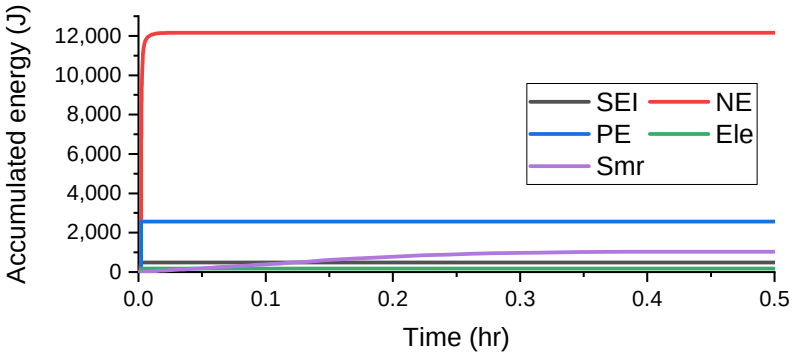

(a) Cell 1

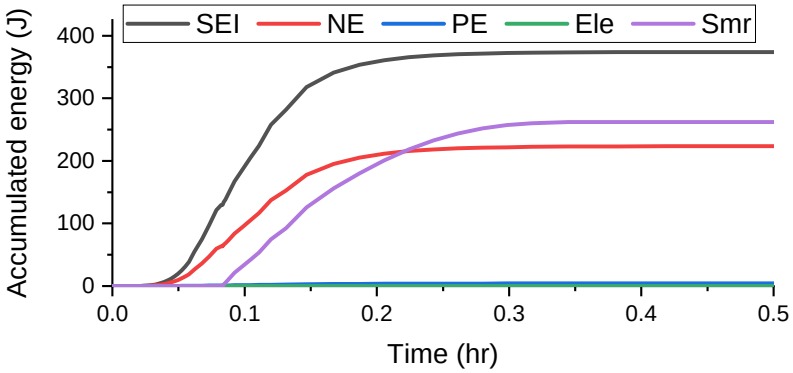

(b) Cell 2

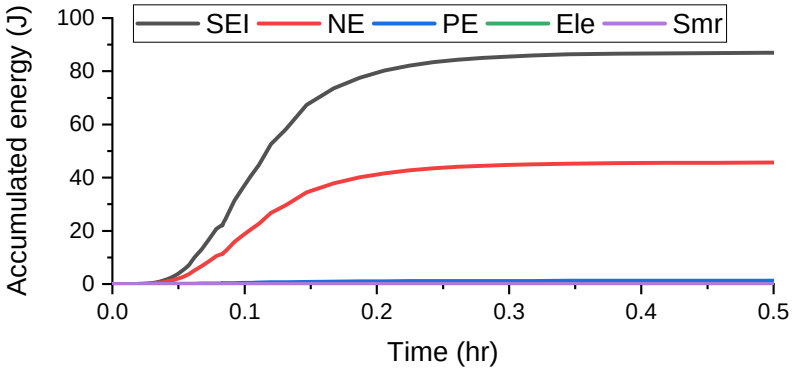

(c) Cell 4

Figure B.8: Accumulated energy of individual reactions for cells 1, 2 and 4 (parameter set MBH).

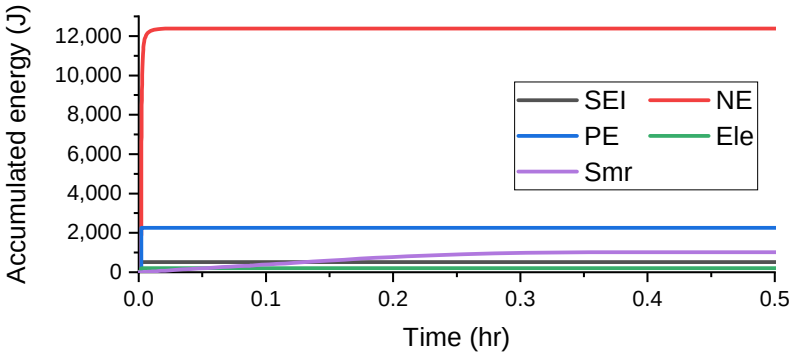

(a) Cell 1

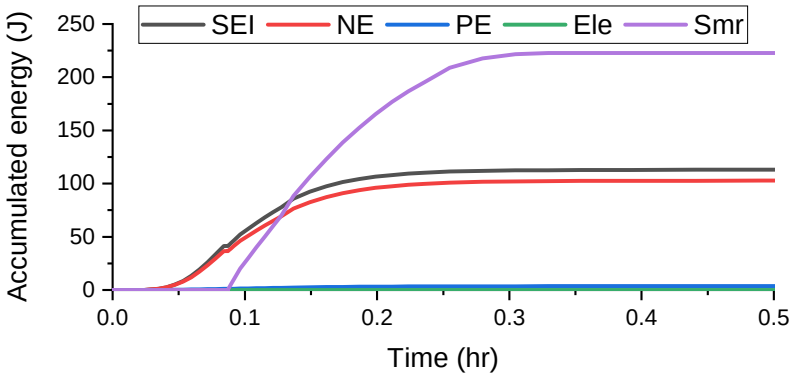

(b) Cell 2

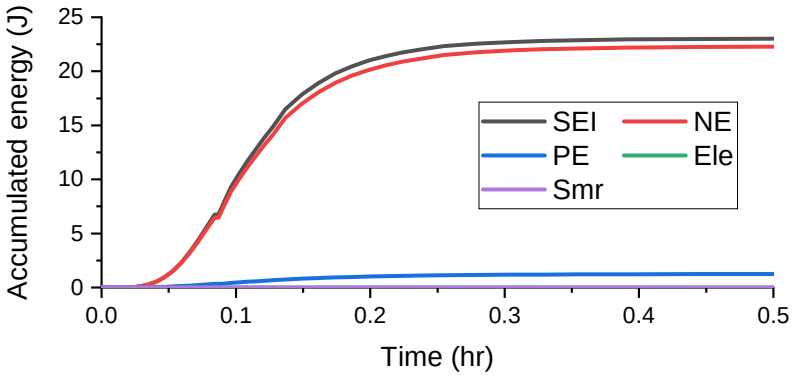

(c) Cell 4

Figure B.9: Accumulated energy of individual reactions for cells 1, 2 and 4 (parameter set MBL).

Table B.2: Heat transfer to/from (positive/negative value) individual cells up to the respective times of maximum cell temperatures with inter-cell spacing $d_{cc} = 1\,\text{mm}$.

Heat transfer	**Cell**								
(J)	**1**	**2**	**3**	**4**	**5**	**6**	**7**	**8**	**9**
				$\varepsilon_{cell} = 0$					
Radiation	0	0	0	0	0	0	0	0	0
Surface conduction	-491	371	-105	2843	744	-3	3	321	121
Tab conduction	-258	3470	1137	-476	459	655	588	73	143
Total	-749	3841	1032	2367	1203	652	590	394	264
				$\varepsilon_{cell} = 0.27$					
Radiation	-133	593	65	808	536	82	55	93	50
Surface conduction	-392	377	-107	2235	488	-36	-19	313	98
Tab conduction	-229	2900	1085	-417	330	652	622	44	152
Total	-754	3870	1042	2627	1353	698	657	450	300
				$\varepsilon_{cell} = 0.54$					
Radiation	-255	1197	129	1567	914	143	106	172	101
Surface conduction	-387	264	-101	1697	303	-23	-5	297	82
Tab conduction	-232	2472	1001	-357	261	607	625	31	151
Total	-874	3933	1030	2906	1479	726	726	500	333
				$\varepsilon_{cell} = 0.8$					
Radiation	-326	1699	205	2190	1242	212	172	272	161
Surface conduction	-335	164	-102	1277	174	4	-17	277	62
Tab conduction	-213	2119	959	-329	193	555	636	8	149
Total	-874	3982	1063	3139	1610	771	791	556	373
				$\varepsilon_{cell} = 1$					
Radiation	-413	2048	276	2612	1501	277	237	361	218
Surface conduction	-329	102	-113	991	78	0	-30	252	42
Tab conduction	-213	1869	931	-297	135	534	639	-8	147
Total	-955	4019	1094	3306	1714	811	846	605	407

Table B.3: Heat transfer to/from (positive/negative value) individual cells up to the respective times of maximum cell temperatures with inter-cell spacing $d_{cc} = 2\,\text{mm}$.

Heat transfer	**Cell**								
(J)	**1**	**2**	**3**	**4**	**5**	**6**	**7**	**8**	**9**
				$\varepsilon_{cell} = 0$					
Radiation	0	0	0	0	0	0	0	0	0
Surface conduction	-574	1250	205	2250	809	-56	-76	266	104
Tab conduction	-175	2396	687	-377	138	583	532	19	79
Total	-749	3645	892	1874	947	526	456	285	183
				$\varepsilon_{cell} = 0.27$					
Radiation	-145	664	87	893	602	111	76	119	57
Surface conduction	-426	1070	168	1719	495	-49	-105	244	82
Tab conduction	-144	1962	664	-337	75	536	585	-1	92
Total	-715	3696	919	2276	1171	598	556	362	231
				$\varepsilon_{cell} = 0.54$					
Radiation	-273	1306	162	1682	1026	190	132	222	114
Surface conduction	-418	801	143	1244	300	-43	-91	229	66
Tab conduction	-145	1648	647	-296	36	514	601	-19	96
Total	-836	3755	953	2631	1362	661	642	432	277
				$\varepsilon_{cell} = 0.8$					
Radiation	-358	1832	242	2326	1384	277	205	326	186
Surface conduction	-377	577	131	899	157	-53	-106	201	39
Tab conduction	-136	1411	623	-290	-2	497	627	-23	100
Total	-871	3819	997	2936	1539	721	726	504	325
				$\varepsilon_{cell} = 1$					
Radiation	-422	2166	308	2688	1624	351	266	420	253
Surface conduction	-354	441	115	676	56	-57	-98	170	9
Tab conduction	-130	1251	601	-239	-23	468	615	-32	101
Total	-906	3859	1024	3125	1657	762	784	558	363

Table B.4: Heat transfer to/from (positive/negative value) individual cells up to the respective times of maximum cell temperatures with inter-cell spacing $d_{cc} = 4\,\text{mm}$.

Heat transfer	**Cell**								
(J)	**1**	**2**	**3**	**4**	**5**	**6**	**7**	**8**	**9**
				$\varepsilon_{cell} = 0$					
Radiation	0	0	0	0	0	0	0	0	0
Surface conduction	-575	895	64	1566	571	56	48	147	66
Tab conduction	-156	2305	614	-217	96	307	256	25	38
Total	-731	3201	678	1349	666	363	304	171	104
				$\varepsilon_{cell} = 0.27$					
Radiation	-160	698	116	904	641	154	105	162	66
Surface conduction	-409	750	53	1141	306	31	35	113	37
Tab conduction	-125	1813	559	-197	18	281	291	-9	58
Total	-694	3261	728	1848	965	466	431	266	161
				$\varepsilon_{cell} = 0.54$					
Radiation	-267	1374	200	1714	1099	261	173	285	128
Surface conduction	-366	539	31	763	146	3	20	89	20
Tab conduction	-117	1472	544	-189	-19	284	337	-27	65
Total	-750	3385	776	2289	1226	547	530	347	213
				$\varepsilon_{cell} = 0.8$					
Radiation	-369	1898	278	2313	1446	365	241	411	203
Surface conduction	-349	377	28	491	41	-16	19	60	-4
Tab conduction	-114	1230	520	-168	-46	269	358	-45	66
Total	-832	3505	825	2636	1441	618	617	426	266
				$\varepsilon_{cell} = 1$					
Radiation	-468	2231	351	2663	1698	450	311	511	265
Surface conduction	-351	284	-2	329	-34	-24	-3	35	-19
Tab conduction	-115	1070	515	-136	-74	246	375	-57	64
Total	-934	3585	864	2856	1590	672	683	490	310

Table B.5: Heat transfer to/from (positive/negative value) individual cells from respective times of peak cell temperatures to end of simulation with inter-cell spacing $d_{cc} = 0\,\text{mm}$.

Heat transfer	**Cell**								
(J)	**1**	**2**	**3**	**4**	**5**	**6**	**7**	**8**	**9**
				$\varepsilon_{cell} = 0$					
Radiation	0	0	0	0	0	0	0	0	0
Surface conduction	-26909	-3825	-1036	-1364	-941	-652	-810	-293	-312
Tab conduction	-5212	-787	-51	-1866	-509	-40	62	-210	-14
Total	-32121	-4612	-1087	-3230	-1450	-692	-747	-504	-326
				$\varepsilon_{cell} = 0.27$					
Radiation	-3811	-301	-62	-154	-82	-45	-45	-25	-18
Surface conduction	-23403	-3486	-968	-1405	-931	-629	-779	-294	-320
Tab conduction	-4748	-790	-71	-1781	-525	-52	32	-225	-17
Total	-31963	-4578	-1100	-3340	-1538	-726	-791	-543	-355
				$\varepsilon_{cell} = 0.54$					
Radiation	-6278	-468	-80	-209	-132	-64	-55	-28	-20
Surface conduction	-21030	-3374	-982	-1578	-967	-644	-806	-329	-347
Tab conduction	-4397	-814	-62	-1754	-538	-53	16	-230	-18
Total	-31704	-4655	-1124	-3541	-1636	-762	-845	-587	-385
				$\varepsilon_{cell} = 0.8$					
Radiation	-8165	-604	-82	-267	-184	-76	-49	-24	-13
Surface conduction	-19264	-3273	-988	-1743	-990	-641	-859	-364	-380
Tab conduction	-4128	-827	-77	-1712	-553	-77	8	-241	-21
Total	-31558	-4705	-1147	-3721	-1726	-794	-900	-629	-414
				$\varepsilon_{cell} = 1$					
Radiation	-9490	-710	-75	-318	-225	-84	-38	-22	-7
Surface conduction	-18138	-3202	-1011	-1860	-1004	-647	-900	-395	-406
Tab conduction	-3952	-842	-77	-1696	-569	-89	-6	-246	-26
Total	-31581	-4754	-1163	-3874	-1797	-820	-944	-663	-439

Table B.6: Heat transfer to/from (positive/negative value) individual cells from respective times of peak cell temperatures to end of simulation with inter-cell spacing $d_{cc} = 4\,\text{mm}$.

Heat transfer	**Cell**								
(J)	**1**	**2**	**3**	**4**	**5**	**6**	**7**	**8**	**9**
				$\varepsilon_{cell} = 0$					
Radiation	0	0	0	0	0	0	0	0	0
Surface conduction	-26385	-2726	-679	-394	-267	-295	-299	-57	-58
Tab conduction	-6433	-575	83	-866	-294	20	59	-51	7
Total	-32818	-3302	-597	-1260	-561	-276	-240	-108	-51
				$\varepsilon_{cell} = 0.27$					
Radiation	-6049	-344	-31	62	-51	-30	-2	16	9
Surface conduction	-21159	-2418	-686	-803	-410	-372	-417	-123	-113
Tab conduction	-5363	-613	68	-1021	-401	22	58	-88	5
Total	-32571	-3374	-649	-1762	-861	-380	-361	-195	-99
				$\varepsilon_{cell} = 0.54$					
Radiation	-9327	-524	-29	105	-98	-47	7	37	24
Surface conduction	-18254	-2339	-711	-1185	-540	-415	-503	-190	-172
Tab conduction	-4662	-686	44	-1135	-484	1	39	-118	3
Total	-32243	-3548	-696	-2215	-1122	-460	-456	-271	-145
				$\varepsilon_{cell} = 0.8$					
Radiation	-11562	-667	-13	85	-165	-59	26	57	41
Surface conduction	-16371	-2297	-758	-1463	-633	-455	-588	-257	-233
Tab conduction	-4164	-743	27	-1197	-537	-17	23	-146	-3
Total	-32097	-3706	-745	-2575	-1335	-531	-539	-346	-195
				$\varepsilon_{cell} = 1$					
Radiation	-12918	-772	-4	41	-245	-63	36	76	60
Surface conduction	-15229	-2284	-773	-1638	-681	-492	-634	-314	-290
Tab conduction	-3839	-776	-6	-1226	-559	-30	-5	-169	-7
Total	-31987	-3832	-783	-2823	-1485	-585	-603	-408	-237